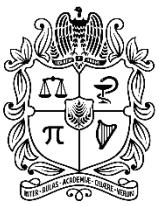

UNIVERSIDAD
NACIONAL
DE COLOMBIA

Extruder for 3D Bioprinting with Composed Bioink Oriented to the Cellular Viability Evaluation in the Generation of Tissues.

Christian Augusto Silva Castellanos.

Universidad Nacional de Colombia.

Faculty of Engineering, Department of Mechanical and Mechatronics Engineering.

Bogotá, Colombia.

2023.

II Extruder for 3D Bioprinting with Composed Bioink Oriented to the Cellular Viability Evaluation in the Generation of Tissues.

Extruder for 3D Bioprinting with Composed Bioink Oriented to the Cellular Viability Evaluation in the Generation of Tissues.

Christian Augusto Silva Castellanos.

The thesis document presented as a partial requirement to qualify for the degree:

Doctor en Ingeniería-Ingeniería Mecánica y Mecatrónica.

Advisor:

Ph.D. Carlos Julio Cortés Rodríguez.

Research Field:

Biomechanics and Tissue Engineering.

Research Team:

Biomechanics Research Group GIBM-UN.

Universidad Nacional de Colombia.

Faculty of Engineering, Department of Mechanical and Mechatronics Engineering.

Bogotá, Colombia.

2023.

Success is knowing your purpose in life, growing to reach your full potential, and planting seeds that benefit others.

(John C. Maxwell)

Declaración de obra original

Yo declaro lo siguiente:

He leído el Acuerdo 035 de 2003 del Consejo Académico de la Universidad Nacional. «Reglamento sobre propiedad intelectual» y la Normatividad Nacional relacionada al respeto de los derechos de autor. Esta disertación representa mi trabajo original, excepto donde he reconocido las ideas, las palabras, o materiales de otros autores.

Cuando se han presentado ideas o palabras de otros autores en esta disertación, he realizado su respectivo reconocimiento aplicando correctamente los esquemas de citas y referencias bibliográficas en el estilo requerido.

He obtenido el permiso del autor o editor para incluir cualquier material con derechos de autor (por ejemplo, tablas, figuras, instrumentos de encuesta o grandes porciones de texto).

Por último, he sometido esta disertación a la herramienta de integridad académica, definida por la universidad.

_____

Nombre: Christian Augusto Silva Castellanos.

Fecha 01/02/2023

Acknowledgments

I want to express my most sincere thanks to the many who assisted me during this research; this thesis could not have been completed without their help.

To the *Universidad Nacional de Colombia,* my “Alma Mater,” to my supervisor, Ph.D. Carlos Julio Cortes Rodriguez for his guidance, support, help, and encouragement.

To FAU *University* and Prof. Dr.-Ing. habil. Aldo R. Boccaccini, who allowed me to do the experimental part of my research in Germany; Colciencias, who supported me with a scholarship for pursuing my doctoral studies; To the *Deutscher Akademischer Austauschdienst* (DAAD), which financially supported my research internship in Germany.

To the *Cellink Company* and Ph.D. Hector Martinez welcomed me in Sweden as a research intern and allowed me to consolidate my research project with Dr. Deepak Kalaskar at the *University College of London* (UCL), who allowed me to develop a research internship to transfer my knowledge to his laboratory in London.

To *Universidad Autónoma de Zacatecas* (UAZ) Mexico, which opened its spaces for me to give a series of conferences and workshops to conduct the transfer of knowledge in the field of 3D bioprinting related to my thesis requested by Colciencias as a product of technological development and innovation to grant the scholarship credit forgiven.

To the *International Journal of Bioprinting WHIOCE,* which published the scientific paper result of my research (Rational Design of a Triple-Layered Coaxial Extruder System: in silico and in vitro Evaluations Directed toward Optimizing Cell Viability).

To *Fabrilab*, a technology-based company that I have created within the creative industries framework in Colombia, to benefit hundreds of people with the knowledge acquired and related during my Ph.D. study period.

To all the people who helped me reach this academic goal, Finally, but not less importantly, my parents, wife, and two little children gave me the strength, courage, and emotional support to keep moving forward with my research.

Resumen

Extrusor para Bioimpresión 3D con Biotinta Compuesta Orientado a la Evaluación de Viabilidad Celular en la Generación de Tejidos.

La bioimpresión 3D es una estrategia de biofabricación emergente que emplea biotintas y modelos generados con herramientas tipo CAD para la fabricación automatizada de andamiajes de tejidos y constructos similares a órganos. A pesar de los avances recientes en materiales y técnicas con gran potencial para lograr la fabricación de tejidos relevantes para aplicaciones clínicas e in vitro, varios aspectos tales como la vascularización de tejidos y la funcionalidad prolongada de las células están limitada a los avances en este campo. Entre las diversas técnicas de bioimpresión 3D, la bioimpresión basada en extrusión (EBB) ha sido concebida como la más prometedora para lograr este objetivo, debido a su versatilidad y disponibilidad. En este documento se informa el desarrollo de sistemas de extrusión de tres y de cuatro capas alineadas axialmente destinados a resolver las limitaciones actuales que se enfrentan al intentar fabricar tejidos vascularizados y estructuras vasculares estables y perfundibles. Combinamos simulaciones in silico con experimentos in vitro para diseñar con precisión múltiples sistemas de extrusión de tejidos en capas axiales con alto grado de viabilidad celular y versatilidad para aplicaciones de bioimpresión 3D. Además, informamos las modificaciones de hardware y software realizadas en impresoras 3D y bioimpresoras disponibles comercialmente para permitir la deposición simultánea de múltiples materiales usando boquillas coaxiales. Finalmente, demostramos la versatilidad y el potencial del sistema de extrusión coaxial de cuatro capas mediante la impresión de constructos vasculares perfundibles y de redes vasculares con algunas biotintas disponibles comercialmente. Nuestro trabajo allana el camino para el diseño racional de sistemas de extrusión coaxial con gran potencial en la fabricación de constructos tubulares huecos relevantes para imitar estructuras que se encuentran en el cuerpo humano.

Palabras clave: Bioimpresión 3D, impresión coaxial, tejidos vascularizados, ingeniería tisular, viabilidad celular.

X Extruder for 3D Bioprinting with Composed Bioink Oriented to the Cellular Viability Evaluation in the Generation of Tissues.

Abstract

Extruder for 3D Bioprinting with Composed Bioink Oriented to the Cellular Viability Evaluation in the Generation of Tissues.

3D bioprinting is an emerging biofabrication strategy that utilizes bioinks and models generated with CAD-like tools for the automated fabrication of tissue scaffolds and organ-like constructs. Despite recent advances in materials and techniques with significant potential to achieve the fabrication of tissues relevant for clinical and in vitro applications, various aspects, such as tissue vascularization and prolonged cell functionality, are limited by the advancements in this field. Among the different 3D bioprinting techniques, extrusion-based bioprinting (EBB) has been conceived as the most promising for achieving this goal due to its versatility and availability. This document reports on developing three- and four-layer extrusion systems axially aligned to overcome the current limitations faced when attempting to manufacture vascularized tissues and stable, perfusable vascular structures. We combined in silico simulations with in vitro experiments to precisely design multiple axial layered tissue extrusion systems with a high degree of cellular viability and versatility for 3D bioprinting applications.

Furthermore, we report the hardware and software modifications made on commercially available 3D printers and bioprinters to allow the simultaneous deposition of multiple materials using coaxial nozzles. Finally, we demonstrate the versatility and potential of the four-layer coaxial extrusion system by printing perfusable vascular constructs and vascular networks with some commercially available bioinks. Our work paves the way for the rational design of coaxial extrusion systems with enormous potential in manufacturing hollow tubular constructs relevant to mimic structures found in the human body.

Keywords: 3D bioprinting, coaxial printing, vascularized tissues, tissue-engineered vascular grafts, cell viability.

Content

List of Figures

List of tables

List of equations

List of symbols and abbreviations

Symbols with Latin characters

Symbol	Term	Unit SI	Definition
A	Area	m^2	$\iint dx\, dy$
G'	Loss modulus	Pa	$kg{\cdot}m^{-1}{\cdot}s^{-2}$
G''	Storage modulus	Pa	$kg{\cdot}m^{-1}{\cdot}s^{-2}$
G*	Complex modulus	Pa	$kg{\cdot}m^{-1}{\cdot}s^{-2}$

Symbols with Greek characters

Symbol	Term	Unit SI	Definition
η	Dynamic viscosity	Pa-s.	
$\dot{\gamma}$	Shear rate	$1/s.$	
δ	Phase angle	Rad.	$360° = 2\pi$ rad
ω	Angular frequency sweep	Rad/s.	dθ / dt
τ	Shear Stress		
ρ	Density	Kg/ m^3	

Index

Symbol	Term
K	Consistency coefficient
n	Power law index or Shear-thinning index

Abbreviations

Abbreviation	Definition
3D	Three-dimensional
EBB	Extrusion-based bioprinting
TE	Tissue engineering
RM	Regenerative medicine
CFD	Computational fluid dynamics
FDM	Fused deposition modeling
2D	Two-dimensional
CT	Computed tomography
MRI	Magnetic resonance imaging
PCL	Polycaprolactone
PEG	Polyethylene glycol
PEO	Polyethylene oxide
ECM	Extracellular matrix
CAD	Computer-aided design
GCODE	Geometry code
STL	Standard Tessellation Language
3MF	3D Manufacturing Format
AMF	Additive manufacturing file format
OBJ	Wavefront object
DSP	Direct sound printing
UV	Ultraviolet
dECMs	Decellularized extracellular matrices
PTFE	Polytetrafluoroethylene
PET	Polyether terephthalate
DLP	Digital light processing
RGD	Sequence of amino acids arginine-glycine-aspartic acid
FDA	The U.S. Food and Drug Administration
hMCs	Human mesenchymal stem cells
hiPSCs	Human-induced pluripotent stem cells
CFR	The Code of Federal Regulations
HESCs	human embryonic stem cells
ATPS	Aqueous two-phase system
SSM	Supportive suspension medium
GFP	Green Fluorescent Protein
SEP	Standard Extrusion Pressure
DEFECOSUFH	Device for freeform embedding coaxial of suspended functional hydrogel.

Associated publications.

The research work presented in this dissertation represents a collaborative effort between the Biomechanics Research Group at GIBM-UN, Universidad Nacional de Colombia, Colombia, and FAU University, Germany, during a research internship under Prof. Dr.-Ing. habil. Aldo R. Boccaccini, I had the opportunity to conduct the experimental part of this study with the support of the Deutscher Akademischer Austauschdienst (DAAD).

Furthermore, I would like to acknowledge the invaluable contributions made by the Cellink Bioprinting Company, Sweden, during another research internship under the supervision of a Ph.D. Hector Martinez. Their involvement played a crucial role in consolidating the experimental aspects of this research project.

It is essential to mention that these collaborations were made possible through the generous sponsorship provided by the Colombian Ministry of Technology, Science, and Innovation (MINCIENCIAS) under Call 647 in 2015.

The culmination of our collective efforts resulted in one associated publication, which is detailed below:

Paper:

C. Silva, C. J. Cortés-Rodriguez, J. Hazur, S. Reakasame, and A. R. Boccaccini, “Rational design of a triple-layered coaxial extruder system: In silico and in vitro evaluations directed toward optimizing cell viability,” Int. J. Bioprinting, vol. 6, no. 4, pp. 1–10, 2020.

Thesis outline

Chapter 1 of this thesis delves into the realms of tissue engineering and regenerative medicine, exploring the lofty aspirations within tissue and organ fabrication domains. This chapter serves as the foundation for the emergence of the biofabrication field. Subsequently, it offers an in-depth exploration of various biofabrication methodologies, particularly emphasizing the intricate techniques employed in 3D bioprinting.

Chapter 2 provides an up-to-date overview of the innovative technologies central to this thesis. It includes a literature review on Embedded Bioprinting (EBB) and its application in creating cell-embedded vascular structures and exploring other bioprinting techniques. The chapter underscores the enduring significance of EBB as the most promising approach for realizing the ultimate objective of manufacturing complex, multilayered, and fully functional vascular structures in vitro. These structures can be utilized as standalone vascular grafts or seamlessly integrated within tissue constructs to establish intricate vascular networks.

Chapter 3 outlines the rational design and in vitro assessment of a triple-layered coaxial extrusion system tailored for Embedded Bioprinting (EBB) technologies. Specifically, it emphasizes the paramount importance of upholding cell viability throughout EBB processes. The chapter provides a comprehensive overview of the proposed workflow for the systematic design of cell-friendly coaxial extrusion systems, which incorporates prototyping and Computational Fluid Dynamics (CFD) simulations to investigate the impact of design parameters on cell viability.

Additionally, the projected outcomes from CFD simulations are experimentally validated in vitro through bioprinting experiments involving the fabrication of single-layered hollow tubular structures. These experiments employ bioinks derived from commonly used biomaterials within the field and employ human cells. This chapter provides details on the methods used, including the specifics of the CFD simulation conditions, the necessary modifications to adapt a Fused Deposition Modeling (FDM) 3D printer for hydrogel deposition, the bioprinting procedures, as well as the comprehensive cell viability assays conducted, among other pertinent aspects.

Chapter 4 This chapter evaluates supplementary findings and practical implementations of developing embedded multilayered vessel-like structures created using a novel four-layered coaxial system integrated with a temperature management system. It is worth noting that, to the best of our knowledge, this unique combination has not been previously documented in the existing literature. The study encompasses the utilization of three distinct human cell lines and four commercially available bioinks.

Furthermore, the chapter investigates the impact of employing different extrusion pressures, ranging from optimal to suboptimal, and explores the influence of two varying temperatures within four-layered coaxial systems. These systems exhibit varying outlet areas for each channel while maintaining controlled temperature regulation at the coaxial nozzles.

In addition to detailing the design and prototyping of the coaxial extrusion system, this chapter covers the hardware and software modifications made to a commercial 3D bioprinter, enabling simultaneous material dispensing through four independent pneumatic extruders. Moreover, it explores the four-layered coaxial extrusion systems' applications in creating multi-material and multiscale vascular channels and structures, utilizing a range of commercially available bioinks and sacrificial materials. Emphasis is placed on the mechanical, electronic, and software adaptations implemented on the 3D bioprinter to accommodate the two additional pneumatic extruders.

Finally**, Chapter 5** presents the conclusions of this thesis and describes a series of final remarks and recommendations for future work that can be derived from the detailed research. Moreover, the limitations of this work are discussed.

Problem Statement and Motivation

Cell viability values on EBB processes are typically between **40 and 80%** [12] [13] [14] [15], mainly because cells are exposed to shear stress induced by extrusion pressure at the moment of deposition through a nozzle.

The TE and RM medicine fields still lack effective patient-specific solutions for replacing or bypassing medium and large-diameter arteries and veins. Current approaches are directed towards using synthetic implants or autologous tissues, such as those obtained from the great saphenous vein, intern mammary artery, or radial artery. However, synthetic implants are often made from non-biodegradable polymers such as PTFE or PET, which have been shown to exhibit an increased risk of thrombosis, stenosis, calcification, and infection [1]. Moreover, these implants fail to mimic the mechanical properties of the native vascular tissue and are not feasible as a long-term solution. Conversely, autologous implants are the preferred solution but are challenging to obtain, mainly because of anatomical reasons and limited availability. In addition, autologous implants obtained from the saphenous vein and utilized as bypass grafts present failure rates of around 50% at ten (10) years [1]. Over the last 30 years, and intending to provide patient-specific and reliable vascular grafts, several researchers have employed TE and RM strategies to overcome these limitations present with synthetic and autologous grafts. Although hundreds of engineered vascular grafts have been developed and evaluated in preclinical models, very few have reached clinical trials. Specifically, as of 2019, only two tissue-engineered vascular grafts were undergoing clinical trials in the United States [2]. Despite the low innovation in the field, the market for vascular grafts is expected to grow to USD 3.3 billion by 2026, which displays the great need for novel and reliable solutions. Moreover, diseases of significant global relevance, such as COVID-19, are expected to worsen the burden of cardiovascular diseases [3], [4]. The virus that causes the disease can attack endothelial cells on the inner walls of blood vessels, thus leading to complications related to thromboembolic disease.

Similarly, the development of engineered tissues and organ-like constructs has been limited by the technologies and materials available for biofabrication. Despite recent advances in novel bioprinting and bio-assembly techniques, the fabrication of complex geometries and multi-material constructs remains an unsolved challenge. Moreover, the size of the bio-fabricated constructs is limited to down-scaled models, as incorporating vascular channels

of heterogeneous sizes that closely mimic those found on native tissues is still impossible [5], [6]. Novel technologies aiming to solve vascularization inside tissue construct by allowing the fabrication of hollow multilayered structures have been devised as the next-generation solution to these limitations. Such technologies include FRESH printing, a printing modality and setup adapted to EBB, and digital light processing (DLP), a modality of stereolithographic printing. **However, the current state-of-the-art developments are still incapable of fabricating multilayered hollow structures when employing cell-friendly conditions**, demonstrating the necessity of improving the technologies and processes used for biofabrication [7]. Advances that tackle the limitations of EBB techniques will have the most significant impact on the field, as it is the most popular and accessible bioprinting technique. Improving cell viability upon deposition and developing crosslinking and bioinks that can guarantee high shape fidelity is crucial [8].

The solutions currently offered for EBB are based on using materials with a high viscosity to maintain the printed construct's structural integrity, which increases the pressure required for the material to be extruded through the nozzle and limits communication between the cells. Even post-crosslinking techniques, including those that use UV light, immersion in an ionic bath agent, or temperature change, may weaken cells at the surface of the printed construct. Additionally, techniques that employ **coaxial nozzles have low viability due to the non-optimal geometrical design** of commercial nozzles, which significantly increases the pressure required to extrude any biomaterial.[9]

Coaxial printing is an emerging technology adaptable to EBB and has excellent potential for the biofabrication of vascular structures and channels [5]. In this technique, a multilayered coaxial extrusion system can be employed to directly bioprint vessel-like structures by the simultaneous extrusion of bioinks, crosslinking agents, and sacrificial materials through different channels, thus generating hollow tubular structures with desired diameters, lengths, and wall widths [10], [11]. Geometry can be precisely controlled by tuning bioprinting parameters, crosslinking schemes, and G-code instructions. In contrast, the functionality can be controlled by incorporating different cell types, like fibroblasts, endothelial cells, smooth muscle cells, stem cells, and their density inside the constructs.

Hypothesis

The bioink's rheological properties influence the extrusion pressure during the bioprinting process, the viscosity profile, and the geometry of the nozzle or needle; this biomaterial mixed with cells must be sufficient to guarantee the structural stability of the bioprinted construct. Hollow structures, such as those bioprinted to mimic vascular tissues, require exceptional structural stability, translating into high viscosity required in the bioink to maintain the 3D structure and avoid its collapse over time. Such high viscosities are required to imply high extrusion pressures, which induce detrimental shear stress on cells while being extruded.

As previously demonstrated, this shear stress is maximum at the nozzle walls [16]. When using multi-layered coaxial extrusion systems, cells are in contact with a greater area of the nozzle wall when compared to traditional single-channel nozzles. It is supposed to yield shallow cell viability values, considering the values already obtained on EBB when using single-channel nozzles and the bioink viscosities required for effectively bioprinting hollow tubular structures. Therefore, the design of coaxial extrusion systems must be directed towards minimizing the shear stress exerted on cells during bioprinting processes. **We hypothesize that combining design parameters for multi-layered coaxial extrusion systems will positively affect the cell viability rates** obtained after coaxial- EBB processes.

Furthermore, we propose that multi-layered coaxial extrusion systems have the potential to achieve the bioprinting of hollow tubular structures with superior structural stability and significantly enhanced cell viability rates. This enhancement can be achieved by incorporating the simultaneous extrusion of crosslinking agents during the bioprinting process and by optimizing the existing geometries of commercially available coaxial nozzles available in the market [17].

As the original Ph.D. thesis proposal outlines, our primary objective is to define a precise set of design parameters for a 3D bioprinting coaxial extrusion system. This system's development aims to optimize cell viability rates when employing the Embedded Bioprinting (EBB) technique. Furthermore, by adopting an embedded approach and implementing this

methodology, we anticipate reducing the bioink's viscosity. This reduction in viscosity will, in turn, lower the required extrusion pressure, effectively alleviating shear stress on embedded cells during the bioprinting process. We aim to attain an overall cell viability rate that surpasses 80%.

Objectives

General aim

This work aims to develop multi-layered coaxial extrusion systems with high cell viability by rationally studying *the effect of design parameters and printing parameters during EBB processes in silico and in vitro*. In this way, it is crucial. "***To determine the design parameters of a coaxial bioink extruder system to ensure greater cellular viability using the EBB technique.***"

Specific aims

- ***To Determine*** *computationally the most significant parameters in the design of the extruder system to allow greater cellular viability in contrast to those reported in the revised bibliography.*

- ***To verify*** *experimentally the design parameters of a Bioink coaxial extruder system to manufacture scaffolds with greater cellular viability in contrast to those reported in the revised bibliography*.

Chapter 1

Introductory remarks

1.1 Introduction

Three-dimensional (3D) bioprinting as an additive manufacturing technology permits the spatial-temporal patterning of hydrogels embedded with cells, namely bioinks, into 3D structures [18], [19]. Its goal is to fabricate cell-embedded constructs that mimic tissues and organs, where cell viability is preserved and overall physiological functionality is replicated [18], [20].

Among its several techniques, extrusion-based bioprinting (EBB) has emerged as the most promising additive manufacturing technique for achieving 3D structures of sufficient complexity since it can work with a broad range of cell densities and printable materials [8], [21]. Moreover, the versatility and affordability provided by EBB systems have contributed to its positioning as the most popular biofabrication technology among researchers worldwide for applications that range from cancer research, drug testing,[22] and evaluation of cosmetic products to tissue engineering [23].

Replicating complex internal tissue structures is still challenging for the available biomanufacturing technologies [20], [23]. In the case of EBB, the time lag between hydrogel

extrusion and subsequent crosslinking is one of the limiting factors in forming complex geometries [24], [25]. This is mainly because the viscoelastic properties of extruded bioinks are often not sufficient to support these geometries before extensive crosslinking schemes are performed [24], [26], [27]. Therefore, the shape fidelity of the printed constructs is significantly compromised, especially in the fabrication of hollow or highly detailed structures.[22]

Despite recent advances in the development of techniques that allow an increased structural complexity of constructs and novel hydrogel formulations that support bioprinting and maturation of tissues, functionality is a challenge that has not been fully addressed yet [7], [20], [28]. To engineer functionally relevant tissues *in vitro*, the inability to recreate the 3D microenvironments seen *in vivo* is a critical restriction that must be overcome. Among the attributes that bioprinted constructs must have to permit appropriate tissue maturation, vascular networks appear to be one of the most important [18]–[20], [29].

The scalability of bioprinted constructs toward clinically relevant sizes is often limited by the accessibility of nutrients throughout the construct, as nutrient access and waste removal depend solely on diffusion-mediated transport. As a result, perfusable networks within bioprinted constructs are imperative to create tissues of clinically relevant size, as they will allow adequate nutrient availability and prevent waste accumulation in the innermost regions of the construct [30], [31]. It, in turn, will facilitate the maturation of multilayered constructs and shorten the gap between native and *in vitro* functionality. In addition, biomanufacturing hollow tubular structures might also be beneficial for generating multilayered large- and medium-diameter vascular grafts for transplantation or disease modeling [10], [32], [33]. [22]

Accordingly, this study aimed to develop multilayered coaxial extrusion systems with a rational design-based strategy for facilitating the fabrication of biomimetic tissues and organ-like constructs for tissue engineering (TE) and regenerative medicine (RM) applications.

Triple-layered and four-layered coaxial extrusion systems were designed, and the effect of their design parameters on cell viability was investigated with computational fluid dynamics (CFD) simulations and bioprinting experiments. These coaxial extrusion systems allowed

the controlled and simultaneous dispensing of three and four different materials, respectively, by using EBB.

First, a triple-layered coaxial extrusion system was designed and prototyped. Simultaneously, a fused deposition modeling (FDM) 3D printer was customized to allow the deposition of hydrogels mounted on syringes. Next, CFD simulations were implemented to investigate the effect of the geometric parameters, mainly the outlet diameter and length of each coaxial extrusion channel, on the stress the materials experienced when deposited.

The obtained results were utilized to predict how this design parameter of the coaxial systems influenced cell viability at the moment of extrusion during EBB. Subsequently, bioprinting experiments of single-layered hollow tubular structures with biomaterial hydrogels and human cells (bioink) were performed to evaluate and validate the predictions from the *in-silico* experiments. Furthermore, an upgraded triple-layered coaxial extrusion system was developed and employed for bioprinting double-layered hollow tubular constructs embedded with multiple human cell lines and using three different commercial bioinks. Cell viability experiments were performed to assess the effect of channel outlet area on cell integrity immediately after bioprinting and after a couple of hours in cell culture.

Second, a four-layered coaxial extrusion system was developed. A commercial 3D bioprinter was modified on hardware and software to operate with four printheads instead of the two initially incorporated. Finally, bioprinting schemes and conditions were designed and implemented to fabricate multi-material and multiscale vessel-like structures, which might be promising as large- and medium-diameter vascular grafts.

The novelty of this work is adding value to the research field of bioprinting with the development of triple-layered and four-layered coaxial nozzles with temperature-controlled management that have the potential to fabricate tissues that can closely mimic the histological and morphological complexity of vascular networks found in the native human with a high cell viability rate. Moreover, this work demonstrates how *in silico* simulations can predict events *in vitro*, facilitating rapidness and cost-effectiveness in developing novel techniques and instruments for TE and RM. In addition, this development has the potential to replicate the wall thickness of a native blood vessel that generally comprises three layers:

the innermost tunica intima layer, made by continuous endothelium cells, followed by the middle tunica layer, which contains smooth muscle cells, and an outermost tunica adventitia layer made of surrounding fibroblast and collagen. Therefore, our work paves the way for the rational development of coaxial nozzles proper for bioprinting multilayered vascular channels or vessel-like constructs that genuinely resemble those found in native organs and organisms.[22]

1.2 Background

1.2.1 Biofabrication of Tissues and Organs

TE and RM have provided solutions to pathologies and conditions that affect human well-being using life sciences and engineering knowledge. These conditions include partly damaged or defective organs and tissues, often resulting from genetic defects, traumatic injuries, diseases, or aging. Interest has been focused on the fabrication of functional human organs and tissues *in vitro* and *in situ*, which might eventually be useful as models to assess new drugs and therapies and to alleviate the lack of human organ donors suitable for transplants.

On this first matter, several studies have demonstrated that two-dimensional (2D) cell cultures and animal subjects, as the traditional preclinical testing models of novel drugs and therapies, fail in recapitulating the complex micro- and macro-environments seen in the human system [34], [35].

As a result, in vitro, 3D tissue models and organs-on-chip have been developed for preclinical testing of novel drugs and therapies since they can be designed to closely mimic cell-cell interactions as well as interactions between cells and their matrix, cellular morphology, access to nutrients and waste accumulation, all of which determine cell behavior and play a crucial role in accurately replicating native tissues, organs, and systems. [34], [36].

Moreover, many patients around the world are on a waiting list for human organ transplants, which, in case of no rejection caused by incompatibility issues, could save their lives at the cost of being under a life-long prescription of immunosuppressant.

The goal of tissue engineers is to develop materials and technologies that allow the on-demand fabrication of patient-specific organs using their cells, thus avoiding immune rejection and the risks posed by being life-long immunosuppressed.

It is pertinent to note that biofabrication emerged from this need of the TE and RM fields to fabricate organs and tissues. As recently defined by leading researchers in this field, it involves the automated creation of biologically functional products with a specific structural organization by using “living cells, biomaterials, bioactive molecules cell aggregates, such as hybrid cell-material constructs or microtissues.”[37].

As this technology matures, it not only holds promise for creating tissues and organs for clinical applications but also opens new avenues for understanding the fundamental aspects of human biology, disease pathology, and the restoration of impaired biological functions.

1.2.2 3D Bioprinting Processes

The wide variety of biofabrication techniques can be classified into two subgroups: bioprinting and bio-assembly. This classification depends on the length scale of the minimum building block that the specific technique employs, which can be either biomolecules or pre-formed multicellular units (spheroids) such as cell aggregates, cell fibers, or cell sheets, respectively [37], [38].

The subgroup can be divided into six steps for the bioprinting process, first described in Murphy and Atala's literature[18]. The first step is collecting human body images via X-ray, computed tomography (CT), or magnetic resonance imaging (MRI). These images can then be used to computationally reconstruct 3D representations of internal structures of the human body, such as whole organs, blood vessels, or specific structures within organs.

The second step consists of establishing a design strategy on which biomimicry, autonomous self-assembly, or mini tissue building blocks approaches can be implemented alone or in combination. In the first strategy, identical reproductions of tissues and their components are manufactured, either with a structure- or composition-wise approach. The second strategy is autonomous self-assembly, which ultimately relies on cells as the primary guides of histogenesis, thus directing the composition and functional characteristics of the tissue. This strategy requires extensive knowledge of tissue development mechanisms and morphogenesis, as these must be manipulated to succeed with this design strategy. Finally, the mini-tissue approach is based on the fabrication and subsequent assembly of functional building blocks. It can be implemented using biomimicry or self-assembly strategies since combining several design approaches and technologies is vital for fabricating relevant and functional tissues and organs.

The third and fourth steps of the bioprinting process consist of the material and cell selection, respectively. The choice of materials to print must be made by considering the structural complexity, mechanical properties, and biochemical composition of the tissue to replicate [24], [27], [39].

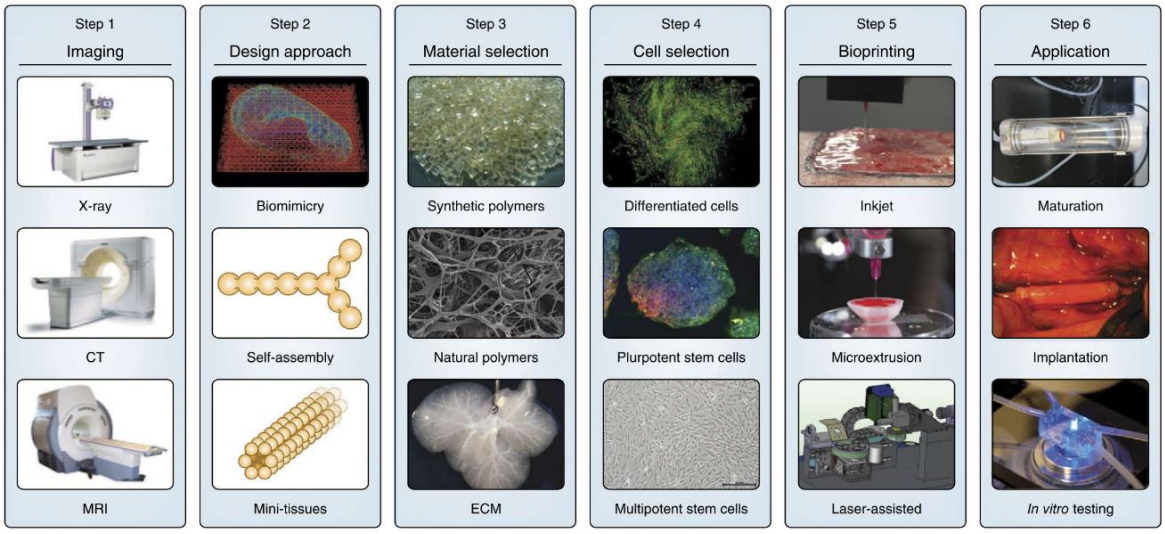

Figure 1 Schematic of the bioprinting process and its six steps: imaging, design approach, material selection, cell selection, bioprinting, and application. Figure adapted from [1].

Depending on their origin, common materials used in 3D bioprinting can be classified as natural or synthetic. Raw materials include gelatine, collagen, chitosan, hyaluronic acid,

and components of the extracellular matrix (ECM), among many others. Despite exhibiting excellent bioactivity, these materials lack sufficient mechanical properties to be printed directly with EBB [8]. Conversely, synthetic materials often lack bioactivity but possess good mechanical properties to print structurally stable constructs.

Some examples of these materials include Polycaprolactone (PCL), polyethylene-glycol (PEG), and polyethylene-oxide (PEO) [40]. After effectively selecting a specific material or a combination thereof, cell selection must be made depending on the application of the construct to be printed based on the tissue to be replicated because different tissues and organs possess distinct cell types, the specific application of the printed constructs might require pluripotent stem cells or fully differentiated and specialized cells. For example, cardiomyocytes are the primary cell type found in cardiac tissue, whereas dermal fibroblasts and keratinocytes are located on the skin. Moreover, a tissue construct aimed at *in situ* regeneration may require the presence of stem cells since these can secrete pro-angiogenic factors and other biomolecules to enhance ECM remodeling and guide the behavior of neighbor cells. On the contrary, a bioprinted construct aimed as an *in vitro* model to assess a novel drug must be fabricated using fully differentiated cells since these are the only ones capable of performing tissue-specific functions to mimic the native organ.

The next step in the overall process is bioprinting, where an automated additive manufacturing machine is provided with instructions to print a 3D computer-aided design (CAD) model. These set of instructions can be provided either complete, as a file with the geometry code of the shape (G-code) extension, or incomplete, as a file with the standard tessellation language (STL), or other extension files such as 3D manufacturing format (3MF), additive manufacturing file format (AMF) or object (OBJ) extension. If these instructions are incomplete, specialized software coupled to the bioprinter is necessary to complete the printing information. In the case of EBB, this information to be completed may include the nozzle dimensions and outlet diameter, infill printing pattern, infill density, layer height profile, extrusion pressure, printing speed, print-bed temperature, and printhead temperature, among several other variables. Finally, after bioprinting, the tissue constructs must undergo a maturation process, in which cells adhere to the matrix and proliferate. Moreover, during the maturation phase, the material used for bioprinting is expected to degrade at a rate that matches the ability of the embedded cells to secrete their EMC proteins and biomolecules and thus remodel their surrounding environment.

1.2.3 3D Bioprinting Techniques

The available bioprinting techniques can be classified into five main groups: extrusion-based, inkjet, stereolithographic, laser-assisted, and direct sound bioprinting (**Figure 2**) [41] [42].

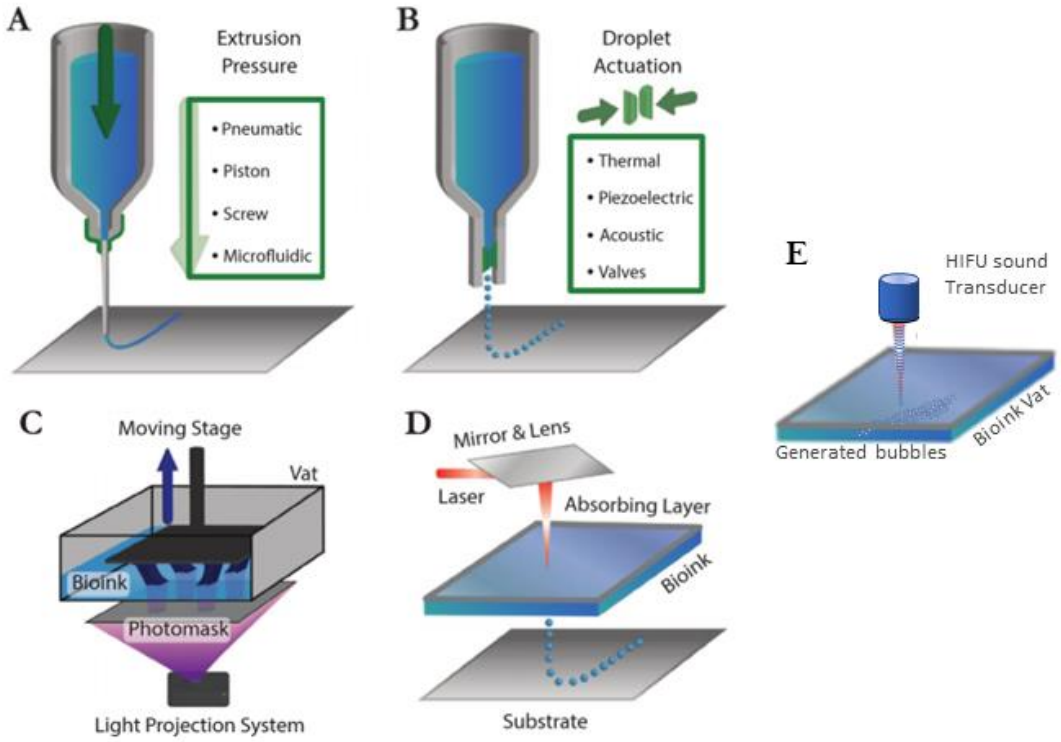

Figure 2. Illustration of (A) extrusion-based bioprinting (EBB), (B) inkjet bioprinting, (C) stereolithographic bioprinting, (D) laser-assisted bioprinting, (E) direct sound bioprinting (DSP). Figure adapted from [41].

Extrusion-based bioprinting (EBB) is one of the most popular techniques, as it is widely available from companies such as Organovo, 3DSystems, Regen-HU, GeSIM, Desktop Health, Advanced Solutions, Rokit, Cellink, among many others, all of which have contributed to the expansion of the field of bioprinting to a larger community of researchers and entrepreneurs over the past seven years [43]. Moreover, this technique is widely popular because it permits the use of a broad range of bioink viscosities, cell densities, and crosslinking schemes.

On EBB, bioinks are held inside syringe-like cartridges and deposited on a surface as a filament in a controlled manner, either by using pneumatic or mechanical pressure, to shape 3D constructs. Despite its significant advantages, the greatest limitation of this technique has been the lack of bioinks that can provide superior structural stability after undergoing cell-friendly crosslinking processes [23].

Inkjet bioprinting was the first biofabrication technique to be implemented. In this technique, the deposition of bioinks is mediated by piezoelectric elements, where piezoelectric crystals are employed to generate acoustic waves that force bioink deposition through a nozzle or by heat, on which pressure pulses that vaporize the bioinks around a heating element are generated [8], [18]. The effect of the frequencies employed with this technique on cell viability is still a matter of concern. In the same way, several studies have demonstrated that the elevated temperatures reached during inkjet bioprinting mediated by heat do not significantly affect cell viability. Among its several advantages, its low cost, rapidness, and easy implementation are the most remarkable. However, shape fidelity is difficult to achieve with this technique depending on the temperature and the biomaterial rheology since bioinks are deposited over a surface as droplets and keeping structural integrity without supporting material is difficult, contrary to EBB where the material is deposited as a filament and cohesion between layers is more straightforward to establish [5].

Stereolithographic printing employs light to crosslink a photosensitive resin or hydrogel in the presence of a photo-initiator molecule. Photoinitiators are prone to photolysis, which yields free radicals that facilitate the formation of covalent bonds in the resin or hydrogel [44]. With this technique, 3D constructs with complex geometries can be built by selectively exposing precise areas of the material to light in a specific wavelength and intensity with the help of a photo-absorber to avoid the penetration of light beyond the intended area, ensuring high-resolution features and structural fidelity. [5], [41].

Recently, stereolithographic printing processes were modified to be cell-friendly since traditional techniques involve toxic resins, photoinitiators, and exposure to environmental conditions that are harmful to cells. Some of these may include elevated temperatures and prolonged exposure to ultraviolet (UV) light, which has been shown to cause genomic damage and induce cell death. The development of hydrogels with rapid photocrosslinking kinetics and photoinitiators responsive to visible light has made the development of cell-

friendly stereolithography-based technologies, such as volumetric bioprinting with Lumen-X bioprinter or Allegro3D with Bionova-X a reality [45].

This technology has made it possible to bioprint geometrically complex structures in a matter of seconds, thus providing remarkable advantages over other 3D bioprinting techniques such as EBB. However, improvements must be made to this technology to allow multi-material bioprinting on the same layer and create more efficient use of bioinks, as the amounts required for the process are several times higher than the bioink used for the constructs and even more when using multi-material strategies.

Laser-assisted bioprinting is considered the most expensive and time-consuming bioprinting technique, given the complex setup required for bioprinting. This technique involves focusing a pulsed laser on a donor substrate, which is covered by an absorbing layer and a bioink layer. [18], [27]. When the laser is focused over the absorbing layer, evaporation occurs, and high-pressure bubbles are generated, which force the bioink to deposit on a surface as droplets. Interestingly, this technique is the best in preserving cell viability in the bioprinting process, which is generally above 95%. Similarly, laser-assisted bioprinting provides the best resolution, allowing the printing of droplets of volumes as low as ten (10) pL [19]. Despite its great attributes, the complex crosslinking schemes required for facilitating structural stability and shape fidelity of bioprinted constructs severely limit the implementation and advancement of this technique, such as the one presented by Poietis with NGB-series bio-printers.

Direct sound bioprinting (DSP) is the most recent technic [42], where an ultrasonic transducer sends focused pulses of ultrasound through a chamber into liquid resin contained within; doing so produces ultrasonic fields with acoustic cavitation, which temporarily causes rapidly oscillating microscopic bubbles to form at specific points in the resin. It is possible to build up a complex 3D object – one tiny pixel at a time but fast.

Furthermore, DSP can produce small, detailed items and print structures non-invasively within other structures with opaque surfaces, enabling the printing of structures inside other structures, for instance, printing shapes within the human body without surgery.

1.2.4 Rheological requirements of bioinks for EBB

Given that EBB has been positioned as the most popular and widely adopted 3D bioprinting technique, the functional requirements of the bioinks to be used within this technology have been thoroughly discussed and characterized [21], [46]–[51].

Besides being biologically suited for hosting the cells, facilitating communication, perfusion, and diffusion of media and nutrients to allow the generation of EMC bioinks should also possess specific rheological properties, which should guarantee printability, enough structural integrity after printing, and a quick gelation point that would allow for the anatomically accurate building of micro and macrostructures for replicating native tissues [24], [52].

One must experimentally determine the mechanical and flux properties of the bioinks for use in EBB, as well as the gelation point that marks the boundary between the hydrogel behaving like a liquid or a solid. Bioinks must be able to form a filament at the moment of deposition, thus facilitating that they can be precisely controlled to form a 3D shape [53].

Overall, a broad selection of biomaterials and polymer concentrations in the bioink must be envisioned to target the tissues' mechanical and biological requirements to be bioprinted. However, this is still challenging since a single biomaterial can rarely provide mechanical robustness and bioactivity when formulated into bioinks. Thus, most approaches are directed towards formulating multi-material bioinks that can harness the mechanical stability of synthetic polymers, like polyethylene-glycol and polycaprolactone, and the biocompatibility and bioactivity of nature-derived materials, such as collagen, gelatin, hyaluronic acid and decellularized extracellular matrices (dECMs).

Among the ideal rheological characteristics of bioinks and hydrogels aimed for use in EBB, shear-thinning behavior stands out as the most relevant [46], [54]. This property allows hydrogels to decrease their viscosity upon stress exerted on them, thus decreasing their yield point and facilitating their flow through extrusion nozzles (i.e., printability). However, the decrease in viscosity reverses upon relieving the stress, which is crucial for achieving controlled deposition, shape fidelity, and structural stability of the hydrogels [21], [48].

Moreover, the advantages that shear-thinning hydrogels provide in terms of printability are also reflected in cell viability upon extrusion [49].

Recently, several researchers from all over the world have focused their efforts on standardizing how printability and shape fidelity are measured qualitatively [21], [41], [48], [50], [52]. The efforts have conveyed defining key rheometric experiments that can elucidate the rheological behavior of hydrogels, such as those aimed at characterizing shear-thinning, flow initiation, and post-printing viscosity recovery. Regarding shear-thinning, the power law model has been extensively implemented for quantitatively assessing the degree of shear-thinning possessed by hydrogels that behave as non-Newtonian fluids [8] [55]. Briefly, a flow sweep experiment measures dynamic viscosity under a shear rate sweep, which usually goes from 0.01 to 200 1/s. Next, the data is adjusted to the power law model and the parameters *K* and *n* are calculated. The parameter 'n' value indicates the hydrogel's flow characteristics. When 'n' approaches zero, the hydrogel exhibits pronounced shear-thinning properties, meaning its viscosity decreases with increasing shear rate. Conversely, as 'n' approaches one, the hydrogel behaves more like a Newtonian fluid, maintaining a consistent viscosity regardless of changes in shear rate. Should 'n' exceed one, the hydrogel demonstrates shear-thickening behavior, wherein its viscosity increases with an increase in shear rate. [8], [21], [48].

Equation 1 Power law model, where η is dynamic viscosity (Pa-s), γ˙ is shear rate (1/s). K Is the consistency coefficient, n is the exponent known as the power law index or shear-thinning index. [8], [21], [48].

$$\boldsymbol{\eta = K.\dot{\gamma}^{n-1}}$$

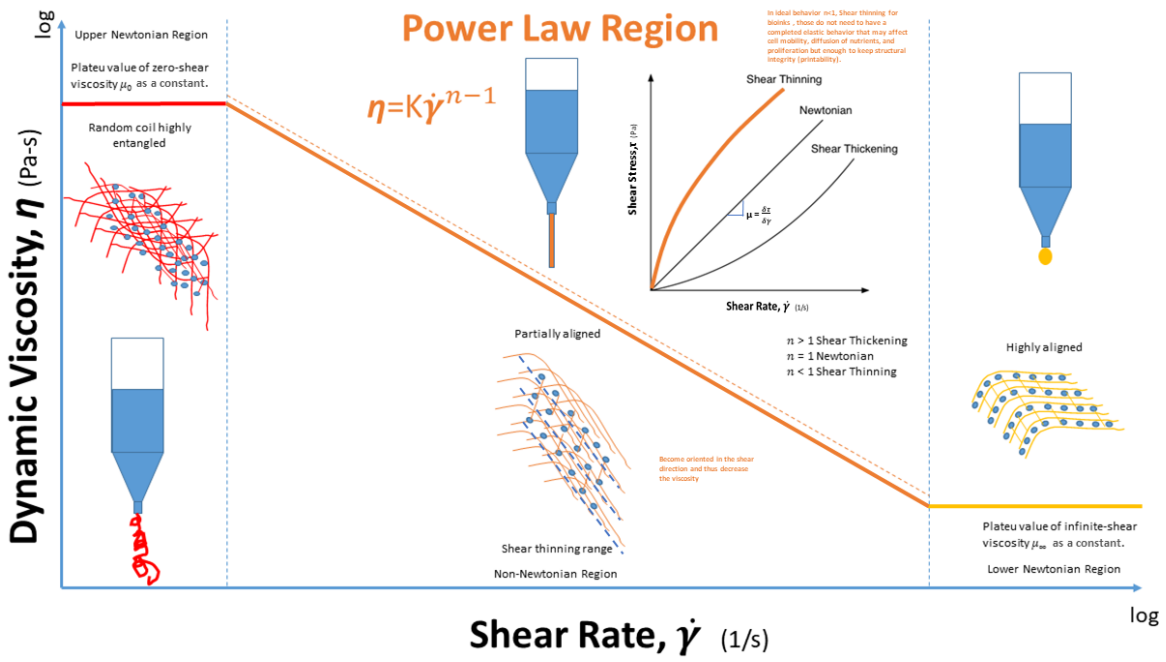

Figure 3 Power Law influence on bioprinting of a bioink [8], [21], [48].

In (**figure. 3**) When a substance is at rest and no shear is applied, some molecules are tightly intertwined in a spherical shape, while others are loosely connected.

When low shear is applied, molecular collisions cause an increase in viscosity for loosely connected molecules. However, collisions lead to disentanglement and orientation along the shear direction for tightly intertwined molecules, reducing viscosity. This results in a constant overall viscosity, known as the zero-shear viscosity plateau value. With a higher shear rate, more molecules become disentangled and oriented in the shear direction, causing decreased resistance to shear and viscosity (shear thinning effect). After reaching a specific shear rate, the macromolecules reach maximum disentanglement, and further increases in shear rate will not decrease viscosity, referred to as the infinite shear viscosity plateau value. [56]

For studying how stress can influence the rheological behavior and deformation of any biomaterial, an (angular frequency sweep) ω needs to be performed under strain (deformation sweep (%)) at a specific temperature with the aid of a rheometer and a solvent trap to avoid evaporation.[51][57]

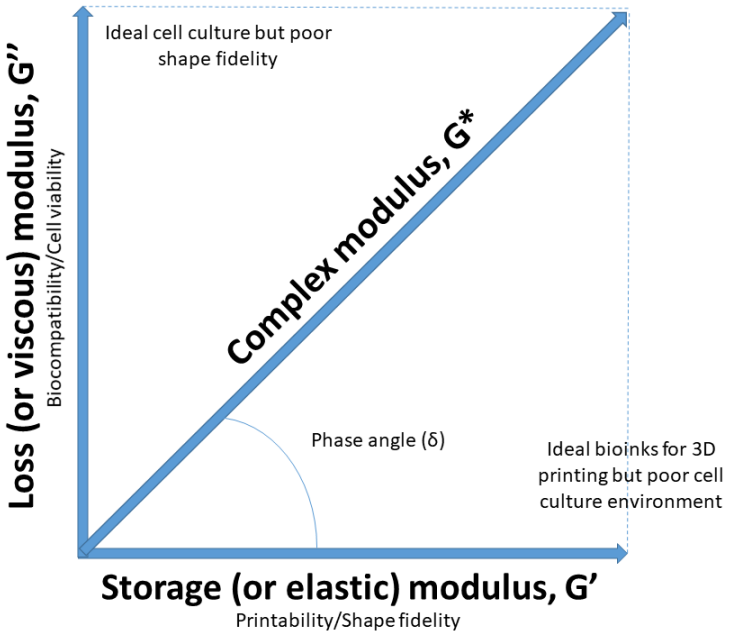

Figure 4 Complex modulus G* and phase angle (δ) influence on printability and viability. [58] [51] [48]

The oscillatory shear rheometric technique can determine the biomaterial mechanical properties and if it is printable or not; with this technique, the biomaterials for bioprinting need to demonstrate for the dependent variables (**figure. 4**) a higher elastic (shear storage modulus (G')) than viscous (shear loss modulus (G'')), indicating that the material is a viscoelastic hydrogel with a shear complex modulus (G*) where the phase angle (δ) tend to values close to 0°, those hydrogels do not need to have a completed elastic behavior that may affect cell mobility, diffusion of nutrients, and proliferation but enough to keep structural integrity (printability) [58] [51] [48]

Rheometry can also determine the shear thinning and gelation behavior of the hydrogels mixed with cells (bioinks), assessing the final shear viscous and elastic modulus of any bioink.

To ascertain the correlation between stress and strain in gel-type bioink and to understand how its shear stresses affect deformation and flow—thereby ensuring the structural integrity of 3D printed scaffolds—rheological testing equipment is employed. This apparatus is

meticulously configured to measure the pertinent variables, allowing for precise control and monitoring of the bioink's response under various stress conditions. The setup for such an examination is designed to capture a comprehensive profile of the bio ink's viscoelastic properties, which are critical for successful extrusion and accurate deposition during the printing process. The rheological testing equipment is used to determine the variables with the following setup:

• Complex, Elastic, and Viscous Modules need to be taken at a time T = 0
• The test temperature needs to be measured at 37 °C degrees [59].

Bioink printability is crucial when developing bioinks for use in bioprinting. Bioinks must meet specific cell viability and printing resolution criteria to be bio-printable, often requiring a balance between polymer concentration and stiffness.

Researchers are constantly expanding the bioprinting window or the range of conditions under which bioinks can be used successfully.

Several methods are used to assess the printability of bioinks, including testing droplets or filaments produced by the bioink using initial printing screening and evaluating more complex, multilayered structures through rheological evaluation, which looks at the flow profile, shear thinning, and viscosity recovery of the bioink after printing.

Specific polymers can improve the printability and shape fidelity of bioinks. Nanocellulose, Xanthan-gum, and Glucomannan are common biocompatible thickeners that stabilize shear-thinning at specific temperatures. For example, combining Alginate with Nanocellulose can result in a material with excellent cell compatibility and printability [60]. Xanthan-gum can also expand the printable temperature window of biomaterials like GelMA. Glucomannan's shear-thinning properties can improve the printability of neutralized Chitosan.

There are several ways to regulate the viscosity of bioinks. These include changing printing parameters like temperature, print speed, and shear rate, adjusting polymer characteristics like concentration and molecular weight, and adding thickener additives. The stiffness of bioinks can also be regulated through various crosslinking options, such as changing the

concentration of the main component, which can be done using a different crosslinking agent or adjusting the crosslinking parameters like time, distance, and intensity.

To increase the interaction between cells and bioinks, researchers can employ proteins like EMC, laminins, fibrogen, and cell attachment peptides like RGD (sequence of amino acids arginine-glycine-aspartic acid). These can improve the attachment and viability of cells within the bioink, resulting in better bioprinting outcomes.

1.2.5 Shear rate and shear stress in a coaxial nozzle

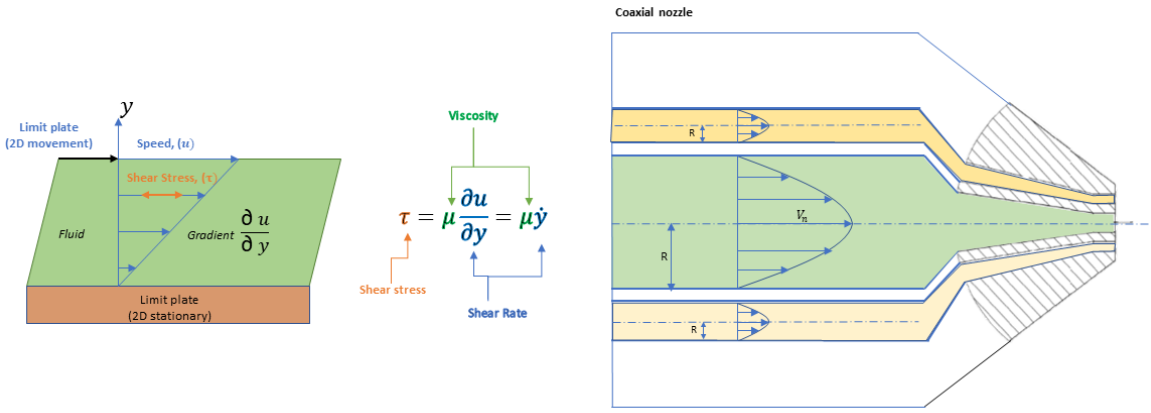

Figure 5 The shear stress equation relates a material's shear rate and viscosity, a schematic of fluid velocity through the cross-section of a coaxial nozzle tip.[16]

Equation 2. Shear stress of a fluid flowing through a nozzle.

$$\tau = \mu \frac{\partial u}{\partial y} = \mu \dot{y}$$

(Equation 2) Describes the shear stress of a fluid flowing through a nozzle; the shear stress is a measure of the force acting on the fluid as it flows through the nozzle and is caused by the deformation of the fluid as it moves through the nozzle. In this equation τ is the shear stress, μ is the dynamic viscosity of the fluid, ∂u/∂y is the shear rate (a measure of the rate at which the fluid deforms as it flows through the nozzle), and $\dot{y}$ It is the shear rate.
The shear stress of a fluid flowing through a coaxial nozzle can be an essential parameter in the fluid flow analysis and can be used to predict the behavior of the fluid under different

conditions. It is combined with the shear rate to calculate the fluid flow rate through the nozzle.

$$\gamma = \left(\frac{-\Delta P}{L}\right)\frac{R}{2}\left(\varepsilon\frac{\lambda^2}{\varepsilon}\right)$$

Equation 3. Expression for the fluid flow through a nozzle's shear rate.

$$\gamma = \left(\frac{V_N}{R}\right)$$

Flow rheology is the study of the flow and deformation of fluids. In the context of a coaxial nozzle, it refers to how the fluid flows through the nozzle and is affected by the shape and size of the nozzle, the properties of the fluid, and the external conditions (such as pressure and temperature).

The flow rheology of a fluid in a coaxial nozzle can be described by a set of equations known as the **Navier-Stokes equations**, which describe the motion of a fluid and the forces acting on it. These equations can be used to predict the **velocity and pressure** of the fluid as it flows through the nozzle, as well as other properties such as the viscosity and density of the fluid [61].

Understanding the flow rheology of a fluid in a coaxial nozzle can be crucial in various applications, such as in the design of propulsion systems or in manufacturing products that require precise control of the flow of fluids.

(Equation 3) is an expression of fluid flow through a nozzle's shear rate. The shear rate measures the rate at which the fluid deforms as it flows through the nozzle. γ is the shear rate, ΔP is the pressure drop across the nozzle, L is the length of the nozzle, R is the internal radius of the nozzle, ε is the flow radius inside the nozzle at a specific point, and λ constant that locates the position of maximum flow velocity. V_N Is the deposition rate of the fluid at the nozzle, and R is the radius of the nozzle.

It is often used to calculate other fluid flow properties, such as the shear stress and the flow rate. The shear rate can be influenced by numerous factors, such as the fluid's properties, the nozzle's shape and size, and external conditions (such as pressure and temperature).

Equation 4 Relates the deposition rate of the fluid at the nozzle (V_N) to the flow rate (Q) and the radius (R) of the nozzle.

$$V_N = \left(\frac{Q}{\pi R^2}\right)$$

The flow rate is the volume of fluid that passes through the nozzle per unit of time, and it is often used to describe the rate or speed at which a fluid flows through a system. Q Is the flow rate, and R is the nozzle radius. (Equation 4) shows that the velocity of the fluid at the nozzle is directly proportional to the flow rate and inversely proportional to the cross-sectional area of the nozzle (which is given by πR^2).

The geometry, such as the nozzle diameter or the cross-sectional area of the syringe-nozzle setup, plays a role in stress distribution. Conical and straight nozzles generate distinct stress profiles. Shear-free extensional stresses occur at the syringe-nozzle junction due to the contraction of the flow path, leading to cell deformation without rotation. This can result in considerable cell death. In the needle body, shear stresses dominate, causing both cell deformation and rotation, with the latter inducing less membrane damage.

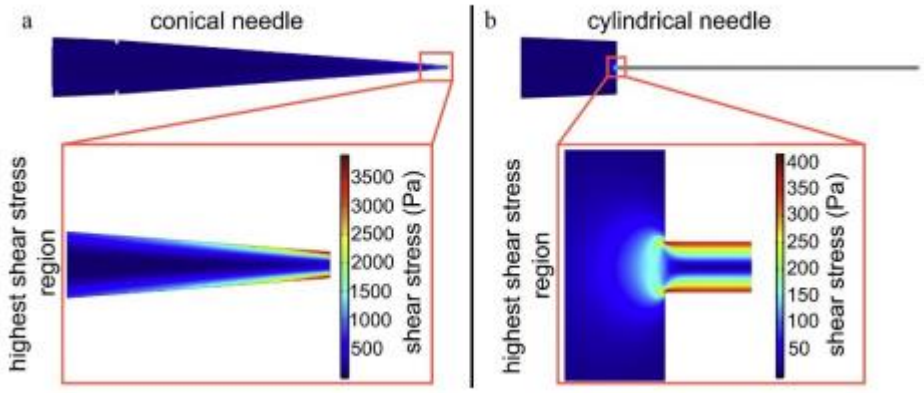

Figure 6 Heat map of the shear stress for (a) a conical and (b) a cylindrical needle [62]

Straight needles, when compared to conical nozzles, have been found to reduce cell viability significantly. Computational fluid dynamics (CFD) studies have shown that in straight needles, high stresses occur at the syringe junction and continue along the needle walls, with the lowest stresses present at the center and dispensing orifice. Conversely, in conical nozzles, stresses increase towards the dispensing orifice. The dispensing orifice diameter also influences cell viability; smaller diameters correlate with reduced viability[62].

1.2.6 Computational modeling (CFD) and equations for flow passing a circular cylinder.

From an engineering standpoint, it is essential to predict the diverse effects that can suffer at various pressures and fluid speeds of a conduit, as it can be a needle or a nozzle, thereby avoiding undesirable phenomena.

Fluid dynamics is expected to use mathematical models to understand and predict the behavior of fluids under various conditions. One example is the study of the flow of an incompressible fluid past a long cylinder placed in a channel with the right angles to the oncoming flow. This type of flow is known as flow passing a circular cylinder. It is often used to simulate flow through a nozzle, such as in bioprinting.

In the case of flow past a circular cylinder, the cylinder creates a wake behind it, characterized by the formation of vortices. These vortices are caused by the fluid's separation from the cylinder's surface and can significantly impact overall flow behavior.

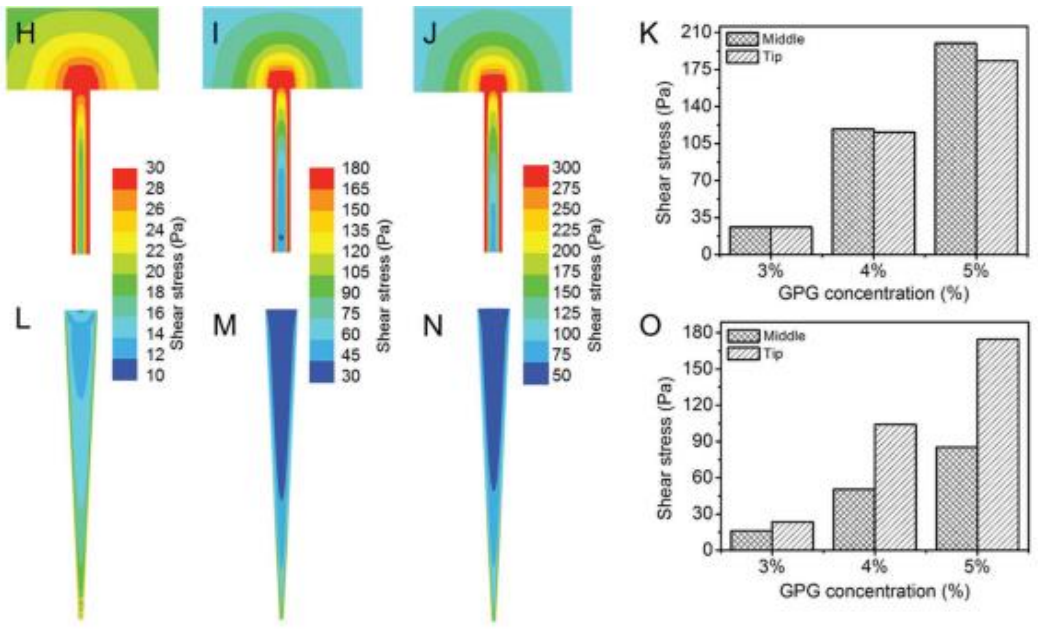

Figure 7 (H–M) Shear stress distribution maps (Ansys) during the bioprinting process using (H–J) a 27G straight needle and (L–N) a 27G cone-shaped nozzle. (K) Quantification of shear stress at the middle of the needle tip (J) with 5% GelMA and (O) the cone-shaped nozzle (N) with 5% GelMA [63]

The flow past a circular cylinder can be either steady or unsteady, depending on the Reynolds number (a dimensionless parameter that describes the ratio of the inertial forces to viscous forces in the flow), where $\boldsymbol{\rho}$ is the density of the fluid, v is the flow speed, D is the diameter characteristic dimension, and μ is the dynamic viscosity of the fluid.

Equation 5. Reynolds Equation.

$$R_e = \left(\frac{\boldsymbol{\rho}\, v\, D}{\mu}\right)$$

Equation 6. Flow through a uniform circular cross-section.

$$Flow = \left(\frac{\partial v}{\partial r}\right)^n = \frac{r\dot{y}_0^{n-1}}{2\eta_0}\frac{\partial P}{\partial z}$$

The inlet velocity profile is critical to describe a flow past a circular cylinder, describing the distribution of velocities within the fluid at the channel's inlet. Where η_0 is the limited viscosity a low shear rate, and $\dot{y}_0^{n-1}$ As the corresponding shear rate, the above equation is integrated between the limits $v = v$ at radius r, considering the pressure gradient. $\frac{\partial P}{\partial z}$ It is a unique value for a deposition system and is a function of the nozzle diameter, the internal geometry, and the pressure applied [16]. In the case of a bioprinting nozzle, the inlet velocity profile is often assumed to be symmetric, with the same velocity at all points across the inlet. However, this symmetry can be disrupted by the presence of a cylinder, which can cause the flow to become asymmetric and initiate vortex formation.

The presence of vortices in the wake of the cylinder can also affect the pressure drop at the system's output. In general, the presence of vortices can increase the pressure drop, as the fluid must work against the swirling motion of the vortices as they flow through the system. This increase in pressure drop can be significant, particularly at high Reynolds numbers, where inertial forces dominate.

In summary, computer models can be used to understand the unsteady, incompressible flow past a long cylinder placed in a channel at right angles to the oncoming fluid. This flow, which simulates a nozzle for bioprinting, requires some asymmetry in the inlet velocity profile to initiate vortex formation and overcome the pressure drop at the system's output. [64]

Non-Newtonian fluids are a class of fluids whose viscosity depends on shear rate (strain rate) or shear stress history, in contrast to Newtonian fluids, whose thickness is independent of these factors. Non-Newtonian fluids can exhibit a wide range of behaviors, including shear thinning (decreasing viscosity under shear), shear thickening (increasing viscosity under shear), and time-dependent density.

There are several non-Newtonian fluids, including dilatant fluids, pseudoplastic fluids, and thixotropic fluids. Dilatant fluids, also known as shear-thickened fluids, exhibit increasing viscosity under the shear. An example of a dilatant fluid is cornstarch suspended in water.

Dilatant fluids can behave like a solid when subjected to sudden impacts or stress but flow like a liquid when subjected to low shear. Pseudoplastic fluids, also known as shear-thinning fluids, exhibit decreasing viscosity under the shear. Ketchup is a classic example of a pseudoplastic fluid exhibiting shear-thinning properties. When the bottle is inverted, the ketchup flows readily due to the force of gravity acting on its structure. However, it retains a thicker consistency at rest or under gentle pressure, making it more pouring-resistant. This behavior is characteristic of pseudoplastic fluids, where their viscosity decreases under applied shear stress, allowing for more effortless flow with increased force. Thixotropic fluids exhibit time-dependent viscosity, meaning their viscosity decreases with time under shear and increases when shear is stopped. An example of thixotropic liquid paint becoming thinner and more fluid when stirred or agitated but eventually returning to its original thickness when left undisturbed.

Non-Newtonian fluids are often used in various applications, such as rheology (studying the flow and deformation of materials), biomedical engineering, and food processing. They can also be used to design protective materials, such as body armor and helmet liners. These materials can absorb impact energy and reduce the likelihood of injury.[65]

To determine the viscosity of a fluid, one of the various non-Newtonian viscosity models that can be applied is the power law; the relationship and interaction between shear stress and shear rate for this type of fluid can be described by the equation already explained in the previous section. (Equation 2). This equation can, therefore, represent the apparent or

dynamic viscosity of a fluid model according to a power law such as that used in most software in computational fluid dynamics (CFD). This equation is perhaps the most frequently used model in the literature on process engineering applications when dealing with viscosity.

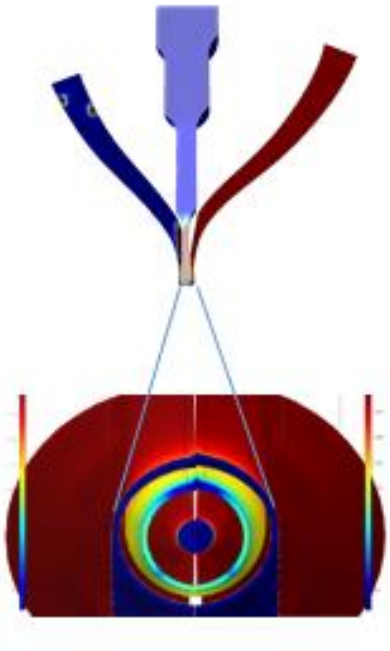

Figure 8 Computational fluid dynamic simulation (CFD-COMSOL) for a coaxial nozzle. (Original work).

Speed and pressure are the main two variables to find in a CFD analysis simulation, but to find it is needed to feed the system with some basic parameters as the following:

Symbol	Variable	Units
$\boldsymbol{\rho}$	Density	Kg/m^3
$\boldsymbol{\eta}$	Dynamic viscosity	Pa. s
$\boldsymbol{n}$	Power Law Index	0 ≤ n ≤ 1
$\boldsymbol{K}$	Consistency coefficient	Pa.s^n
$\boldsymbol{V_0}$	Initial average speed	m/s
$\boldsymbol{P_0}$	Input pressure	Pa
$\boldsymbol{T_0}$	Initial temperature	C°

Table 1 Main variables to consider for a CFD simulation.

It is essential to determine the flow regime. It is necessary to calculate the Reynolds generalized number (N_{GRe}) to find it; in this way, check if the fluid has a laminar behavior:

Equation 7 N_{GRe} Where (D) is the diameter of the conduit, and the flow is traveling, the rest of the variables in the equation are defined in table 1.

$$N_{GRe} = \frac{D^n \cdot V_0^{2-n} \cdot \rho}{K} * \left(\frac{4n}{3n+1}\right)^n$$

For the laminar flow regime, the fanning friction factor (f_F) is the ratio between the local shear stress and the local flow kinetic energy density; the friction factor for Newtonian fluids flowing luminary in round tubes can be expressed as follows:

Equation 8 Fanning friction factor.

$$f_F = \frac{16}{N_{GRe}}$$

To find this factor, it is essential to determine the system pressure drop; in this way, check the variation of pressure in the system to compare with the CFD simulation. To find the pressure drop, the following equation:

Equation 9 Pressure drop equation.

$$\Delta \mathrm{P} = f_F \cdot \frac{2L}{D} \cdot \rho \cdot V_0^2$$

As a rule, when modeling bioink for bioprinting using nozzles, we consider a dense model of a laminar regime in which the solution is based on the pressure and speed of entry into the system along the conduit (L) and where the density of the bioink is constant. However, the viscosity is variable and dependent on the shear rate applied.

For the simulation with the CFD-COMSOL tool, it is crucial to define the boundary and edge conditions according to the geometric restrictions of the immobile walls, the interfaces where there should be a V_0 at the inlet and pressure in the outlet to get a robust configuration with the simulation.

After defining all described above and running the simulation, it will be possible to get the pressure contours and distributions with the respective speed field.

A periodic flow pattern can only be predicted with great difficulty if the necessary simulation time is considered. Nevertheless, the Reynolds number is one of the most reliable predictors for establishing the rate of flow based on cylinder diameters, such as low values (below 100); in the case of nozzles and needles, there is a steady flow.

The flow details can be affected by perturbations in the simulation. Those perturbations can be translated into physical reality quite quickly. Still, to understand the nature of those perturbations, it is necessary to calculate the time-varying forces on the nozzle that can be validated by software at a lower Reynolds number using a direct nonlinear solver so that simple errors can be corrected before the long-term time-dependent simulation starts.

The **Navier-Stokes equations**, named after Claude-Louis Navier and George Gabriel Stokes, are the cornerstone of fluid dynamics for modeling viscous and heat-conducting fluids. By incorporating Newton's second law into the momentum equation and aligning it with mass conservation principles, these equations facilitate precise predictions of **velocity, pressure**, and various flow characteristics in numerous scenarios. In the context of CFD, particularly with tools like COMSOL Multiphysics, they offer an in-depth portrayal of fluid motion around structures, such as a circular cylinder, enabling accurate simulations of fluid interactions for complex engineering and scientific applications [61].

The suite includes the continuity equation for **mass conservation**, the **momentum** equation, which factors in the forces and fluid dynamics, and the energy equation, which delineates the distribution of thermal energy. As the structural foundation of CFD simulations, these equations provide a robust framework for accurately forecasting fluid interaction with cylindrical structures, crucial for analyzing flow rheology in applications such as coaxial nozzles.

The Navier-Stokes equations, central to fluid dynamics, assess the **velocity** field, the cornerstone of flow field kinematics. Unlike the dynamic study of solids focusing on positions, these equations prioritize fluid velocities to solve mechanical problems. The velocity field determination allows for calculating forces like drag and flow rates. This can be approached via Lagrangian or Eulerian methods, with the latter often preferred for its focus on fixed spatial points.

Non-linearity is inherent in these equations due to fluid particle acceleration, leading to complex behaviors like turbulence in certain conditions, such as flow through a narrowing nozzle. The Reynolds number, a dimensionless quantity, plays a pivotal role in characterizing the flow's nature by comparing inertial and viscous forces, influencing the equations' non-linear convective terms.

Turbulence, characterized by chaotic and time-dependent changes in pressure and velocity, poses challenges for numerical simulations due to the need for fine mesh resolution. While direct simulation is often impractical, time-averaged models like Reynolds-averaged Navier-Stokes (RANS) or Large Eddy Simulation (LES) provide alternative approaches for turbulence modeling.

Furthermore, the equations' continuity aspect models fluids as a continuous mass, enabling the application of conservation laws to derive differential equations that describe fluid behavior, assuming the fluid is evenly distributed throughout the occupied space.

The specific form of the Navier-Stokes equations would include two principal forms. The compressible flow variant encompasses state equations linking momentum and mass conservation with the energy equation, allowing for density changes due to pressure and temperature variations within the flow field. Conversely, the incompressible flow form applies to scenarios where fluids, including gases at low speeds, maintain a constant density, thus decoupling the energy equation from momentum and mass conservation. Nonetheless, if heat transfer is involved, the energy equation is reintegrated.

Equation 10. The Navier Stokes equations.

$$\rho\left(\frac{\partial \mathrm{u}}{\partial t}+(\mathrm{u}\cdot\nabla)\mathrm{u}\right)=-\nabla p+\nabla\left[\mu\left(\nabla\mathrm{u}+(\nabla\mathrm{u})^{\mathrm{T}}-\frac{2}{3}(\nabla\cdot\mathrm{u})\mathbf{I}\right)\right]+F$$

- The continuity equation for **mass** conservation,
- The **momentum** equation, which is a statement of Newton's second law applied to fluid motion and
- The **energy** equation if thermal effects are significant.

These equations are typically expressed in partial differential form, reflecting the complexity of fluid behavior in response to internal and external forces. (F) Which typically represents

the body forces per unit volume acting on the fluid. These forces could include, for example, gravitational, electromagnetic, or other field forces that act throughout the volume of the fluid.

The Euler equations form a foundational aspect of the Navier-Stokes equations, describing fluid motion for ideal, inviscid fluids where viscosity and thermal conductivity are negligible. These equations conserve momentum, mass, and energy in certain conditions, making them suitable for modeling both compressible and incompressible flows, provided the flow's velocity divergence is near zero. While they require adjustments to simulate the more complex behavior of real fluids, they are pretty effective in practical scenarios such as aerodynamic simulations around wings and water wave modeling. However, the inviscid theory does not account for certain phenomena, such as D'Alembert's paradox, which describes the absence of drag on spherical objects in a fluid and the inability to remove dust from a moving car due to the lack of frictional forces in an inviscid model.

The Euler equation reads as follows:

Equation 11. Euler equation.

$$\rho\left(\partial \mathrm{u}/\partial \mathrm{t} + (\mathrm{u}\cdot\nabla)\,\mathrm{u}\right) = -\nabla \mathrm{p} + \rho \mathrm{F}$$

Where u is the velocity of the flow field, ρ is the density, p represents the pressure functions in terms of space and time, and F is the other body force acting on the fluid continuum.

The continuity equation is a conservation law that states that the mass of a fluid within a fixed control volume is constant over time. It can be written as:

.

Equation 12 Continuity equation-Mass conservation equation

$$\partial(\rho u)/\partial t + \nabla\cdot(\rho u) = 0$$

or

$$\partial u/\partial x + \partial v/\partial y + \partial w/\partial z = 0$$

Where ρ is the density of the fluid, u is the velocity vector, and (t) is time. The term $\partial(\rho u)/\partial t$ represents the rate of change of mass within the control volume due to the flow of fluid into or out of the volume, and the term $\nabla\cdot(\rho u)$ represents the net mass flux (flow per unit area) through the surface of the control volume.

The momentum equation describes the balance of forces acting on a fluid element and is derived from Newton's second law of motion. It can be written as:

Equation 13 Momentum equation.

$$\partial(\rho u)/\partial t + \nabla\cdot(\rho uu) = -\nabla p + \nabla\cdot\tau + \rho g$$

or

$$\partial(\rho u)/\partial t + \partial(\rho uu + p)/\partial x + \partial(\rho uv)/\partial y + \partial(\rho uw)/\partial z = -\partial(\tau xx)/\partial x - \partial(\tau xy)/\partial y - \partial(\tau xz)/\partial z$$

In these equations, u, v, and (w) are the velocity components in all the x, y, and z directions. p is the pressure of the fluid, and v is the kinematic viscosity of the fluid. The symbols $\partial/\partial x$, $\partial/\partial y$, and $\partial/\partial z$ represent a partial derivative with respect to x, y, and z, respectively, and $\partial/\partial t$ represents a partial derivative with respect to time.

τxx, τxy, and τxz are the stress tensor components, and g is the gravitational acceleration vector. The term $\partial(\rho u)/\partial t$ represents the rate of change of momentum within the control volume due to fluid flow into or out of the volume, and the term $\nabla\cdot(\rho uu)$ represents the net

momentum flux through the surface of the control volume. The term ∇p represents the force due to pressure gradients, ∇·τ represents the viscous forces.

($\mathbf{I}$) on the (equation-10) represent the identity matrix. In the term $\frac{2}{3}(\nabla \cdot u)\mathbf{I}$ this identity matrix is used in the context of a stress tensor operation. The divergence of the velocity field $(\nabla \cdot u)$ is a scalar, and when multiplied by the identity matrix ($\mathbf{I}$) it creates a tensor that can be subtracted from the stress tensor to account for the volumetric expansion or compression in the flow, which is related to the fluid's compressibility. This adjustment is part of the stress tensor in a Newtonian fluid's constitutive equation.

The energy equation describes energy conservation; the energy aspect of fluid flow would be considered thermal energy transport, including conduction, convection, and any heat sources or sinks within the fluid. It is typically a separate equation that complements the Navier-Stokes equations in a complete fluid dynamic analysis in the system and can be written as:

Equation 14. Energy equation

$$\partial(\rho E)/\partial t + \nabla\cdot(\rho E u) = -\nabla\cdot q + \rho u\cdot\nabla\cdot u + \nabla\cdot(uv)$$

or

$$\partial(\rho E)/\partial t + \partial(\rho E u + pv)/\partial x + \partial(\rho E v + pw)/\partial y + \partial(\rho E w + pu)/\partial z = -\partial(qx)/\partial x - \partial(qy)/\partial y - \partial(qz)/\partial z$$

Where E is the total energy per unit mass, qx, qy, and qz are the components of the heat flux vector. The term ∂(ρE)/∂t represents the rate of change of energy within the control volume due to fluid flow into or out of the volume, and the term ∇·(ρEu) represents the net energy flux through the surface of the control volume. The term ∇·q represents the heat transfer due to temperature gradients, the term ρu·∇·u represents the work done by the fluid, and the term ∇·(uv) represents the viscous dissipation.

These equations and appropriate boundary conditions can be solved using numerical methods to simulate the flow past a circular cylinder and predict various flow characteristics, such as temperature distributions.

Description of Navier-Stokes equation

After establishing the fundamental equations that govern the behavior of Newtonian fluids, we can extend these principles by applying Euler's theorem to fluid mechanics. This extension incorporates the critical viscosity factor, allowing for a more comprehensive description of fluid motion. The resulting formulation is presented in Equation 10, which is the well-known Navier-Stokes equation:

Equation 15. Navier Stokes equation.

$$\rho\left(\frac{\partial \mathrm{u}}{\partial t}+\mathrm{u}\cdot\nabla\mathrm{u}\right)=-\nabla p+\nabla\sigma+F$$

In the Navier-Stokes equation, the term ∇·σ introduces the deviatoric stress tensor, which accounts for the differential stresses within the fluid. On the left-hand side, the equation delineates the acceleration of the fluid continuum, encompassing both temporal and convective influences, which introduce non-linearity into the system. The right-hand side features two gradient operators, ∇p and ∇·σ, representing the pressure gradient and viscous forces, respectively. These correspond to the isotropic part of the stress tensor and the viscous effects.

Several other equations can be used in a CFD simulation of a flow past a circular cylinder, depending on the analyzed problem. Some examples include:

The turbulence equations describe the behavior of turbulent flow, characterized by random fluctuations in velocity and other quantities. Turbulence can significantly impact the flow past a circular cylinder, particularly at high Reynolds numbers, so it is important to model it accurately. Various approaches to modeling turbulence include the Reynolds-averaged Navier-Stokes (RANS) equations and the large-eddy simulation (LES) equations.

The k-ω turbulence model is widely used for predicting turbulent flows. This model is based on the transport equations for the turbulent kinetic energy (k) and the specific dissipation rate (ω), which can be written as:

Equation 16. Turbulence equation.

$$\partial(\rho k)/\partial t + \nabla\cdot(\rho k u) = \partial(\tau k k)/\partial x + \partial(\tau k y)/\partial y + \partial(\tau k z)/\partial z + \rho P k - \rho\omega 2$$

or

$$\partial(\rho\omega)/\partial t + \nabla\cdot(\rho\omega u) = \partial(\tau\omega k)/\partial x + \partial(\tau\omega y)/\partial y + \partial(\tau\omega z)/\partial z + (1/T\omega)\,(P\omega - C\omega 2\omega + G\omega)$$

Where ρ is the density of the fluid, u is the velocity vector, t is time, and the other terms represent various turbulence-related quantities. The k-ω model is an improvement over the simpler k-ε model, as it can capture the behavior of both the turbulent kinetic energy and the specific dissipation rate.

The Reynolds-averaged Navier-Stokes (RANS) equations are a set of average equations describing the mean flow properties of a turbulent flow. These equations are used to model the time-averaged behavior of turbulent flows and are typically solved using a turbulence model to account for the effects of small-scale turbulent motions. The RANS equation can be written as:

Equation 17. Reynolds-averaged Navier-Stokes equation.

$$\partial(\rho u)/\partial t + \nabla\cdot(\rho u u) = -\nabla p + \nabla\cdot(\mu\nabla u) + \rho g$$

where ρ is the density of the fluid, u is the velocity vector, p is the pressure, μ is the dynamic viscosity, ∇u is the velocity gradient tensor, g is the gravitational acceleration vector**,** the term $\partial(\rho u)/\partial t$ represents the rate of change of momentum within the control volume due to fluid flow into or out of the volume. The term $\nabla\cdot(\rho u u)$ represents the net momentum flux through the surface of the control volume or the forces acting on the fluid element. The term ∇p represents the force due to pressure gradients, $\nabla\cdot(\mu\nabla u)$ represents the viscous forces, and ρg represents the force due to gravity.

These equations, along with appropriate boundary conditions, can be used to simulate the motion of a fluid in a flow field and predict various flow characteristics.

The Large Eddy Simulation (LES) equations are a set of equations that describe the motion of the large-scale turbulent eddies in a flow field. These equations can be used to model the behavior of turbulent flows with high accuracy but are computationally expensive and require a high-resolution grid.

The k-epsilon model is a turbulence model that predicts a fluid's turbulent flow properties. This model assumes that the turbulent flow can be described in terms of two variables: the turbulent kinetic energy (k) and the rate dissipation of the turbulent kinetic energy (epsilon).

The k-omega model is another turbulence model used to predict a fluid's turbulent flow properties. This model assumes that the turbulent flow can be described in terms of two variables: the turbulent kinetic energy (k) and the specific rate of dissipation of turbulent kinetic energy (omega).

The boundary layer equations describe the fluid's behavior near the cylinder's solid surface, where viscous effects are significant. The boundary layer equations are used to predict the thickness and velocity profile of the boundary layer, which can significantly impact the overall flow field.

These are examples of the many different equations and models that may be used in a CFD simulation of the flow past a circular cylinder. The choice of equations and models will depend on the specific goals. It is also worth noting that these equations are typically coupled and must be solved simultaneously to predict the fluid's behavior accurately. This solution is typically done using numerical methods such as the finite element method (FEM), the finite volume method (FVM), or the finite difference method.

1.2.7 Cell Damage in EBB Processes.

While Extrusion-Based Bioprinting (EBB) has shown tremendous promise in the engineering of complex tissue constructs, the bioprinting process itself can induce significant mechanical stress on embedded cells, potentially leading to cell damage or compromised viability and function [54] [66] [67]. It is well-established that shear stress significantly influences cell communication. Moderate shear stress can alter the levels of calcium within cells, which in turn affects various signaling routes, such as those involving extracellular signal-regulated kinases (ERKs) and nitric oxide synthase [68][69]. These alterations can lead to changes in both cell growth and differentiation [67].

The high viscosity required for optimal printing can cause significant cell stress, leading to injury or death and lower cell viability than other methods. Mechanical dispensing systems, especially those that are screw-driven, tend to increase the pressure on high-viscosity bioinks, compromising cell survival. The shear stress, a significant culprit in cell damage, is influenced by the printing process (nozzle size, nozzle length, printing speed, and operating pressure) and the bioink's properties (viscosity), thereby reducing cell viability.

The nature of cell damage in 3D bioprinting involves various stress types – shear stress, thermal, and radiation are some examples. The extent of damage depends on the intensity and duration of these stresses, with excessive stress potentially leading to irreversible damage and cell death, primarily through **apoptosis**, **necrosis, and Lysis**. Different bioprinting techniques expose cells to specific stress types; for example, nozzle-based methods mainly cause high shear stress. [67] This induces significant cell stress, mainly due to the high shear stress. Factors influencing this stress include the viscosity of the bioink, nozzle size, nozzle length, and dispensing pressure. Optimizing these parameters is vital for reducing cell damage.

External environmental factors, including temperature and pH, significantly influence cell viability. They can alter the properties of bioinks, affecting their rheological characteristics and gelation, which in turn impacts cell health. Cell death mechanisms in this context include apoptosis, a regulated process often termed "programmed cell death," and necrosis, an unregulated process resulting from severe damage or external factors. These processes are governed by specific molecular pathways, with caspase activation playing a

crucial role in apoptosis, particularly in response to shear stress and lysis, where the cell membrane is disrupted, and the cellular contents are released into the surrounding tissue.

Apoptosis, Necrosis, and Lysis are three distinct forms of cell death in EBB.

Apoptosis, commonly known as "programmed cell death," is a highly regulated and controlled process through which cells systematically disassemble and die as part of normal physiological functions. This mechanism serves as a means for the body to eliminate damaged or superfluous cells in a non-detrimental manner to the surrounding tissue. Apoptosis is distinguished by a series of distinct morphological and biochemical alterations, including cell shrinkage, chromatin condensation, and the fragmentation of DNA, ultimately leading to the orderly and efficient removal of these cells from the organism.

Necrosis represents a type of cell death that is traumatic and typically arises from external stressors like infection, exposure to toxins, or physical trauma. This process leads to the uncontrolled breakdown of cells. Unlike the orderly nature of apoptosis, necrosis is characterized by a chaotic destruction of cellular structures. This often triggers an inflammatory response, as the ruptured cells release their internal contents into the surrounding tissue, potentially causing further damage and eliciting a response from the immune system.

Lysis induced by shear stress poses a critical challenge in numerous biomedical contexts, especially in fields such as 3D bioprinting and other cellular manipulation techniques. These processes include pumping, injecting, or extruding cell suspensions for applications like flow cytometry. Shear stress, encountered during these manipulations, can inflict physical damage on cells, leading to their rupture. This rupture, or lysis, occurs when the cell membrane is disrupted, releasing cellular contents into the surrounding environment. The implications of such cell damage are significant, as they can affect the viability and integrity of cells in biomedical applications, underscoring the need for careful management of mechanical forces in these technologies.

Molecular Pathways in Apoptosis and Necrosis: These distinct forms of cell death are initiated by unique molecular pathways, in contrast to lysis, which primarily results from external and mechanical factors. These pathways are activated in response to various cellular stressors, indicating a complex and specific regulatory mechanism underlying each form of cell death.

Caspase Activation in Apoptosis: Caspases are a family of protease enzymes that play a vital role in apoptosis. They exist in cells as inactive precursors (procaspases) and are activated in response to pro-apoptotic signals. Once activated, these enzymes execute the apoptotic process by cleaving various cellular proteins. Shear stress, such as that experienced in bioprinting processes, can initiate caspase activation, leading to apoptosis. This pathway is intricately regulated and ensures that cells undergo apoptosis in a controlled manner. [67]

Pathways in Necrosis: Necrosis is less regulated than apoptosis and often results from severe or sudden cell damage. The molecular pathways leading to necrosis are varied and can involve factors like mitochondrial dysfunction, depletion of ATP (the energy currency of the cell), or the influx of calcium ions.

Cell viability in EBB, typically ranging from 40% to 80% [12] [13] [14] [15], can be improved through the optimization of nozzle design and operational conditions. Despite the higher viscosity required for optimal printing, which causes significant stress and potentially lowers cell viability, appropriate adjustments in the printing process and bioink properties can mitigate these effects. However, with ongoing research and development, it is possible to maintain or even enhance cell viability after printing and during subsequent culture.

Despite the inherent stresses of bioprinting processes, it is possible to achieve high cell viability. This requires careful control and optimization of printing conditions and bioink properties. Over time, after days of the bioprinting process and with appropriate conditions, cells can recover and show improved viability post-bioprinting [11], especially when using shear-thinning bioinks, which are preferred to minimize this stress.

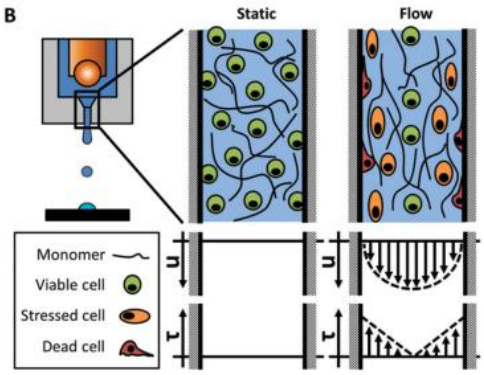

Figure 9 B) Schematic illustration of the velocity and shear stress distribution and the stress impinged on cells inside a bioprinter nozzle.[54]

The extrusion mechanism in EBB imposes pressure on the bioink through a constricted aperture, subjecting the encapsulated cells to various forms of mechanical stress:

Shear Stress: As bioink is propelled through the printing nozzle, shear forces act upon the cells. Elevated shear stress levels can compromise the integrity of the cell membrane, precipitating cell lysis or triggering apoptotic pathways.

Extensional Stress: The acceleration of bioink through the nozzle exerts extensional forces, which can elongate cells. Overextension may lead to cytoskeletal disruption, affecting overall cell integrity and function.

Compression Stress: Within the confines of the nozzle or under subsequent layers of deposited material, cells may experience compressive forces, which can be particularly damaging in high-density cell-laden bioinks.

Impact Stress: The abrupt contact between the bioink and the substrate upon deposition can also introduce stress that may be detrimental to cell health.

Cellular responses to these mechanical stimuli during EBB are complex and multifaceted [70]:

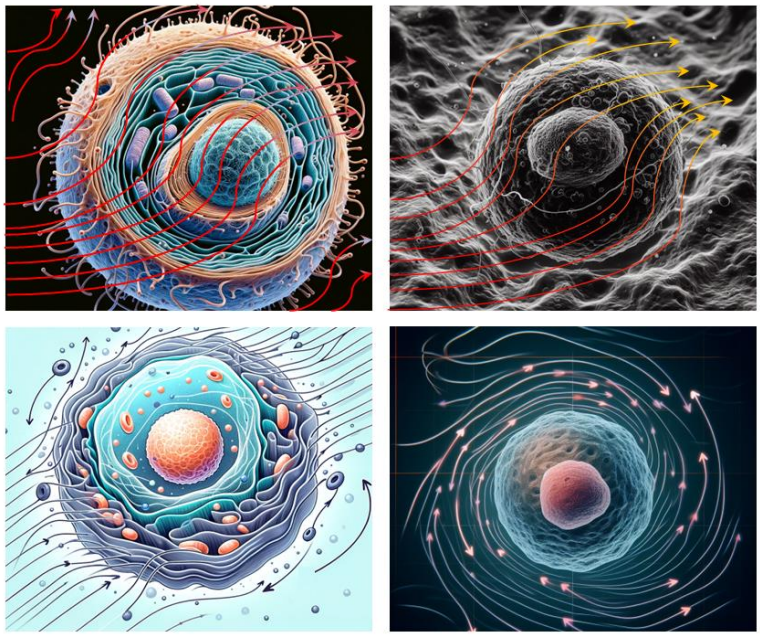

Figure 10 is an artistic representation of the hydrodynamic forces interacting with a biological cell (Image generated by OpenAI´s DALL-E 3) (Original work).

Membrane Disruption: Cell membranes are inherently susceptible to physical forces. Excessive stress can cause disruptions (Lysis), leading to the leakage of cellular contents or the unregulated entry of ions and molecules, with potential cytotoxic outcomes.

Cytoskeletal Damage: Serving as the cell's structural framework, the cytoskeleton is integral to cellular transport and mitosis. Mechanical forces can destabilize cytoskeletal components, such as actin filaments, microtubules, and intermediate filaments, potentially impairing cell division and transport mechanisms.

Signal Transduction Alterations: Mechanical stresses may initiate or suppress various signaling cascades. Shear stress, for example, activates mechano-transduction pathways, influencing gene expression and protein synthesis, with far-reaching implications for cell fate and function.

Cell Death: Severe stress may precipitate cell death, either through necrosis, resulting from acute injury, or apoptosis, because of sustained or intense stress.

DNA Damage: The structural integrity of DNA is not immune to mechanical stress, which can cause breaks in DNA strands and chromosomal anomalies, potentially leading to mutations or halting the cell cycle.

Alteration of Cell Function: Survival through the extrusion process does not guarantee normal cell function; post-process cells may exhibit diminished capabilities. Pluripotent stem cells, for instance, might forfeit their ability to differentiate, or specialized cells could be stripped of their specific functionalities.

Alternative Approaches for Measuring Cell Damage:

Energy Dissipation Rate Assessment:

In the realm of cell damage analysis, the investigation into how cells dissipate energy under various conditions and geometries provides valuable insights. A critical method in this research is the study of the impact of cell extrusion through a micropipette, an approach that closely mirrors the conditions encountered in Extrusion-Based Bioprinting (EBB). As depicted in **Figure 11**, this technique is instrumental for comprehending the influence on animal cells within standard laboratory settings, especially when employing micropipettes.

Notably, observations from **Figure 11** indicate that the local energy dissipation rates in these experiments were significantly lower than those required to induce catastrophic cell damage. This finding raises important considerations about the thresholds of energy dissipation that cells can tolerate without leading to severe damage.

Building on this foundation, previous research, such as that of Mollet et al. (2004), has delved into the potential of energy dissipation rates as a factor in cell damage. Mollet's earlier work in 1996 also focused on the implications of acute hydrodynamic forces and their role in inducing cell apoptosis. These studies contribute to a deeper understanding of the mechanical stresses cells can endure and the limits beyond which damage becomes inevitable. [71] [72]

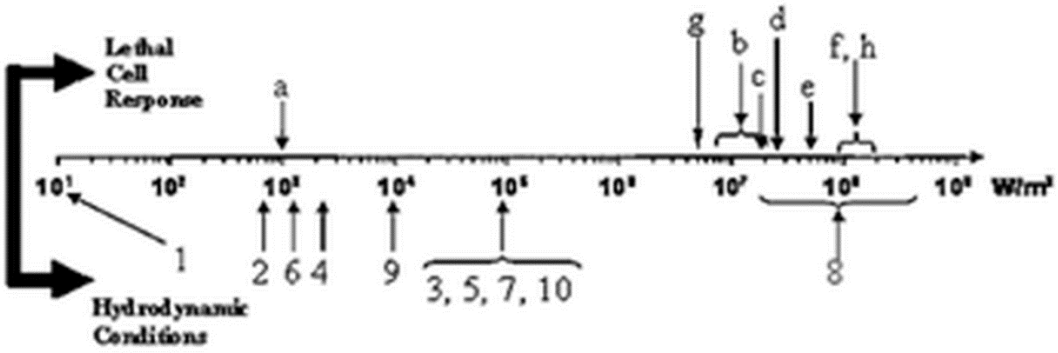

Lethal Cell Response

Symbol	Cell	Mode of growth	Reference
a	CHO-K1	Anchoraged	Gregoriades et al. (2000)
b	Hybridoma	Suspended	Thomas et al. (1994); Zhang et al. (1993)
c	MCF-7	Suspended	Ma et al. (2002)
d	Mouse myeloma	Suspended	McQueen and Bailey (1989)
e	HeLa S3, mouse L929	Suspended	Augenstein et al. (1971)
f	CHO-K1, SF-9, HB-24	Suspended	Ma et al. (2002)
g	Uninfected and viral infected PERC6 cells	Suspended	Submitted
h	Enthomopathogenic nematodes	Suspended	Fife et al. (2004)

Hydrodynamic Conditions

Symbol	Process	Description	Reference
1	Agitation	Volume average in typical animal cell bioreactors.	Varley and Birch (1999)
2	Agitation	Volume average in a 10 L mixing vessel (RT, 700 RPM)	Zhou and Kresta (1996)
3	Agitation	Maximum in the 10 L mixing vessel (RT, 700 RPM)	
4	Agitation	Volume average in a 22,000 L mixing vessel (RT, 240 RPM)	Wernersson and Tragardh (1999)
5	Agitation	Maximum in the 22,000 L mixing vessel	
6	Agitation	Maximum in spinner vessel (200 RPM)	Venkat et al. (1996)
7	Bubble rupture	Pure water, bubble diameter: 6.32mm	Garcia-Briones et al. (1994)
8	Bubble rupture	Pure water, bubble diameter: 1.7mm	Boulton-Stone and Blake 1993); Garcia-Briones et al. (1994)
9	Flowthrough pipe	Pure water, 100 mL/min, 1 mm diameter	Mollet et al. (2004)
10	Flowthrough a micropipette tip	Flowthrough a 200 μL micropipette tip in 0.2 sec	Mollet et al. (2004)

Figure 11 Summary of the reported energy dissipation rate at which cells are damaged and the reported levels of energy dissipation rate in various bioprocess environments. Our focus flows through a micropipette tip, which resembles a phenomenon happening in EBB. Adapted from Ma et al. (2002) and Mollet et al. (2004) [71] [72]

In addition to mechanical factors, other factors can influence cell damage during the EBB process, such as:

Temperature: The EBB process can generate heat due to friction or the chemical reaction of the bioink components. Heat can alter the structure and function of cellular proteins and induce thermal stress or shock, which can denature proteins and disrupt cellular function.

pH: The pH of the bioink can vary due to the release or consumption of hydrogen ions during the EBB process. An inappropriate pH can affect the acid-base balance of cells, as well as enzyme activity and the stability of biological molecules, potentially disrupting cellular metabolism and function.

Oxygen: Oxygen is essential for cellular metabolism and energy production. However, the EBB process can limit the supply of oxygen to cells or generate reactive oxygen species (ROS) that can cause oxidative stress or oxidative damage, leading to cellular dysfunction or death.

To mitigate these factors, researchers control the temperature of the bioink and the printing environment, adjust the pH of the bioink with buffering agents, and add antioxidants or chelating agents to the bioink to reduce the harmful effects of oxygen [67].

Furthermore, chemical stressors can also play a role in cell viability:

Toxicity from Bioink Components: Certain components of the bioink, such as crosslinkers or unreacted monomers, can be cytotoxic. Ensuring that all materials within the bioink are biocompatible and non-toxic to the encapsulated cells is crucial.

Nutrient Deprivation: During the printing process, cells may be deprived of essential nutrients and growth factors critical for their survival and proliferation, especially if the bioink's density hampers diffusion.

Immune Response: When bioprinted tissues are implanted, the host's immune response can cause additional cell stress. Biocompatibility and the potential for immune rejection must be considered when selecting bioink materials.

To address these chemical and biological stressors, bioprinting strategies may include using bioinks formulated with components that support cell survival and function, such as

natural polymers that mimic the extracellular matrix, growth factors, and nutrients that promote cell health and proliferation.

Researchers focus on meticulously optimizing bioprinting parameters to minimize cell damage during EBB. This includes selecting the appropriate nozzle diameter, angles, and lengths, adjusting extrusion pressure, and calibrating the printing speed to ensure that the mechanical forces applied to the cells are within a tolerable range. The rheological properties of the bioink—its viscosity, yield stress, and thixotropy are finely tuned to align with the delicate balance required for maintaining cell viability while achieving the desired shape fidelity of the bioprinted construct. This rheological tuning often involves incorporating shear-thinning agents such as Xanthan gum, which can facilitate smoother extrusion and reduce shear forces, thereby enhancing printability and cell viability [62].

Maintaining cell viability is vital, but so is preserving the cell's original characteristics or capability to develop into various cell types, which is crucial for the practical application of bioprinting in clinical settings [73]. Human mesenchymal stem cells (hMSCs) have been successfully bioprinted from sources like fat and bone marrow and have been shown to differentiate into cartilage and bone cells, proving that the extrusion process through a needle does not hinder their differentiation potential [74][75]. Similarly, human-induced pluripotent stem cells (hiPSCs) and human embryonic stem cells (hESCs) have been bioprinted using valve-based and direct extrusion methods [76] [77]. Research by Faulkner-Jones and colleagues showed that both hESCs and hiPSCs could be printed without losing elevated levels of viability or pluripotency, and the printing did not unintentionally cause the cells to differentiate. Under suitable conditions, these stem cells were later encouraged to transform into liver-like cells. Furthermore, hiPSCs have been printed with mature chondrocytes using alginate-nanocellulose bioinks. Following the introduction of a chondrogenic medium, these cells were cultivated for five weeks, which led to the production of a collagen type II matrix, as confirmed through immunohistochemical analysis [76].

Methods to Reduce Cell Damage:

To maintain high cell viability, which is critical for the functionality of bioprinted constructs, the stress from both materials and the printing process must be managed. Suitable materials for 3D bioprinting should have good biocompatibility, biodegradability, mechanical

strength, crosslinking properties, and rheological behavior. Combining natural and synthetic materials, like interpenetrating network hydrogels, can optimize these properties. Crosslinking methods also affect cell viability, with ionic mechanisms being less harmful than chemical crosslinking. Process optimization, such as adjusting printing parameters and nozzle design, can reduce cell stress. Substrates that cushion the impact of cell-laden droplets also aid in increasing cell survival. [67]

Regarding materials, ideal characteristics include good biocompatibility, biodegradability, mechanical strength, crosslinking ability, printability, and rheological properties. Natural polymers, while biocompatible, often lack the necessary mechanical strength, whereas synthetic hydrogels provide better physical properties but are less biocompatible. This dilemma is partially addressed by interpenetrating network hydrogels (IPNs), which combine multiple hydrogels to harness their respective advantages. However, different crosslinking mechanisms of hydrogels can complicate the printing process and extend the duration. Special attention is required for materials with photocrosslinking mechanisms, like GelMA, to prevent excessive cell damage due to prolonged light exposure. Ionic crosslinking methods are less harmful than chemical crosslinking and are preferred for higher cell viability.

Process optimization is also crucial for improving cell viability. Reducing shear stress on cells is vital in nozzle-based bioprinting (e.g., inkjet and extrusion-based). This can be achieved by optimizing printing parameters and modifying the nozzle design. The choice of substrate also plays a role in enhancing cell survival, with materials like wet Matrigel or polytetrafluoroethylene (PTFE) providing a protective cushion.

Future Directions:

Developing new bioinks with enhanced shear thinning properties is necessary to improve bioprinting outcomes. Current research in this field leverages experimental studies, computational modeling, and, increasingly, machine learning algorithms better to predict cell behavior and outcomes during the bioprinting process. By combining these approaches, researchers can develop more sophisticated and nuanced models of nozzles that account for the complex interplay of physical, chemical, and biological factors affecting cell damage. This comprehensive approach aims to refine bioprinting techniques to ensure elevated cell viability and functionality levels, advancing the field toward successfully applying bioprinted tissues and organs in clinical settings.

1.2.8 Future perspectives of 3D Bioprinting.

3D bioprinting emerges as an innovative technology harboring immense potential across a broad spectrum of biomedical fields. Its applications are diverse, ranging from tissue engineering (TE) and regenerative medicine (RM) to the intricate realms of biosensor research, culinary science through food printing, and the advancement of medical devices. Additionally, it is pivotal in industrial biotechnology, precision micropatterning, the creation of complex vascular networks, microfluidic systems, organoid production, and disease modeling [78]. The scope extends to sophisticated 'body-on-a-chip' systems, controlled drug delivery mechanisms, toxicological assessments, and cosmetic bioassays. It also lends itself to developing more accurate 3D models for drug discovery and the intriguing field of biohybrid robotics (see Figure 12).

Among the many applications, several stand out due to their transformative potential and current impact. Tissue engineering and regenerative medicine are at the forefront, revolutionizing the approach to healing and tissue replacement [79][80]. The creation of 3D drug discovery models significantly enhances the pharmaceutical industry's ability to screen and develop new therapeutics [81]. The novel concept of food bioprinting is reshaping the future of culinary arts and nutrition [82]. Lastly, the advancements in biosensor research are opening new frontiers in diagnostic and monitoring tools [83] [84].

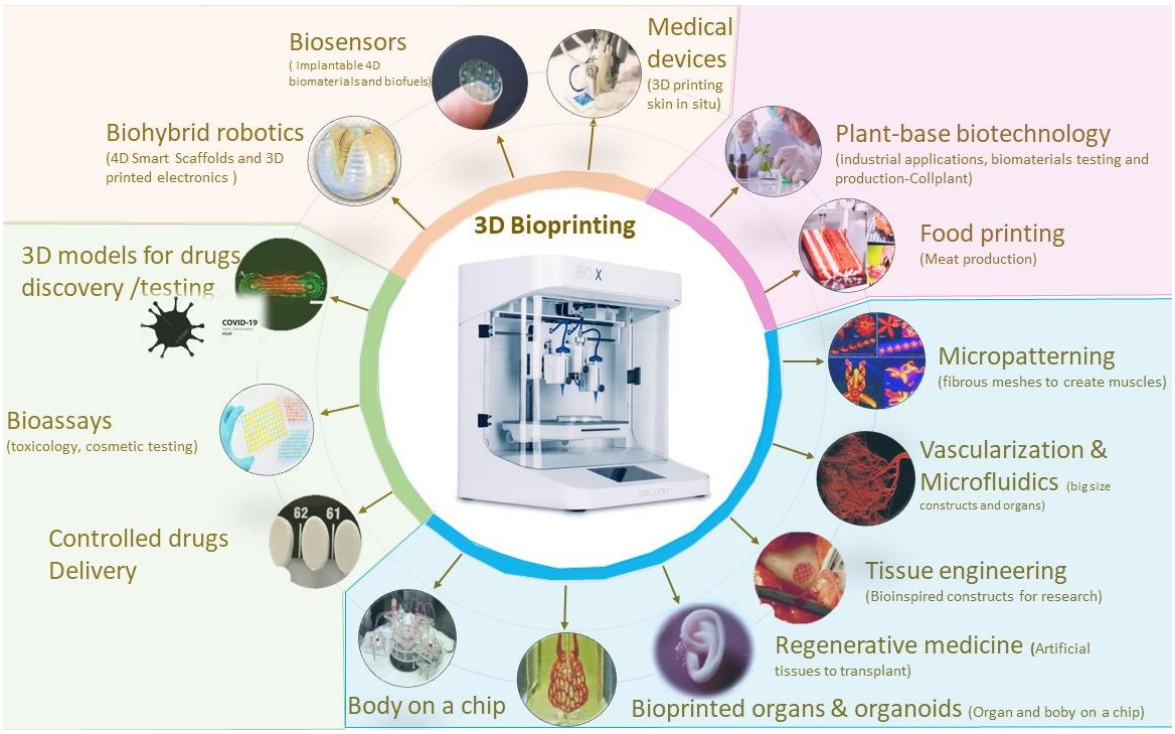

Figure 12 Illustration of the different biomedical applications that can benefit from 3D bioprinting technologies. [79][80] [83] [84].

Regarding the first, 3D bioprinting can contribute to the fabrication of high-performance biosensors that are useful for detecting substances and monitoring physiological parameters by combining biological and physicochemical components [85]. These devices consist of a transducer element and an electronic system element. The transducer element can be bioreceptors, such as nucleic acids, live cells, antibodies, or enzymes, coupled to electrical interfaces based on nanoparticles or nanowires [86]. Although many biosensors based on these components have been readily fabricated, most are only aimed for *in vitro* applications. For translating these devices towards clinical settings, a part of the sensor must be implanted in the body, and the sensors' biocompatibility, controllability, and size must be extensively studied and assessed. 3D bioprinting technologies will be paramount for overcoming these drawbacks since they can be used to precisely position multiple bioreceptors within a biosensor while patterning biocompatible materials in the process, leading to high throughput, highly-sensitive and dynamic biosensors for improving human health [83].

Additionally, in the near future, 3D bioprinting is expected to facilitate the development of 3D tissue and organ models that can genuinely resemble those found in humans, thereby eliminating the necessity of animal models for testing novel compounds in drug discovery, toxicology, and cosmetic testing [87]. Several researchers and institutions have recently raised their concerns about the responsible use of animals for experimentation. This is because their use is mandatory for obtaining approvals from regulatory agencies. However, the scientific information gathered by using them, in some cases, might not be significant for translating novel devices, drugs, and therapies to the clinic. [88], [89].

Still, therapeutics such as vaccines must be assessed on an entire organism's combined systems, requiring animal models until whole systems can be recreated *in vitro*.

In the not-so-near future, 3D bioprinting is envisaged to provide an alternative cruelty-free food source for humanity. It is well known that livestock is one of the essential manufacturing activities affecting climate change and that animal cruelty is widespread within the livestock industry [90]. Several research groups and private companies are investigating the feasibility of manufacturing animal meat through 3D bioprinting technologies by designing tasty biomaterials embedded with muscle cells that mimic animal meat's sensory profile. However, methods for propagating muscle cell lines derived from animals at vast scales and bioreactor systems capable of supporting the maturation of constructs while preserving their properties are needed before this application can be further advanced.

Finally, 3D bioprinting has the potential for fabricating anatomically relevant and fully functional tissues and organs that can be used for transplantation to humans, which is the ultimate goal of tissue engineering [91]. Despite the significant advancements made during the last 20 years toward this goal, bioprinted organs have not been used directly on humans. Given its simple anatomy and the fact that it is the largest and most accessible human organ, skin cartilage, and bone are expected to be the first organ replaced with 3D bioprinting technologies [78]. The Wake Forest Institute of Regenerative Medicine team in North Carolina stands at the forefront of the transition of 3D bioprinting technologies from laboratory research to clinical application. Their recent development, an Extrusion-Based Bioprinting (EBB) system, is designed to be fully compatible with operating room environments, enabling the direct bioprinting of skin onto wound sites [92]. This innovative

system begins by utilizing a laser to scan the wound, creating an accurate 3D model that distinguishes the various layers of skin tissue. With this model, the EBB system proceeds to methodically print skin directly onto the wound, employing specialized bioinks for each distinct layer, thus facilitating the repair of the damaged tissue with precision. While currently validated in porcine models, the institute is actively pursuing the necessary steps to initiate clinical trials, aspiring to make this the inaugural instance of 3D bioprinted skin being applied in human medicine.

The EBB system's capability to bioprint in situ would be a significant breakthrough, marking a new era in regenerative medicine and trauma surgery. This technology tailors the healing process to the individual, adapting advanced personalized medical treatments to the exigencies of emergency care. Its meticulous method of replicating the intricate structures of skin is essential for restoring the function and appearance of injured tissue. Having demonstrated efficacy in animal studies, the next phase of research is focused on human trials, which requires careful consideration of regulatory standards and the assurance of consistent, successful outcomes across diverse patient populations and wound conditions that must be validated by regulatory authorities such the FDA and CFR.

Despite the EBB system's innovative approach and demonstrated potential, its path to becoming a standard clinical practice is challenging. A pivotal concern is the formulation of bioinks that meet biocompatibility requirements and faithfully reproduce human skin tissue's structural and functional complexities. Furthermore, ensuring the long-term survival and integration of bioprinted cells within the patient's existing tissue matrix is an ongoing area of investigation. There are also significant ethical, economic, and educational barriers to consider: the ethical implications of pioneering treatments, the cost implications for healthcare systems, and the necessity for specialized training for medical professionals to operate these sophisticated bioprinting devices. Addressing these issues is essential for the EBB system to realize its potential to transform reconstructive surgery and set the stage for future advancements in the bioprinting of complex organs.

1.2.9 Limitations of 3D Bioprinting

Despite the several advantages of EBB, it is not yet capable of fabricating anatomically relevant and functional tissues. Among the drawbacks hampering this technology, the difficulty of including vascular networks inside the constructs is one of the most relevant since their presence is essential for bioprinting to guarantee cell survival and tissue maturation [7]. Despite recent advancements in techniques that allow for the fabrication of complex structures with EBB, such as the freeform reversible embedding of suspended hydrogels (FRESH) [93], several limitations must first be overcome before specific applications can be considered. First, bioprinting techniques should be capable of building multi-material tissue constructs rapidly and under cell-friendly conditions, thus avoiding the risks that prolonged UV exposure, shear stress, harmful temperatures, and toxic materials represent to cell integrity. Second, maturation processes and instruments, such as bioreactors, that can simultaneously support the in vitro development of constructs containing multiple cell types must be developed [5]. For example, a serum-free cell culture medium capable of supporting various cell lines simultaneously is essential for ensuring reproducibility and adequate tissue maturation. Third, the development of bioinks capable of mimicking the composition and mechanical properties of native tissues must be fully addressed. Finally, incorporating vascular channels within bioprinted constructs and their innervation with native vasculature must be solved [29], [30]. To provide a vascular channel that is contractible, distensible, a platelet and erythrocyte-friendly environment that does not facilitate thrombogenesis, such channels should be structured like those found in the body, which is composed of muscular and endothelial layers. These biomimetic characteristics must be complied with by tissue-engineered vascular grafts, envisioned as the next-generation solution for replacing or bypassing medium and large-diameter arteries and veins.

Chapter 2

State-of-the-art coaxial printing

2.1 3D bioprinting with multi-layered coaxial extrusion systems

Coaxial systems consist of a deposition outlet that connects two or more independent channels, thus allowing the deposition of multiple materials simultaneously but preserving their independence before deposition.[94][95][96][97] These systems permitted the controlled fabrication of multi-layered hierarchical structures, such as heterogenous fibers, tumor models, and vascular constructs.[98][99][100] In the first decade of this century, they were first reported for tissue engineering, where electrospinning was employed to manufacture biomaterial scaffolds [76][77]. However, the use of coaxial systems in 3D bioprinting was first reported in 2013 by Ibrahim T. Ozbolat's research group at the University of Iowa [11], [103]. These original articles employed a double-layered coaxial nozzle coupled to a robotic bioprinting system to fabricate tubular structures with and without embedded cells. The authors implemented crosslinking schemes during the printing process, as an alginate hydrogel was deposited from the outer channel and calcium chloride from the inner channel. It facilitated the fabrication of cell-laden perfusable tubular structures with high structural stability, which was impossible with conventional biofabrication technologies. Additionally, they characterized the cell viability of the bioprinted constructs as a function of dispensing pressure and coaxial nozzle size. Their

findings demonstrated the relevant effect of these two parameters on cell viability, as these have the most considerable influence on the shear stress exerted on cells during deposition.

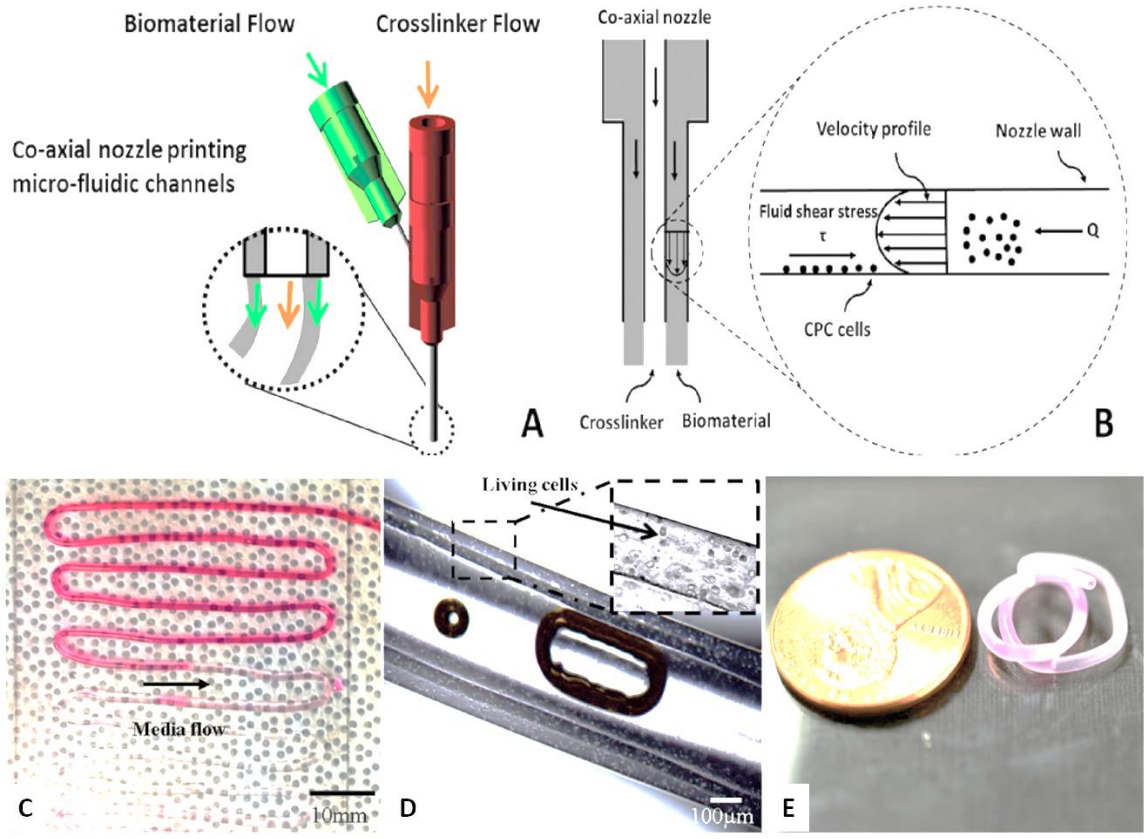

Figure 13 Illustration of a double-layered coaxial extrusion system and the vessel-like constructs fabricated using a coaxial nozzle. Figure adapted from [73].

Since then, coaxial bioprinting technology has been further developed and implemented by other research groups for the fabrication of perfusable vascular channels [33], [104]–[107]. Recently, Gao and colleagues utilized a double-layered coaxial extrusion system to bioprint free-standing, perfusable, and functional vascular models [10]. They developed a blend bioink consisting of human endothelial cells, extracellular matrix derived from vascular tissue, and alginate. This blend bioink was extruded in the outer channel of the coaxial nozzle, while a sacrificial synthetic polymer supplemented with calcium chloride was extruded through the inner channel. The vascular constructs developed well-matured endothelium following the maturation process and displayed representative vascular functions.

Similarly, by employing triple-layered coaxial bioprinting, Pi and colleagues recently reported fabricating cell-embedded, multi-layered, perfusable vessel-like structures [104]. They employed bioinks with high crosslinking efficiencies, such as gelatine methacryloyl, alginate, and eight-arm polyethylene-glycol PEG acrylate. With this technology, the authors fabricated vessel-like tissues like urothelial and vascular, last by combining an inner layer of human endothelial cells and an outer layer of human smooth muscle cells. However, the materials used did not correctly match the mechanical properties of native vascular tissue nor guarantee structural stability under constant perfusion during the maturation process. Moreover, their model still lacks an outer layer consisting of a fibrous and collagenous matrix of fibroblasts, which is required for vascular tissue constructs to be functional and biomimetic [108]. Although the necessity of this cell-embedded triple-layered composition for vascular tissue constructs is relevant for research and clinical use, **traditional biofabrication methods cannot fabricate these with high structural stability and precision as it is made in comparison by using the coaxial bioprinting approximation** [96]**.**

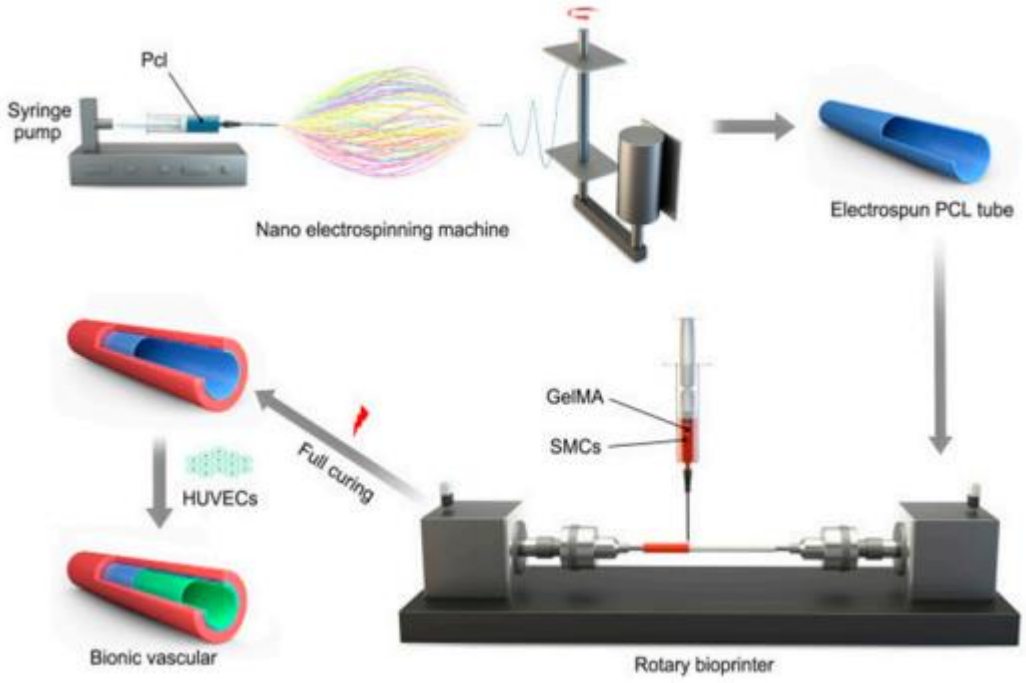

Figure 14 illustrates a coaxial method for creating small-diameter artificial vascular tissue by integrating nanofiber electrospinning and rotary bioprinting. [109]

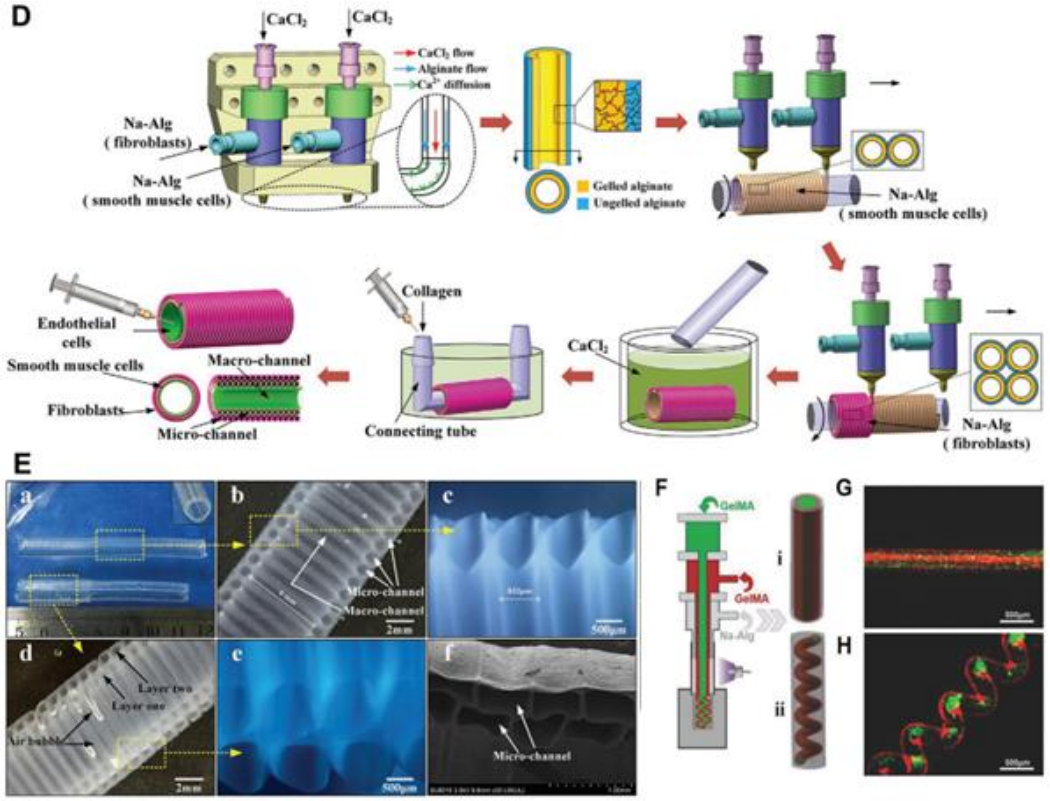

Figure 15. D. multiscale fluidic system makes alginate structures. E. Multi-scale perfusable vessel-like constructs. (a) Samples of single-layer and double-layer constructs, b, c) photographs of single-layer constructs, d, e) photographs of double-layer constructs, f) scanning electron microscopy of longitudinal sections. F. Multi-material microfibers, multilayer patterns. Figures adapted from [94]

With microfluidic printheads and co-axial nozzles, it is possible to fabricate more complex fibers, such as multi-compartmental ones. Q. Gao proposed in 2017 that using an innovative rotate approach, it is feasible to construct vascularized tissues using multi-scale fluidic systems (i.e., macro channels and microchannels), as explained in [100] and [105].

Multi-material constructs can be created using the liquid rope-coil effect [110][111]. Shao et al. GelMA microfibers with various morphologies were formed using co-axial bioprinting with multi-materials. [112] In the nozzle, non-viscous GelMA was surrounded by viscous alginate, resulting in a laminar co-axial flow. To obtain multi-compartmental microfibers, a similar methodology was employed with different cell-laden hydrogels as core bioinks [94]. In 12 days of culture, HUVEC-laden GelMA was also found capable of migrating toward the borders of GelMA coils when used as a core bioink.

2.2 Embedded bioprinting

Embedded bioprinting consists of the controlled deposition of bioinks inside a support bath. Embedded printing involves extruding the hydrogel (bioink) into an emulsion that supports the fidelity of the printed structure, which is not printable via conventional 3D printing techniques. Embedded printing can fabricate freeform constructs while printing extremely low-viscosity inks through an aqueous two-phase system (ATPS). [113][114][111][110][115][94][70].

One of the first techniques to include natural materials and living cells was reported in 2015 by Hinton and colleagues: freeform reversible embedding of suspended hydrogels (FRESH). It is a 3D printing technique that emerged to overcome limitations when attempting to print hydrogels in highly complex geometries [93]. In this technique, a support bath based on microparticles of sacrificial materials (such as gelatine, agarose, and pluronic) prints overly complex structures that are challenging to achieve with direct printing, even with the most mechanically suited bioinks. This technique was first reported in 2015 by Highley and colleagues from the University of Pennsylvania [116]. Their technique made it possible to print shear-thinning hydrogels into self-healing support hydrogels. They developed supramolecular hydrogels based on biochemically modified hyaluronic acid with either adamantine or cyclodextrin, which formed guest-host bonds upon mixing.

Despite this being the first published report on embedded bioprinting, a similar article published later the same year by Hinton and colleagues from Carnegie Mellon University is typically acknowledged as the breakthrough to the field [93], as it proposed a more straightforward process with solely nature-derived materials. In this work, the authors demonstrated the additive manufacturing of hydrogels made from natural materials that are impossible to bioprint with structural stability and shape fidelity by using direct EBB. Their method involved depositing hydrogels composed of gelatine microparticles inside a support bath. Using gelatine microparticles for the support bath is their inverse temperature response from collagen and their rheological behavior. In particular, collagen is widely used for bioink formulation since it is the most abundant protein in almost every human tissue [117]. At temperatures below ten (10) ºC, collagen has a liquid-like viscosity, while gelatin forms a gel.

Conversely, collagen forms a gel at temperatures between 30 and 40 ºC, and gelatin behaves like a liquid. This inverse behavior displayed by the materials allowed the authors to print overly complex structures made mainly from the collagen inside a support bath of gelatine by maintaining a low temperature during the process. After the print was complete, the flask containing the support bath and the print were transferred to an incubator, where collagen self-assembled into a gel and gelatin was liquefied and subsequently washed away. Furthermore, collagen-based hydrogels exhibit shear-thinning behavior [52], while gelatin microparticles behave as Bingham plastic [118]. This difference causes the support bath to self-heal while the collagen hydrogel is deposited inside, thus maintaining the printed structure. To demonstrate the potential of this technique, the authors also managed to print alginate and fibrinogen hydrogels by crosslinking during the bioprinting process. Specifically, they supplemented the support bath with calcium chloride when printing with alginate and thrombin when printing with fibrinogen.

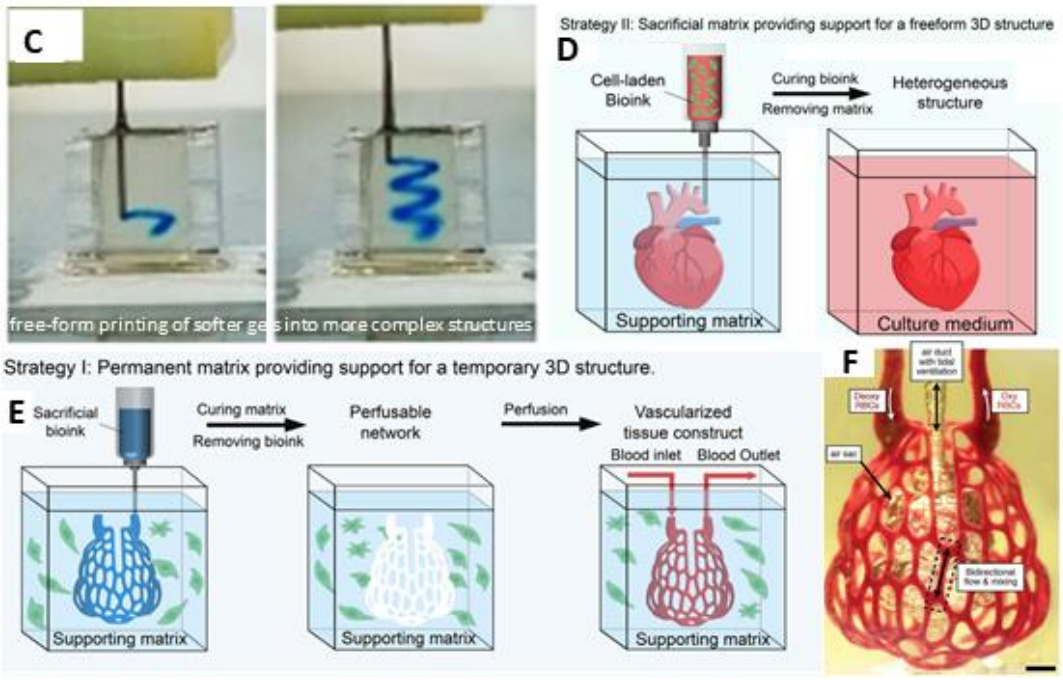

Figure 16. Hinton and colleagues first reported a schematic illustration describing the FRESH bioprinting technique in 2015. Collagen-based hydrogel is deposited inside a support bath consisting of gelatine microparticles under room-temperature conditions. Upon incubation of the setup at 37 ºC, collagen forms a gel, and gelatine liquefies. C. Microgels jammed together to allow more complex structures to be printed in a free-form way. D. and E. A typical fabrication strategy for embedded EBB. Figures adapted from [118][119][120].

Since it was first reported, several research groups have implemented the FRESH technique or embedded bioprinting for fabricating complex structures with mechanically soft hydrogels and bioinks. In particular, this technique has been used for bioprinting corneal [121], cardiac [115], [122]–[124], cancer [125], [126], and muscle [127] tissues. Moreover, it has also been used for bioprinting highly detailed perfusable channels within tissue constructs [128]. In particular, Skylar-Scott and colleagues at Harvard University developed the sacrificial writing into functional tissue (SWIFT) technique, in which the support bath contained cellular aggregates embedded in an extracellular matrix hydrogel and a sacrificial material was deposited within it [129]. By using this technique, they bioprinted vascularized and densely populated tissue models.

Several research groups have recently implemented extrusion-based printing inside support baths to build relevant-sized and vascularized tissue constructs. For instance, by printing collagen inside a support bath, Lee and colleagues built functional tri-leaflet heart valves and a fully-scaled neonatal human heart [115]. Furthermore, their latest work reported the fabrication of a full-size model of the human heart using FRESH printing of alginate inside a support bath made mostly from gelatine microparticles and calcium chloride [124]. Although these works are advancing the field through developing techniques that permit the scale of tissue models, their lack of functionality is still a significant limitation that must be overcome. To provide functionality, tissue models must be embedded with multiple cell lines native from the tissue of interest and with structures, polymers, and cells aligned and oriented in an axial direction, parallel to the flow of the fluid those will contain that will allow this to grow and mature to consolidate a tissue with sufficient mechanical properties to withstand high perfusion pressures such as those delivered by the heart to its own veins and arteries, their fate must be purposely directed via a maturation process.

Conversely, using the sacrificial writing into functional tissue (SWIFT) technique, in which the support bath contains cells and a sacrificial ink is printed instead, Skylar-Scott and colleagues bioprinted vascularized and densely populated tissue models [129]. Although previous efforts using these techniques focused on printing complex and highly detailed structures, an alternative application could entail bioprinting low-viscosity bioinks, otherwise unprintable.

2.3 Addressing Flow Property Challenges through Suspended Bioprinting.

Several teams have overcome the challenges associated with bioink by altering the printing environment instead of the ink itself. Specifically, they have moved from a 2D printing surface to a 3D printing environment filled with a supportive suspension medium (SSM). This medium supports the bioink as it is extruded before the final structure is stabilized by cross-linking [130]. The suspension medium behaves like a solid at rest or below its yield stress. However, when the stress that exceeds the yield stress is applied, such as when a needle moves and deposits bioink, the medium becomes fluid-like, allowing it to flow and be displaced. Once the stress is removed, the suspension medium quickly returns to its solid-like state in a self-repairing action, securing and holding the bioink in place before cross-linking [131].

This technique, also known as freeform, embedded, or gel-in-gel printing, enables printing in any direction and overcomes the constraints of overhangs, building direction, internal gaps, and complex scaffold shapes. Crucially for the scope of this discussion, **bioinks with exceptionally low viscosity, like collagen solutions, can be used to create intricate shapes**. The Lewis group pioneered this method in 2011, and since then, various approaches have been developed, including the use of chopped slurries, fluid gels, nano-clays, microgels, polymer networks with dynamic or reversible bonds, and viscous solutions. This advancement has significantly enhanced the capability to print complex shapes, including vascular networks within tissue constructs [122].

2.4 Bioprinting within thick hydrogels.

Shear-thinning fluids with high viscosity have been utilized as carrier matrices in 3D printing applications, especially in embedded bioprinting. The suspended bioprinting technique was demonstrated by the Lewis group in 2011 when they created intricate 3D microvascular structures using a Pluronic F127 gel, which was altered with diacrylate to allow for photocrosslinking. Their printing material, also based on Pluronic F127, was employed just above its critical micelle concentration, giving it shear-thinning properties while retaining a filamentous shape upon extrusion. Immediately after being extruded, the space left by the needle in the carrier matrix was filled by an acrylate-modified version of the same Pluronic F127. This pioneering work paved the way for the development of shear-thinning hydrogels

that are highly self-repairing, eliminating the need for a secondary material to fill in gaps created by the printing process [132].

One particularly notable study by Highley and colleagues highlighted using hydrogels modified with adamantane and cyclodextrin-based hyaluronic acid, serving as both the suspension medium and the printing material. This approach allowed for printing various cell-laden structures without being constrained by the orientation or shape of the constructs. Moreover, adding methacrylate to the mix could form channels within the hydrogel structures to support fluid flow[133]. Another recent experiment utilized xanthan gum to fabricate free-standing, tubular structures and a composite hydrogel infused with cells capable of sustaining perfusable channels. The bioinks used in such suspended extrusion-based printing (sEBP) methods can also be designed for photocrosslinking, as illustrated by a bioink composed of acrylamide, bisphosphonate, and hyaluronic acid that was extruded into a matching bisphosphonate-hyaluronic acid suspension medium[134].

2.5 Embedded bioprinting with complex structural organization.

Cardiovascular tissue is a functional organ composed of blood vessels that carry oxygen and nutrients throughout the body. It also has several chambers of the circulatory system for pumping blood and a heart valve that prevents the backflow of blood.[120] [135]

Replicating anatomical structures in artificial constructs is critical to cardiac functions in vitro. Bioprinting applications may mainly be used in disease modeling, drug testing, or regenerative medicine applications for cardiac tissue [28][119]. The use of extrusion-based embedded bioprinting provides an innovative method for fabricating functional cardiovascular tissues with heterogeneous materials and complex structural arrangements.

A hierarchical branching microchannel network was fabricated with Pluronic F127 as the sacrificial bioink by Wu et al. [132]. The Pluronic F127 bioink, unmodified and stored in its pure state at four (4) °C, was liquefied and washed away at a low temperature by a diacrylate-functionalized Pluronic F127 matrix. **(Figure 10-a).** Song et al. To fabricate well-defined microchannels for long-term perfusion, printed methacrylate-modified hyaluronic acid as the support matrix and unmodified hyaluronic acid as the sacrificial bioink [136][132] [120].

The pressure-driven flow was used to remove the printed bioink after photocrosslinking the supporting matrix. Fluorescent beads were perfused into the microchannel to demonstrate its connectivity. A confluent vascular-like construct was formed after HUVECs were perfused for two days with dynamic perfusion **(Figure 10-b).** Biological systems rely on the filamentous nature of ECM to regulate cellular behavior [137][138]. Recent studies have used fibrillar hydrogels derived from plant-derived cellulose nanocrystals to create artificial fibrillar networks in biological models [139]. In addition to supporting sacrificial bioinks for constructing magnificent structures, cellulose hydrogels exhibit thixotropic properties. Removing sacrificial bioinks such as Pluronic F-127 makes it possible to fabricate perfusable and cell-compatible microchannels quickly. A further advantage is that cellulose matrix fibrils better mimic the ECM's interstitial permeability for the diffusion of biomolecules. This can affect the functional outcomes of the fabricated in vitro models [140][141][120].

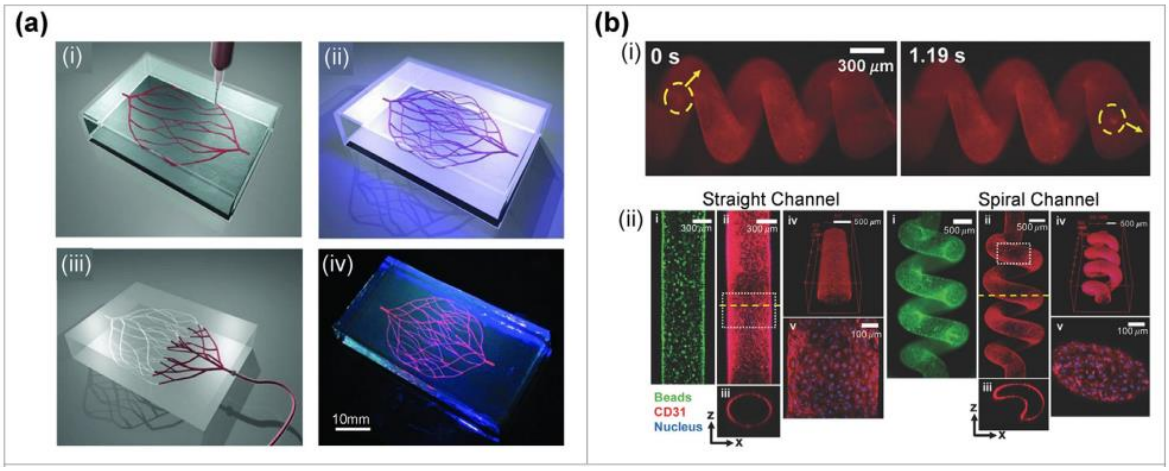

Figure 17 (a) Using extrusion to embed bioinks in vascular-like networks as sacrificial bioinks, printing sacrificial bioinks within a photocurable matrix to fabricate hierarchical, perfusable channel networks. Hierarchical branching networks were printed using a photopolymerized Pluronic F127-diacrylate matrix. Photopolymerization is then performed on the supporting matrix. In the process of liquefying and removing the bioink, the channels were exposed by perfusing the channel network with dyed red.[132] John Wiley & Sons, 2011. All rights reserved. In (b), a method is described for fabricating perfusable microchannels. The interconnection of fluorescent beads was demonstrated by perfusing them. Microchannels that were endothelialized and had a straight or spiral configuration. [142] Published by John Wiley & Sons. Copyright 2018. Figure adapted from [142]

Noor et al. fabricated a heart model with prominent blood vessels within alginate-bio ink and xanthan gum matrix. [122] Several decellularized bioinks were used to print cardiac

constructs with blood vessels, including cardiomyocytes and endothelial cells. The integrity and mechanical stability of the printed cardiac constructs could be maintained after the gelation of the bioinks, demonstrating a similar structural organization to the heart tissue. (**Figure 11-a).**[120]**.**

Researchers have developed a dual-material embedded bioprinting strategy to fabricate human contractile ventricles more efficiently and reliably. Using collagen bioink as the printing material, the inner and outer walls of the ventricle were printed, and cardiomyocytes derived from hESCs and cardiac fibroblasts were used to print the central core region of the ventricle. (**Figure 11-b).**[120]**.**

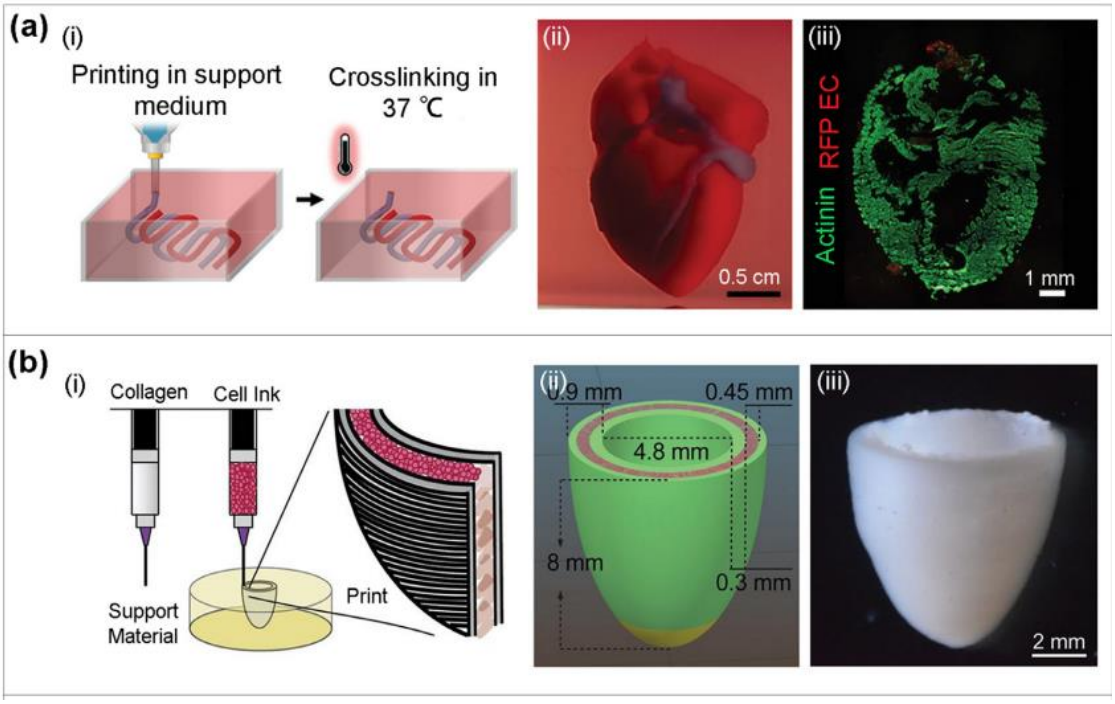

Figure 18 In an embedded bioprinting process based on extrusion, living tissue constructs can be embedded using multiple materials. They were embedding major blood vessels in a bioprinted human heart model. (a-i) Schematic of dual-material extrusion-embedded bioprinting. Printed human heart model (a- ii, iii) side view and cross-section. This work is licensed under CC-BY and published by the American Association for the Advancement of Science—copyright 2019. Extrusion-embedded bioprinting produces a contractile cardiac ventricle model—(b-i) Diagram showing how the ventricle model is printed. (b-ii) The model of the cardiac ventricle has been designed and printed, adapted from [120].

A 7-day culture of the printed living construct showed that it could respond to electrical stimulation (1 and 2 Hz) and synchronous contraction activities with a spontaneous beat rate of 0.5 Hz. Moreover, the calcium waves propagated spontaneously and in a directional

direction at a speed of 1.97 cm/s at the cellular level. It was also found that embedding the tri-leaflet valves in a functional adult-scale heart was possible using extrusion-based embedded bioprinting. Continuously opening and closing valve leaflets can be accomplished with the help of a perfusion system. A maximum transvalvular pressure of more than 40mmHg was observed, which is higher than the physiological pressure in the tricuspid and pulmonary valves, which a pressure less than 20mmHg can physiologically maintain.[143] Kupfer et al. It has been demonstrated that a human-chambered muscle pump with two chambers and a vessel inlet and outlet can be successfully printed using cell-laden bioinks within a gelatine support matrix [120]. A six-week culture of hiPSCs resulted in the differentiation of hiPSCs into cardiomyocytes and the development of adjacent muscle tissues. In the printed constructs, there were measurable pressure and volume changes with contractions, and pharmacological agents and electrical stimulation caused synchrony and reactivity in the contractions, along with measurable changes in pressure and volume.[123].

2.6 Bioprinting vascular networks.

A significant yet unresolved issue in the field of tissue engineering is the integration of a vascular network within a large tissue construct. When an engineered tissue construct is implanted, the body’s inflammatory response often triggers the formation of vessels [144]. However, in the context of larger tissue constructs, the pace of vessel growth is inadequate, leading to the development of a necrotic core within the engineered tissue. The advent of suspended printing technology has provided a solution to this problem. This technology allows for the creation of tubular structures and vascular networks, overcoming previous geometry and bottom-up fabrication constraints.

One way to print a vascular channel is to use a material that can be removed later as a filler in a cross-linkable media. The media is then solidified, and the filler is washed away, leaving a hollow tube [122] [145] [146] [142] [147]. Compaan et al. used a mix of gelatin and gellan-based microgels in a gelatin media to print vascular structures with a 2% alginate filler. They cross-linked the gelatin media with transglutaminase (TG), but this had a brief time window, as the gelatin started to solidify as soon as TG was added. They also observed significant changes in the shape of the printed filament after 30 minutes of adding TG [148].

In the research conducted by Song et al., they printed two tubular structures using guest-host chemistry for both the suspension media and the sacrificial ink. The suspension medium was a viscous fluid hydrogel bath made of adamantane, norbornene-modified hyaluronic acid (HA), and cyclodextrin-modified HA. After extruding a sacrificial ink, the media was crosslinked through a thiol-ene reaction between a di-thiol crosslinker and the norbornene groups.

One of the “vessels” was seeded with endothelial cells (HUVECs), while the other was used to circulate angiogenic growth factors (VEGF, PMA, and S1P). The growth factors were released into the protease degradable support hydrogel, which allowed the endothelial cells to sprout directionally towards the channel containing the growth factors. Over three days, the endothelial cells were observed to invade the central region, with branches extending up to approximately 400 micrometers [129].

The Lewis group has advanced the formation of vessels even further with their “sacrificial writing into functional tissue” (SWIFT) technology. Instead of using suspension media, they used hundreds of thousands of cell spheroids in a continuous collagen/matrigel phase to print a vascular network with a sacrificial hydrogel. The resulting structures closely resemble actual tissue, with a high cell density that mimics native tissues.” The resulting structures are one of the closest resemblances to tissue that has been produced in bioprinting” [129]

Brassard and colleagues also presented an inverted version of this system. They deposited organoids of HUVEC, MSC aggregates, and intestinal organoids into a Matrigel-collagen suspension media before crosslinking. With the right growth factors, they demonstrated the self-organization of specific tissues to form connected vessel-like structures on a millimeter-to-centimeter scale. They also created gradient structures by co-extruding multiple types of organoids, mimicking the stomach-intestine transition [149].

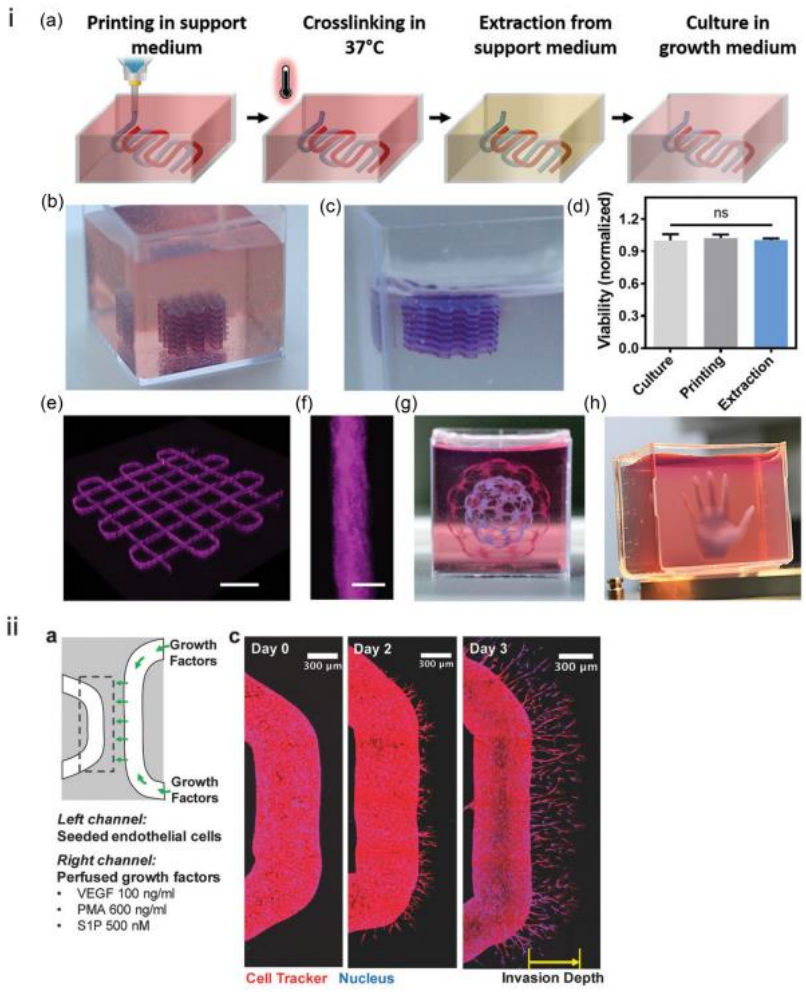

Figure 19 Here are some notable instances of suspended printing and printable geometries in the field of 3D bioprinting:(i) Suspended Printing Examples:(a) Extrusion, cross-linking, retrieval, and culture of omentum hydrogel bioink within an alginate/xanthan gum support bath. (b)–(h) Additional relevant examples. (ii) Printing of Tubular Structures in Guest-Host Hydrogels:(a) Schematic process representation. (c) Temporal formation of vascular sprouting towards the growth factor channel [70].

All suspended printing techniques have similar rheological properties, exhibiting minimal thixotropic behavior. However, a lack of standardization between labs limits the comparisons that can be made between each technique. To facilitate better comparisons and identify the most suitable medium for a bioink, it is suggested that the following should be reported at a minimum: frequency sweeps, oscillatory strain, and stress sweeps, thixotropic recovery, and, in the case of particulate media, particle size analysis and volume fraction. The minimum feature sizes achieved using each technique are often reported without including cells, which limits their relevance in practical applications.

2.7 Coaxial embedded bioprinting.

Coaxial embedded bioprinting [150][151] is a variation of embedded extrusion bioprinting that uses a coaxial nozzle to produce vertical filament arrays in a support matrix, mimicking natural linear structures. This method can create villus-like or veins-like structures with a dual-layer support matrix miming the varying microenvironments in the human intestinal or vascular systems. By optimizing bioprinting parameters such as nozzle speed, materials, and cell concentration in the support base, structures like native human intestinal villi or veins can be obtained. This method has been shown to result in positive cellular activity, including cell aggregation, viability, proliferation, and biomarker expressions.

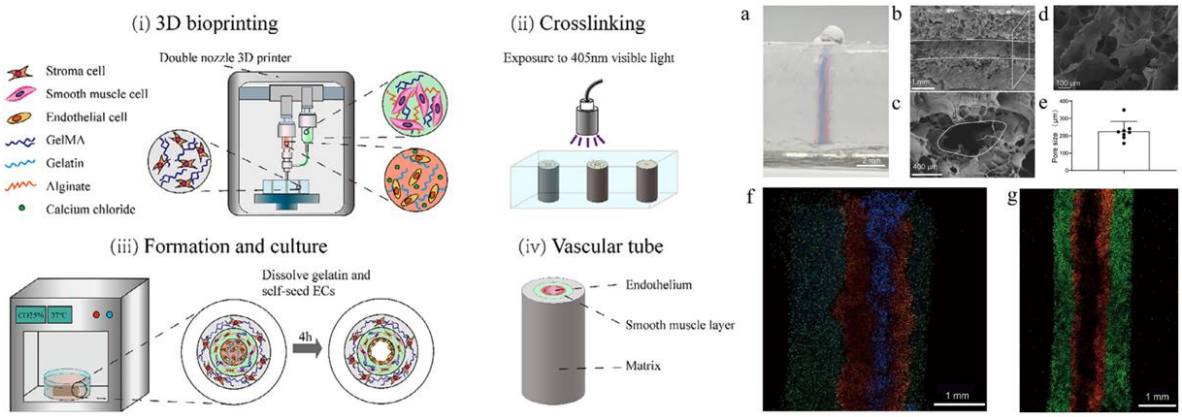

Figure 20 The text describes coaxial embedded bioprinting, a multilayer tube. Through scanning electron microscopy (SEM), distinct color dyes visualize the multilayer tube's structure. Furthermore, SEM is used to show the pore sizes of the generated coaxial construct, and statistics of the pore diameter were provided. Using fluorescent particles, green, red, and blue particles indicate the boundaries between the layers of the multilayer tube. adapted from [151]

In conclusion, the techniques presented in this chapter raise the question of whether it is possible to use coaxial-embedded bioprinting to create complex structural organizations. To date, there is a lack of literature on this topic, and we hope to address this question and answer our research objectives in **Chapter 4**.

2.8 Non-planar bioprinting.

Non-planar bioprinting" refers to an innovative technique within the realm of bioprinting technology aimed at crafting three-dimensional (3D) structures that deviate from flat or planar configurations. This method diverges from the conventional practice of depositing materials in flat layers. Instead, it involves the precise deposition of bioink or materials in multiple dimensions, enabling the intricate formation of complex 3D shapes and structures. Non-planar bioprinting holds paramount importance in the field of regenerative medicine and tissue engineering, as it empowers researchers to fabricate intricate and functional tissues and organs that closely emulate the natural complexity of biological systems. This technique endows the bioprinter with the capability to traverse non-planar directions, facilitating the creation of exceedingly intricate and sophisticated structures on custom regions.[152]

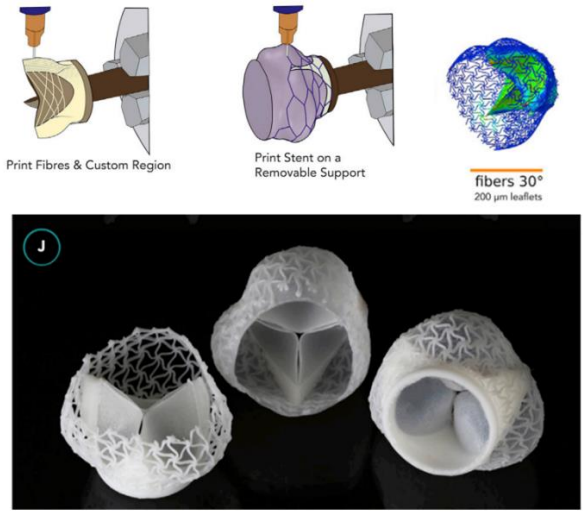

Figure 21 Personalized Heart Valve Fabrication within a Customized Anatomical Region using a non-planar bioprinting technique. Figure adapted from [152]

In the realm of biofabrication, non-planar bioprinting has been instrumental in the generation of structures that closely replicate the geometry and microstructure found in natural tissues. As an illustrative example, Song et al. conducted a groundbreaking study employing non-planar bioprinting to fashion biomimetic vascular structures. They harnessed a method known as bioprinting embedded non-planar tissues (BENT) to craft a vascular network that meticulously adhered to the contours of biological tissues. This method has demonstrated a remarkable enhancement in fidelity for multi-material printing, yielding accurate heart valve leaflet structures with customizable properties.[153]

Chapter 3

Optimizing Cell Viability of Coaxial Extruder Systems by Implementing Rational Design based on In Silico and In Vitro Evaluations.

3.1 Summary

Tissues and organ biomanufacturing is a rapidly evolving field whose primary goal is the fabrication of three-dimensional (3D) cell-laden constructs that closely mimic native tissues and organs. Although considerable advances in the materials and techniques used to achieve this goal have been made during the last 20 years, aspects such as prolonged cell functionality and tissue vascularization hamper its bench-to-bedside translation. Due to its wide availability and versatility, coaxial-extrusion-based 3D bioprinting (EBB) has been devised as a promising biofabrication technology to overcome these limitations. In this study, we have presented the development of a triple-layered coaxial nozzle that could fabricate vascular networks and vessel-like structures in a biofabrication process.[22] To optimize the design of the coaxial system to guarantee high cell viability upon extrusion, in silico evaluations and subsequent in vitro validations through bioprinting with alginate-based bioink have been undertaken to optimize the design of the coaxial system.

Based on the results of the in-silico experiments, the pressure and velocity distribution values that the model predicted resulted in more than 80% cell viability. The results also demonstrated that the layer's extrusion pressure and thickness significantly affected the cells' viability. The results of our research should pave the road for the rational design of multi-layered coaxial extrusion systems that can be used in biomanufacturing approaches to reproduce the complex structures found in native organs that can be replicated in laboratory biomanufacturing approaches.[22]

3.2 Introduction

Extrusion-based bioprinting (EBB) is a rising 3D bioprinting strategy with incredible notoriety among tissue engineers because of its versatility, wide availability, and potential to manufacture complex tissues. It utilizes the spatiotemporally controlled patterning of bioinks as building blocks for fabricating living tissues. However, mimicking complex native tissue structures is still challenging for the available biomanufacturing technologies [20], [23]. In the case of EBB, the time lag between bioink deposition and subsequent crosslinking is one of the limiting factors in forming complex geometries [24], [25]. This is mainly because the viscoelastic properties of extruded bioinks are often not sufficient to support these geometries before extensive crosslinking is applied [24], [26], [27].
Moreover, extensive crosslinking schemes are often detrimental to cell viability since they require toxic chemicals or exposure of cells to harmful conditions, like UV light. Some of these chemicals that can be toxic to cells include commonly used crosslinking agents in tissue engineering, such as glutaraldehyde, N-(3-dimethyl-amino-propyl)-N’-ethyl-carbodiimide (EDC), genipin, and N-hydroxysuccinimide (NHS). Since this extensive crosslinking technique is hampered by its harmfulness to cells, the shape fidelity of the printed constructs is significantly compromised, especially in the fabrication of hollow or highly detailed structures. A balance must be found between acceptable cell survival and appropriate crosslinking of the printed structure, which remains one key challenge in 3D bioprinting.

Emerging 3D bioprinting techniques, such as the freeform reversible embedding of suspended hydrogels (FRESH) [93] and volumetric printing [154], have contributed to alleviating some of these limitations by allowing the formation of complex structures. In the

FRESH technique, hydrogels are printed in a support bath of sacrificial microparticles, which provides structural support. In contrast, the hydrogel is crosslinked and guarantees a high degree of shape fidelity [39]. Despite the superior printing resolution achieved in constructs manufactured with this technique, results have not yet been reported when depositing cell-embedded hydrogels [20], [115]. Similarly, volumetric bioprinting allows the fabrication of complex free-form geometries with the spatially selective exposition of cell-embedded photocrosslinkable hydrogels to ultraviolet (UV) or blue light. In particular, this technique has demonstrated the rapid fabrication of anatomically relevant hollow structures with high cell viability [45]. However, the current technology cannot include or takes a long time to wash and replace photo inks when using multiple materials within the same layer in the same bioprinting process. It can lead to unwanted heterogeneous stiffness of the constructs, dramatically limiting their exploitability.

Accordingly, here we report the development of a triple-layered coaxial extruder system to fabricate single-layered tubular structures that allow the simultaneous dispensing of three different materials using EBB systems. We aimed to study how this system's distinctive design parameters and bioprinting conditions affect the viability of embedded human cells upon extrusion. Computational analyses were initially implemented to optimize the design parameters of the coaxial extruder system based on predicted pressure distributions. These findings were then validated experimentally in bioprinting experiments using human cells in alginate-based hydrogels. In addition, the triple-layered design allowed immediate bioink crosslinking upon extrusion by including a crosslinking solution as the outermost layer of the printed tubular structures and the formation of hollow structures by posterior removal of sacrificial material contained in the innermost layer.

3.3 Materials and methods

3.3.1 *Geometrical Coaxial Nozzle Design and In-silico* Evaluation.

The first prototype of a triple-layered coaxial nozzle was fabricated by assembling commercially available plastic nozzle parts (Nordson EFD, Dunstable, Bedfordshire, UK). A mixture of a cyanoacrylate solution, cotton, and sodium bicarbonate was employed to adhere the different components into a single structure. From a transverse view, the coaxial nozzle comprised three walls, two rings, and one cylinder, with calibers ranging from 13G to 25 G. This configuration led to three different flow channels, namely, channels *a*, *b,* and *c*, as shown in (**Figure. 14)**.

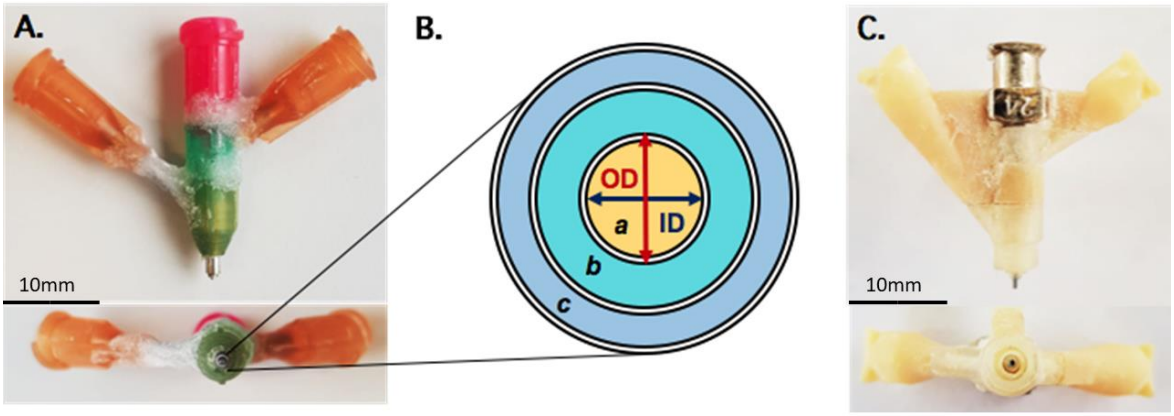

Figure 22 (A) Lateral and frontal view of the initial prototype of the triple-layered coaxial nozzle assembled with commercially available nozzle parts. (B) Schematic representation of the transverse view at the tip of the coaxial nozzle. The outer diameter and inner diameter of each channel were defined according to the results of the computational fluid dynamics simulations. Channels a, b, and c are defined in picture (C) as Three-dimensional printed coaxial nozzles. This figure was published in [22].

Next, the body of this prototype was further improved by using metallic nozzle parts for the channel (a) and then by 3D printing and assembling four parts made using biocompatible photopolymer resins (**Figure. 22**). The same adhesive mixture described for the prototype was used for assembling the second and third prototypes.

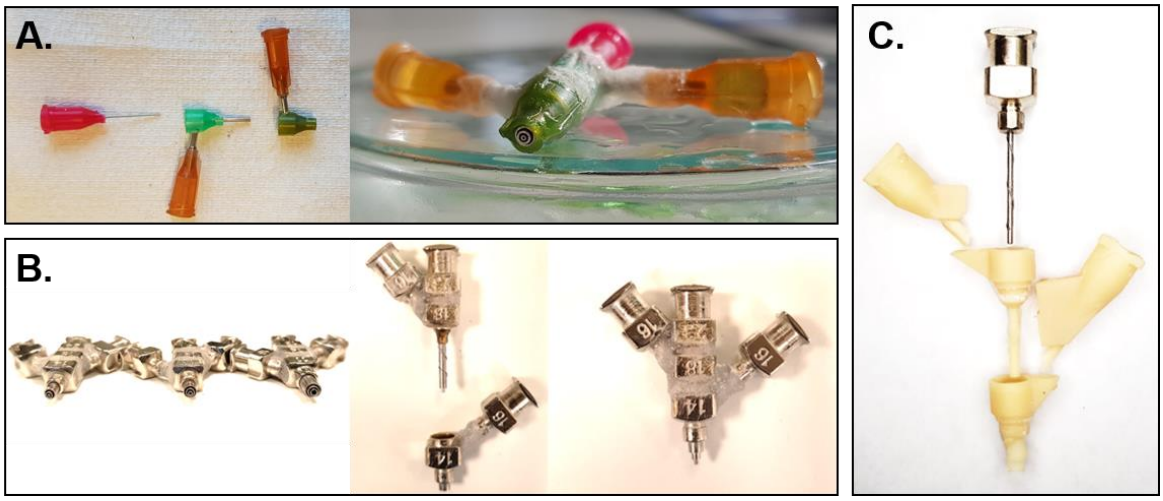

Figure 23 (A) The initial prototype of the triple-layered coaxial extrusion system was constructed using commercially available plastic nozzle components. (B) For the second prototype, enhancements in stability were achieved by integrating metallic nozzle parts, offering a significant improvement over the first prototype's assembly. (C) The third and final prototype of the coaxial extrusion system was developed by combining 3D-printed components with a metallic nozzle part, culminating in a robust and refined design (Original Work) [22].

Based on the third prototype, a computationally aided design model of the three flow channels was developed and studied using computational fluid dynamics simulations in the **COMSOL Multiphysics® CFD software.** The design parameters studied were the area created between the walls of the diameters at the outlet of the nozzles, the length of the nozzle, and the tilted angle of the nozzles, including the surface where the material is to be deposited. Ideal values for the diameter at the outlet are between 150 and 610 μm [13], which is the range where appropriate shape fidelity can be achieved. Moreover, the nozzle length must be between 4 and 18 mm [155] since excessively long nozzles risk not fitting in commercial bioprinters and may elevate internal pressure, while overly short ones might not align with standard luers and cartridges. The ideal angle between the nozzle walls and the deposition surface is identified to be between 125 and 180º. These parameters aligned closely with commercial nozzles, aiming to create a compelling and readily manufacturable coaxial system.

The simulation utilized the **Laminar Flow (spf)** and **Ternary Phase Field (terpf)** Physics in COMSOL, specifically engineered to determine the **velocity and pressure fields** within a single-phase and ternary-phase fluid under laminar flow conditions. Laminar flow is characterized by maintaining a Reynolds number below a specific critical threshold. When this number is surpassed, the flow becomes susceptible to disruptions that may trigger a

transition to turbulence. The exact critical Reynolds number varies with the situation, a notable instance being pipe flow, where it is approximately 2000.

This interface is adept at handling both types of flows: incompressible and compressible, with the latter being relevant at low Mach numbers, generally below 0.3. Additionally, it is equipped to manage non-Newtonian fluids, such as a shear-thinning hydrogel.

At its core, the Laminar Flow interface **resolves the Navier-Stokes equations, pivotal for the conservation of momentum, alongside the continuity equation**, crucial for **mass conservation.**

The simulations established two-dimensional axisymmetric and three-dimensional domains between flow Channels on a glass printing surface, separated by a 250 µm air interface.

The simulations were optimized for both stationary (steady-state) and dynamic (transient) analyses; Fluid Flow, Single Phase Flow with **Laminar Flow (spf),** and Multi-Phase Flow, Three-Phase Flow with **Ternary Phase Field (terpf)** interfaces become particularly essential for **Time-Dependent** studies. In such scenarios, the flow characteristically evolves to be time-dependent and three-dimensional.

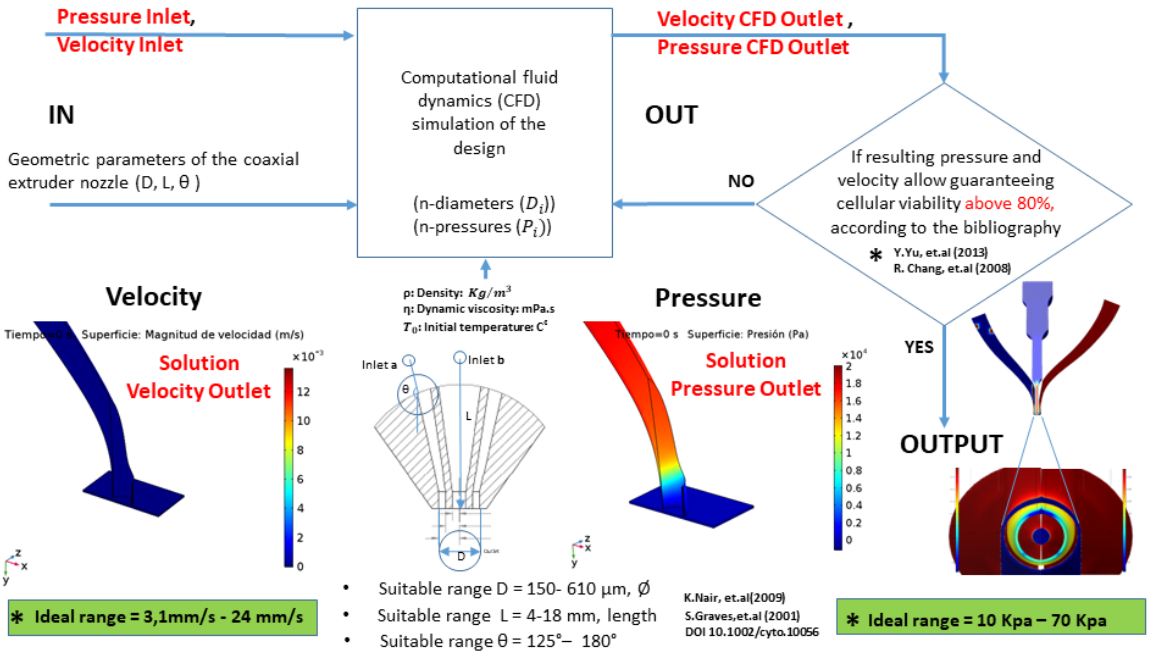

Figure 24: The workflow diagram of the procedure for performing the in-silico simulations led to defining key parameters that guaranteed cell-friendly values of outlet velocity and pressure at the tip of the nozzles (Original Work) [22].

3.3.2 Triple-layered coaxial nozzle CFD simulations

The simulation objective was to analyze the design of the triaxial nozzle to obtain concepts regarding the system's behavior and determine approximate parameters for the experimental prototypes. The analysis was conducted independently for each coaxial nozzle domain, considering the fluid-air-glass interaction located 250 µm from the nozzle outlet. The results were:

- Nozzle outlet velocity in 1[m/s]
- Nozzle outlet pressure in [Pa]

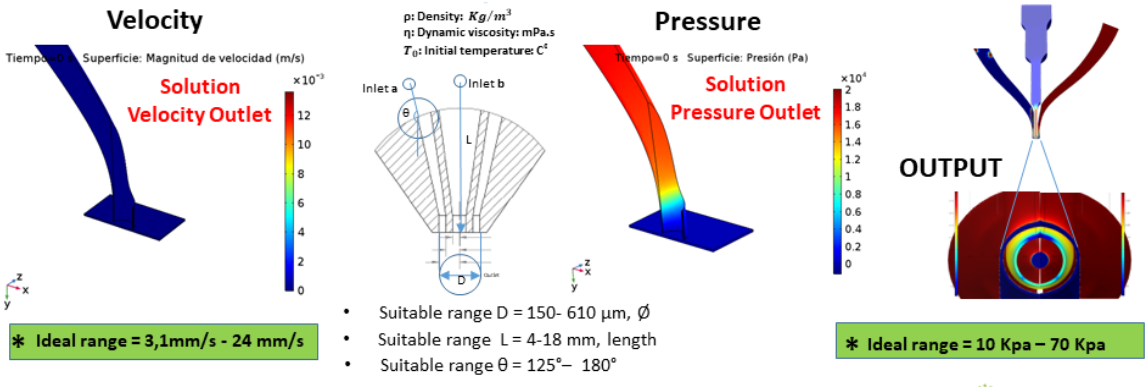

Figure 25 In silico simulations conducted on **Channel (b)** to determine the output parameters, explicitly focusing on velocity and pressure (Original Work) [22].

The simulation involved selecting inputs and testing various coaxial nozzles with differing lengths, angles, and areas defined by the nozzle wall diameters. Post-simulation, the velocity and pressure outcomes at the nozzle outlet were analyzed. This analysis aimed to ascertain if these values align with the cell viability threshold of over 80%, as reported in the bibliography by sources [156], [13], [155], [15], and [157].

The subsequent table details the material parameters incorporated into the Computational Fluid Dynamics (CFD) simulation utilizing COMSOL Multiphysics.

	$CaCl_2$ Solution	**Methylcellulose**	**Alginate-Based Bioink ***	**Air**
Density [kg/m^3]	994	1100	1343	1243
Dynamic viscosity [mPa s]	0,69	520	66	0,018
Nozzle	Right side	Central nozzle	Left side	Interface

Material	**Elasticity modulus**	**Poisson's ratio**	**Density**
Glass	50 Giga Pascal.	0,22	2500 [kg/m^3]

Table 2 shows the parameters introduced to the CFD COMSOL Simulation, such as density and dynamic viscosity (Original Work) [22].

Additional parameters introduced into the CFD simulation tool included inlet velocity, inlet pressure, and the initial temperature of all materials involved in the simulation. The geometry of the nozzle was represented primarily by three parameters: diameter, length, and angle. **Boundary conditions**, such as walls and outlets, were also considered. The interaction between fluid, air, and glass was also modeled, occurring 250 µm from the nozzle outlet.

The simulations covered a range of inlet pressures and nozzle geometries, depicted in **Figures 30, 31, and 32**. Subsequently, the pressure results obtained from these simulations were compared with experimental data from prototypes. This comparison was crucial to validate the accuracy of the simulation outcomes, **Figure 38**.

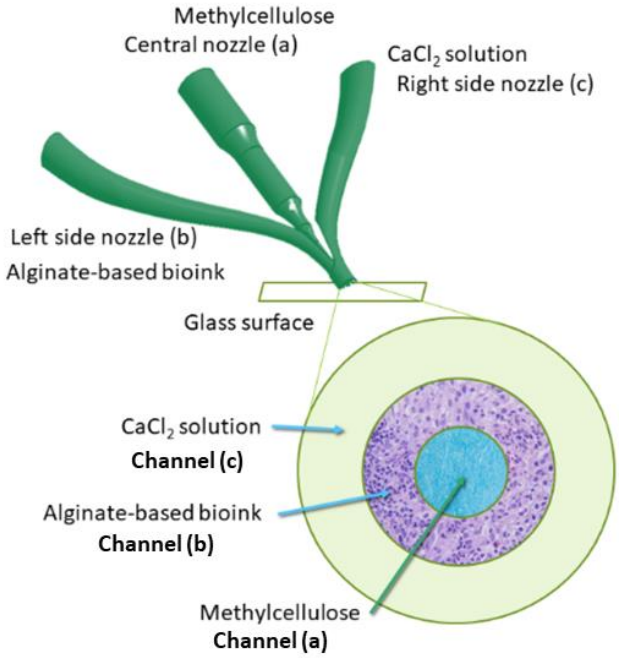

Figure 26 Biomaterials distribution for simulation on the coaxial nozzle prototype (Original Work) [22].

The materials utilized during the simulation were carefully chosen to align with the experimental setup. **Calcium Chloride solution** ($CaCl_2$) was utilized in the outer layer (right-side nozzle), **Methylcellulose** in the (central nozzle), and an **Alginate-based bioink** in the (left-side nozzle). These materials were simulated based on their respective density and dynamic viscosity data.

The materials were selected based on their mechanical and physical properties and biocompatibility with cells, essential in 3D bioprinting. Calcium Chloride solution was chosen for its ability to crosslink alginate, making it a suitable choice for the outer layer. Methylcellulose was chosen for its ability to provide a stable and consistent structure and ease of removal while washing with PBS, making it ideal for the central nozzle to create a lumen after removal. Alginate-based bioink was selected for its cell compatibility, ability to form shear-thinning hydrogels, and crosslinking capability in combination with $CaCl_2$.

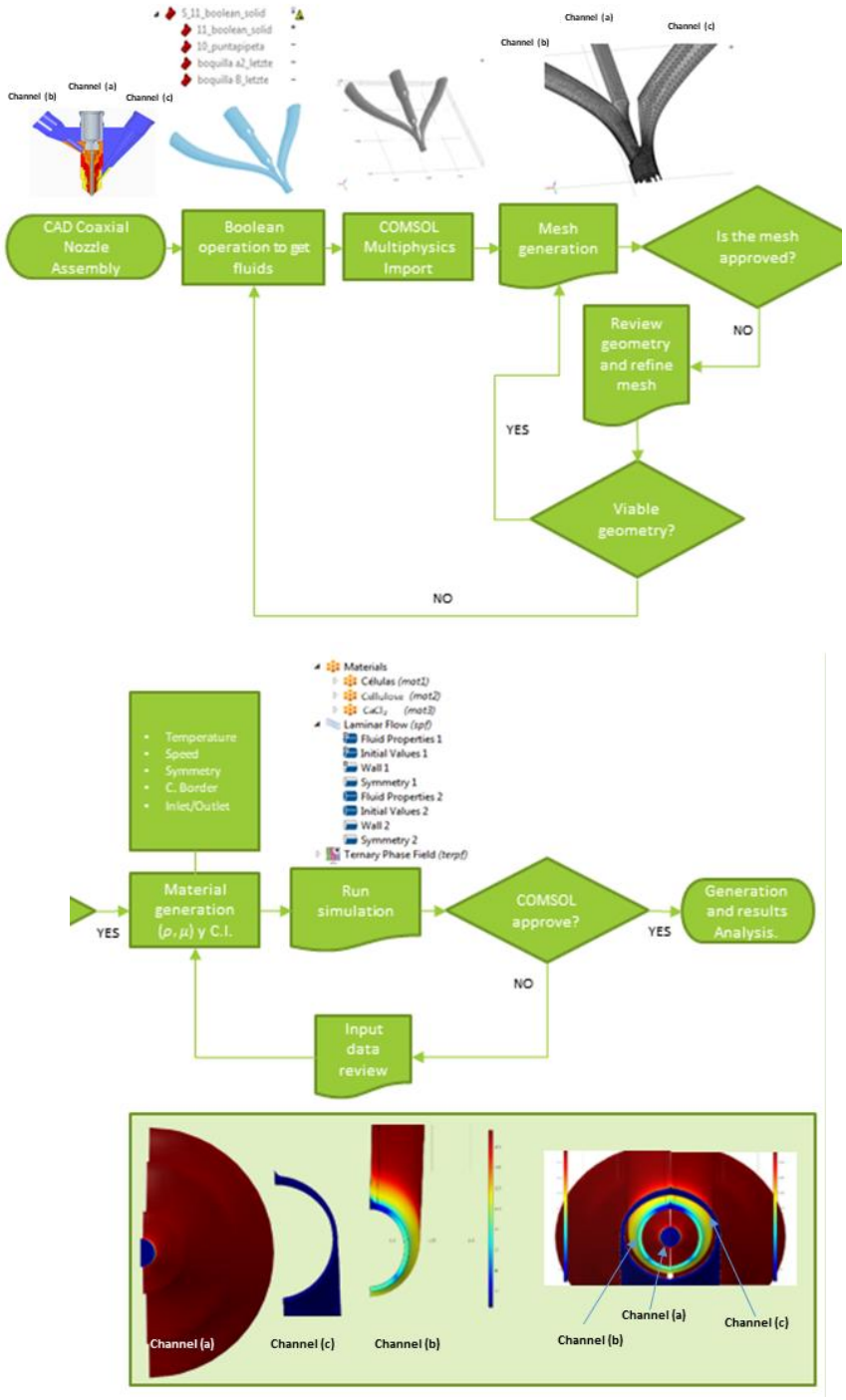

Figure 27 Computational fluid dynamic simulation workflow (CFD) nozzle simulation workflow in COMSOL- Multiphysics (Original Work) [22].

The simulation workflow using COMSOL Multiphysics to analyze the coaxial nozzle assembly involves detailed steps to ensure accurate modeling and practical analysis. The process initiates importing the coaxial nozzle model, domain by domain of the coaxial nozzle assembly, into COMSOL-CFD software. To clarify this workflow, the following is a step-by-step breakdown of the workflow phases, as depicted in **Figure 27**, highlighting their importance in the setup process within the CFD software. This procedure necessitates using the supported CAD files format (STL) of the coaxial nozzle assembly and includes essential pre-processing steps such as refining the nozzle geometry and streamlining complex features of the coaxial nozzle's parts and components. These measures are critical for enhancing simulation efficiency and achieving precise mesh generation with enough accuracy and no distortion.

The focus of the simulations was centered on the section conducting the bioink between flow Channel (b)-nozzle inner wall, and Channel (a)-nozzle outer wall, on a glass printing surface, separated by a 250 μm air interface.

All coaxial nozzle domains were simulated using **two-dimensional axisymmetric and three-dimensional domains**. The selected Physics for the generated domains was represented by using **Fluid-Flow>Single-Phase-Flow>Laminar-Flow(spf)** and **Multiphase-Flow>Three-Phase Flow>Ternary-Phase-Field(terpf)**. This setup was modeled and simulated to reflect the overall design of the coaxial nozzle.

As described before, Channel (b) was a focal point of interest, as it is designed to extrude a single-layered tubular structure using a cell-laden hydrogel (bioink). While **Channel (a)** and **Channel (c)** were also simulated, those received less emphasis in the study compared to channel (b), which plays a crucial role in conducting the bioink. The hydrogel was conceived as a **non-Newtonian fluid**, and its physical parameters, such as **density** and **dynamic viscosity**, were used as input for calibrating the models. Air was conceived as a **Newtonian fluid**, and its density and dynamic viscosity were also provided as input for the simulations.

A **time-dependent** study incorporating **parametric** analysis was conducted across all domains by varying the inlet pressure in each channel. The 'Global>Step' parameter was set to execute a singular progression from 0 to 1 second, with increments of 0.01 seconds, allowing for a detailed examination of changes over this time frame.

Boolean operations delineated the channels within the coaxial geometry, including difference, union, intersection, and compose. These operations facilitated the model's precise definition and integration of distinct channel structures.

These advanced Boolean techniques are crucial for managing complex assemblies like the coaxial nozzle. Each nozzle component is simulated individually, focusing on the walls, and later to integrate all simulations into a cohesive coaxial nozzle assembly. This approach, including strategically handling overlapping or intersecting geometries, is vital for resolving conflicts or issues during simulations, ensuring accuracy and efficacy in the final model and channels.

In Channel (a), between nine different pressures in the range of (14.1 and 69.63) kPa, all simulations were defined for three different lengths between (9 to 18) mm and four different nozzle diameters between 25 to 18 Gauge, (0.250 and 0.84) mm.

The channel (b) between four different pressures into the range of (20 to 64) kPa was simulated for nine different diameter gauge nozzle combinations between (15 to 25) Gauge, (1.36-0.250) mm with areas between defined walls that varied from (0.18 to 1.24) mm^2, three different lengths from (9 to 18) mm and three different angles from 90° to 140°

The channel (c) between four different pressures in the range of (1 to 64) kPa was simulated for five diameter gauge nozzle combinations with wall areas that varied from (0.18 to 1.27) mm^2, three different lengths from (9 to 18) mm, and three different angles from 90° to 140°.

Finer free tetrahedral meshes defined by triangles were generated by the CFD software for each domain to accurately define interfaces between fluid and solid regions, “tetrahedral” is a type of polyhedron with four triangular faces, six straight edges, and four vertex corners. The smaller the tetrahedra, the finer the mesh, and typically the higher the simulation resolution. The "free" aspect refers to the mesh not being constrained by a predefined pattern; it can adapt the size and distribution of tetrahedra based on the geometry of the domain and the physical phenomena being modeled. **Refining the mesh** or modifying the boundary conditions as **remodeling the model source** but respecting limits into specific ranges for all geometric parameters such as diameters, lengths, and angles was a crucial approach in creating the boundaries of the model and effectively capturing boundary layer effects, ensuring a more detailed and representative simulation

of the physical phenomena. Adaptive mesh refinement was sometimes required in some domains to automatically refine the mesh in areas of high gradient, such as near walls or in regions that presented turbulent flow.

Boundary Definitions are established by **explicitly** specifying the **domain walls, inlets,** and **outlets** for each coaxial nozzle domain. This explicit definition ensures precise control over the simulation parameters and boundary conditions in each distinct area of the coaxial nozzle model.

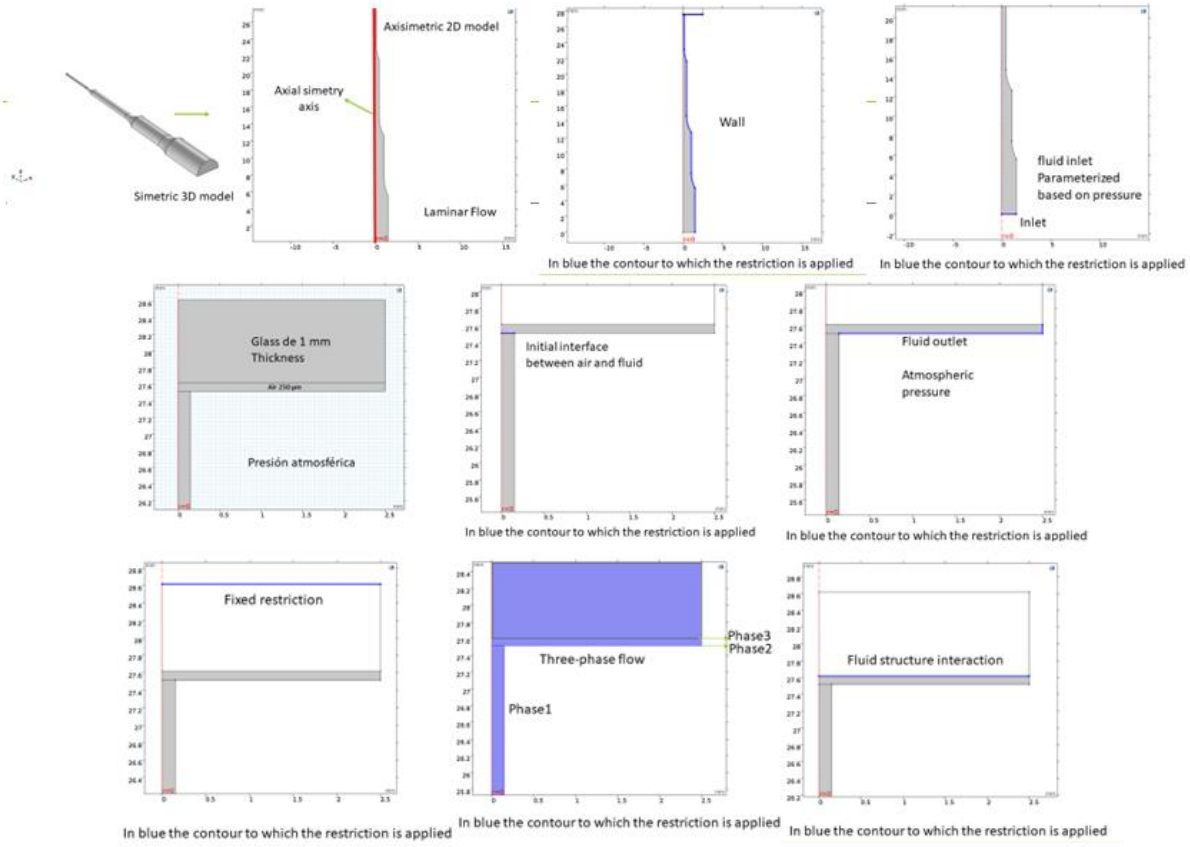

Figure 28 The nozzle simulation for Channel (a) employs an axisymmetric 2D model to streamline computation while specifying boundary conditions for accurate fluid dynamics analysis. It includes a laminar flow profile, pressure-based inlet conditions, and atmospheric pressure at the nozzle's glass walls and outlet. Initial multiphase interfaces and fixed geometric restrictions are incorporated to model complex flows. Lastly, fluid-structure interactions are considered to evaluate the nozzle's velocity and pressure performance (Original Work) [22].

Boundary conditions across the simulation domains were meticulously defined to enhance the precision of parameter control. The original symmetric 3D model was transformed into an axisymmetric 2D framework, leveraging the inherent geometrical symmetry of the nozzle to diminish computational intensity while maintaining high fidelity to physical behaviors. The model imposes laminar flow regimes throughout the nozzle, with sections demarcated in blue delineating tailored restrictions to accurately mimic the desired flow profiles. A pressure-parameterized boundary condition modulates The fluid's ingress at the inlet, ensuring regulated entry into the domain.

The nozzle's walls have been designed to reflect the dimension between the inner and outer diameters of the assembled nozzles for Channel (b) and Channel (c), specific to each nozzle combination under examination. A fine-tuned interface of 250 microns is placed between the air and fluid phases, abutting a glass surface to facilitate the precision modeling of multiphase flows within the nozzle's confines. Upon reaching the nozzle's terminus, the fluid exits subject to ambient pressure and 37 °C—a conventional approach for modeling open system dynamics designed to be used in biological environments.

A designated domain with a fixed restriction encapsulates a static geometrical and flow boundary, acknowledging the unyielding nature of the materials simulating the nozzle walls. The simulation also portrays a three-phase flow scenario, pivotal in dissecting the nuances of complex interactions among disparate fluid phases. Conclusively, integrating fluid-structure interaction within the model is paramount, as it deciphers the nuanced dynamics between the fluid currents and the nozzle's structural limits, a critical element for evaluating the pressure and velocity profiles under real-world operational conditions **Figure 29.**

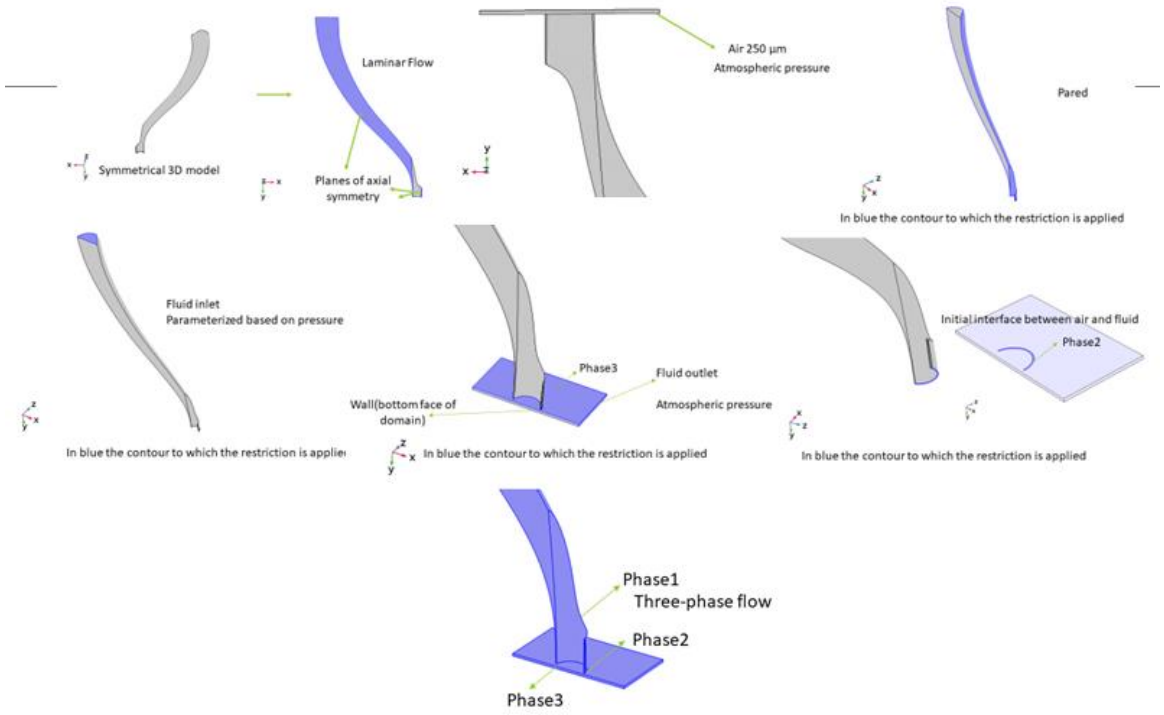

Figure 29 For channel (b) and Channel (c), the nozzle's fluid dynamics are analyzed using a 3D axisymmetric model to enhance computational efficiency and accuracy. This approach incorporates laminar flow, pressure-driven inlets, and atmospheric boundary conditions along the nozzle, glass interface, and outlet. The model accounts for complex multiphase interactions and imposes static geometric constraints while evaluating fluid-structure dynamics to determine the nozzle's performance metrics like pressure and velocity (Original Work) [22].

3.3.3 CFD simulation designs.

The simulation framework has been significantly optimized for improved computational efficiency. Back in 2018, using the computing resources available, each simulation took roughly **six hours** to complete. However, the landscape changed dramatically prior to 2020 and the physical construction of the coaxial nozzles. Acquiring a high-performance computer equipped with an advanced graphics card slashed each simulation time to an average of **four minutes**. This breakthrough was crucial, especially given the ambitious plan to conduct **612 simulations**. These simulations were aimed at analyzing velocity and pressure characteristics across various coaxial nozzle configurations, significantly accelerating the pace of our research outcomes.

Recent technological advancements in 2023, including the release of Comsol Multiphysics CFD version 6.2 and the introduction of graphics cards like the Nvidia RTX 4090, have further enhanced our capabilities. These technologies enable advanced post-processing techniques, such as particle tracing, for improved flow visualization of biological cell particles, making them more computationally viable. Despite this, we initially did not include these advanced techniques due to the large volume and processing time of simulations required for our current research. However, incorporating them in future studies is a promising avenue for broadening our research scope.

As mentioned, our study entailed a meticulous, time-sensitive parametric evaluation spanning all domains. This process involved fine-tuning the inlet pressure for each channel. To achieve a balance between precision and computational efficiency, we configured the '**Global>Step**' feature to execute a sequential run from **0 to 1 second** at intervals of **0.01 seconds**. This decision was made after considering that a finer resolution of 0.001 seconds while offering higher timing accuracy, would significantly increase both the time and computational resources required. Therefore, our chosen approach allowed us to examine the temporal variations within the specified timeframe while maintaining an optimal balance between accuracy and processing time.

Simulation designs for all three channels are presented in the subsequent images (**Images 30, 31, and 32**). These images illustrate variations in lengths, diameters, pressures, and angles, with each image highlighting a specific nozzle configuration subjected to simulation on each channel.

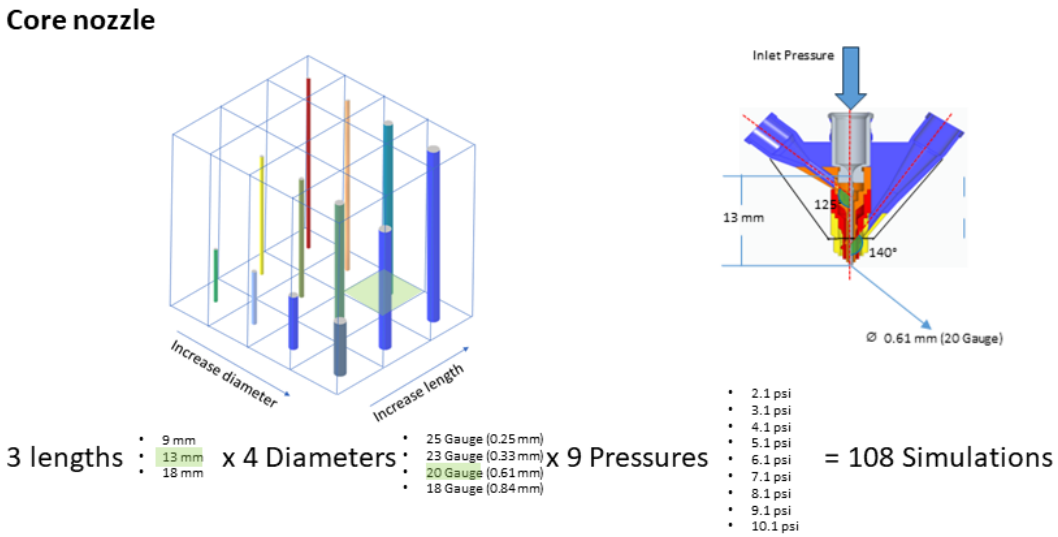

Figure 30 Simulations were conducted on the core nozzle within **channel (a),** encompassing variations across three lengths and four diameters. Each configuration was assessed under nine distinct pressure conditions. Among the total **108 simulations**, the figures prominently highlight in green one specific nozzle configuration that was subjected to this comprehensive simulation process (Original Work) [22].

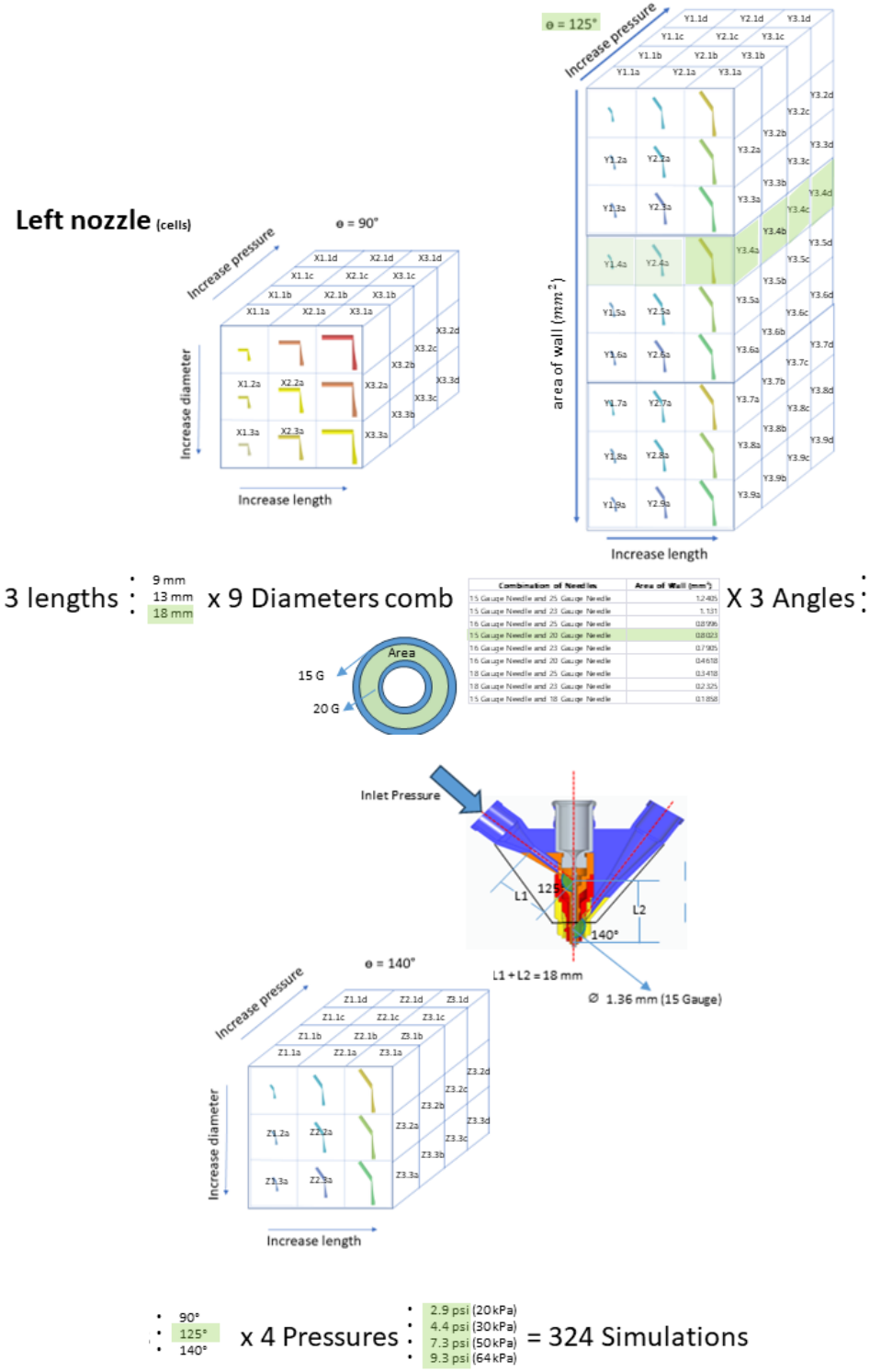

Figure 31 Simulations were conducted on **channel (b),** encompassing variations across three lengths, 9 diameter combinations, and 3 different angles. Each configuration was assessed under four distinct pressure conditions. Among the total **324 simulations**, the figures prominently highlight in green one specific nozzle configuration that was subjected to this comprehensive simulation process (Original Work) [22].

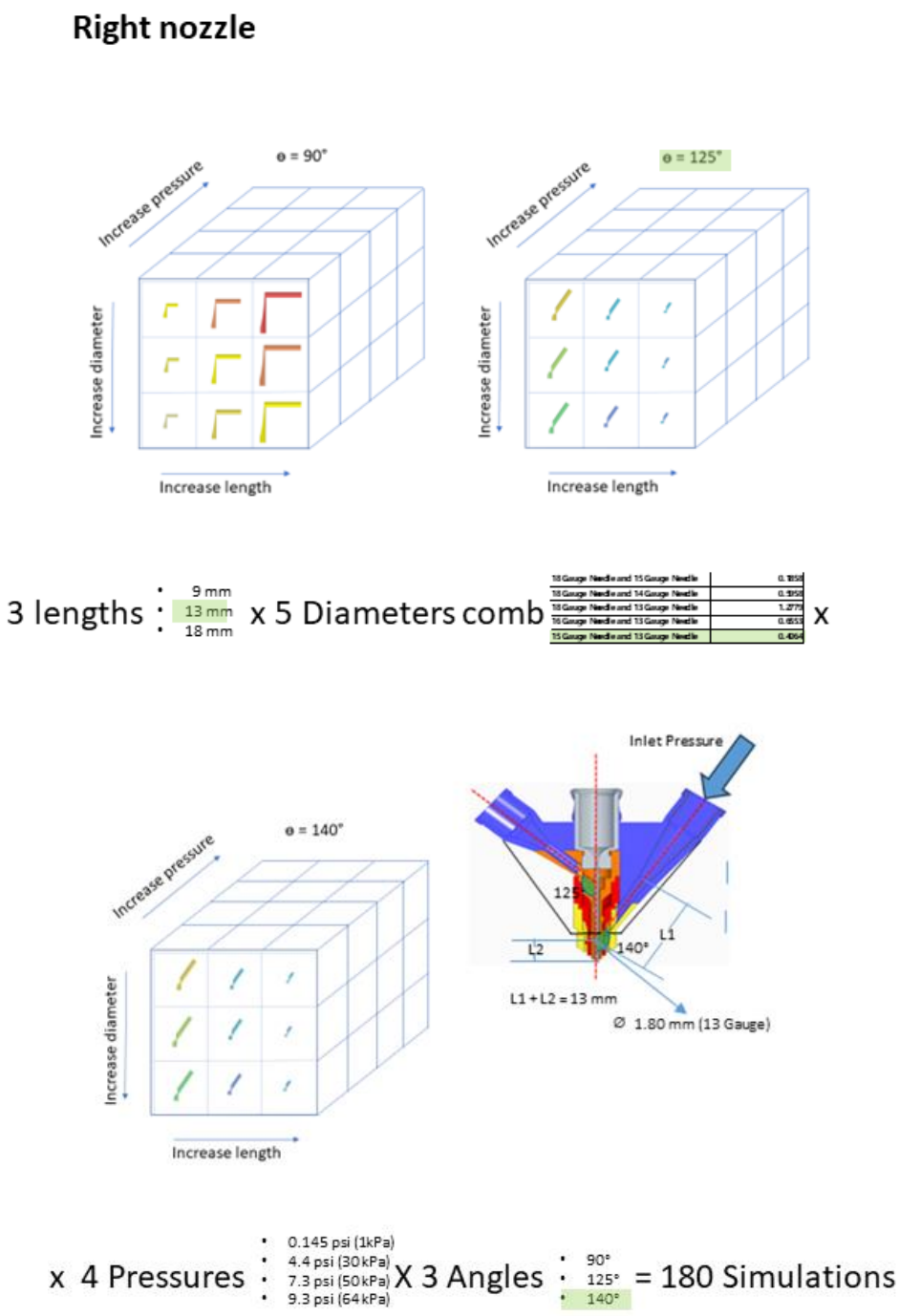

Figure 32 Simulations were conducted on **channel (c),** encompassing variations across three lengths, 5-diameter combinations, and 3 different angles. Each configuration was assessed under four distinct pressure conditions. Among the total of **180 simulations**, the figures prominently highlight in green one specific nozzle configuration that was subjected to this comprehensive simulation process (Original Work) [22].

3.3.4 CFD simulations results

Outlet **velocity** and **pressure** values were scrutinized across the entire nozzle's geometry, focusing on outlet values. This was crucial for determining bioink shape fidelity and cell survival during the bioprinting process. To validate our proposed design in terms of cell viability, the data for velocity and pressure at the nozzle outlets were benchmarked against previously published literature, references explicitly [156], [13], [155], [15], and [157]

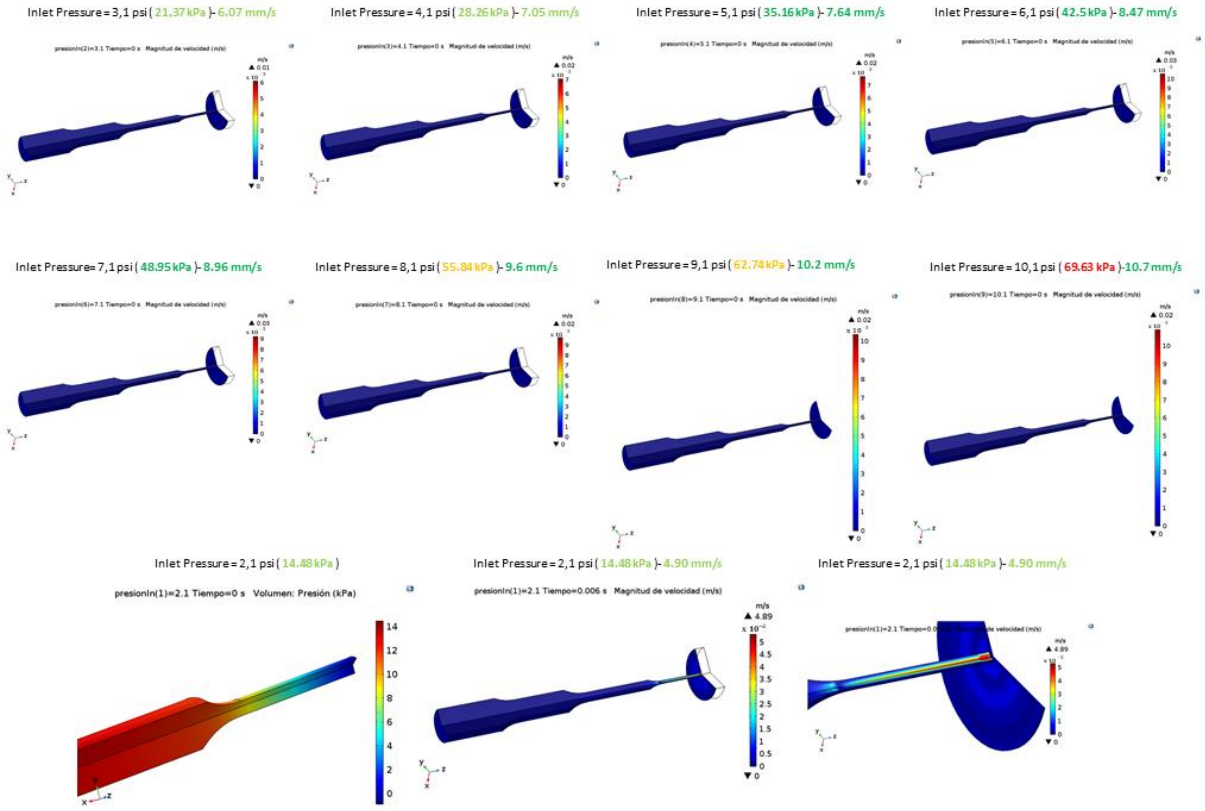

Figure 33 Computational fluid dynamic simulation (CFD) core nozzle simulation for methylcellulose considering air interface of one two hundred fifty (250) µm and the glass deposition surface (Original Work) [22].

The central nozzle of the coaxial nozzle was assessed to evaluate its performance under a range of pressure conditions. The pressure range assessed was between 14.48 kPa and 63.63 kPa. The nozzle's geometry, diameter, and length were adjusted during these tests

into a certain specific range respecting the length and diameters predefined in **figure 29** to facilitate the posterior construction of the nozzle. This nozzle serves as the inlet for the core material (methylcellulose), which is responsible for maintaining the lumen shape prior to the alginate crosslinking of the surrounding layer. The results of these tests were used to optimize the nozzle's design for optimal extrusion speed.

Based on current knowledge, practical experience, and research in the field of bioprinting [158], it has been generally established that the optimal extrusion speed for bioprinting should fall within a range of **3.1mm/s and 24 mm/s**, depending on the nozzle diameter and length. For the simulations, we used diameters between **0.25 mm and 0.84 mm** with lengths between **9 mm to 18 mm**.

In our scenario, the simulation yielding the most favorable results for pressure and extrusion speed utilized a nozzle with a diameter of 0.84 mm (18 Gauge) and a length of 9 mm. However, given the assembly and construction complexities, integrating this design with standard cartridges and luer connections was highly challenging. As a result, we chose to slightly increase the size of the coaxial nozzle to the smallest viable dimension that facilitates easy assembly with luers and cartridges, which is 20 Gauge (0.61mm) with a length of 13 mm.

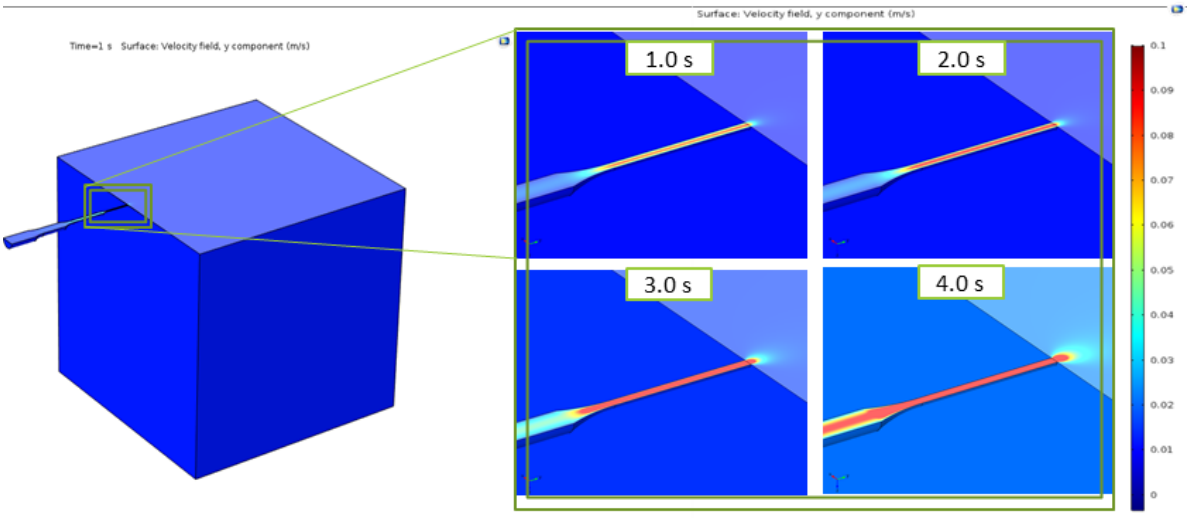

Figure 34 CFD simulation interaction with gas phase (Original Work) [22]

One of the most challenging aspects of the simulation was defining the boundary conditions to accurately represent the air interface of 250 µm on the glass deposition surface. This

simulation required utilizing a **ternary phase field (terpf) Physics** approach, which accounts for the interaction between the three distinct phases present at the interface: the gas phase, the nozzle tip, and the glass surface, as depicted in the accompanying illustration. The complexity of the biphasic flow interactions between these phases made it particularly challenging to define the boundary conditions in a way that would accurately reflect the real-world scenario.

Moreover, the simulation had to account for the dynamic nature of these interactions, as the behavior of the gas phase is significantly influenced by the changing elevation position of the nozzle and the rate of material deposition on the glass surface. This required iterative adjustments to the boundary conditions to capture the transient flow characteristics accurately.

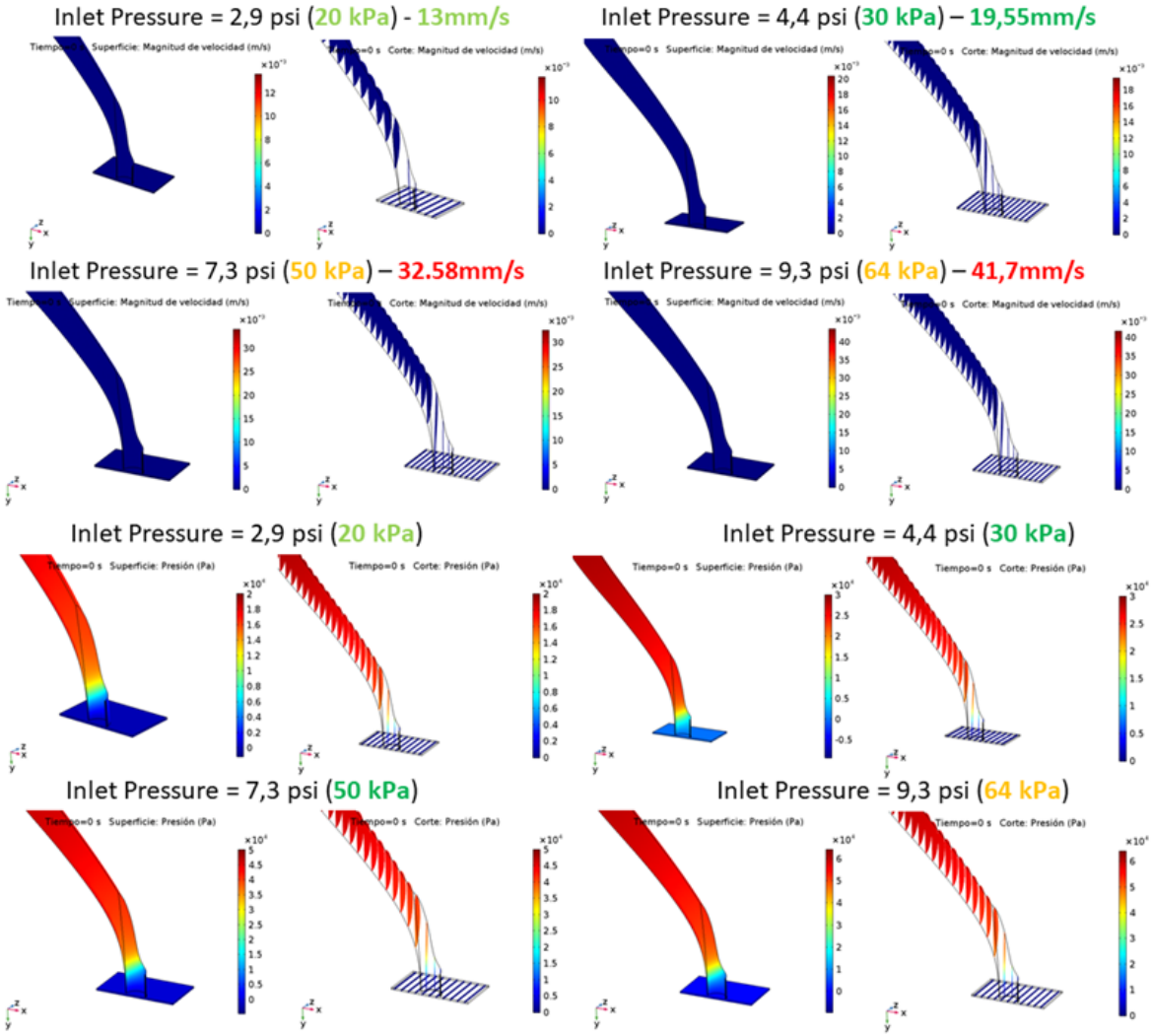

Figure 35 Computational fluid dynamic simulation (CFD) Nozzle (b), for alginate-based bioink biomaterial, left side nozzle (Original Work) [22].

The left side nozzle of the coaxial nozzle was assessed to evaluate its performance under a range of pressure conditions. The pressure range assessed was between 20 KPa and 64 KPa. The nozzle's geometry, diameter, angle, and length were adjusted during these tests into a certain specific range respecting the length, angle, and diameters predefined in **figure 31** to facilitate the posterior construction of the nozzle. This nozzle is the shell that surrounds the core material (Alginate-base), which creates the lumen shape after crosslinking with the $CaCl_2$ Solution. The results of these tests were used to optimize the nozzle's design for optimal extrusion speed and pressure, as the material in this nozzle is intended to contain the cells to bioprint.

As described before, we used wall areas between 0.1858 mm^2 and 1.2405 mm^2 with lengths between 9 mm to 18 mm for the simulations and angles between 90 ° to 140 °

In our study, the simulations that yielded the best results regarding pressure and extrusion speed used nozzle diameters (15G-25G), defining an area of 1.2405 mm² and using a length of 9 mm. However, the complexities involved in assembly and construction posed significant challenges in adapting this design to standard cartridges and Luer connections. Consequently, we decided to increase the coaxial nozzle's size to the smallest practical dimension, allowing for straightforward assembly that could fit with luers and cartridges (15G-20G) and 18 mm long.

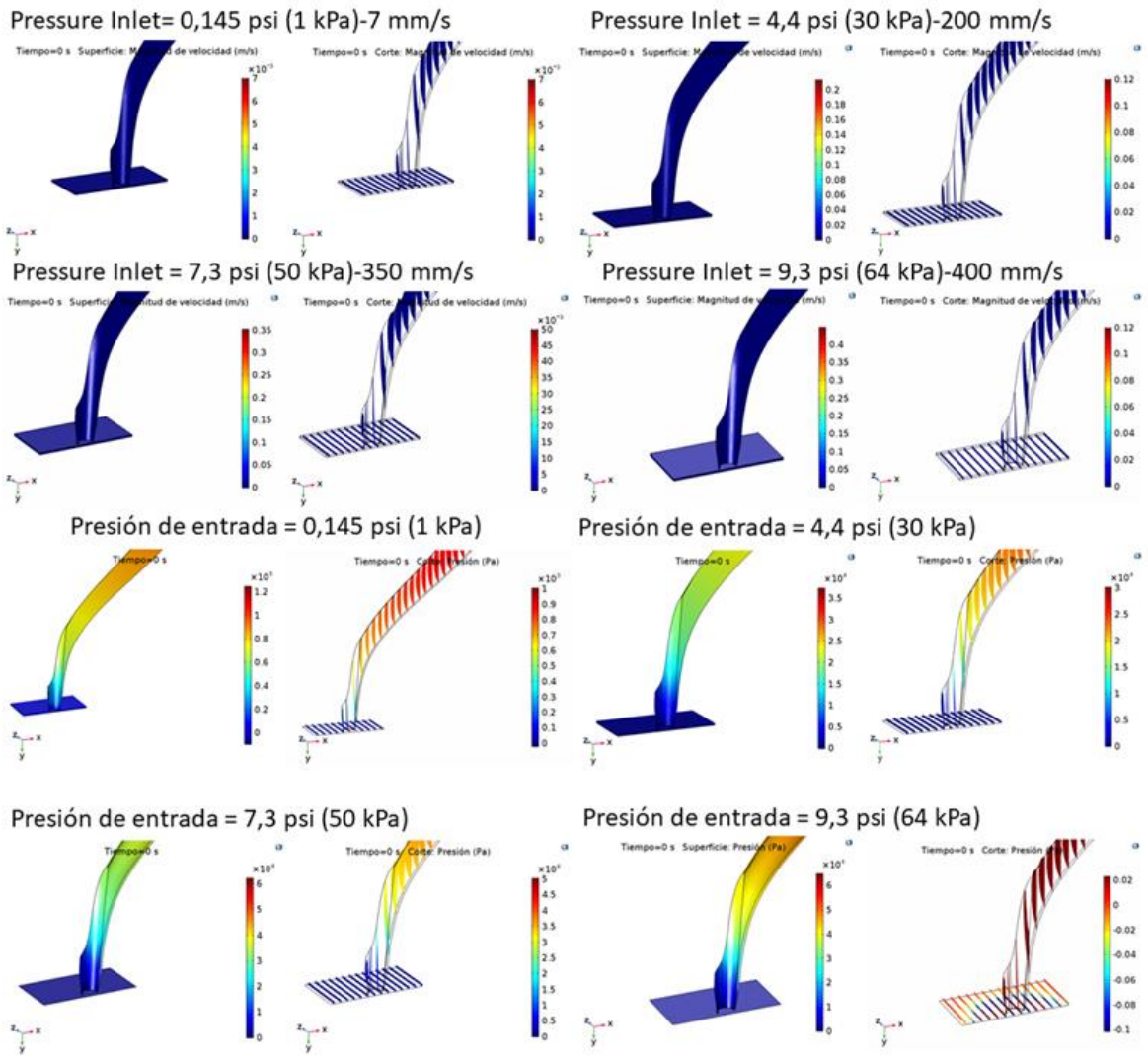

Figure 36 Computational fluid dynamic simulation (CFD) nozzle simulation for $CaCl_2$ solution, right side nozzle (Original Work) [22].

The performance of the right-side nozzle in the coaxial assembly was evaluated under various pressure conditions, ranging from 1 KPa to 64 KPa. We adjusted the nozzle's geometry, diameter, angle, and length during these tests. This nozzle, serving as a shell for the alginate-based bioink, plays a crucial role in crosslinking with the CaCl2 Solution. We conducted these tests to fine-tune the nozzle's design for optimal extrusion speed and pressure control. Since the nozzle is intended for liquid flow, we varied the testing pressure range to achieve the best extrusion speed profile and minimize turbulence during printing.

Our simulations evaluated five nozzle diameter combinations, with areas ranging from 0.1868 mm² to 1.2779 mm², lengths varying from 9 mm to 18 mm, and angles between 90 ° to 140 °. The configuration that provided the most favorable results regarding extrusion pressure and speed had a nozzle size between 18G and 13G and a length of 9 mm. However, incorporating this design into standard cartridges and luer connections proved a significant challenge due to the complexities of assembly and construction. Consequently, we decided to slightly increase the size and length of the coaxial nozzle to the smallest practical dimension. This modification, aimed at facilitating more accessible and faster assembly, did lead to lower extrusion speed and pressure—these changes aligned with the experimental component's outcomes, ensuring the design's high viability. Ultimately, we settled on a final nozzle configuration between 15G and 13G, corresponding to a defined inter-wall area of 0.4054 mm² and a length of 13 mm.

After thoroughly evaluating simulations and comparing results for nozzle lengths in the range of 9 mm to 18 mm, wall areas between (0.1858-1.2405) mm^2 for the left nozzle defining the channel (b) containing alginate-based bioink, we selected three optimal coaxial nozzle configurations for prototyping and experimentation in the bioprinting phase of our research. All nozzles' configurations in different groups were chosen based on their performance, and if any of its velocity values fell into the defined secure green area, as depicted in **Figure 37,** Displays the specific diameters of the selected coaxial nozzle area for the channel (b), (15G-20G), length 18 mm and angle 125° configurations prototyped and built, described geometrically in **Table 3.**

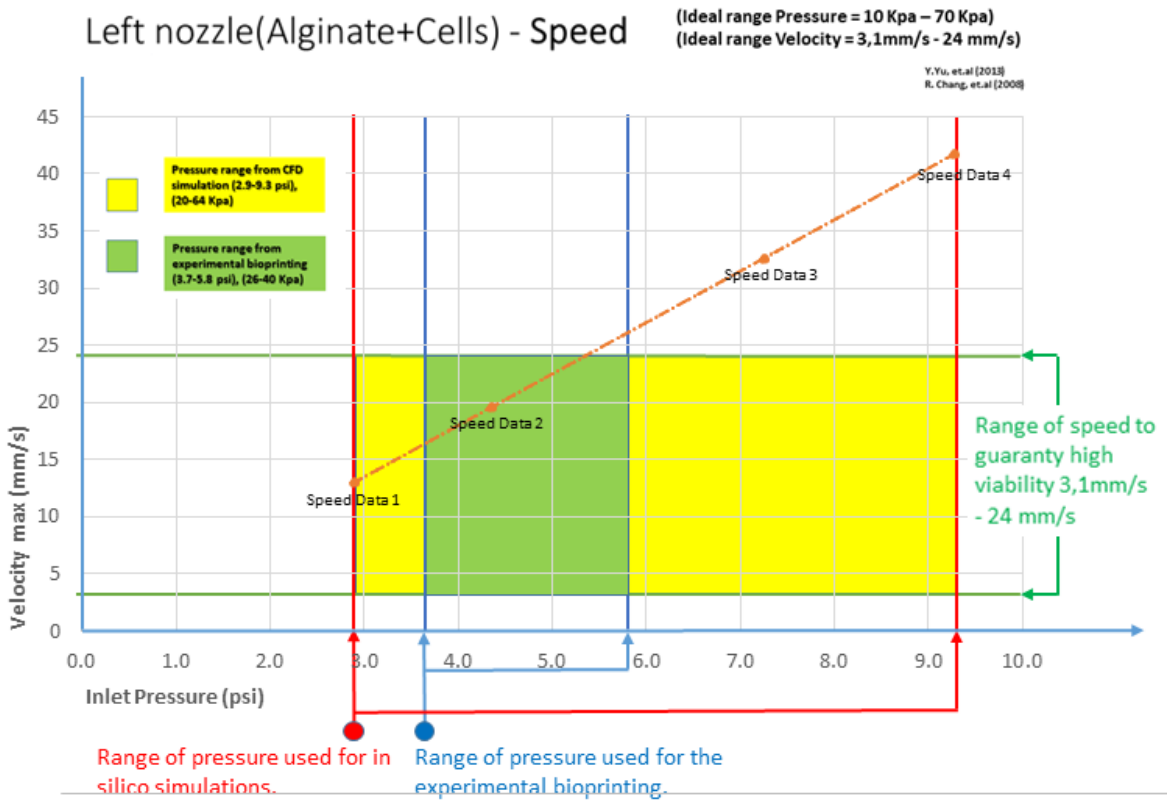

Figure 37 Combined area for pressure range used in CFD simulations and pressure used during experimental bioprinting, secure area velocity range intercepted in green shows where Alginate-based bioinks can guaranteed high viability for the selected nozzle configuration channel (b) (15G-20G), length 18 mm and angle 125°, according to bibliographic references and described in **figure 24** (Original Work) [22].

The range of pressure used on the CFD simulations for the defined coaxial channel (b) was compared with the pressure values used in the experimental part. Then, values were confined by the velocity-secured range for high cell viability defined in [158][67][155]. It was used as the main criteria method for coaxial nozzle selection.

The selection and discrimination criteria of the coaxial nozzle are explained in section 3.3.6, “CFD simulation results.”

For validation, simulation results from the nozzle corresponding to channel (a) were compared with experimental data, mainly focusing on sensor-flow measurements to mitigate uncertainties in the simulated data. Unfortunately, the flow in the other two channels could not be measured and similarly validated due to measurement adaptation limitations posed by their thin walls and sensors.

3.3.5 Utilizing experimental data for simulation validation.

The flow velocity at the tip of **Channel (a)** of the coaxial nozzles, measured in mm/s, underwent experimental validation to ensure alignment with simulation margins and physical results. This validation was achieved by measuring the flow through the nozzle at specific pressure values. We used the Sensirion SLF3S-0600F flow sensor and its Sensirion evaluation software to corroborate the data measured in the CFD software simulations. The flow rate was recorded in ml/min, and the cross-sectional areas of the nozzles were defined according to sizes 25 Gauge, 23 Gauge, 20 Gauge, and 18 Gauge, which correspond to the selected diameters for Channel (a). To calculate the velocity in mm/s, we first converted the flow rate from ml/min to mm^3/s. Then, we divided this value by the cross-sectional area of each nozzle to determine the velocity under the applied pressure.

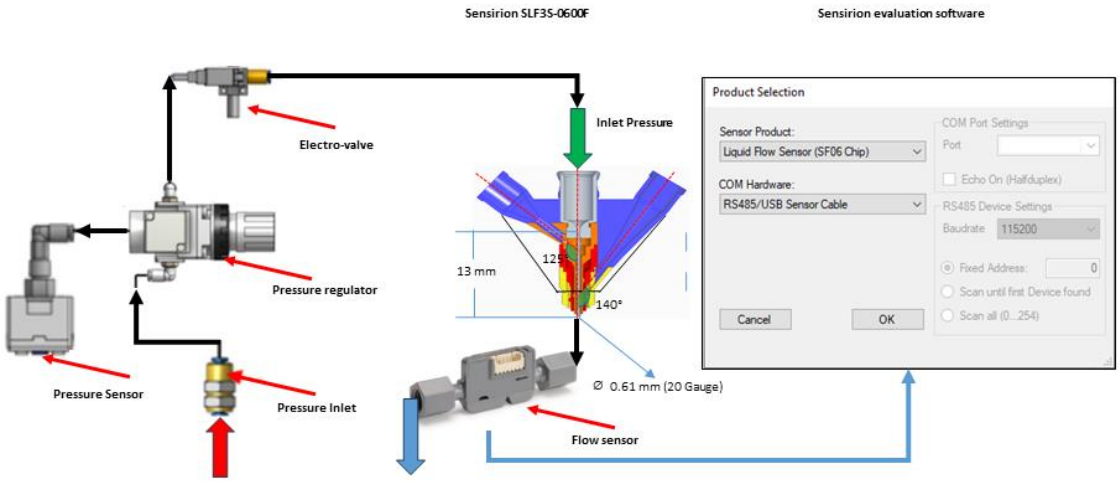

Figure 38 Setup for measuring flow with a Sensirion flow sensor, designed to quantify velocity in millimeters per second (mm/s) and facilitate comparison with Computational Fluid Dynamics (CFD) simulation data on Channel (a) (Original Work) [22].

The deviation between the measured velocity at the nozzle's tip and the velocity predicted by the CFD tool was **less than 10%.** This close approximation contributed to validating the experimental data for the CFD simulation accuracy. In the validation process, the flow velocity at the tip of Channel (a) of the coaxial nozzles was measured in mL/min and then converted to velocity in mm/s, ensuring its alignment with both the simulation predictions

and the actual physical outcomes. This validation was achieved by monitoring the flow through the nozzle under various pressure conditions, as described in **Figure 38**.

To thoroughly analyze the behavior of velocity (measured in mm/s) in Channel (a) in response to variations in pressures and areas (measured in mm²), cubic interpolation was applied across all 108 CFD registered simulations. This method was essential for generating detailed surface plots, which provided more precise insights into how velocity changes under different pressure and area conditions.

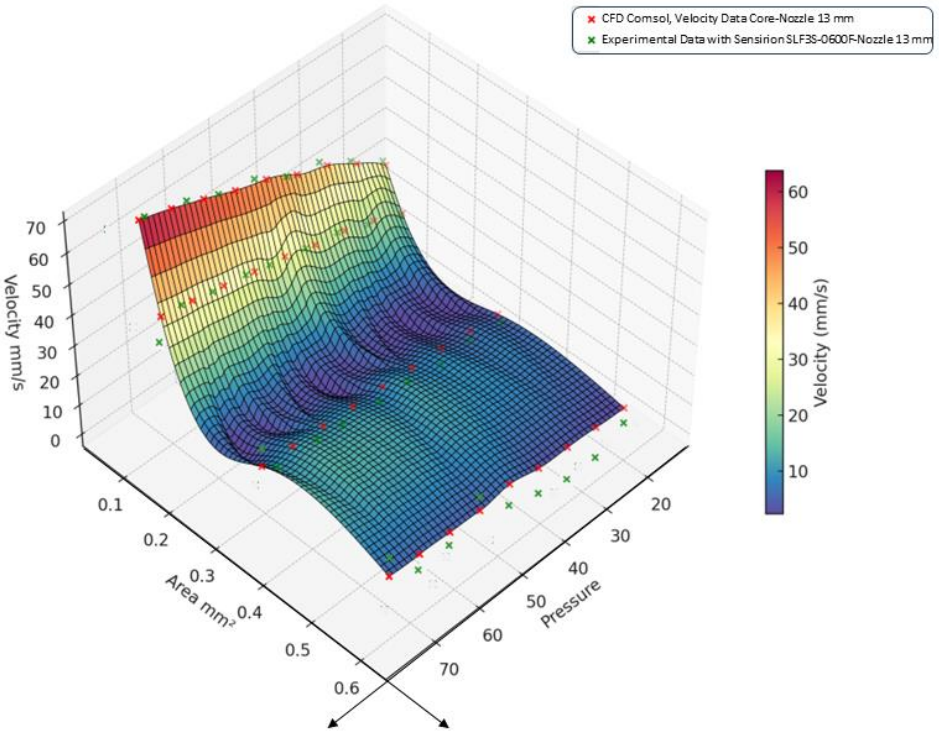

Figure 39 This figure depicts the velocity variation inside the core nozzle Channel (a) at different diameters and pressures, illustrating the interplay between pressure, cross-sectional area, and velocity within a nozzle. Red points represent CFD COMSOL simulation results, while green points indicate experimental data from the Sensirion flow sensor (Original Work) [22].

Overall, the CFD simulations offered crucial insights into the triaxial nozzle's performance, highlighting key design parameters for optimization in experimental prototypes. These parameters include minimal lengths, considering the use of commercial and standard parts like luer adaptors and connectors to cartridges. Developing smaller coaxial nozzles with improved velocity and pressure profiles is theoretically possible. However, adapting these to commercial bioprinters poses challenges, as the inlets and adaptors may not be directly compatible with the nozzle design.

3.3.6 Criteria for Selecting Coaxial Nozzles Based on (CFD) Results

Three different coaxial nozzles were selected from the complete set of simulations looking for a variation in channel's area *(b), (left channel nozzle)* in (**Figure. 31**).

To establish a selection criterion for Channel (b), we utilized a technique that considers both the limited velocity range and construction feasibility. This approach effectively enabled us to choose the ideal nozzle dimensions from the 324 simulations corresponding to Channel (b). This selection was based on analyzing the pressure and velocity outcomes derived from the CFD simulations, ensuring that our choices fit into the ideal velocity range between (3.1-24) mm/s.

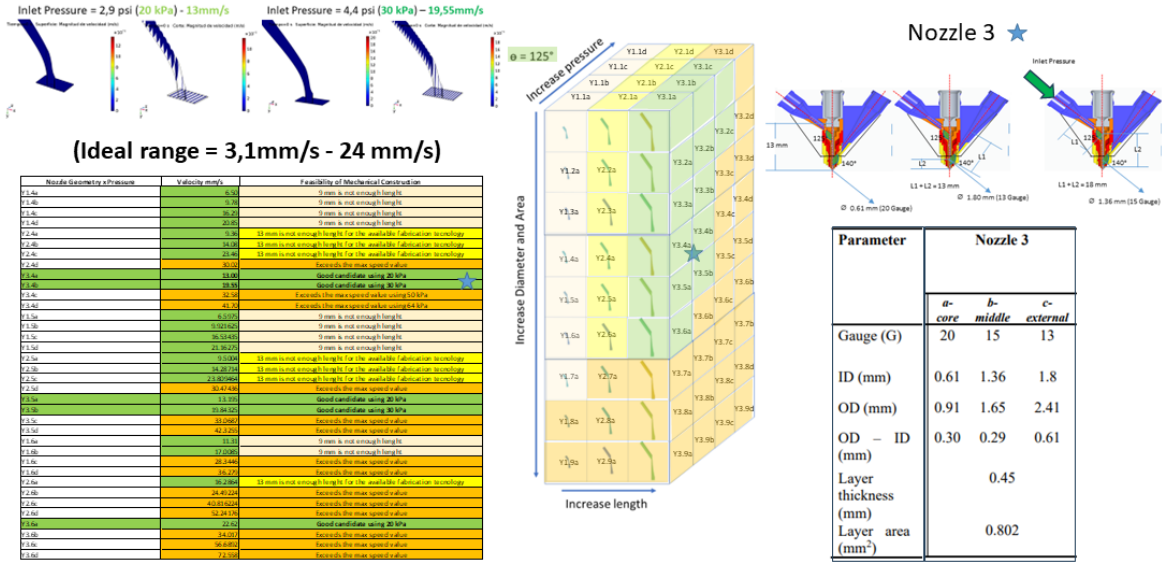

Figure 40 illustrates the established selection criteria workflow for choosing three coaxial nozzle configurations for the experimental section based on the admissible velocity range and construction feasibility (Original Work) [22].

All CFD results were systematically tabulated and organized, prioritizing the variables most significantly affecting the outcome velocity. These variables include (1) an increase in length, (2) an increase in diameter area, and (3) an increase in pressure. This specific ordering was crucial to simplify the process of sorting different configurations. It facilitated the identification of configurations that not only fall within the permissible velocity range but are also viable from a construction feasibility standpoint.

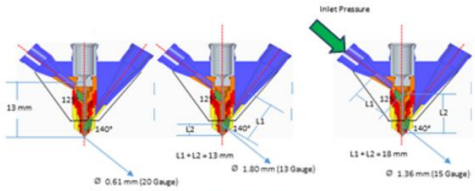

Parameter	Nozzle 3		
	a- core	*b- middle*	*c- external*
Gauge (G)	20	15	13
ID (mm)	0.61	1.36	1.8
OD (mm)	0.91	1.65	2.41
OD – ID (mm)	0.30	0.29	0.61
Layer thickness (mm)		0.45	
Layer area (mm^2)		0.802	

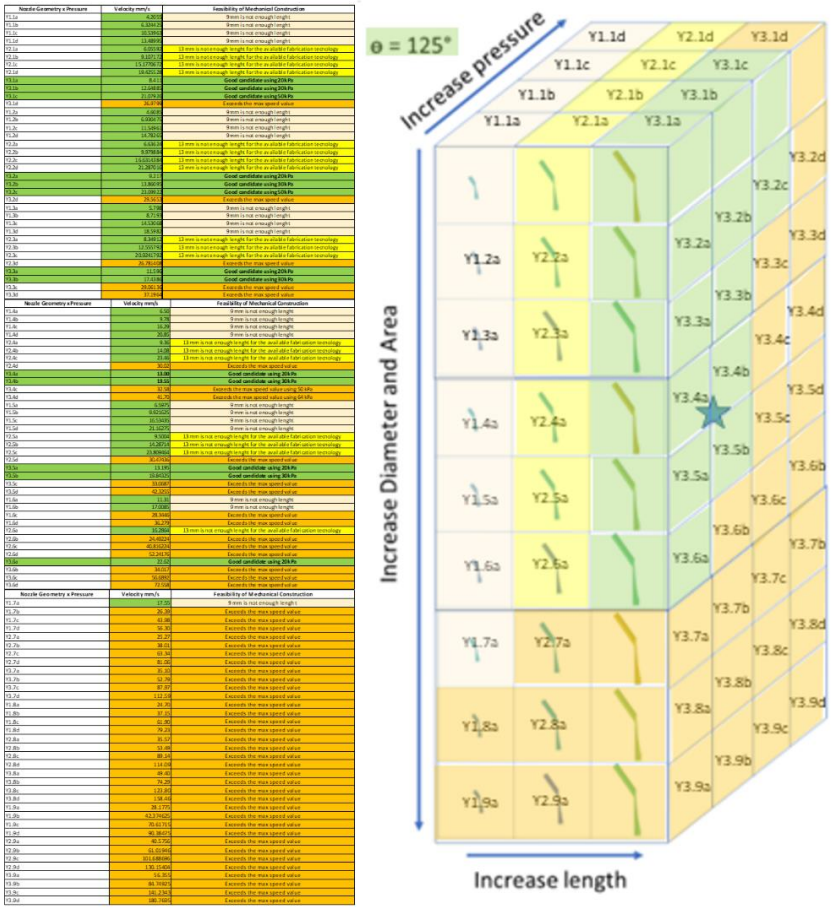

Figure 41 The selection criteria for the Nozzle 3 configuration, set at an angle of 125°, are visually represented using color coding and tabulated with three alphanumeric values. This approach simplifies the sorting process, allowing for efficient organization based on the Admissible Velocity Range and the Construction Feasibility Criterion. (Original work).

The table and corresponding cuboid defined by 9 rows and 3 columns in **Figure 41** utilize a color-coding system to indicate the feasibility of various configurations based on pressure, length, and area for mechanical construction and their inclusion within the admissible velocity range. In this method, pink signifies configurations that are not feasible due to length limitations. Yellow indicates configurations that are constrained by the limitations of available fabrication technology. Green highlights configurations that are viable candidates for mechanical construction. Lastly, orange denotes configurations that exceed the maximum limit of the admissible velocity range.

Velocity Results analysis

The comprehensive plot analysis provided insightful revelations about the relationship between the nozzle's structural characteristics and fluid dynamics. It was observed that both the pressure within the nozzle and its cross-sectional area profoundly impact the fluid's flow velocity. This core observation was substantiated by a series of simulations, offering a robust validation of the theoretical models in use.

We employed cubic interpolation on the selected dataset to refine our understanding further. This advanced statistical technique allowed us to model the nuanced relationship between the nozzle dimensions and the resulting flow characteristics precisely. Particularly in channel (b), a pattern emerged clearly: as the area of the channel decreased, the velocity of the fluid correspondingly increased. This effect was compounded by the presence of higher pressures, which also served to accelerate the fluid flow.

The graphical representation of this data is marked by red points, which delineate the interpolated surface. These points effectively define what we have termed the 'secure range,' within which the system operates optimally regarding cell viability.

One of the most striking aspects of the analysis was the identification of a critical velocity threshold. At a velocity of 24 mm/s, delineated on our graph by a distinctive green plane, we noticed a significant shift in fluid behavior. This critical point represents a threshold beyond which the fluid dynamics change in character, potentially impacting the cell viability. Understanding this threshold is crucial for optimizing nozzle design and ensuring fluid systems' safe and efficient operation. **Figure 42**

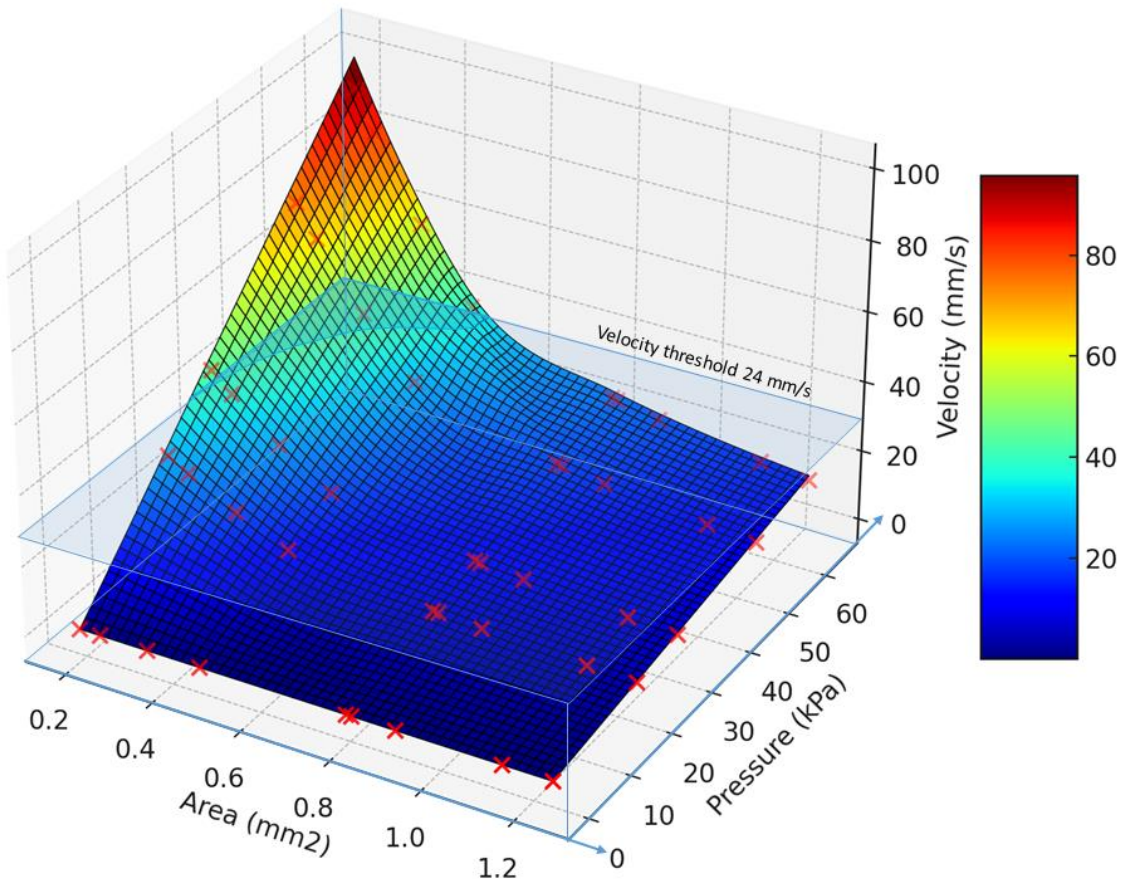

Figure 42 Plot visualizes the relationship between area, pressure, and velocity, demonstrating that smaller nozzle areas and higher pressures result in increased fluid velocity (Original Work) [22].

The image in **Figure 42** is a 3D surface plot visualizing the relationship between area, pressure, and velocity. The x-axis represents the area in square millimeters (mm^2), ranging from 0.2 to about 1.2 mm^2. The y-axis represents pressure in kilopascals (kPa), with values from zero to approximately 60 kPa. The z-axis indicates velocity in millimeters per second (mm/s), ranging from 0 to 100 mm/s.

The surface plot is color-coded according to the velocity, with a corresponding color bar to the right of the graph indicating the gradient from low (blue) to high (red) velocities. The highest velocities are shown at the plot's peak, corresponding to smaller areas and higher pressures, while lower velocities are evident in regions with larger areas and lower pressures.

Red **points** scattered across the plot represent CFD Velocity data used to generate the surface using cubic interpolation.

The graph visually represents the fluid dynamics within a system, demonstrating that smaller nozzle areas and higher pressures result in increased fluid velocity. The critical point of 24 mm/s marked on this graph corresponds to the light blue color area on the velocity gradient.

After the selection of the coaxial nozzle's configurations within the permissible velocity range but are also viable from construction feasibility, 3D printed using biocompatible photopolymer resins, namely, dental SG FLSGOR01 and dental LT clear (**Figure. 21**) were created. The dimensions of each Coaxial nozzle are reported in **Table 3** below, along with the area of flow Channel (*b)* (used for cell-laden hydrogel), which continuously increases from Nozzle Coaxial 1 to Nozzle Coaxial 3.

Parameter	**Nozzle 1**			**Nozzle 2**			**Nozzle 3**		
	a-core	***b-middle***	***c-external***	***a-core***	***b-middle***	***c-external***	***a-core***	***b-middle***	***c-external***
Gauge (G)	23	18	14	25	18	14	20	15	13
ID (mm)	0.33	0.84	1.54	0.25	0.84	1.54	0.61	1.36	1.8
OD (mm)	0.64	1.27	1.83	0.52	1.27	1.83	0.91	1.65	2.41
OD – ID (mm)	0.32	0.43	0.29	0.27	0.43	0.29	0.30	0.29	0.61
Layer thickness (mm)		0.20			0.32			0.45	
Layer area (mm^2)		0.232			0.341			0.802	

Table 3 Geometric data of the designed coaxial nozzles. ID and OD stand for inner diameter and outer diameter, respectively. The three flow channels of each nozzle are labeled as (a), (b), and (c), as shown in **Figure 22-B** (Original Work) [22].

3.3.7 Experimental Section.

3.3.8 Preparation of hydrogels

Varied materials were used during the printing process for each channel (a, b, and c) described in section 3.3.2. While **Channel (*c)*** was perfused with **$CaCl_2$ solution**, the other channels were perfused with two different hydrogel compositions. **Channel (*a)*** was used to print a support structure in the core based on a methylcellulose-gelatine sacrificial ink, as described by Dranseikiene and colleagues [159]. Briefly, the sacrificial biomaterial ink in the **channel (b)** is composed of 9 % (w/v) **methylcellulose** (Sigma-Aldrich, St. Louis, MO, USA) and 5 % (w/v) gelatin (Sigma-Aldrich, St. Louis, MO, USA) and was shown to exhibit good support characteristics after printing, while dissolving in culture conditions after one week. The hydrogel used for printing with cells was an **alginate-based bioink** prepared with a pre-crosslinking technique utilizing calcium carbonate ($CaCO_3$) and D-Glucono-δ-lactone (GDL). Concisely, a 2 % (w/v) alginate (VIVAPHARM® alginate PH176, JRS PHARMA GmbH & Co. KG, Rosenberg, Germany) solution was pre-crosslinked with 20 mM $CaCO_3$ (Calcium carbonate precipitated for analysis EMSURE®, CAS 471-34-1, Merck KGaA, Darmstadt, Germany) and 40 mM GDL (CAS 90-80-2, Merck KGaA, Darmstadt, Germany) at four (4) °C. As a result of continuous stirring for 48 hours, the hydrogel was allowed to warm to room temperature and mixed with cells after 48 hours.

3.3.9 Rheological characterization of hydrogels

Rheometric experiments were performed to study how stress can influence the rheological behavior and deformation of the bioink. An angular frequency sweep between 0.01 and 10 rad/s was performed under a 2% strain and at 30 ºC, with the aid of a solvent trap to avoid evaporation, in a 25 mm parallel plate geometry (CVOR-200 HR Rheometer, Bohlin Instruments, Malvern, United Kingdom). Data for loss (G') and storage (G'') moduli and complex viscosity was collected from the experiments.

3.3.10 Setup for 3D bioprinting with coaxial nozzles

One FDM, fused deposition modeling 3D printer (Anycubic Prusa I3, ANYCUBIC 3D Printing, Shenzhen, China) was customized to allow the controlled deposition of hydrogels (**Figure. 43**). For this purpose, three independent piston-driven extrusion systems were coupled to the machine, and the feed rate (mm/s) was translated into pressure units (kPa) with the aid of an external measurement system. Next, printheads suited for 12 mL Luer-lock syringes were adapted to the extrusion systems, and their outlet tips were connected to the inlets of the 3D-printed coaxial nozzles.

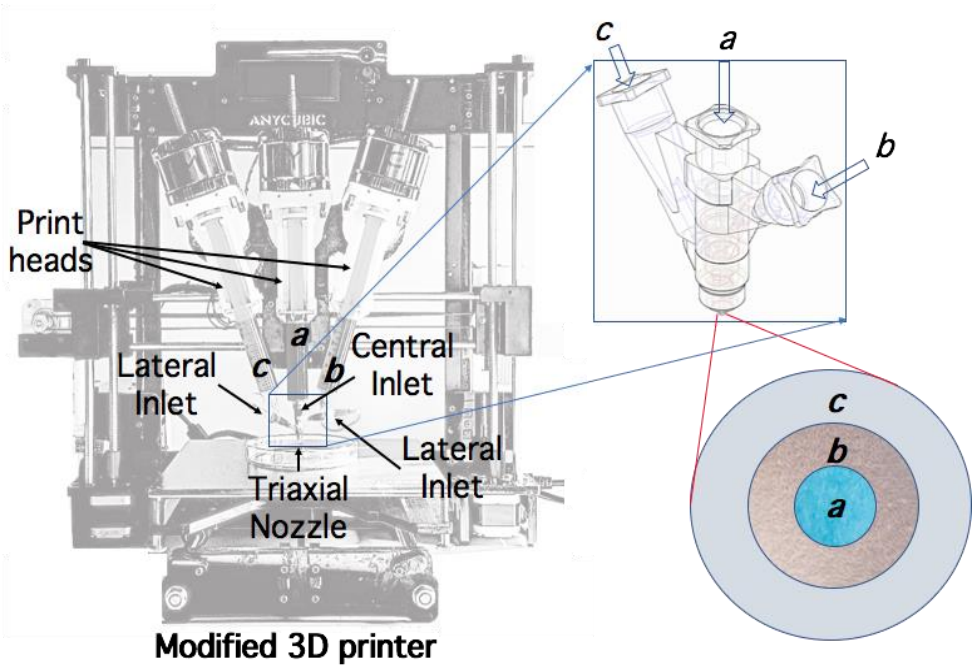

Figure 43 Three-dimensional (3D) bioprinter setup for bioprinting experiments. Setup of a three-dimensional (3D) bioprinter for bioprinting experiments. A fused deposition modeling 3D printer with piston-driven extrusion systems was equipped with three printheads and a triple-channel coaxial nozzle. Each flow channel is labeled at the inlet and outlet of the coaxial nozzle to assist the reader. This figure was published in [22].

3.3.11 Cell culture

Before bioprinting experiments of single-layered hollow tubular structures, human bone osteosarcoma cells **MG-63** (ATCC® CRL-1427™) were cultured in a complete growth medium consisting of Dulbecco's one modified Eagle Medium supplemented with 10% (v/v) fetal bovine serum including 1% (v/v) Penicillin-Streptomycin (10,000 U/mL) and maintained in a CO2 incubator at 37°C. Upon the culture reached a confluence of approximately 80–90%, cells were harvested with the aid of a 0.25 % (w/v) trypsin solution (Gibco™, Thermo Fisher Scientific, Waltham, MA, USA). The cell concentration of the obtained suspension was then estimated by staining with trypan blue and hemocytometer counting. Subsequently, cells were carefully embedded in the alginate-based hydrogel. The hydrogel (without cells) was filled into a 12 mL Luer-lock syringe and connected to another syringe containing an 11×10^6 cells/ml cell suspension. The two components were extruded back and forth to guarantee homogeneous mixing at least twenty (20) times. The volume ratio was 10:1 (hydrogel: cell suspension), resulting in a final cell density of **1×10^6 cells/ml** in the bioink.

We determined this number by referencing Study [156] to understand cell density clearly. This study provides a comprehensive analysis of cell viability within the context of bioprinting, exploring how variables such as cell density and sodium alginate concentration impact cell viability post-bioprinting. It examines the influence of coaxial nozzle size and pressure, finding that cell viability decreases with increased pressure on the biomaterial and improves with larger nozzle diameters. Additionally, the research observed no significant differences in cell viability across varying cell densities, ranging from 2 x 10^6/ml to 8 x 10^6/ml cells. This finding was a crucial factor in choosing the designated cell density for the study, as it simplifies the process of counting cells for assessing viability (live/dead) during fluorescent microscopy procedures and with the CELLCYTE Life Cell Imaging System.

We have chosen MG-63 cells in our research, guided by several pivotal reasons. These cells are renowned for their robustness and reproducibility, displaying robust growth and

remarkable consistency. This is crucial for achieving dependable research results, as they are one of the less prone to variations in laboratory conditions, especially in comparison to primary cells. This stability ensures more reliable experimental outcomes.

MG-63 cells are also preferred for their ease of culture and maintenance, making them ideal for regular experimental use and simplifying cell culture procedures.

Furthermore, the extensive research history of MG-63 cells provides a rich foundation for comparative analysis, particularly in Extrusion Based Bioprinting. This vast array of data aids in understanding their behavior under different conditions, enhancing the reliability and validity of findings in bioprinting and tissue engineering research. [160][161][162]

Notably, the choice of MG-63 cells was strategic in minimizing external factors that could influence cell viability. Our research specifically focuses on the effects of shear stress, inlet pressure, and nozzle geometry in Extrusion Based Bioprinting. The inherent stability of MG-63 cells makes them an exemplary model, as it is more likely that any changes in cell viability are due to the bioprinting conditions rather than other environmental factors. This accuracy in variable control is essential for maintaining the integrity and precision of our research findings.

3.3.12Bioprinting of single-layered hollow tubular structures

For bioprinting experiments, the coaxial nozzles were submerged in 70% (v/v) ethanol for one (1) night before experiments and subsequently washed with sterile one × PBS in a biosafety cabinet. The modified 3D printer was thoroughly wiped with 70% (v/v) ethanol and exposed to UV germicidal light for 1 hour inside a biosafety cabinet.

Each nozzle comprised three flow channels at the tip, namely *a*, *b,* and *c,* in (**Figure 26**). Two different hydrogels and a crosslinking solution were employed for bioprinting hollow, tube-like structures. A methyl cellulose-based hydrogel was used as a sacrificial material for the lumen (flow Channel (*a)* an alginate-based bioink embedded with human bone osteosarcoma MG63 cells was used for the central tubular channel (flow Channel (*b)* a Calcium chloride ($CaCl_2$) 0.1 M solution was expelled through the outer channel of the coaxial nozzle (flow Channel (*c)* since it served as a crosslinking agent for the alginate bioink. All materials were dispensed coaxially by mechanical extrusion of the three separate printheads simultaneously. The resulting tubular structures were then perfused through the core channel with warm sterile one (1) × PBS to wash away the sacrificial material.

This bioprinting procedure was performed with the three designed nozzles varying the extrusion pressure of the printhead connected to Channel (*b)* since the cell-laden bioink was dispensed through this channel. The extrusion pressure of the other two channels was adjusted to achieve the same extrusion rate as that of Channel (*b)*. Coaxial tubular structures were dispensed with three extrusion pressures, 26, 34, and 40 kPa, through each designed nozzle. Each combination of bioprinting parameters was performed **in triplicates,** resulting in **27 extruded tubular structures** plus **three (3) control samples,** as described in **Figure 44**.

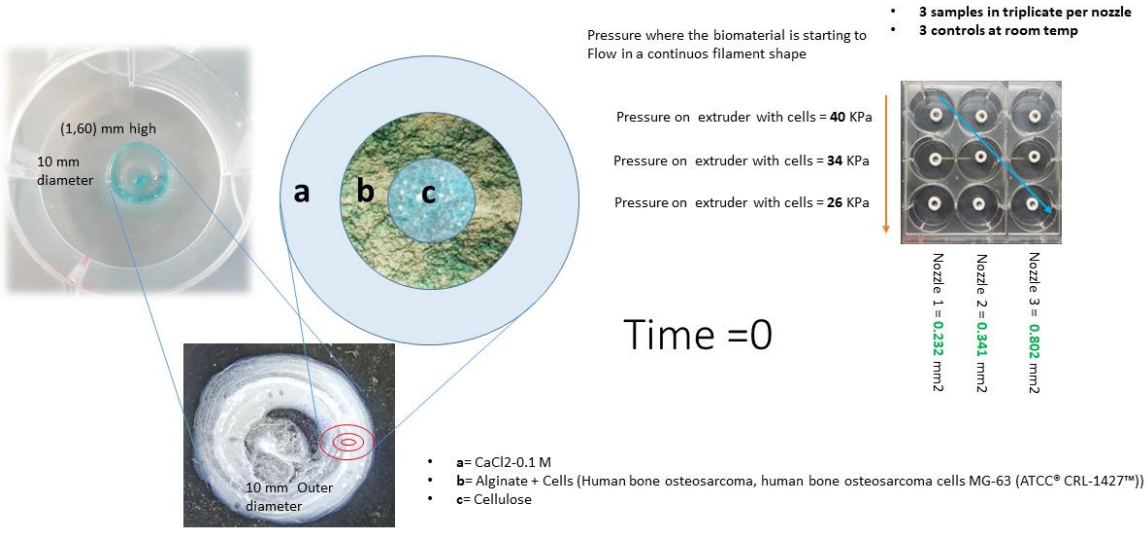

Figure 44 Methodology for the experimental part: 27 samples were printed, and 3 control samples were produced by combining 3 different pressures and 3 different coaxial nozzles (Original Work) [22].

3.3.13 Cell viability assessment

A Live/Dead (Sigma-Aldrich, St. Louis, MO, USA) assay was performed on the bioprinted tubular structures to study the effect of the inlet extrusion pressure and the different coaxial nozzle geometries on cell survival. Briefly, constructs were stained with calcein acetoxymethyl ester (calcein-AM) and propidium iodide (PI) immediately after bioprinting and fluid perfusion through the lumen to visualize live and dead cells, respectively. The staining solution was prepared according to the manufacturer's instructions. Bioprinted constructs were submerged and incubated for 15 min at room temperature (~22ºC), protected from light. Samples were then washed with one (1) × PBS and imaged using an epifluorescence microscope (ZEISS Axio Observer, Carl Zeiss AG, Oberkochen, Germany). Three images from random locations were captured from each sample and later analyzed using the ImageJ software, bringing the following viability numbers described in **Table 4**

Table 4 shows the viability values obtained using ImageJ software, presenting the mean values for each sample group throughout the bioprinting process (Original Work) [22].

single values					average			
Viability % (life)	n1= 0,232 mm2	n2= 0,341 mm2	n3= 0,802 mm2	Control	Viability % (life)	n1= 0,232 mm2	n2= 0,341 mm2	n3= 0,802 mm2
p1= 40 KPa	73,76	78,78	81,08	94.97 %	p1= 40 KPa	73,02	77,78	82,26
	73,88	76,76	82,52					
	71,42	77,8	83,19					
p2= 34 Kpa	79,41	81,46	89,87		p2= 34 Kpa	79,71	81,77	90,76
	79,51	82,11	91,85					
	80,22	81,75	90,56					
p3= 26 Kpa	80,92	82,61	94,88		p3= 26 Kpa	81,42	83,24	93,93
	82,19	82,65	94,42					
	81,14	84,47	92,5					

3.3.14 Statistical analysis

Cell viability data were statistically analyzed using Graph-Pad Prism software (GraphPad Software, La Jolla, CA, USA). The statistical distribution of the data was first studied with the Shapiro-Wilk normality test, and a two-way ANOVA with Tukey's multiple comparisons tests was subsequently performed.

3.4 Results and discussion

Three different prototypes of triple-layered coaxial extrusion systems were developed. The first consisted of commercially available plastic nozzle parts assembled with the aid of an adhesive (**Figure. 23-A**). This prototype was upgraded to a second one based on metallic nozzle parts, which conferred superior structural stability and were easier to sterilize when compared to the plastic nozzle parts (**Figure. 23-B**). Finally, the second prototype based on metallic nozzle parts was upgraded using 3D-printed nozzle parts. These nozzle parts were fabricated with photopolymer resins commonly used in dentistry, demonstrating their durability, ease of sterilization, and biocompatibility (**Figure. 23-C**). This final prototype of the triple-layered coaxial extrusion systems could be easily disassembled for a more reliable sterilization process and to allow changing the diameter of any channels. Moreover, this modular design also incorporated a fourth channel, yielding a four-layered coaxial extrusion system, described in depth in **Chapter 4** of this document.

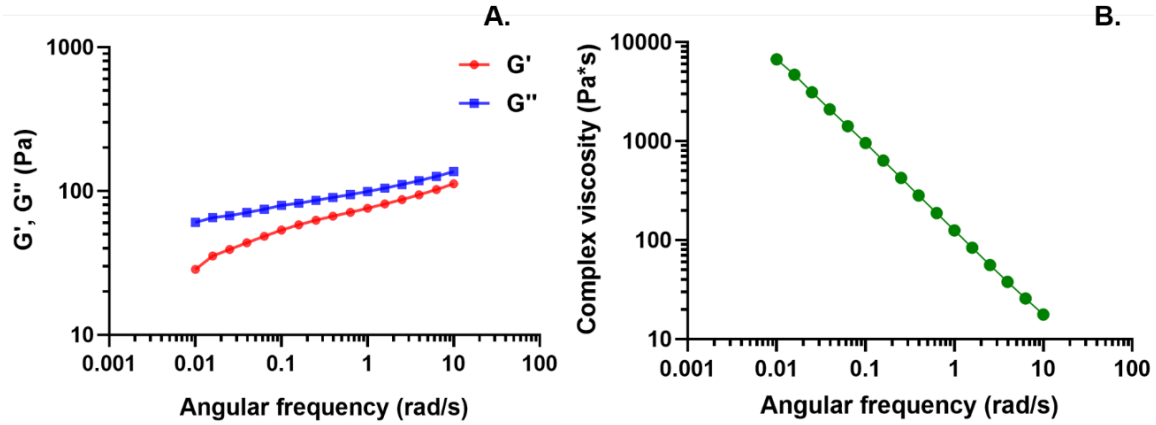

Figure 45 (A) Results from the rheological frequency sweep of the alginate-based bioink, where storage (G') and loss moduli (G'') were assessed as a function of angular frequency and (B) where complex viscosity was examined at varying values of angular frequency (Original Work) [22].

Figure 44 presents a two-part graphical analysis of the rheological properties of the alginate-based bioink. Part A displays the results of a frequency sweep test, where the storage modulus (G') and loss modulus (G") are plotted as functions of angular frequency. The storage modulus, depicted by red symbols, represents the material's elastic or 'solid-like' behavior, indicating how much energy is stored and recovered per deformation cycle. The loss modulus, represented by blue symbols, reflects the viscous or 'liquid-like' behavior,

showing the energy dissipated as heat. Both moduli increase with angular frequency, suggesting a viscoelastic behavior where the material exhibits both solid and liquid characteristics under stress.

Part B of the image focuses on the complex viscosity of the bioink, illustrated by green symbols. Complex viscosity combines both the viscous and elastic aspects of the material's response to deformation. The graph shows an apparent decrease in complex viscosity as the angular frequency rises, a hallmark of **shear thinning behavior**. This is a critical property for bioinks during the printing process, as it allows the material to flow more easily under the force of extrusion and then quickly solidify when the force is removed, maintaining the structure's shape. The downward trend in complex viscosity with increasing angular frequency indicates that the bioink's resistance to flow decreases as the rate of applied shear increases, which is advantageous for bioprinting applications where precise control over material flow and stability is necessary.

In silico simulations, varying extrusion pressures were performed to investigate the impact that the overall design of the coaxial nozzle might have on cell viability. Since this nozzle is intended to fabricate single-layered tubular structures, cell-laden hydrogels will only be extruded through Channel (*b)*, even though simulations were performed for all channels. Fluid velocity and pressure distribution through the entire Channel (*b)* geometry were collected from the simulations **Figure 35**. The outlet's minimum and maximum fluid velocities were 13 and 43 mm/s, respectively. Moreover, velocity remained constant throughout the entire geometry for all extrusion pressures studied and, in each layer/ area, into the nozzle geometry. However, that was not the case for pressure distribution since it seemed to decrease as the fluid approached the air interface between the nozzle and the collecting glass slide.

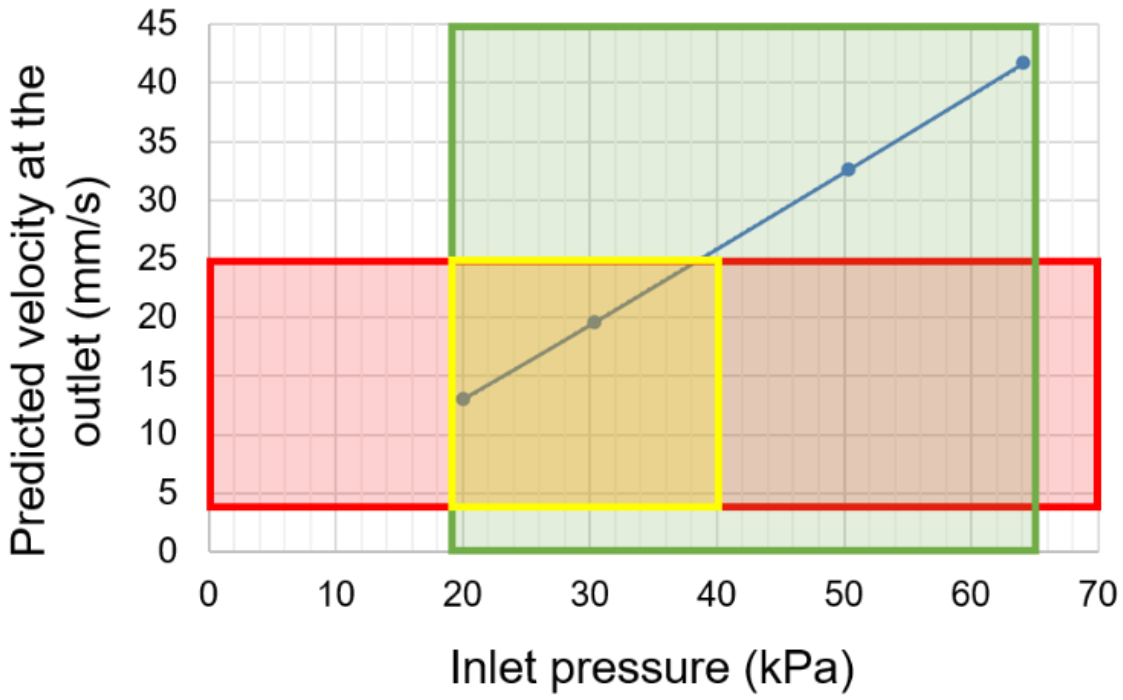

Figure 46 Explained deeply in **Figure 37,** depicting a plot displaying the fluid's predicted velocity (mm/s) at the coaxial nozzle outlet as a function of inlet pressure (KPa), according to in silico simulations. The green rectangle encloses the range of inlet pressures predicted to be safe for cells since the pressure at the outlet was below 70 kPa. The red rectangle encloses the range of velocities at the outlet predicted to be safe for cells. The area depicted in yellow, which is enclosed by the red and green rectangles, indicates the “safe zone” for cells, where the predicted values for outlet pressure and outlet velocity fall within values that can preserve cell viability according to previous studies (Original Work) [22].

According to the simulations, pressure distribution values at the tip of the flow channels fell between 2 and 10 kPa. In comparison, pressures between 20 and 64 kPa could be experienced at the uppermost regions of the *in-silico* flow channels. These values were then compared to those validated experimentally by previous studies for ordinary [16], [54], and coaxial [11] nozzles. Nair *et al.* reported that cell viability decreases exponentially due to increasing shear stress, with cell viability above 60 % for pressures below 100 kPa and nozzle diameters between (150 and 400 µm) [16]. Yu and colleagues investigated this same relationship on coaxial nozzles and obtained very similar results [11]. Although these estimations depend widely on the rheological properties of the studied hydrogel and the specific response of the cells utilized, we might be able to predict the high viability of cells bioprinted with the present coaxial nozzle. According to these previous studies, the predicted values collected for pressures experienced by the cells during the bioprinting process fall within a safe range for cells.

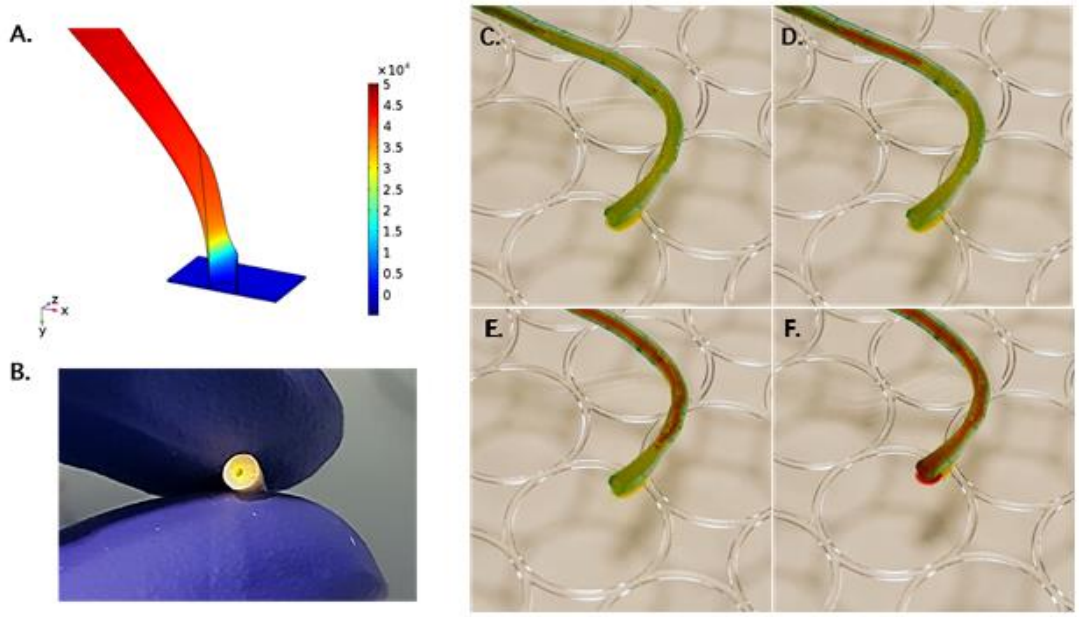

Figure 47 (A) Pressure distribution profiles along the geometry of one of the studied flow channels (flow Channel (b)). Values on the color bar are displayed in Pa × 〖10〗^4. (B) Transverse view of one of the printed and perfused hollow vessel-like structures. (C), (D), (E), and (F) display one of the hollow structures being perfused with one (1) × PBS stained with red food coloring. This figure was published in [22].

To confirm these notions and to investigate the effect of nozzle geometry, precisely the flow channel Gauge, on cell viability, bioprinting experiments were conducted with three different nozzles. As shown in **Table 3**, nozzles 1 and 2 allow the fabrication of single-layered hollow tubular structures of equal outer diameter (OD) but with different layer thicknesses. Likewise, nozzle 3 allows the fabrication of structures with a greater diameter and layer thickness than nozzles 1 and 2. These nozzles were subsequently 3D printed with biocompatible photopolymer resins and adapted to a commercially available and modified 3D printer for bioprinting experiments (**Figure 43)**. These nozzles allow the fabrication of vessel-like structures of diameters in the range of (0.52-0.91) mm (ID) and (0.84–1.36) mm (OD), which fall within the average dimensions of human veins [163], single-layered vessel-like structures were successfully fabricated and perfused with a red-stained solution of 1 × PBS for demonstration purposes **Figure 46**.

Life/Dead Test.

In addition to nozzle geometry, the effect of inlet pressure on cell viability was studied experimentally by varying the applied pressure of the mechanical extruder of flow Channel (*b)* within 26–40 KPa. Three different values of extrusion pressures within this range were selected according to printing experiments with the alginate-based hydrogel. These values were 26, 34, and 40 KPa, and the three fell within the material's printing window, as they allowed controlled and continuous deposition of a filament. An alginate-based bioink embedded with MG-63 cells was chosen for this evaluation since alginate is a widely used biocompatible material, easily extrudable, and features rapid crosslinking upon exposition to divalent cations, which enables excellent shape fidelity in bioprinted constructs [164].

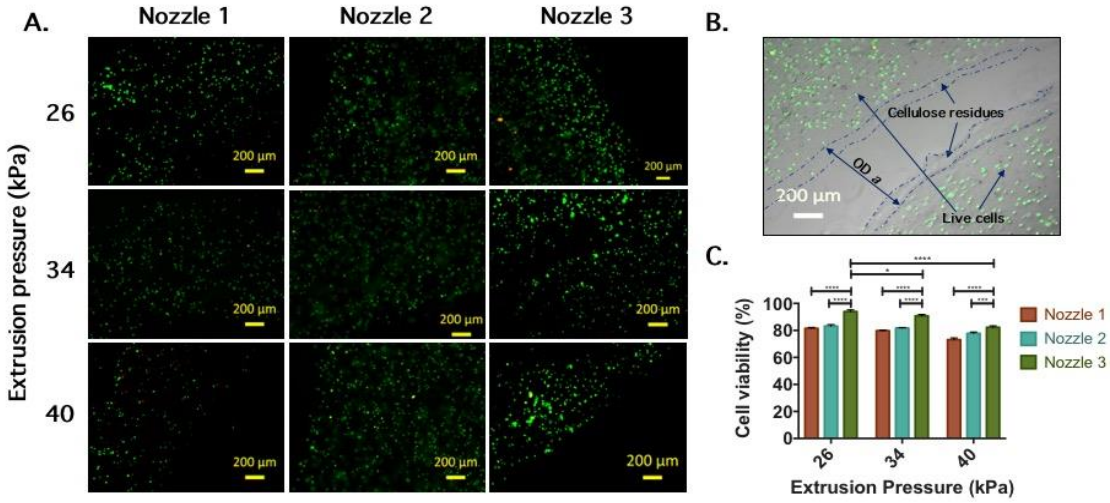

Figure 48 (A) Live/dead assay images of 3D printed vessel-like constructs with the three designed nozzles varying extrusion pressure of Channel (b). (B) Epifluorescent microscopy image of a vessel-like construct after removal of the innermost sacrificial material. Cells embedded in the bioink extruded through Channel (*b)* remain viable. (C) Cell viability of constructs immediately after bioprinting using the three designed nozzles and varying extrusion pressure between 26, 34, and 40 kPa. All configurations show high cell viability, but Nozzle 3 and low extrusion pressures yield the best results. This figure was published in [22].

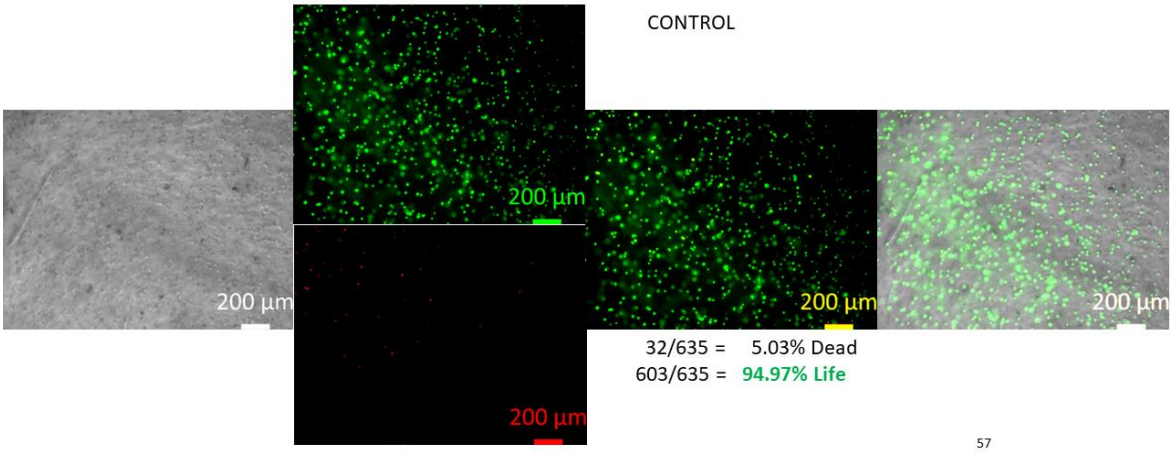

Figure 49 Control: Images from live/dead assays, created using bioink that was mixed without undergoing extrusion. As indicated in the image, the viability for these control samples achieved a life value of 94.97% (Original Work) [22].

As shown in (**Figure. 47**), most cells remain viable immediately upon deposition with all evaluated extrusion pressures and nozzles. The normal distribution of the data was first confirmed with the Shapiro-Wilk test ($P = 0.508$) before a two-way ANOVA on the data was performed. Extrusion pressure ($P < 0.0001$) and nozzle geometry ($P < 0.0001$), as well as their interaction ($P < 0.001$), were to have a significant effect on cell viability according to statistical analyses. Specifically, the viability of bioprinted structures through all nozzles seems to be significantly diminished with the rise of inlet extrusion pressure. In addition, all extrusion pressures evaluated through nozzle three yield significantly higher cell viability than nozzles 1 and 2, which suggests that a broader diameter in the tubular structures significantly reduces the stress to which cells are exposed during extrusion. Moreover, the viability of constructs extruded through nozzle 2 is only significantly different from those extruded through nozzle 1 when the inlet pressure high is (40 kPa), which indicates that layer thickness affects viability but to a lesser extent than the extrusion pressure. Given that a cell viability threshold of 80% was established, the findings imply that utilizing any of the three coaxial nozzles for bioprinting hollow tubular structures is feasible, provided that the inlet extrusion pressure is maintained below 34 kPa.

The main goal of this research, including the objectives, is to optimize the development of triple-layered coaxial nozzles for facilitating the fabrication of biomimetic tissues and organ-like constructs for tissue engineering and regenerative medicine applications. Furthermore, the enhanced development of triple-layered coaxial nozzles can help solve vascularization issues, which remain one of the field's key bottlenecks [165]. The next step in our current research is to apply these same concepts in developing a four-layered coaxial nozzle, whose advantages will be noted compared to the coaxial nozzle presented here. With one more layer, it will be easier to closely mimic the vascular network's complexity, considering that the current state-of-the-art tissue conventional culture technique is limited to only triple co-culture (3 types of cells). Advancements in tissue culture techniques are necessary to address the bottleneck of maturing bioprinted multi-cellular 3D tissue constructs into functional tissues with a wide range of cells and biomaterials with differentiated layer co-culture within one single bioprinted construct.

The novelty of this work is adding value to the research field of bioprinting with a triple-layered coaxial nozzle development that has the potential to closely mimic the complexity of vascular networks found in the native human body in terms of histological and morphological of these vascular constructs by keeping high cell viability. Moreover, this development has the potential to simulate the wall thickness of a native blood vessel, which is generally composed of three layers, with an innermost tunica intima layer made up of continuous endothelium cells, followed by a middle tunica layer composed of elastic, smooth muscle cells, and an outermost tunica adventitia layer composed of surrounding fibroblasts and collagen. Those three layers should comprise an ideal tissue-engineered blood vessel. As a result of the use of this coaxial nozzle, the wall thickness of this type of tissue can be reduced [108], closely mimicking the wall thickness of small arteries and veins in a natural human body.

Live Cell Imaging, Alternative method.

Considering the variable results stemming from the randomly selected location of triplicated samples for each combination of pressure and nozzle diameter (as detailed in **Figure 44**), which were captured at random spots within the printed constructs, we have implemented an additional method for live cell imaging: the CELLCYTE X (CYTENA) system. This system can be placed within a humidified incubator and enables simultaneous imaging of 96-well plates. It allows capturing images at either 4X or 10X magnification for each well, thereby providing a more detailed and comprehensive analysis of the 3D cultures involved in this experiment.

The CELLCYTE X system accommodates a 96-well plate format for sample evaluation, with each well-functioning as an individual chamber to maintain samples for analysis. This setup enables multiple assessments of the printed samples. We ensured consistent cell counts across experiments by printing coaxial droplets in each well. The cells were monitored using microscopy over time, t= 0 to t= 120 min, with steps every 10 minutes. The system's automated imaging and analysis capabilities greatly aid this process. Data collected from each well is then analyzed to discern the effects of the applied conditions on the cells.

CELLCYTE X can measure bright-field images and up to three fluorescent channels (red, blue, green) at the same time. Through this, cell behavior can be detected in real-time. The CELLCYTE software "CELLCYTE Studio," the brightfield and fluorescent microscopy images can be superimposed or visualized separately. The data collected can then be analyzed directly with CELLCYTE Studio software.

The bioprinting coaxial droplet option was chosen as this simulates a transversal cut of the coaxial sample and facilitates the overall evaluation of the viability of the whole transversal surface of the construct (droplet). Enhanced contour on the imaging system mode was selected for 3D droplets. The green channel was set up for 3D bioprinted droplet size, as shown in **Figure 50.**

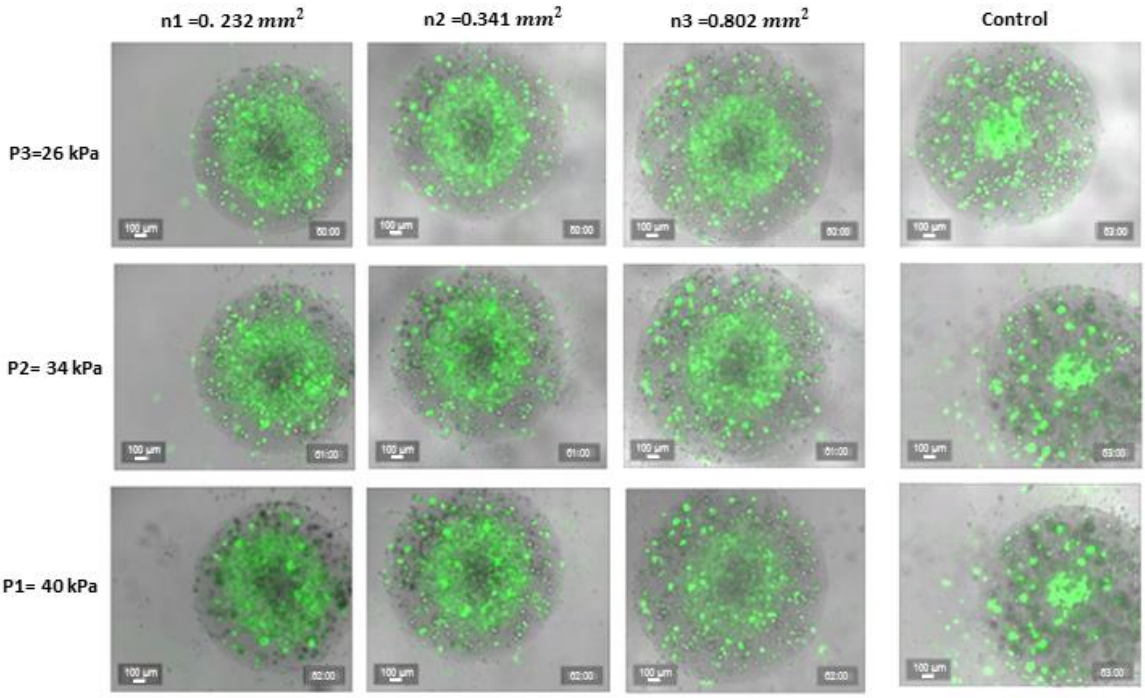

Figure 50 Exemplary Images of Live GFP-Labelled MG-63 Cells in Bioprinted Droplet Cultures, Alongside Controls in Complete Growth Medium. Observation of Cells for two hours via CELLCYTE X System (4x Magnification, Brightfield, and Green Fluorescence Imaging). Scale Indicator: 100 Micrometres (Original Work) [22].

The CELLCYTE X system chooses the optimal exposure time and gains (100 ms and 3 dB) using auto exposure on the green channel for the enhanced contour mode. The imaging was set up for one image per well, imaged in 10-minute intervals.

Exposure time and gain setup in CELLCYTE X for the culture within 2 hours MG-63 Cells tagged in-house with green fluorescent protein (GFP) were used in this experiment.

Table 5 Normalized total green fluorescence intensity analysis of GFP-tagged MG-63 cells in bioprinted droplet culture; samples were printed in triplicate. The standard deviation between the wells is displayed as error bars. Cells were monitored for 2 hours; samples were taken every 10m minutes using the CELLCYTE X system (Original Work) [22].

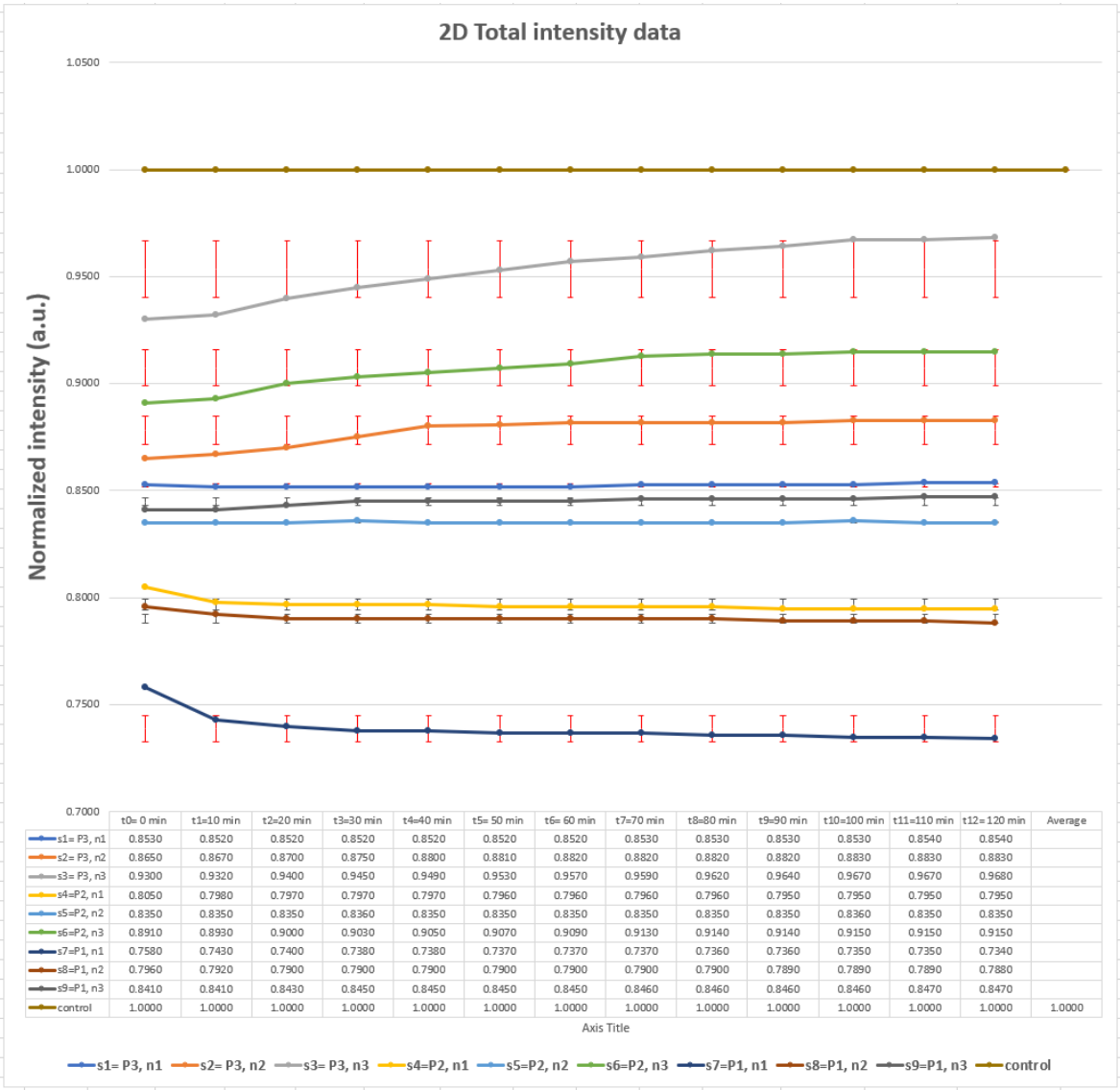

	t0= 0 min	t1=10 min	t2=20 min	t3=30 min	t4=40 min	t5= 50 min	t6= 60 min	t7=70 min	t8=80 min	t9=90 min	t10=100 min	t11=110 min	t12=120 min	Average
s1= P3, n1	0.8530	0.8520	0.8520	0.8520	0.8520	0.8520	0.8520	0.8530	0.8530	0.8530	0.8530	0.8540	0.8540	
s2= P3, n2	0.8650	0.8670	0.8700	0.8750	0.8800	0.8810	0.8820	0.8820	0.8820	0.8820	0.8830	0.8830	0.8830	
s3= P3, n3	0.9300	0.9320	0.9400	0.9450	0.9490	0.9530	0.9570	0.9590	0.9620	0.9640	0.9670	0.9670	0.9680	
s4=P2, n1	0.8050	0.7980	0.7970	0.7970	0.7970	0.7960	0.7960	0.7960	0.7960	0.7950	0.7950	0.7950	0.7950	
s5=P2, n2	0.8350	0.8350	0.8350	0.8360	0.8350	0.8350	0.8350	0.8350	0.8350	0.8350	0.8360	0.8350	0.8350	
s6=P2, n3	0.8910	0.8930	0.9000	0.9030	0.9050	0.9070	0.9090	0.9130	0.9140	0.9140	0.9150	0.9150	0.9150	
s7=P1, n1	0.7580	0.7430	0.7400	0.7380	0.7380	0.7370	0.7370	0.7370	0.7360	0.7360	0.7350	0.7350	0.7340	
s8=P1, n2	0.7960	0.7920	0.7900	0.7900	0.7900	0.7900	0.7900	0.7900	0.7900	0.7890	0.7890	0.7890	0.7880	
s9=P1, n3	0.8410	0.8410	0.8430	0.8450	0.8450	0.8450	0.8450	0.8460	0.8460	0.8460	0.8460	0.8470	0.8470	
control	1.0000	1.0000	1.0000	1.0000	1.0000	1.0000	1.0000	1.0000	1.0000	1.0000	1.0000	1.0000	1.0000	1.0000

Presto Blue HS

PrestoBlue HS is a cell viability reagent containing resazurin. Resazurin is reduced to resorufin in living cells. During this process, the blue color of resazurin is changed to the pink color of resorufin. The pink fluorescence of resorufin can be measured, and the more living cells per well, the higher the signal. PrestoBlue HS is a purified version of resazurin, which reduces the background fluorescence caused by resazurin contaminants by more than 50 % compared to other resazurin-based cell viability reagents.[166]

Cell Viability Assays

CELLCYTE X The GFP (Green Fluorescent Protein)-the signal of the cells was measured using the green, fluorescent channel in the CELLCYTE X. The CELLCYTE X measures green fluorescence for an excitation wavelength of 473-491 nm, and an emission wavelength of 502-561 nm. The cell viability image analysis in the CELLCYTE Studio was set up as follows. The object count recipe, where the system detects fluorescent objects, was chosen for the green fluorescent channel. Through this, the change in fluorescence signal per well is detected, which gives information about the live cells inside each well. This change in fluorescent signal is called "total intensity" and is measured in arbitrary units. Only live cells emit the signal, and the more cells there are in the well, the higher the signal. An increase in total intensity is assumed to correspond to an increase in cell culture growth, and a decrease in signal corresponds to cells dying. Through this, the total intensity data was used to monitor and analyze the cell viability of the cultures.

PrestoBlue HS

PrestoBlue HS (Invitrogen) was initially brought to room temperature. Subsequently, a 10% solution of PrestoBlue HS was prepared by combining it with the complete growth medium. For each well in a 96-well plate containing only control samples, 100 µL of this cell viability solution was added using a pipette. As a negative control, a few 96-well plates were treated exclusively with the PrestoBlue HS solution just before their analysis in the NIVO plate reader. The cell viability solution's color change was monitored visually until it turned pink, indicating readiness for measurement.

At this stage, a VICTOR Nivo (PerkinElmer, USA) plate reader was employed to assess the fluorescence across the entire well containing only control samples. Fluorescence measurements were recorded for the overall well plate. For accurate data interpretation, the fluorescence values from the negative control were subtracted from the readings obtained from all wells.

Data analysis

The data analysis process begins with the normalization of live cell imaging. The CELLCYTE X system, using a 4X magnification, captures images covering the entire construct in each 96-well plate. However, it is essential to note that the raw total intensity data represents the middle area of the well. To address this, we normalized the fluorescence data recorded at each timepoint by CELLCYTE X against the initial fluorescence observed at timepoint 0 hours. This normalization ensures that the data accurately reflects the number of cells in each image.

Next, we processed both the total intensity data from CELLCYTE X and the fluorescence data from the PrestoBlue HS assay. Viability values, derived from only the control samples using Presto-BLUE, were matched with the intensity values recorded for these control samples in CELLCYTE. Each intensity value was correlated with its corresponding viability value by employing a simple rule of three.

In the experiment conducted in triplicate, we averaged the total intensity data with the referenced fluorescent data. We then compared the intensity data from CELLCYTE X and the fluorescent data from PrestoBlue HS, pertaining to the 3D droplet bioprinted construct cultures, with their respective controls.

Table 6 Displays the viability metrics, derived by averaging normalized data from CELLCYTE and transforming them into viability values. This is achieved through contrasting and applying a basic rule of three, using control viability samples obtained with PRESTO BLUE. It presents the mean values for each sample group across the bioprinting process (Original Work) [22].

Viability % (Life)	n1 =0. 232 mm^2	n2 =0. 341 mm^2	n3 =0. 802 mm^2	Control
P1=40 kPa	72.85	77.92	83.81	98.61
P2=34 kPa	78.56	82.35	89.46	
P3=26 kPa	84.08	86.58	94.00	

We conducted a comparative analysis between two sets of data. The first set was acquired from a fluorescent microscopy life/dead experiment, where samples were randomly selected in triplicate from various spots on the bioprinted samples **Figure 48**. The second data set was obtained using CELLCYTE and PrestoBlue HS, which provided comprehensive coverage of the entire surface of the constructs. From this comparison, we were able to derive the following results:

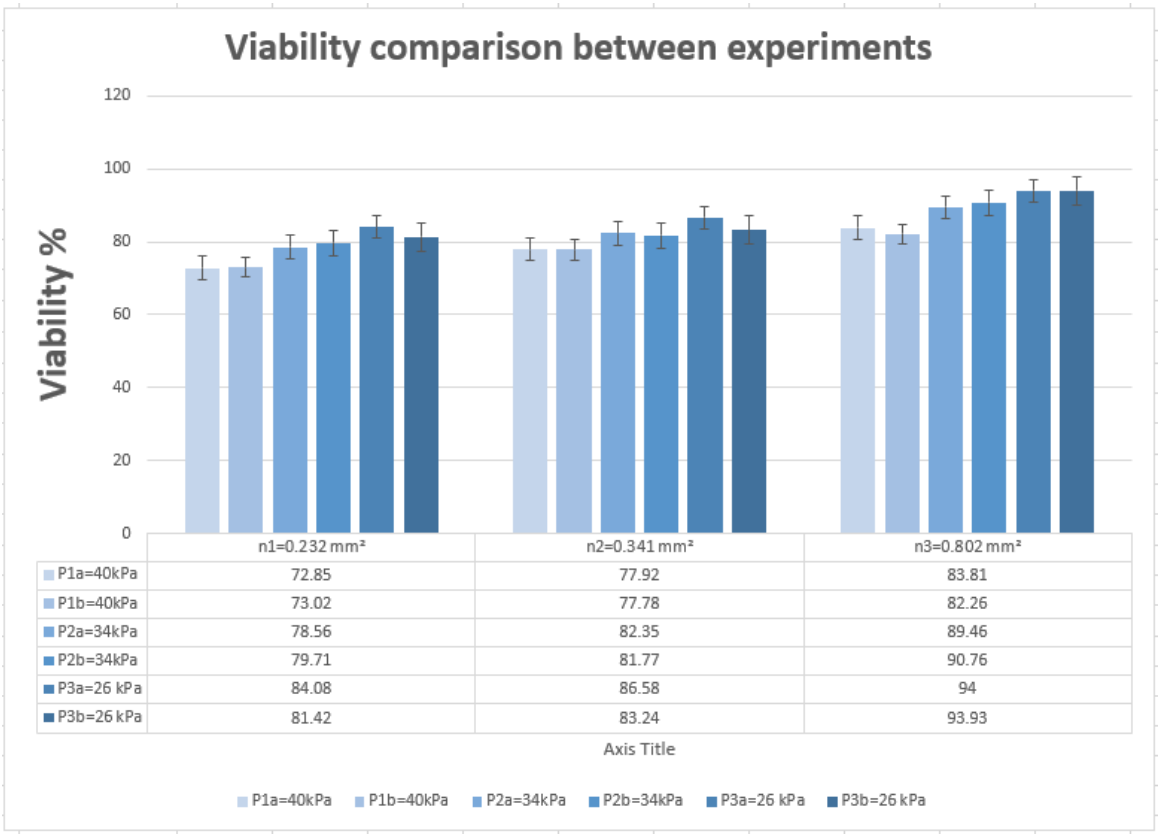

	n1=0.232 mm²	n2=0.341 mm²	n3=0.802 mm²
P1a=40kPa	72.85	77.92	83.81
P1b=40kPa	73.02	77.78	82.26
P2a=34kPa	78.56	82.35	89.46
P2b=34kPa	79.71	81.77	90.76
P3a=26 kPa	84.08	86.58	94
P3b=26 kPa	81.42	83.24	93.93

Figure 51 Viability comparison between the two sets of data, one obtained with life/dead test in Figure 48, and another obtained by using CELLCYTE and Presto Blue HS (Original Work) [22]

Figure 51 shows the viability percentages of diverse groups across varying areas in coaxial nozzles, aiming to understand clearly how group categorization and area size impact viability. Figure 51 illustrates the viability percentages for groups P1a, P1b, P2a, P2b, P3a, and P3b, across three distinct areas: 0.232 mm², 0.341 mm², and 0.802 mm². Each bar in the chart represents the mean viability percentage for its respective group and area. For ease of analysis, the data were organized into two sets: Set A (P1a, P2a, P3a) representing viability from life/dead experiments, and Set B (P1b, P2b, P3b) representing values from CELLCYTE and PrestoBlue HS. This grouping allows for effective comparison and analysis of the data, revealing clear correlations.

The ANOVA test conducted on this dataset indicates significant effects of 'Group' and 'Area' on viability percentages. The 'Group' factor, differentiating the six experimental groups, shows a highly significant impact on viability, with a p-value of 2.62×10^-6, indicating a statistically significant variance in viability among the groups. Similarly, the 'Area' factor,

representing the sizes of the different areas, also significantly influences viability, evidenced by an even lower p-value of 5.70×10^-8, suggesting that the size of the area is a crucial determinant of viability. The F-statistics for both factors are notably high, indicating that a significant portion of the variance in viability can be attributed to these two factors. In summary, our comprehensive analysis reveals that the categorization of experimental groups based on varying pressures, along with changes in area size, markedly influences viability percentages in coaxial nozzle studies. This finding not only corroborates previously gathered data but also validates new data collected through two distinct methods for assessing viability (life/death evaluations). Our study underscores the significance of these factors in coaxial nozzle research and contributes valuable insights into methodological approaches in this field.

3.5 Conclusions

In silico simulations were performed to study the pressure distribution exerted on cells during the bioprinting process and the outlet velocity at the tip of three different flow channels. Our results confirmed those of previously reported studies and demonstrated the usefulness of *in silico* experiments in helping to optimize *in vitro* experiments. The results can help guide the future development of improved multi-layered coaxial nozzles.

Three triple-layered coaxial nozzles with different geometries were first studied *in silico* by varying extrusion pressures and then successfully designed to fabricate single-layered hollow tubular structures of different dimensions. All nozzles displayed adequate bioprinting conditions to guarantee cell viability above 80 % in alginate-based hydrogels when extrusion pressure was kept below 34 kPa, meaning they are all suitable for bioprinting with bioinks with similar composition or rheological properties to the one studied in this thesis.

Chapter 4

Supplementary Findings and Practical Implementations.

4.1 Summary

Bioengineered tissues and organ-like structures have been devised as the next-generation solution for the lack of organ transplant and ultimately provide functionality in regenerative therapies based on engineered tissues. However, one of the main limitations of harnessing the development of tissues relevant in size and functionality is incorporating vascular networks within these constructs. The complexity of these interconnected networks is difficult to achieve even with state-of-the-art techniques. However, their presence in engineered tissues guarantees oxygen and nutrient access and successful waste disposal. Moreover, the biofabrication of patient-specific vessel-like structures suitable for vascular grafts could help solve the limitations of the currently available autologous and synthetic grafts. Here, we demonstrated the fabrication of multilayered embedded vessel-like structures by employing coaxial bioprinting with temperature control management combined with human cells and printable hydrogel biomaterials. We aimed at partly mimicking the native architecture of large- and middle-diameter vessels by fabricating triple-layered vessel-like structures and perfusable channels via direct 3D bioprinting and embedded 3D printing. All those were possible by customizing a commercial bioprinter regarding a mechanic reconversion, electronic adaptation, and software reprogramming to

integrate new parts and have four complete functional printheads with a coaxial nozzle in a standalone system. As observed from microscopy images, our results showed the successful fabrication of triple-layered vessel-like constructs. Furthermore, we demonstrated that extrusion pressure is the most critical printing parameter that determines cell viability on these multilayered tissue constructs fabricated with the aid of coaxial extrusion systems with temperature control management and shear-thinning hydrogels.

4.2 Introduction

Vascular networks are crucial for distributing oxygenized blood through the entire body's tissues and organs and collecting deoxygenized blood and metabolic wastes that result from normal cellular function [167]. Vascular conduct can be found at diameters ranging from 10 μm, as is the case for capillaries, up to 3 cm, for the case of the largest arteries. Aside from capillaries, all blood vessels in the human body are made of three layers [163]. The outermost layer, known as the tunica adventitia, is composed mainly of connective tissue and provides structural and shape support to the vessel [168]. The middle layer, known as tunica media, is composed of muscular tissue for facilitating and regulating the contractibility and distensibility of the vessel, which are mediated by mechanical and biochemical cues. Finally, the innermost and thinnest layer, known as tunica intima, comprises endothelium to provide a frictionless surface that ensures blood flow [168].

The fabrication of perfusable vascular conducts is critically relevant for advancing the biofabrication field towards tissue and organ-like constructs of sizes relevant to the human body [169], [170]. Furthermore, perfusable vascular structures with biomimicry are in need for use as medium- and large-diameter vascular grafts since current solutions are hampered by their low availability, in the case of autologous grafts, and by their lack of resemblance of native tissue, in the case of synthetic grafts [1]. Ideal vascular grafts must be biodegradable at a pace that matches the ability of cells to excrete ECM components to remodel their matrix and non-immunogenic to avoid unwanted rejection by the immune system [1]. Moreover, ideal vascular grafts must possess good mechanical properties, which are crucial for guaranteeing their functionality in distending and contracting as a dynamic response to the pulsatile blood flow and biochemical cues, such as hormones.

Among the different biofabrication technologies available, Extrusion-Based Bioprinting (EBB) is the most promising in fabricating complex structures with multiple biomaterials [8]. However, one of its main limitations is in the fabrication of multilayered hollow structures, where conventional nor emerging techniques, like direct bioprinting [8] and freeform reversible embedding of suspended hydrogels (FRESH) [103] [124], respectively, can provide sufficient structural support and printing speed. A wise combination of appropriate bioink properties, both on rheological behavior and cross-linking kinetics [47], [40] and cell-friendly bioprinting techniques must be achieved to build these complex tissue structures [39].

Accordingly, here we report the development of triple-layered hollow tubular structures aimed at resembling native medium and large-diameter vessels like single-layered hollow structures. For this, a group of four-layered coaxial extrusion systems with different geometries were fabricated. A commercially available 3D bioprinter (INKREDIBLE+™, Cellink AB, Gothenburg, Sweden) was modified on hardware, electronics, and software to operate simultaneously with four printheads instead of the two initially incorporated by the company. Next, the effect on cell viability of coaxial system geometry with temperature management and extrusion pressure was studied via bioprinting experiments using commercially available bioinks (CELLINK) and three different human cell lines (fibroblast, smooth muscle cells, and endothelial cells). Our work demonstrates the importance of bioink selection, temperature, nozzle geometry, printing parameters, such as pressure on cell survival when using coaxial extrusion systems, and the technical feasibility of modifying commercially open-source available 3D bioprinter for yielding low-cost and reliable multi-printhead instruments for advancing biofabrication.

4.3 Materials and methods

4.3.1 Modifications to the hardware and software of a commercial open-source 3D bioprinter.

A commercial open-source 3D bioprinter was kindly provided by Cellink AB (INKREDIBLE+™, Cellink AB, Gothenburg, Sweden). This bioprinter features two printheads, a cartridge-heating system, and Clean Chamber Technology (CCT). Its CCT allows it to operate in sterile conditions without using a biosafety cabinet, thanks to its HEPA-filtered positive air pressure and UV light arrangement inside the printing chamber.

To operate the INKREDIBLE+™ bioprinter with the herein-developed four-layered coaxial extrusion with temperature management systems, several modifications on hardware and software were performed on the instrument to incorporate a third and fourth printhead. All modifications were approved by the bioprinter manufacturer and vendor (Cellink AB, Gothenburg, Sweden) in compliance with the legal regulations. Moreover, since most of the mechanical parts used for the hardware modifications were the same for fabricating the original bioprinter, the manufacturer kindly provided these and the firmware (Torks base in Marlin RepRap Project) for adaptation and integration with the newly assembled parts. For incorporating two additional printheads, the following machine parts were utilized: a pair of digital pressure monitors, pressure regulators, monostable valves, bistable valves, plastic tubing, and pneumatic airline connectors. To integrate all four printheads into the bioprinter, software variables were renamed, new M-commands were created and added to the firmware, board ports were renumbered, further firmware actions were added, and an additional heated circuit board was added.

4.3.2 Four-layered coaxial nozzle with temperature control management design and prototyping

Four--layered coaxial extrusion systems were built using CAD designs and 3D printing prototyping models based on previous CFD analysis simulations [22], assembled using commercially available metallic nozzle parts. The design parameters of the four channels of each coaxial extrusion system are described in **Table 7**, which outlines the layer thickness and layer area of Channels (*b)*, (*c), and (d)* (**Figure. 52 A**), as well as the overall dimensions of the nozzle parts used for the coaxial extrusion systems.

Parameter	**Coaxial system 1**				**Coaxial system 2**				**Coaxial system 3**			
	a	***b***	***c***	***d***	***a***	***b***	***c***	***d***	***a***	***b***	***c***	***d***
Gauge (G)	18	14	11	8	21	16	13	10	24	18	14	10
ID (mm)	0.84	1.82	2.50	3.55	0.51	1.37	2.00	3.00	0.30	0.84	1.82	3.00
OD (mm)	1.27	2.00	3.05	4.20	0.84	1.61	2.40	3.50	0.54	1.27	2.00	3.50
OD – ID (mm)	0.43	0.18	0.55	0.65	0.33	0.24	0.40	0.50	0.24	0.43	0.18	0.50
Layer thickness (mm)		0.55	0.50	0.50		0.53	0.39	0.60		0.30	0.55	1.00
Layer area (mm^2)		1.33	1.77	2.59		0.92	1.11	2.54		**0.33**	1.33	**3.93**
$\sum$ areas (mm^2)		**5.69**				4.57				5,59		

Table 7 Geometric data of the designed coaxial systems. ID and OD stand for inner diameter and outer diameter, respectively. The four flow channels of each nozzle are labeled as (a), (b), (c), and (d), as shown in (**Figure. 52 B, C**) (Original Work).

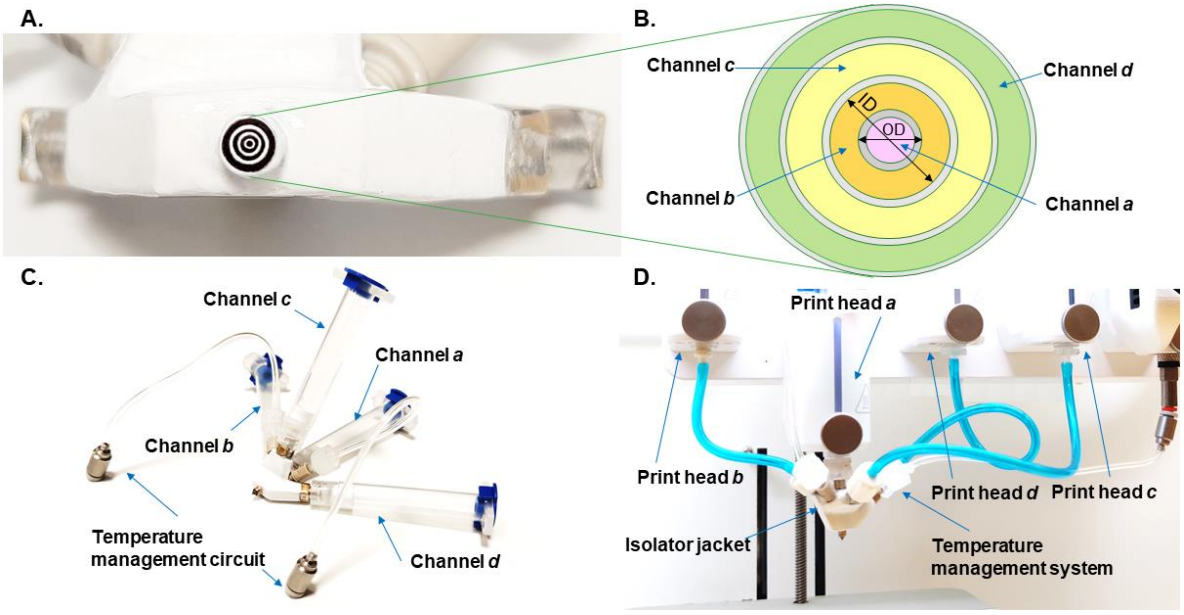

Figure 52 (A) Bottom view of the developed four-layered coaxial extrusion system and (B) an illustrated close-up of its multichannel outlet. (C) The four-layered coaxial extrusion with temperature management circuit holding cartridges attachments to each inlet, labels indicating the channel corresponding to each inlet, (D) The coaxial and temperature control management system as attached to the reconverted 3D bioprinter (Original Work).

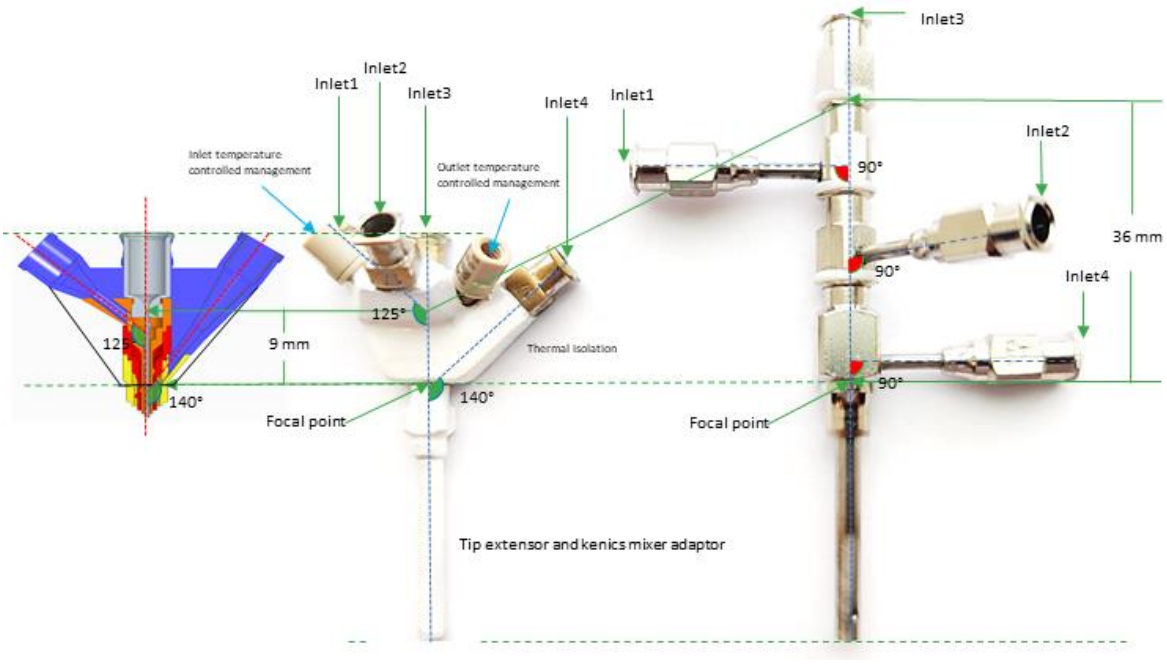

Figure 53 The above shows the dimensions of a coaxial nozzle commercial solution on the right (Ramé Hart instruments co.) commercial solution, and the developed four-layered coaxial extrusion with a temperature control management system on the left compared with the CAD-validated CFD model. A tip extender for embedded coaxial bioprinting and a static mixer (kenics mixer) adapter is included in this development (Original Work).

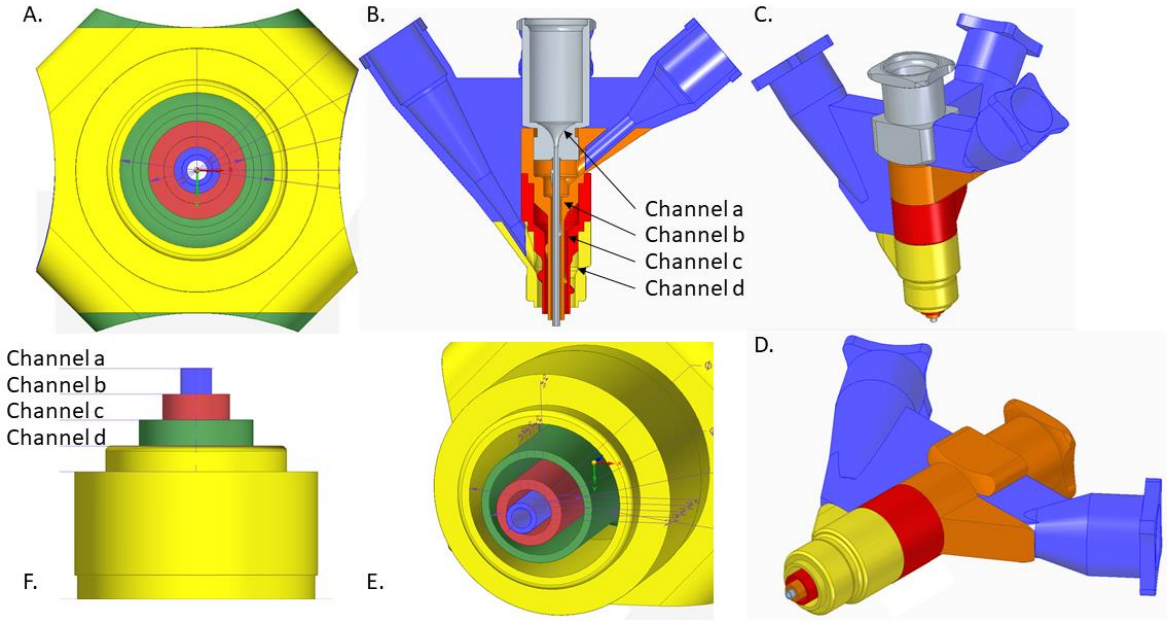

Figure 54 (A) CAD design bottom view of the developed four-layered coaxial extrusion system and, (B) Longitudinal cut four-layered coaxial nozzle, (C) The four-layered coaxial extrusion in isometric perspective, (D) Bottom-lateral assembly view of the four-layered coaxial extrusion, (E) an illustrated close-up of the tip nozzle multichannel outlet. (F) Lateral close-up of the coaxial nozzle tip with its different channels (Original Work).

Among the reasons for this improvement in comparison with a previous development [22] was the possibility of including an extra channel to replicate the whole structure of a vascular tissue by adding an extra layer with smooth muscle cells, along with the possibility of using temperature-dependent and biologically relevant biomaterials such as collagen or GelMA, which could also be interesting to use to replicate the whole structure of a vascular tissue.

The coaxial extrusion nozzle with temperature control management was designed to be covered by an isolator jacket containing two additional inlets (**Figure. 55)** for the temperature control management circuit that allows the temperature of the overall nozzle to be controlled within a range of 8 °C to 60 °C**.**

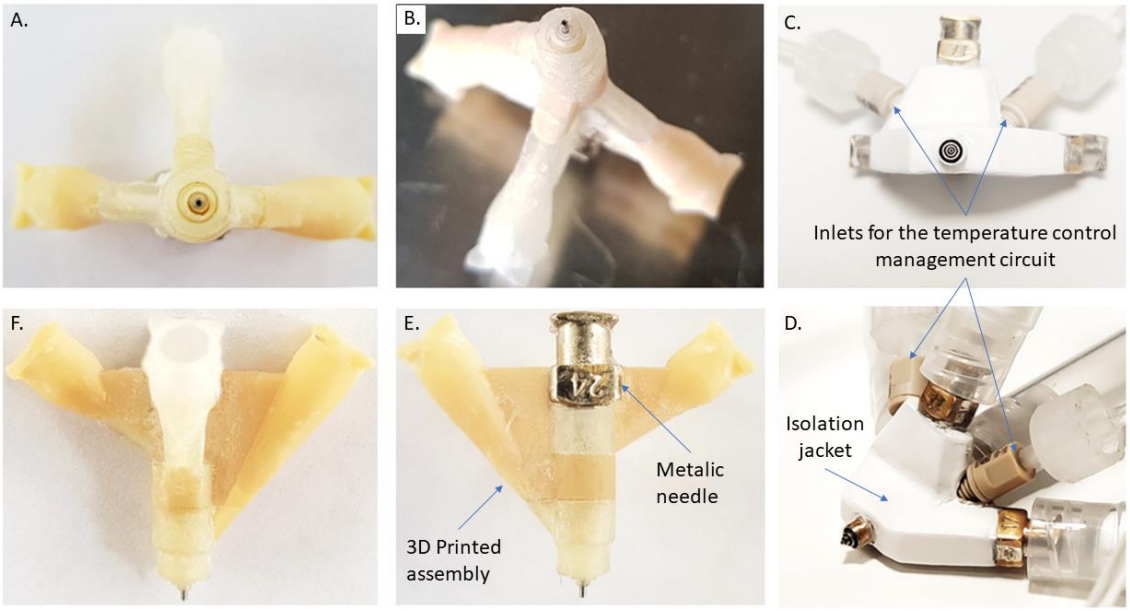

Figure 55 (A) Bottom view of the 3D printed prototype development of the four-layered coaxial extrusion system and (B) Bottom view in perspective of the multichannel outlet. (C) Bottom view of the four-layered coaxial extrusion with the two additional inlets for the temperature control management circuit (D) Lateral view perspective of the four-layered coaxial extrusion with the two additional inlets inserted in the isolator jacket for the temperature control management circuit (E) Frontal view of the 3D printed prototype of the four-layered coaxial extrusion (F) Backward view of the four-layered coaxial extrusion (Original Work).

One key reason for developing our coaxial nozzle with integrated temperature management was to gain a deeper insight into the thermal dynamics of the deposition process. Specifically, we aimed to analyze how temperature gradients affect the viscosity and flow of the deposited material. By incorporating these aspects into our experimental framework, we aim to thoroughly understand the deposition process with temperature-dependent biomaterials and cells at biological temperature (37 °C). This knowledge is critical for refining the nozzle design, thereby enhancing efficiency, increasing cell viability, and precision of material deposition.

.

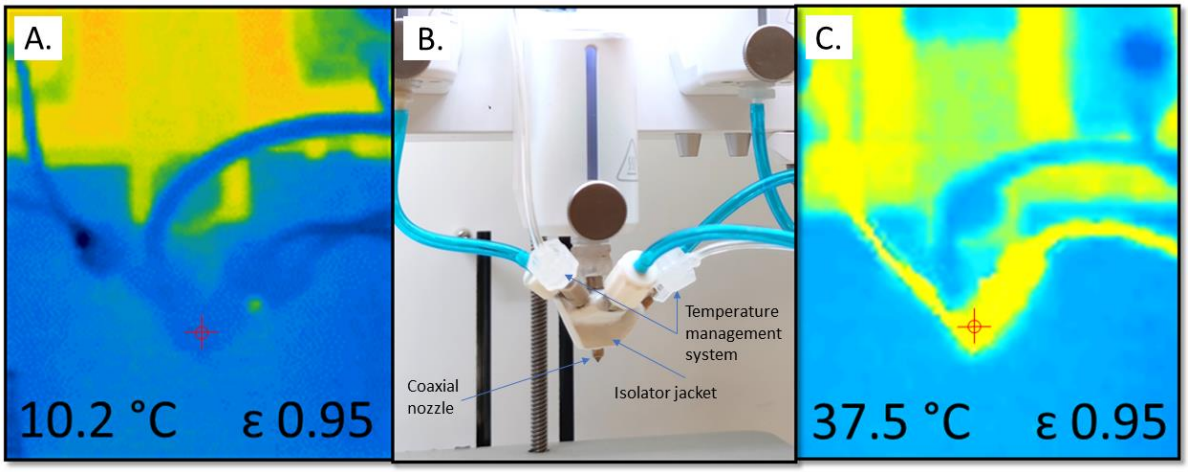

Figure 56 (A) Developed four-layered coaxial extrusion system controlling the temperature at ten (10) °C for 20 minutes, (B) The coaxial and temperature control management system attached to the bioprinter has a temperature control range from 8 °C to 60 °C (C) Developed four-layered coaxial extrusion system controlling the temperature at 37°C for 20 minutes (Original Work).

Among the four channels described, three are in a specific way designed to contain biologically relevant biomaterials with cells; the coaxial extrusion nozzle with temperature control management contained bioinks in this order (Channel (b), Channel (c), and Channel (d)).

Human foreskin fibroblasts HFF-1 (ATCC® SRCR-1041™), human primary aortic smooth muscle cells (HASMC) (ATCC® PCS-100-012™), human primary umbilical vein endothelial cells (HUVECs) (ATCC® PCS-100-010™) were used for bioprinting experiments.

The fibroblasts were cultured in a growth medium consisting of Dulbecco's Modified Eagle Medium (DMEM) with 15 % (v/v) supplemented fetal bovine serum (FBS), including 1 % (v/v) penicillin-streptomycin (10,000 U/mL).

The smooth muscle cells (HASMC) were cultured in a vascular cell basal medium (PCS-100-030) supplemented with a vascular smooth muscle growth kit (PCS-100-042) provided by the same manufacturer.

The endothelial cells were cultured in Endothelial Cell Basal Medium-2 (EBM-2) (Lonza, Basel, Switzerland) supplemented with the Microvascular Endothelial Cell Growth Medium-2 SingleQuots™ Kit provided by the same manufacturer.

All cell lines were maintained separately in a 5% CO_2 and incubated at 37 ºC. Upon the cultures reached a confluence of approximately 80%, cells were detached from the bottom of cell culture flasks with the aid of a 0.25 % (w/v) trypsin solution (Gibco™, Thermo Fisher Scientific, Waltham, MA, USA) and subsequently collected by centrifuging. The cell concentration of the pellets obtained from all cell lines was estimated using a system named Countess II Automated Cell Counter, Thermo Fisher Scientific Inc, and subsequently adjusted each at one (1×10^6) cells/mL in their corresponding fresh complete growth medium.

4.3.3 Preparation of bioinks

For bioprinting experiments with the four-layered coaxial extrusion systems, four (4) commercially available bioinks were employed: CELLINK FIBRIN, CELLINK LAMININK-121, CELLINK LAMININK+, CELLINK PLURONIC, and cross-linking agent CELLINK.

CELLINK PLURONIC 40% was used as a sacrificial material for the core channel of the triple-layered vessel-like constructs that were subsequently washed out to yield a hollow cannular structure, namely **Channel *(a).*** in (**Figure 52-A, B**). This biomaterial ink is composed of Pluronic® F-127 and can be easily washed with PBS 1X by decreasing the temperature of the printed construct below 13 °C.

CELLINK LAMININK+ is a biomaterial ink composed of sodium alginate, nano-fibrillar cellulose, laminin-111, laminin-121, laminin-411, and laminin-521. Laminins are a group of glycoproteins that comprise part of the extracellular matrix of tissues and play critical roles in influencing cell differentiation, migration, and adhesion.
Laminins are one of the most abundant and essential families of structural glycoproteins found in Extracellular Matrix (ECMs) [171]. Moreover, laminins provide anchoring sites for cells to attach and can actively modulate cell behavior [172]. Thanks to their biological relevance in native tissues, laminins have been widely employed for Tissue Engineering (TE) and Regenerative Medicine (RM) applications [173]–[178].

For example, Stamati and colleagues demonstrated that laminin could promote vascular network formation in vitro inside collagen type I hydrogels embedded with human bone marrow stromal cells and HUVECs [179]. Their results showed that the presence of laminin in the cultures significantly increased VEGF uptake by HUVECs, thus promoting vascular network formation. These results support laminin and HUVECs in this study for fabricating vessel-like tissues.

To prepare the bioink to be extruded on **Channel (*b)*** of the coaxial system (**Figure 52-A, B**), 6 mL of CELLINK LAMININK+ was loaded into a 12 mL Leuer-lock syringe and connected to another syringe containing 1 mL of the suspension of HUVECs. Next, the two components were gently and slowly extruded back and forth at least twenty (20) times to guarantee a homogeneous mixture. The final cell density on this bioink was around 1.43×10^6 cells/mL.

CELLINK LAMININK-121 is a biomaterial ink comprised of sodium alginate, nano-fibrillar cellulose, and laminin-121, a protein containing three subunits referred to as an α-chain, β-chain, and γ-chain. The basal lamina is a component of the cell membrane's outer surface that lines the basal lamina's surface. Many tissues rely on its cross-like structure as a basis for their development. This protein is expressed extensively during the embryonic and initial stages of developing organs and tissue linings. It is found in the placenta, skeletal muscle, kidney, brain, and liver tissues. As a base material for the 3D culture of skeletal muscle, CELLINK LAMININK 121 is suitable for use as a 3D culture medium. A 12 mL Leuer-lock syringe was used to load six mL of CELLINK LAMININK-121 into a syringe containing 1 mL of the suspension of HASMCs connected to another syringe containing six mL of CELLINK LAMININK-121 to prepare the bioink for extrusion in a channel of the coaxial system (**Figure 52-A, B**). To achieve the same cell density as the previous bioink, the two components were carefully mixed the same number of times as the previous bioink.

CELLINK FIBRIN is a biomaterial ink composed of sodium alginate, nano-fibrillar cellulose, and fibrinogen, all of which are nature-derived materials. Alginate is a biocompatible material obtained from algae and can be readily cross-linked in the presence of divalent cations, such as those obtained from calcium chloride solutions.

Fibrinogen is a fibrous glycoprotein complex that circulates freely in the blood and plasma, responsible for the formation of clots upon its conversion to fibrin, which is enzymatically

mediated by thrombin [172]. The cross-linking solution developed for this bioink is based on thrombin, an enzyme that mediates the cleavage of fibrinogen into fibrin monomers that can polymerize [180]. Thus, after cross-linking, CELLINK FIBRIN yields a combination of polymerized fibrin networks and a small portion of unreacted fibrinogen. Both these proteins can bind to growth factors of crucial relevance in angiogenesis and tissue regeneration, such as vascular endothelial ECM and growth factor (VEGF) and fibroblast growth factor-2 (FGF-2) [181]. Fibrin clots are significant in stopping bleeding from injuries and providing a wound-healing environment. Additionally, nano-fibrillar cellulose is a polysaccharide produced by bacteria, providing printability to bioinks.

Hence, the presence of fibrinogen and fibrin in the triple-layered bioprinted vessel-like structures may facilitate appropriate tissue maturation by retaining growth factors necessary for guiding cell thrive [182].

CELLINK FIBRIN was loaded into a 12 mL Leuer-lock syringe and connected to another syringe containing 1 mL of the suspension of HFF-1 cells to create the bioink to be extruded on **Channel (d)** for the triple-layered construct of the coaxial system (**Figure 52-A, B**). Then, the two components were carefully extruded back and forth the same number of times as the previous bioink, obtaining the same cell density.

Before bioinks were used to print with coaxial extrusion systems, food coloring mixed with all mentioned biomaterials without cells was used to show the differences between one bioink and another. The purpose of this was to visualize the different layers in a more precise way.

A cross-linking agent, CELLINK, was poured across the top of the constructs and perfused to remove pluronic from the lumen while acting as a crosslinker; it was used as a divalent cation solution. It consists primarily of calcium chloride (50mM), HEPES buffer (10mM), and water (H_2O).

Finally, CELLINK GELMA, which is a photocrosslinkable biomaterial based on methacryloyl-modified gelatin, serves as a supportive environment to embed and immobilize the 3D printed structure as a microfluidic device, built wholly of biomaterials and

allows it to withstand perfusion pressure until cells in the cannular structures can proliferate, mature, and generate tissue.

4.3.4 Printing vessel-like structures

To demonstrate the feasibility of printing multilayered and perfusable vessels using the four-layered coaxial extrusion system, triple-layered perfusable structures were fabricated using embedded bioprinting. A commercially designed bioreactor for bioprinting tissues with incorporated perfusable channels was used [183] (CELLINK VASKIT, Cellink AB, Gothenburg, Sweden). This bioreactor permits connecting a cell-embedded construct to perfusion tubing while visually inspecting the tissue throughout the maturation process. The CELLINK VASKIT device is made from medical grade polymers, medical grade resins, glass, and stainless steel, which make it reusable and easy to sterilize, and it was used in this study for bioprinting cellular tissue constructs incorporated with perfusable channels. CELLINK GELMA was used for the infill, whereas CELLINK PLURONIC, CELLINK LAMININK+, CELLINK LAMININK-121, and CELLINK FIBRIN were bioprinted through the four-layered coaxial extrusion system for yielding channels within the infill. Moreover, these same bioinks were used without the bioreactor to yield more prominent and longer vessel-like structures.

4.3.5 Bioprinting of triple-layered hollow tubular structures

For bioprinting experiments, the coaxial nozzles were submerged overnight in 70% (v/v) ethanol and washed with sterile one (1) × PBS in a biosafety cabinet immediately before the experiments. The modified 3D bioprinter was thoroughly wiped with 70% (v/v) ethanol and exposed to UV germicidal light for one (1) hour inside a biosafety cabinet.

Each coaxial extrusion system comprised four flow Channels, (*a)*, (*b),* (*c),* and *(d),* in (**Figure 52-A, B)**. Four different hydrogels were employed for bioprinting hollow, triple-layered tube-like structures. Crosslinking agent CELLINK was poured on the top of the constructs and perfused through the lumens to cross-link the vessel constructs right after the extrusion. CELLINK FIBRIN bioink embedded with human fibroblasts was used for the layer corresponding to the outermost layer Channel (d). CELLINK LAMININK-121 embedded with HASMCs was used in the Channel (c) layer.

CELLINK LAMININK+ embedded with HUVECs was used for the innermost layer. In addition, a sacrificial ink, namely CELLINK PLURONIC, was deposited as the core structure and subsequently washed to yield hollow structures. The deposition of the bioinks through the four-layered coaxial extrusion systems in 12-well plates, each containing a cross-linking solution based on calcium chloride ($CaCl_2$), thrombin cross-linked alginate, and fibrinogen, respectively, in addition to the cross-linking agent CELLINK. Alginate was a component of CELLINK FIBRIN, CELLINK LAMININK-121, and CELLINK LAMININK+, while fibrinogen was only present in CELLINK FIBRIN.

This bioprinting procedure was performed with the three (3) designed coaxial extrusion systems varying the extrusion pressure of the printheads connected to Channels (*b), (c), and (d) s*ince the cell-laden bioinks were dispensed through these channels. The extrusion pressure of Channel (*a),* which deposited the sacrificial material, was fixed at a specific value depending on the nozzle geometry. (**Table 8**). Shows the extrusion pressures employed for depositing the several bioinks through the different coaxial systems. Constructs fabricated with each set of extrusion pressures, standard extrusion pressure (SEP), and *+40%* in (**Table 8)** were bioprinted in triplicate for each sample where cell viability was evaluated, i.e., immediately after bioprinting.

For each bioink, the SEP (Standard Extrusion Pressure) was determined by varying and optimizing the bioink flow through a specific channel of each coaxial extrusion system. **This pressure was defined by quantitatively identifying the value on which the material could be deposited as a continuous filament** without accumulating at the outlet or stopping flowing. For experiments, this standard pressure was defined as *SEP* for all bioinks on each coaxial system (**Table 8**). The (+40%) plus 40 percent value was defined as the standard extrusion pressure plus 40 percent for CELLINK FIBRIN, CELLINK LAMININK-121, and CELLINK LAMININK+. Cellink PLURONIC, which did not contain any cells and was used only as a sacrificial material for the core layer of tubular structures, was fixed at the same pressure as SEP, as its variation in pressure was not intended.

The difference of pressure for the experiment Plus, 40 percent (+40%) was chosen as it was the taken value that could be measured on average for all four inlets on the **commercial coaxial nozzle solution from Ramé-Hart** to make possible the extrusion of the same used biomaterials in comparison with the pressures used on the developed coaxial extrusion nozzle system (CS2).

Bioink	Coaxial system 1		Coaxial system 2		Coaxial system 3	
	SEP	***+40%***	***SEP***	***+40%***	***SEP***	***+40%***
Cellink Fibrin (KPa) Channel d.	**15**	**21**	**15**	**21**	**10**	**14**
Cellink Laminik-121 (KPa) Channel c.	**35**	**49**	**50**	**70**	**40**	**56**
Cellink Laminik+ (KPa) Channel b.	**40**	**56**	**61**	**85**	**70**	**98**
Cellink Pluronic (KPa) Channel a.	**120**	**120**	**170**	**170**	**200**	**200**

Table 8 Extrusion pressures utilized for bioprinting triple-layered hollow tubular structures with each of the three (3) coaxial extrusion systems developed at a controlled temperature of 37 ºC (Original Work).

As it is shown in **Table 8**, CELLINK FIBRIN was deposited through flow Channel (d), CELLINK LAMININK-121 was deposited through flow Channels (c), CELLINK LAMININK+ through flow Channel (b), while CELLINK PLURONIC in Channel (a).

4.3.6 Cell viability assessment

For studying the effect of the inlet extrusion pressure and the different coaxial extrusion system geometries with and without temperature control on cell survival immediately after bioprinting, a Live/Dead (Sigma-Aldrich, St. Louis, MO, USA) assay was performed on the bioprinted triple-layered tubular structures. Briefly, constructs were stained with calcein acetoxymethyl ester (calcein-AM) and propidium iodide (PI) immediately after bioprinting and fluid perfusion through the lumen to visualize live and dead cells, respectively. The staining solution was prepared by following the manufacturer's instructions. Bioprinted constructs were submerged and incubated for 15 min at room temperature (~21ºC), protected from light. Samples were washed with the cross-linking agent and then one (1) × PBS and imaged using an epifluorescence inverted microscope system (Olympus IX73, Sweden). Three images from random locations were captured from each sample and later analyzed using the ImageJ software.

.

4.4 Statistical analysis

Cell viability data were statistically analyzed using Graph-Pad Prism software (GraphPad Software, La Jolla, CA, USA). The statistical distribution of the data was first studied with the Shapiro-Wilk normality test, and a two-way ANOVA with Tukey's multiple comparisons tests was subsequently performed.

4.5 Results and discussion

CELLINK INKREDIBLE+ bioprinter modified in this research work (**Figure. 57**), (**Figure. 58**), was used to print CELLINK bioinks composed mainly of sodium alginate and nano-fibrillar cellulose [184], CELLINK FIBRIN, CELLINK LAMININK-121 and CELLINK LAMININK+ which are all based on these two components but supplemented with other biomaterials or modified with functional moieties, depending on the aimed application. Those three biomaterials were chosen for bioprinting triple-layered hollow tubular structures because their composition resembles native vascular tissue. Moreover, to operate these materials with the developed four-layered coaxial extrusion systems, several modifications on hardware and software were performed to the INKREDIBLE+ bioprinter. Two additional printheads were included in the bioprinter, as well as the digital pressure monitors, pressure regulators, monostable valves, and bistable valves necessary for its operation.

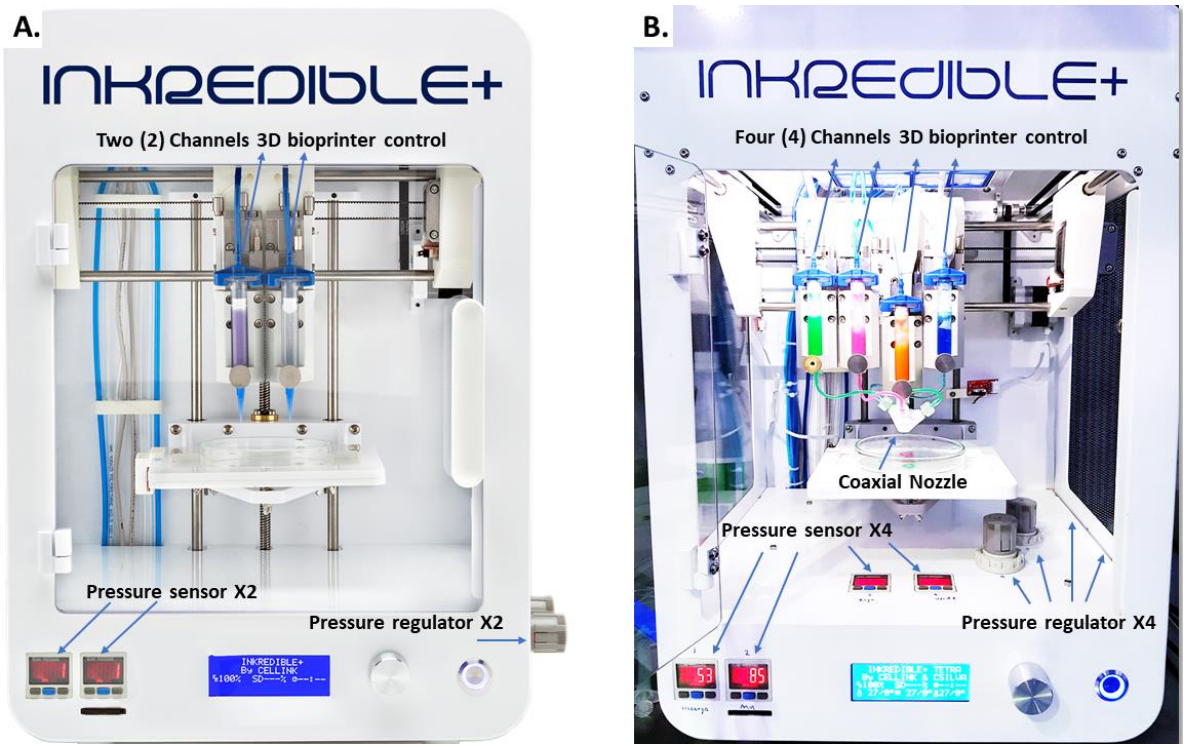

Figure 57 (A) The INKREDIBLE+™ bioprinter with two printheads is commercially available and advertised on CELLINK's webpage (www.cellink.com). (B) INKREDIBLE+™ bioprinter was modified with two additional printheads to complete four (4), where the blue arrows label the additional digital pressure monitors and pressure regulators (Original Work).

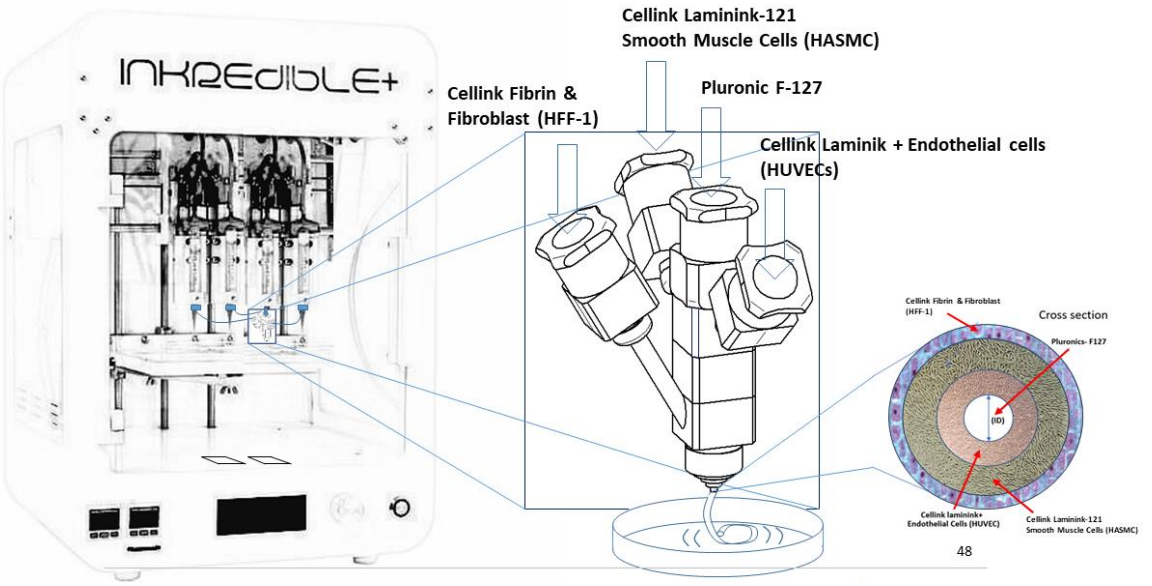

Figure 58 Coaxial nozzle configuration for the material distribution through all four different inlets (Original Work).

Hardware modifications.

These two added printheads made part of the hardware modifications required for the bioprinter, including a third and fourth biomaterial inlet for the coaxial nozzle. The assembly of the new parts that were incorporated into the commercial 3D bioprinter to operate with four printheads simultaneously included a pair of pressure regulators, two pressure sensors coupled with digital monitors, monostable and bistable valves, which were all connected to plastic hollow tubing allowing the flow of pressurized air from an external air compressor as described in **Figure 59.**

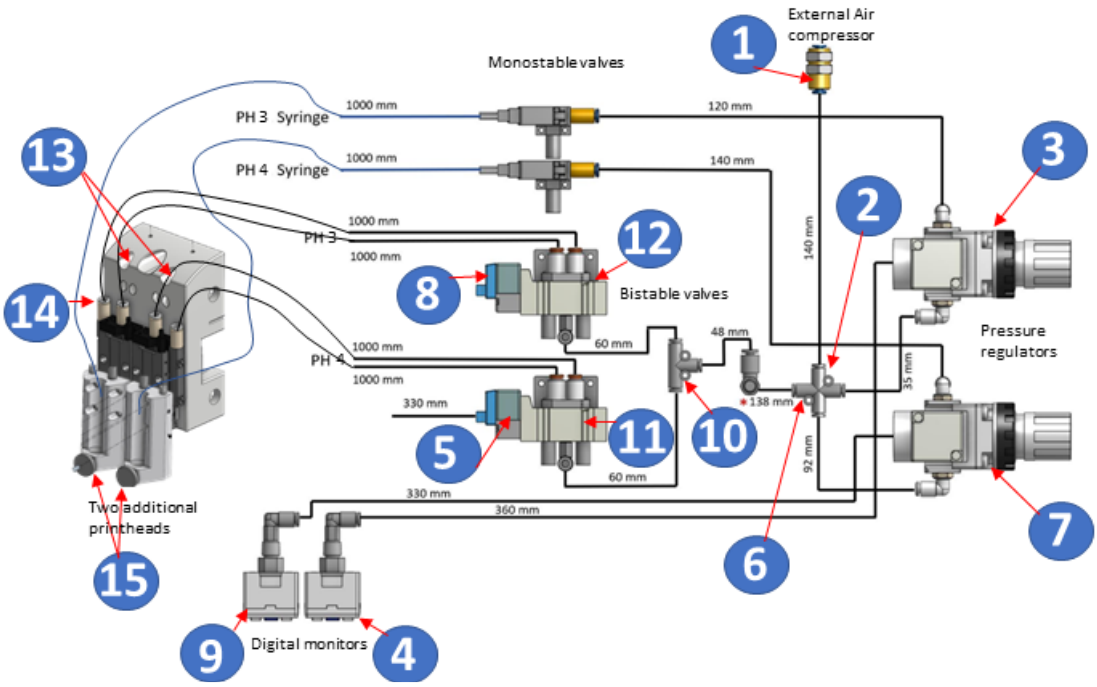

Figure 59 The assembly of machine parts and components incorporated into the commercial 3D bioprinter (Inkredible +) to operate with four printheads simultaneously. Briefly, two additional printheads (15) were incorporated by assembling pressure regulators (3 and 7), pressure sensor coupled with digital monitors (4 and 9), monostable valves (5 and 8), and bistable valves (11 and 12), all connected with plastic hollow tubbing that allowed the flow of pressurized air coming from an external air compressor (1) (Original Work).

We modified the hardware, but we modified electronics and software accordingly to enable the addition of the new components explained previously; changes to the firmware were made mainly to change the functionality of some ports intended to be the heaters on the INKREDIBLE+.

Software modifications.

Torks is a firmware based on Marlin Rep Rap; the firmware modifications included the creation of new variables and M-codes to activate and deactivate the function of the new four electro-valves included in the new configuration.

Changing those ports in the firmware and enabling the function of those ports as outputs to control the mono and bistable valves was necessary to achieve precise control over the material flow in the 3D printing process. By assigning dedicated M-codes to each electro-valve, we could more accurately manage the activation and deactivation sequences, ensuring that the material deposition was both timely and accurate. This was particularly important for complex prints where precise timing and flow control are crucial for the integrity of the final printed construct. Additionally, the modification allowed for greater customization in the printing process, enabling the use of multi-material applications and more intricate designs. This enhancement in the firmware not only improved the overall

functionality of the 3D printer but also expanded its capabilities, paving the way for more innovative and precise 3D printing applications with the use of 4 printheads.

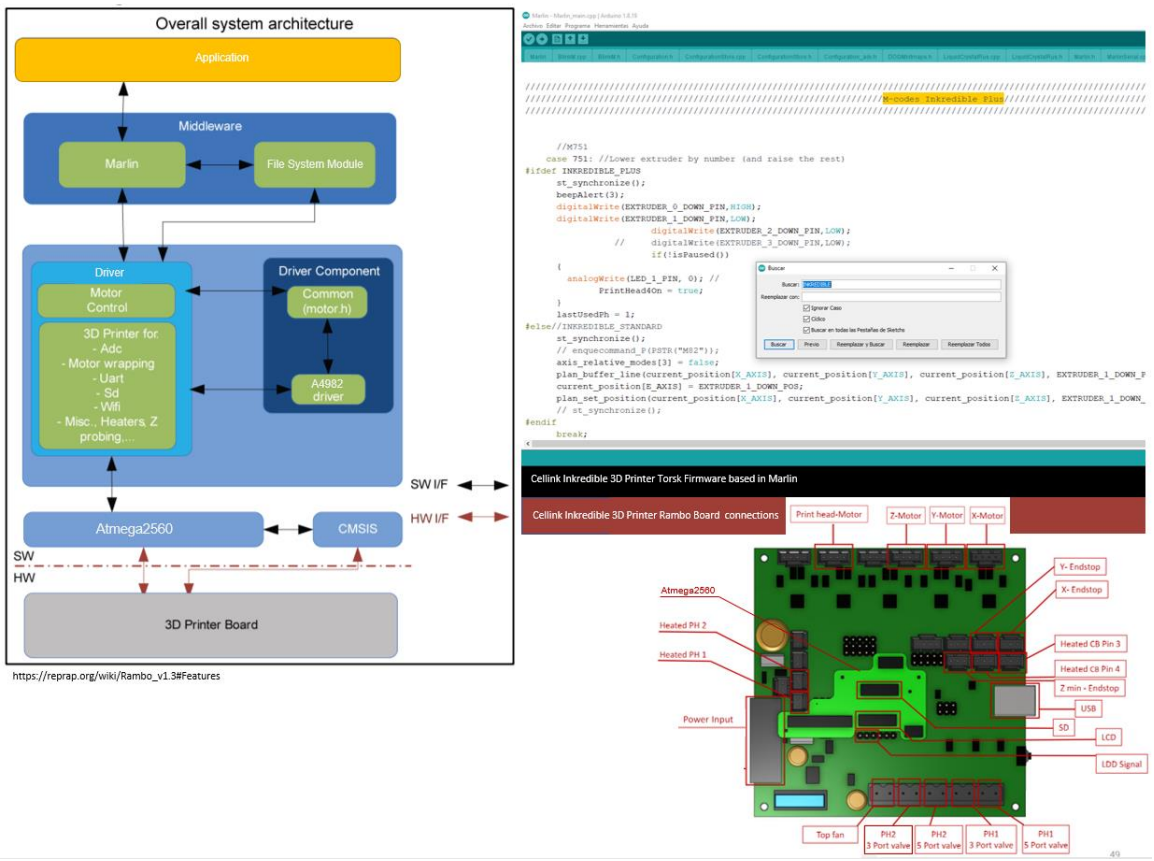

Figure 60 Overall system architecture mother-boar (Rambo v1.3) and integration with Torsk Firmware (Marlin), changes in the firmware replaced ports for heaters and enabled additionally monostable and bistable valves for the configuration of the INKREDIBLE+ with 4 Printheads (Original Work).

From the biomaterial's perspective, the use of fibrin and laminin-based hydrogels feature composition-wise resemblance of the tissue of our interest, their mechanical properties, and structural stability should also be considered for their use in 3D bioprinting with coaxial multilayered nozzles.

Besides biocompatibility and bioactivity, CELLINK FIBRIN and CELLINK LAMININK also display shear-thinning behavior (**Figure. 61.)** and sufficient structural stability upon deposition, thanks to their formulation and cross-linking schemes. Shear-thinning materials experience a decrease in viscosity upon exerting shear stress, which translates into facile flow through a nozzle when extruded. Moreover, in combination with an appropriate nozzle geometry, the shear-thinning behavior of hydrogels has been shown to provide superior

cell survival in EBB applications. [114] Therefore, confirming the suitability of the biomaterial hydrogels employed for bioprinting by evaluating the effect on cell survival using the printing parameters for the proposed four-layered coaxial extrusion system was studied.

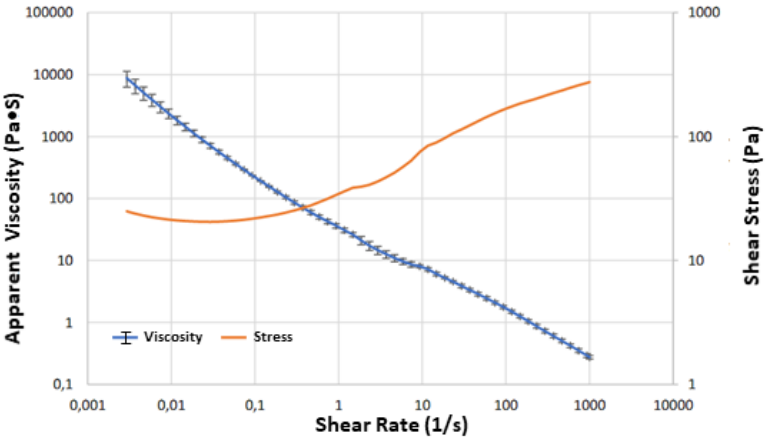

Flow curves of **CELLINK LAMININK** illustrating Apparent Viscosity (Pa.s) Versus Shear Rate (1/s) (blue), and Shear Stress (Pa) versus Shear Rate (1/s) (orange).

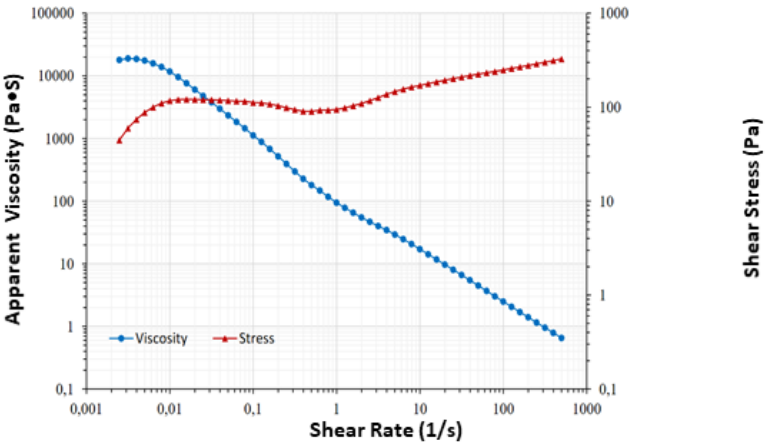

Flow curves of **CELLINK FIBRIN** illustrating Apparent Viscosity (Pa.s) Versus Shear Rate (1/s) (blue), and Shear Stress (Pa) versus Shear Rate (1/s) (red).

Figure 61 Flow curves of CELLINK FIBRIN & LAMININK illustrating Apparent Viscosity (Pa.s) Versus Shear Rate (1/s) and Shear Stress (Pa) versus Shear Rate (1/s) (Cellink Bioprinting).

Moreover, using fibrin for engineering vascular grafts has shown several advantages over other materials. For example, Gui and colleagues developed small-diameter vascular grafts by cultured smooth muscle cells and dermal fibroblasts in a fibrin-based gel under pulsatile stretching [185]. These grafts exhibited strong mechanical properties and remarkable collagen and elastin deposition by the embedded cells, which were features not seen on polyglycolic acid-based grafts embedded with the same cells and cultured under the same conditions. Moreover, the developed fibrin-based grafts were the first polymer-based

engineered vessels to contain mature elastic fibers, and vital muscle tissue components. Smooth muscle cells and fibroblasts worked synergistically to provide functionality to the engineered tissues, demonstrating the advantages of using multicellular approaches.

Although this work achieved sufficient resemblance of the mechanical and biochemical characteristics of the middle and outermost layers of native vessels, **it lacked the endothelium layer,** which we tackled in this paper as we know how critical it is to permit blood flow through engineered vascular tissues [186].

The effect of coaxial system geometry and inlet pressure on cell viability upon deposition was investigated via bioprinting experiments. Given the multilayered structure of native blood vessels and considering that the thickness of each layer varies depending on its function and position across the vascular system, bioprinting strategies must be able to comply with this structural variability. Therefore, we designed and fabricated three different coaxial extrusion systems capable of printing vessel-like structures with varying layer thicknesses (**Table 8**). The layers areas in an individual and added fashion between **Channel (*b).*** (second layer), **Channel (c).** and **Channel (*d)***. (fourth layer) from the developed coaxial systems varied incrementally from 0.33 mm^2 up to 3.93 $mm^{2.}$ **Table 7** shows that these layer areas closely mimic those found in small-diameter native blood vessels [187], [188].

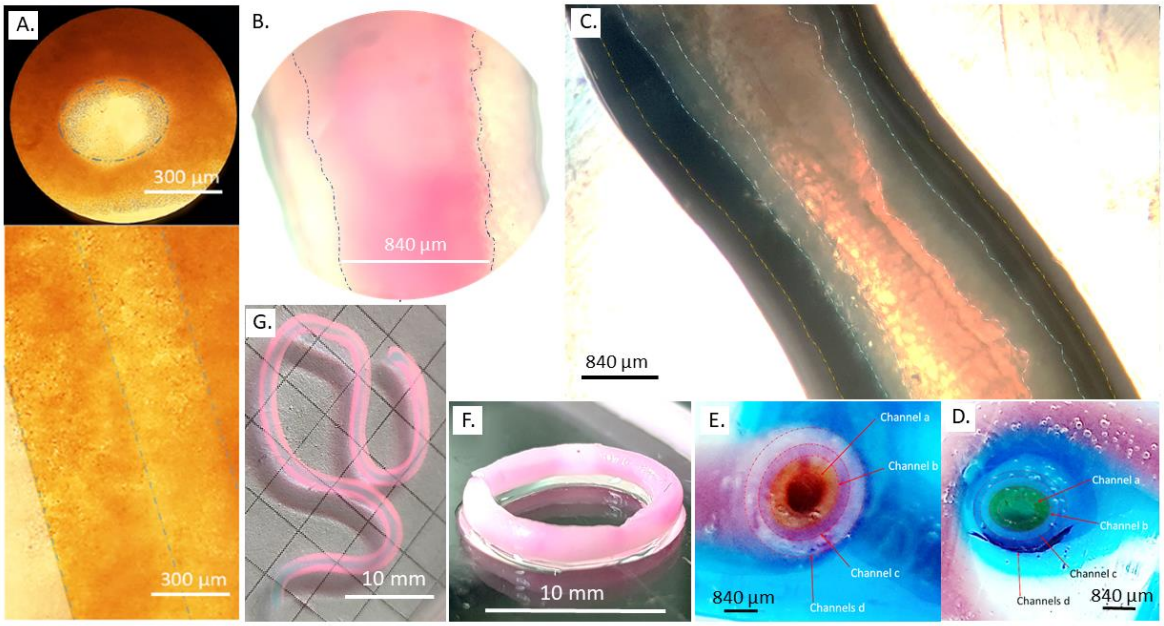

Figure 62 (A) Cannular structure without perfusion and with remanent sacrificial material adhered to the wall surface after submerging in PBS at 37 C° (B) Cannular structure after perfusion with cell medium at 37 C° (C) Cannular structure with Pluronic before washing it out (D) The microscopy image of the bioprinted structure displays the core layer enclosed by blue dashed lines after removing the innermost sacrificial material (E). A transversal view of the cannular structure displays the core layer enclosed by red dashed lines after removing the innermost sacrificial material (F) 3D printed cannular structure perfused with cell media. (G) The long construct was extruded with the coaxial nozzle (Original Work).

Several vessel-like structures were printed in different fashions to demonstrate the functionality and multiple applications of the four-layered coaxial extrusion systems. First, a simple double-layered vessel-like structure was built by direct printing over a flat surface (**Figure 62**). For this, a sacrificial bioink based on Pluronic was printed through the core Channel (a), while a bioink made from alginate was extruded through Channel (b). In addition to facilitating the cross-linking of the alginate-based bioink, a cross-linking solution CELLINK, based on calcium chloride, was deposited parallel through the outer channel. After printing, the resulting cannular structures were submerged in a PBS solution at 37 ºC to dissolve the sacrificial biomaterial completely. Remnants of the sacrificial biomaterial were washed out by perfusing the cannular structure with a cell culture medium at 12 ºC. The resulting hollow cannular structure featured a core diameter of about 300 µm.

Next, a bioreactor assembly was employed to print double- and triple-layered perfusable channels embedded in a biomaterial matrix. This system allows perfusion with an external tubbing system, essential for maturing mid and large-scale bioprinted tissues [189]. (**Figure. 63 A)** shows the bioreactor assembly with the printed double-layered perfusable channels, where the coaxial extrusion system was employed to print the channels inside a hydrogel support bath. (**Figure. 63 B**) shows a close-up of the printed channels after a red dye was perfused through one end. Moreover, the coaxial extrusion system proved to help fabricate interlocked perfusable channels, as depicted in (**Figure. 63 C**). Two independent channels of 0.3 mm and 0.84 mm core diameters were printed in a tangled assembly and perfused with blue and red dye, respectively. (**Figure. 63 D**) The multilayer-like vascular construct was printed using four (4) channels resembling the three layers of vascular tissue. (**Figure. 63 E).**

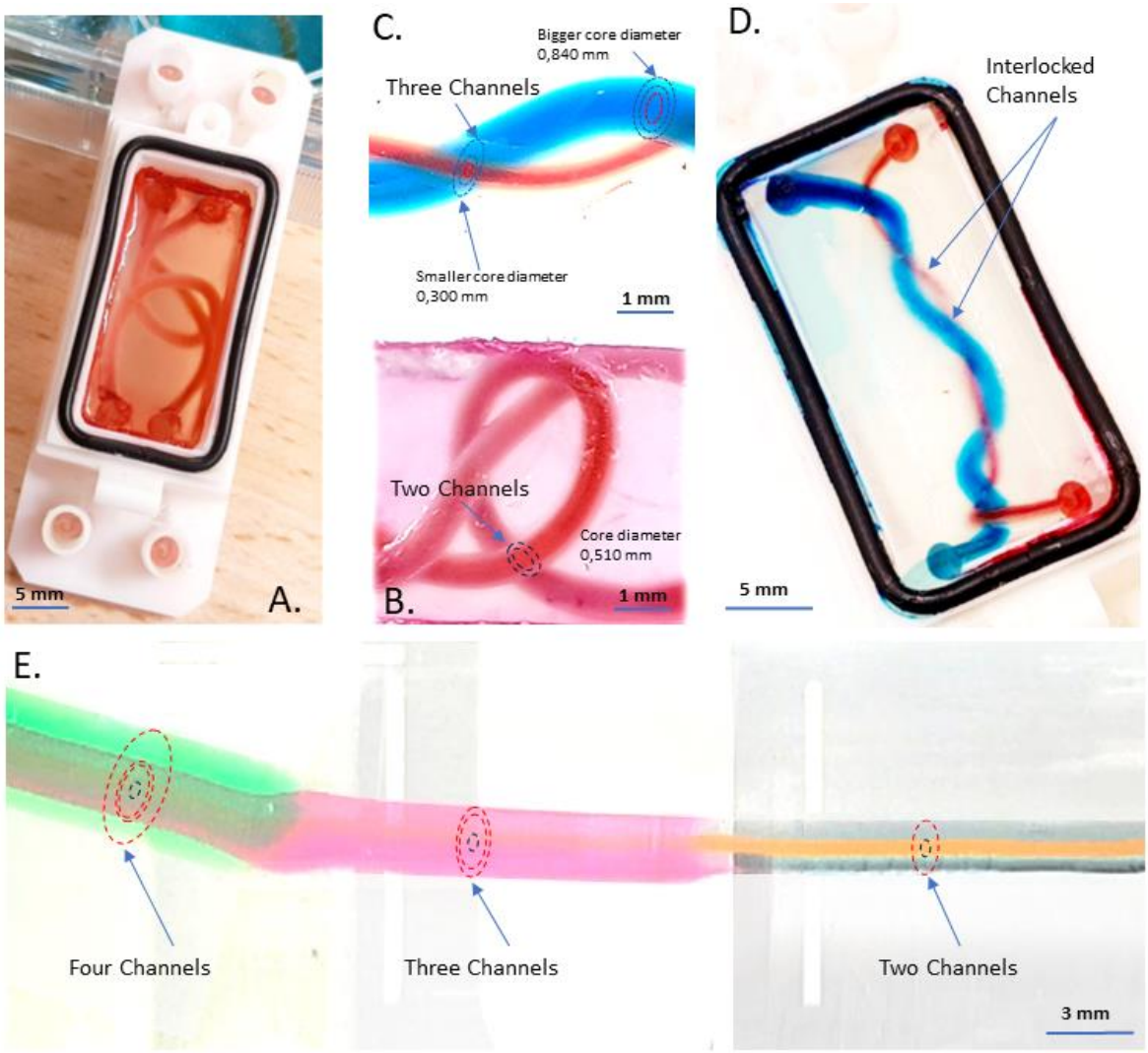

Figure 63 (A) Perfusable channels printed in a support bath inside a vascular bioreactor system and a (B) close-up of the printed cannular structure after perfusing a red dye through one of its ends. (C) Two cannular structures of different diameters are printed within the same bioreactor system, perfused with blue and red dye, and (D) a close-up of the intersecting channels. (E) The multilayer-like vascular construct was printed using four (4) channels resembling the three layers of vascular tissue (Original Work).

Finally, double, and triple-layered vessel-like structures were printed inside a support bath made of CELLINK GELMA, a photocrosslinkable biomaterial based on methacryloyl-modified gelatin. CELLINK PLURONICS was employed for the core channel, as it serves as a sacrificial material that can be washed out to yield a hollow cannular structure. The second, third, and outer layers comprised CELLINK LAMININK+, CELLINK LAMININK-121, and CELLINK FIBRIN, respectively. Before being used for printing with the coaxial extrusion

systems developed, the bioinks were stained with food coloring to help visualize the different layers for the following high-contrast pictures.

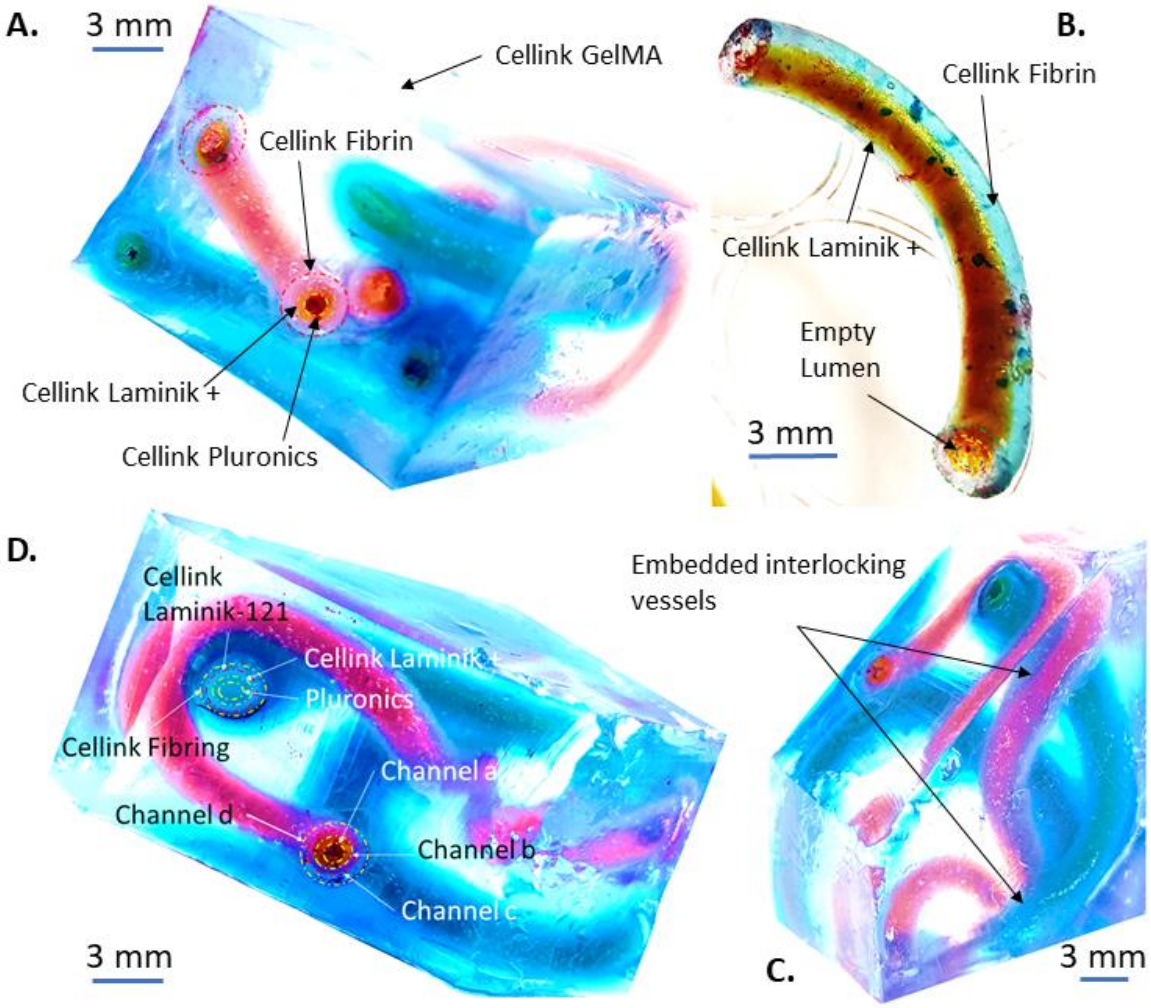

Figure 64 (A) Cannular structures are printed using three materials: CELLINK PLURONIC F127, CELLINK LAMININK+, CELLINK FIBRIN, and embedded in CELLINK GELMA. (B) Cannular structure with two layers innermost of CELLINK LAMININK+, outermost of CELLINK FIBRIN, (C) Embedded 3D printed interlocking vessels in CELLINK GELMA block. (D) Cannular structures are printed using four materials: CELLINK PLURONIC F127, CELLINK LAMININK+, CELLINK LAMININK-121, CELLINK FIBRIN, and embedded in CELLINK GELMA (Original Work).

Results for bioprinted constructs analyzed after bioprinting showed that, for all coaxial system geometries evaluated that use three (3) layers (HFF-1, HUVECs, HASMC) to build the bioprinted vascular structure, cell viability was maintained above 80% when using Standard Extrusion Pressure (SEP) inlet pressures and temperature at 37 °C by using the nozzle temperature management system. (**Figure. 56**). However, a plunge in cell viability was observed for all coaxial system geometries when increasing inlet pressure by +40% and slightly more when not using temperature control at 37 °C.

A two-way ANOVA with Tukey's multiple comparisons test was performed to analyze data. Results from statistical analysis showed that **inlet pressure** was an extremely significant factor affecting cell viability (p-value < 0.0001). The coaxial **nozzle geometry (**diameter area) also showed an extremely significant factor affecting cell viability (p-value < 0.0001). The **change in the temperature** between room temperature (18 °C to 21 °C) and 37 °C was an extremely significant factor affecting cell viability (p-value < 0.0001)., The interaction between **geometry vs. pressure** when the temperature was 18 °C had no quite significant factors (p-value = 0.0606); the interaction between **geometry vs. pressure** when the **temperature was 37** °C had extremely significant factors (p-value = 0.0003); the interaction between **temperature vs. pressure** had a significant factor (p-value = 0.0213), and finally, the interaction between **geometry vs. temperature** had no significant factors (p-value = 0.6844)—**Figure 65 B.**

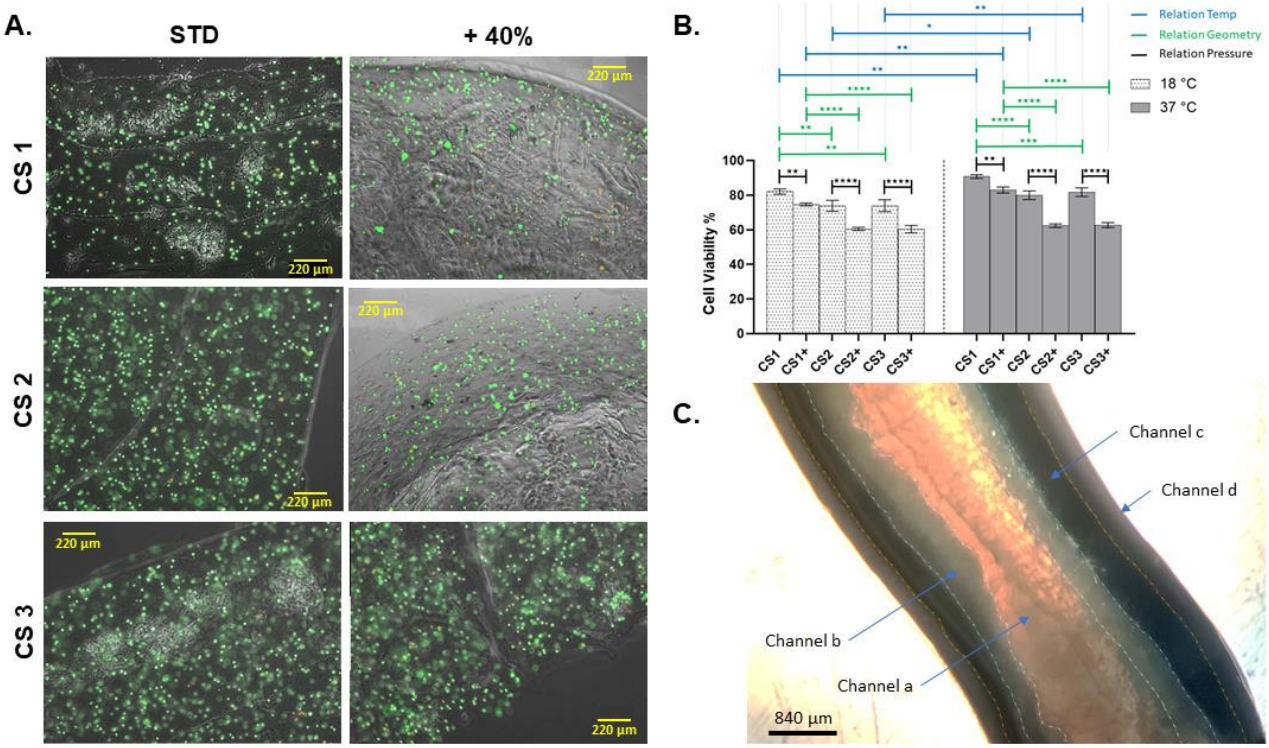

Figure 65 (A) Live/dead assay images of 3D bioprinted triple-layered vessel-like constructs with the three different Coaxial Systems (CS) and varying inlet pressures by 40% on the three channels with cells. (B) Cell viability of constructs immediately after bioprinting using the three designed nozzles and varying inlet pressures by 40%. All nozzle configurations show high cell viability when using Standard Extrusion Pressure (SEP) on the inlets combined with temperature control management at 37 °C. In contrast, viability is compromised when increasing inlets pressure by 40% or when not controlling the nozzle temperature at 37 °C for a specific pressure range. (C) Microscopy image of the bioprinted structure displaying the core layer enclosed by white dashed lines (Channel (*a)*), followed by the inner layer enclosed by white and light blue dashed lines (Channel (*b)*), middle layer enclosed by light blue and yellow dashes lines (Channel (c)), and outer layer enclosed by yellow dashed lines (Channel (*d)*), before removal of the innermost sacrificial biomaterial made of Pluronic (Original Work)..

All results shown in (**Figure. 65**) suggest that the layer area can be tuned at will within the studied range (0.32 to 3.93 mm^2) **Table 7,** with a significant effect on cell viability. In turn, inlet pressure must be carefully set to optimal values to preserve viability, significantly affecting cell viability. This optimal value must be the minimum where the bioink can be deposited as a continuous filament, which ultimately depends on the outlet area and the bioink printability. Although the performed experiments for cell viability do not permit to discriminate between fibroblasts, smooth muscle cells, or endothelial cells, which could have been attractive for collecting further information on the effect of the evaluated parameters on each cell line, the results obtained suggest that none of the cell lines in average were particularly affected by the bioprinting process. The same cell density was used for all bioinks with cells, i.e., CELLINK FIBRIN with HFF human fibroblasts, CELLINK'S LAMININK-121 with smooth muscle cells HASMCs, CELLINK LAMININK+ with HUVECs overall cell viability above 80 % was obtained for two of the three coaxial systems being the third quite close to 80% when using the SEP inlet pressure and temperature nozzle control system. Moreover, previous experiments using a triple-layered coaxial extrusion system but with a different cell line, specifically human bone osteosarcoma cells, MG-63, demonstrated similar viability results (~ 80 %) when bioprinting single-layered tubular structures [22].

Future research should prioritize evaluating cell functionality and biomechanical properties in bioprinted tubular structures. Observing the cell's post-maturation under dynamic culture conditions is essential to assess cell functionality. These conditions, facilitated by peristaltic pump-induced perfusion, closely replicate the native vascular tissue environment, offering valuable insights for the clinical translation of these tissue constructs. While the primary focus of our current research has been to validate the efficacy of the coaxial embedded nonplanar bioprinting technique in maintaining cell viability, a detailed exploration of cell functionality and biomechanical characteristics is beyond this thesis's scope. However, forthcoming studies will address these critical aspects, thereby contributing to this bioprinting technology's broader understanding and application.

4.6 Conclusions

The conclusions presented herein are derived from the findings in **Chapter 3** and serve as **complementary insights**.

The herein-developed four-layered coaxial extrusion systems demonstrated their versatility in bioprinting multilayered cannular structures of varying layer areas. In particular, the diameters of the bioprinted cannular structures cover those found on small-diameter human blood vessels (< 6 mm) [188], [190], and the layer areas of the bioprinted cannular structures varied from 0.33 to 3.93 mm^2, which covers a wide range of layer areas also found on small-diameter human blood vessels [187]. Moreover, the proposed geometry of the coaxial systems showed no detrimental effects on cell viability upon bioprinting with two or three different biomaterial hydrogels and two or three different human cell lines. However, the bioprinting experiments demonstrated the importance of carefully adjusting printing parameters, such as extrusion pressure and nozzle temperature, to optimal values, as these can significantly affect cell viability when using the developed coaxial system. Therefore, parametric analyses should be performed to balance printing parameters and resolution with cell survival.

A change in pressure into a range of 40% does not affect in a considerable proportion the cell viability when the viability value is over 82 % but not lower than 81.69%, finding a breaking limit value at that point, under that percentage, the viability can be decreased significantly by just keeping a difference of pressure of 40%.

The temperature change from room temperature up to 37 °C for the bioinks can favor the cell viability in a significant way when the viability value is over 73.86% but not lower than 73.82 % at room temperature, finding a breaking limit value at that point, over that **percentage, the viability can be increased over 10.62% just by increasing the temperature to 37 °C** reaching a limit of 13.3% for the control sample at human physiological temperature.

The change in pressure affects them in a more significant way the cell viability compared to the way the temperature change can affect cells, even though we can take advantage of

the coaxial nozzle with temperature management control when we need to increase the viability of our constructs by over 10% in a certain specific range as it was explained before.

Developing a **coaxial nozzle with temperature management adds invaluable extra flexibility to the bioprinting field**, as printing with temperature-dependent biomaterials and biologically relevant biomaterials such as GelMA or Collagen is now feasible.

As one of the resulting developments in this research was a multilayered coaxial extrusion nozzle with temperature control management, and we have bioprinted confined GelMA microfluidic devices using a nonplanar 3D print manner with this nozzle, we decided that the best name that fits with this technology should be **DEFECOSUFH** (Device for freeform embedding coaxial of suspended functional hydrogel).

4.7 Applications

According to data from [191], more than 109,000 people are on a life-saving organ transplant waiting list, and every 9 minutes, a person is added to that list. However, only around 39,000 transplants are performed yearly, and more than 17 people die each day waiting for a lifesaving organ transplant [191]. Furthermore, 60 % of US adults are signed up as organ donors, and only three out of 1,000 people die of the lack of organs for donation. It shows that even if 100 % of US adults were signed up as donors, their organs would not be enough to match the ever-growing waiting list. Therefore, public health efforts should not rely solely on increasing the organ donor list but on investigating and developing tissue engineering technologies that can supply the shortage of these organs.

Among tissue engineering technologies, those focused on advanced biomanufacturing techniques have been constantly developed and evaluated over the past 20 years [43]. Their ultimate goal is to recreate *in vitro* personalized organs for transplantation, which is the most straightforward clinical solution for organ malfunction or total failure [192]. Moreover, this strategy would solve one of the main drawbacks of organ transplantation, which is the need for lifelong immunosuppression to avoid immune organ rejection by the receiver [193]. However, creating complex functional organs in the laboratory (such as kidneys, livers, and hearts) is still a significant challenge in bioengineering. It is not expected to be feasible, at least for the next 15 or 20 years. In the meantime, advanced biomanufacturing techniques, which include freeform reversible embedding of suspended hydrogels (FRESH) [93], [115], [124], sacrificial writing into functional tissues (SWIFT) [129], volumetric bioprinting [45], coaxial printing [10], [22], [33], [194] and cell electro writing [195], are altogether taking the field a step closer towards developing functional models of human tissues and organs. Before being used for clinical transplantation, these functional models might first serve as *in vitro* platforms for testing drug efficacy and safety in a personalized manner [196]–[198], as well as for studying disease progression and intercellular interactions within individual tissues.

During the last 30 years, tissue engineers have directed their efforts toward developing suitable vascular substitutes. However, autologous grafts are still the gold standard for

vascular tissue replacement, demonstrating the enormous difficulties faced when fabricating these tissues from scratch *in vitro*.

Coaxial bioprinting has recently been proven to be a critical technology for biofabrication-engineered vascular structures, which is why developing this technology is so important. Coaxial bioprinting has the potential to revolutionize the treatment of cardiovascular disease, as it could enable the creation of personalized and functional replacement blood vessels for patients. It can also be used in developing other tissue engineering applications, such as creating functional tissues such as skin or organ structures. Overall, coaxial bioprinting is a promising technology with the potential to benefit patients and improve healthcare outcomes significantly.

A significant amount of progress has been made in the development of skin models using tissue engineering techniques to date. Although it is still, a limitation in the biofabrication of a full-skin equivalent construct remains despite advances in making skin constructs for clinical applications. (**Figure. 66)** shows the design of skin tissue, including bone baseline with embedded vascular tissue. Native skin consists of three main layers: the epidermis, dermis, and hypodermis; under those structures, the vascularized layer includes the muscle layer, and the deeper layer, in the case of articulation, includes cartilage and bone as the baseline.

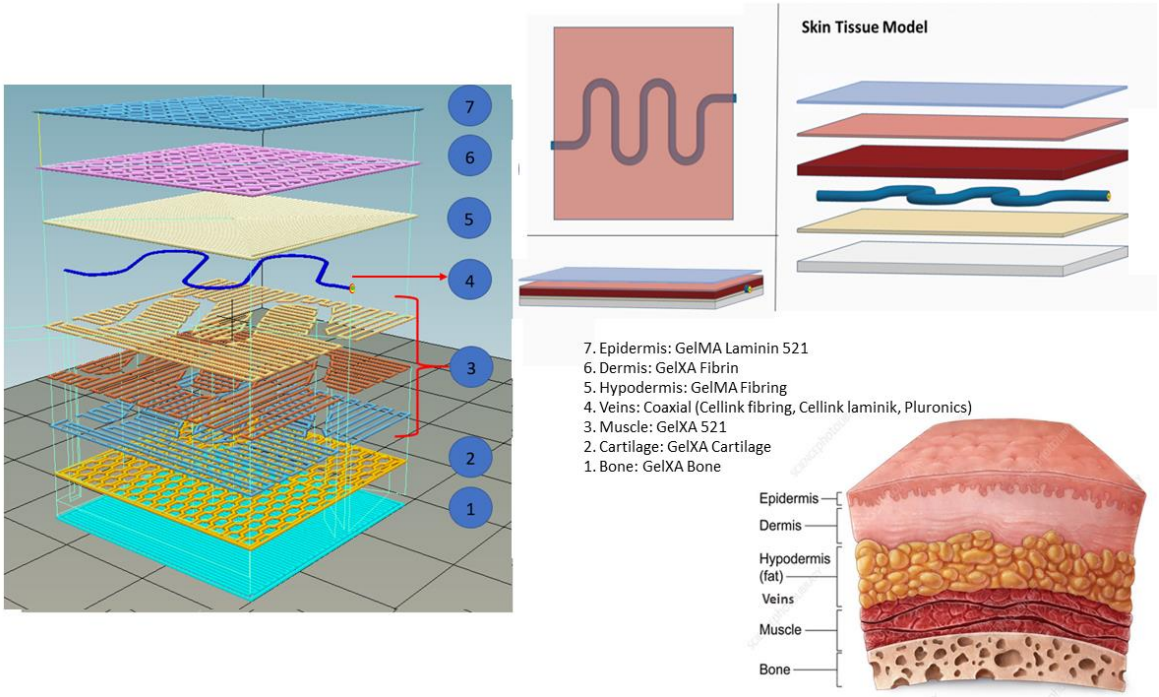

Figure 66 The skin tissue model uses seven layers, including three for the coaxial structure. This model resembles the following layers: (1) Bone, (2) cartilage, (3) muscle, (4) vascular structure (tunica adventitia, tunica intima), (5) Hypodermis, (6) dermis, and finally (7) Epidermis (Original Work) Skin construct adapted from [92].

The coaxial structure in this setup is essential to perfuse the tissue of medium size as it is in the model with the following dimensions: 25 mm depth, 25 mm width, and 3 mm height.

The coaxial serpentine allows the media to reach each scaffold area, increasing the probability of cell survival during the time, weeks, and even months before the potential transplantation.

The initial design and fabrication of the coaxial structure are crucial for ensuring optimal tissue perfusion and media diffusion. The flow rate of the media must be closely monitored and adjusted to ensure proper delivery to the scaffold area.

The geometry of the coaxial serpentine can be modified to optimize perfusion in different tissue types; in this case, the choice of materials used in the coaxial structure can significantly impact the durability and longevity of the scaffold.

Using a coaxial serpentine design can be beneficial in promoting cell growth for improved tissue generation. In the following **(Figure. 67)**, we 3D printed a coaxial design structure

resembling a hypothalamus, then it was photo-crosslinked with UV light and perfused with media.

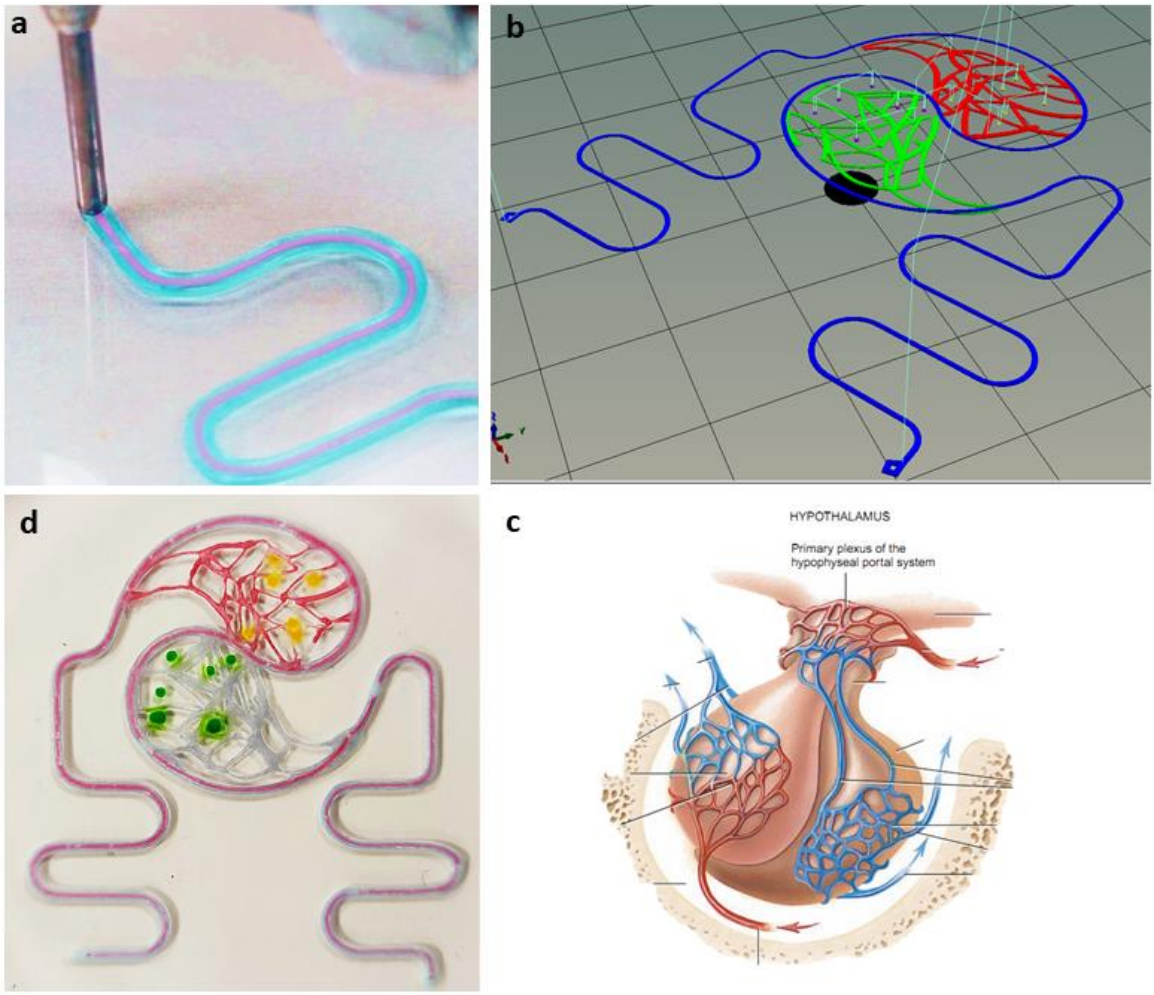

Figure 67 (a) Bioprinting with coaxial nozzle light blue (cannular structure), pink core perfused with media (b) coaxial print designed using G-code to feed a 2D structure resembling a hypothalamus, (c) Full perfused printed structure that resembles the hypothalamus vascular system, (d) Hypothalamus (Original Work), illustration from [199].

The use of the structure, modeled after the hypothalamus, serves as a powerful demonstration of how this strategy can be effectively applied to perfuse medium to large areas of tissue where nutrient delivery is essential for maintaining elevated levels of tissue viability over extended periods.

While 2D structures that are 3D printed and perfused may provide some benefits, it is essential to note that non-planar 3D printed structures more closely replicate the native cellular environment.

To fully explore the potential of this approach, we have implemented the use of microfluidic-embedded coaxial bioprinting techniques to create structures that closely mimic the native tissue environment. **(Figure. 68)** helps to understand this technology as it was explained before as **DEFECOSUFH** (Device for freeform embedding coaxial of suspended functional hydrogel).

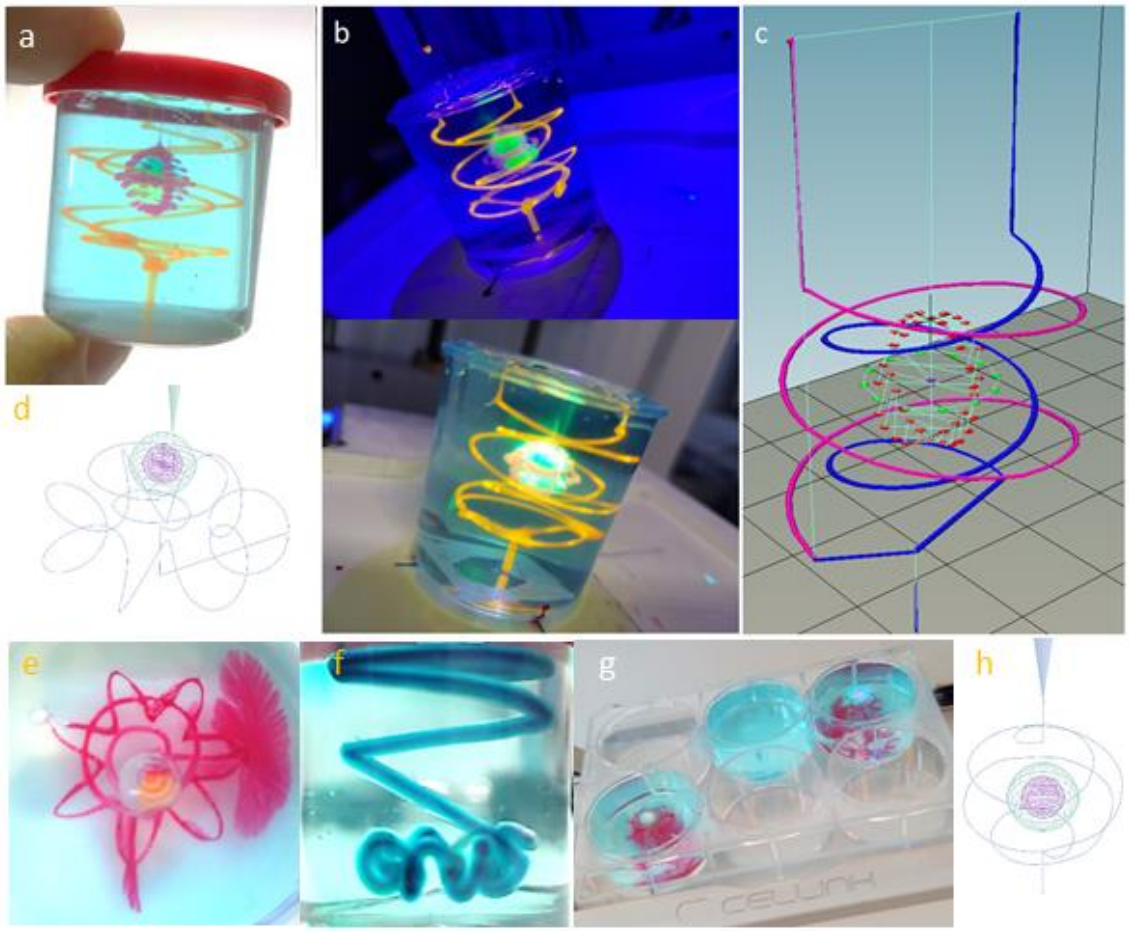

Figure 68. DEFECOSUFH applications (a) Model of organoid fed by diffusion through the spiral vascular structure, create a microfluidic arrangement in 3D, (b) Microfluidic structure under UV light, (c) 3D organoid model. (d) 3D model of organoid surrounded by coaxial microfluidic channel. (f) Nonplanar microfluidic coaxial channel, dark core in red, surrounded with a shell in blue (g) organoids printed inside a six-well plate. (h) 3D model of organoid surrounded by a microfluidic channel (Original Work).

We leveraged coaxial non-planar bioprinting to print a tumoroid within a vascularized channel. The non-planar technique allows for the creation more complex 3D tissue models with variations in curvature or thickness, such as tumoroids, organoids, and even the shapes of the spine and ear. This approach could significantly improve tissue biofabrication in regenerative medicine and the generation of organ models.

Chapter 5

Concluding remarks and future perspectives

The aims of this research are as follows:

- ***To determine the design parameters of a coaxial bioink extruder system to ensure greater cellular viability using the EBB technique.***

- ***To determine*** *computationally the most significant parameters in the design of the extruder system to allow greater cellular viability in contrast to those reported in the revised bibliography.*

- ***To verify*** *experimentally the design parameters of a Bioink coaxial extruder system to manufacture scaffolds with greater cellular viability in contrast to those reported in the revised bibliography*.

Our study successfully achieves its objectives, as evidenced by the thorough exploration and evaluation of various coaxial extrusion systems. These systems have demonstrated their effectiveness in fabricating cell-embedded, multilayered cannular structures, as well as perfusable vascular networks within hydrogels. Notably, **both triple- and four-layered coaxial systems proved highly efficient in the bioprinting process. They consistently maintained cell viability above 80%** across a variety of human cell lines, including osteoblasts, fibroblasts, smooth muscle cells, and endothelial cells. Additionally, these

systems demonstrated versatility in handling multiple biomaterials effectively. These findings collectively affirm the successful fulfillment of our study's aims, marking a significant advancement in the field of bioprinting.

Silico simulations played a pivotal role in optimizing our coaxial extrusion systems. These simulations allowed us to analyze the impact of various geometric parameters, such as diameter, length, and angles, on pressure distribution and velocity during the extrusion process. **Our method for sorting and classifying coaxial nozzle designs, utilizing velocity data from computational fluid dynamics (CFD) tools, emerged as a robust approach. It enabled us to effectively sift through numerous design possibilities, identifying those most conducive to enhancing cell viability during the extrusion process.**

In the experimental phase of our research, we rigorously assessed cell viability using various methods, including live/dead assays, CELLCYTE, and PrestoBlue. These tests were instrumental in verifying the efficacy of the coaxial nozzles selected through **our proposed classification and sorting method using CFD data. The data demonstrated that these chosen design parameters were optimal, consistently yielding high cell viability rates, exceeding 80%. This strong correlation between our nozzle design choices and the achieved cell viability underscores the robustness of our methodology and its potential impact in the field of bioprinting.**

Our findings align with existing research, highlighting that inlet pressure has a more significant impact on shear stress and velocity than the geometry of the nozzle. However, **we found that the internal pressure within the nozzles can be effectively modulated by selecting the appropriate geometrical parameters.** This critical insight was confirmed through the viability results of our bioprinting experiments using human cells, which **demonstrated the efficacy of our optimized methodology in finding the proper geometrical nozzle setups to create coaxial constructs with high viability.**

This considerable progress is highly promising for various bioprinting and tissue engineering applications. It underscores the importance of combining detailed simulations with meticulous design optimization to develop advanced bioprinting technologies. By fine-tuning these parameters, **our study contributes to the evolution of the coaxial**

bioprinting technique, paving the way for more sophisticated and functional tissue constructs with temperature-dependent biomaterials.

One **significant advancement is the development of a multilayered coaxial extrusion nozzle with integrated temperature control intended for embedded bioprinting, named 'DEFECOSUFH' (Device for Freeform Embedding Coaxial of Suspended Functional Hydrogel).** This technology is pivotal in bioprinting temperature-sensitive biomaterials, such as GelMA or Collagen, at an optimal 37 °C, which is crucial for cell viability. The embedded bioprinting approach inherent in this method enables the creation of high-density, viable tissue-like constructs.

Moreover, our study underscores the importance of adjusting printing parameters, such as extrusion pressure and nozzle temperature, for optimal results. The findings suggest that pressure variations have a more pronounced effect on cell viability than temperature changes. However, **temperature management is beneficial for specific cell types and biomaterials at certain viability levels, helping, in some cases, to increase the viability of a construct in more than ten (10) units over the base percentage level.**

In conclusion, this study advances the design of multilayered coaxial extrusion systems for bioprinting, with the **potential to create complex, functional tissue constructs, including small-diameter human blood vessels**. While promising, further research is needed to refine these systems and explore their application in various tissue engineering contexts. The potential for these technologies in drug development, disease modeling, and the creation of artificial organs and microfluidic devices is immense. However, challenges remain, such as ensuring long-term cell viability and the clinical translation of these technologies for human transplantation.

Conflict of interest

All authors declared no conflicts of interest.

Bibliography

[1] S. Pashneh-Tala, S. MacNeil, and F. Claeyssens, “The tissue-engineered vascular graft - Past, present, and future,” *Tissue Eng. - Part B Rev.*, vol. 22, no. 1, pp. 68–100, 2016, doi: 10.1089/ten.teb.2015.0100.

[2] Y. Matsuzaki, K. John, T. Shoji, and T. Shinoka, “The evolution of tissue engineered vascular graft technologies: From preclinical trials to advancing patient care,” *Appl. Sci.*, vol. 9, no. 7, 2019, doi: 10.3390/app9071274.

[3] A. Huertas *et al.*, “Endothelial cell dysfunction: a major player in SARS-CoV-2 infection (COVID-19)?,” *Eur. Respir. J.*, 2020.

[4] Z. Varga *et al.*, “Endothelial cell infection and endotheliitis in COVID-19,” *Lancet*, vol. 395, no. 10234, pp. 1417–1418, 2020, doi: 10.1016/S0140-6736(20)30937-5.

[5] Z. Gu, J. Fu, H. Lin, and Y. He, “Development of 3D bioprinting: From printing methods to biomedical applications,” *Asian J. Pharm. Sci.*, no. xxxx, 2020, doi: 10.1016/j.ajps.2019.11.003.

[6] I. Matai, G. Kaur, A. Seyedsalehi, A. McClinton, and C. T. Laurencin, “Progress in 3D bioprinting technology for tissue/organ regenerative engineering,” *Biomaterials*, vol. 226, no. September 2019, p. 119536, 2020, doi: 10.1016/j.biomaterials.2019.119536.

[7] R. Levato, T. Jungst, R. G. Scheuring, T. Blunk, J. Groll, and J. Malda, “From Shape to Function: The Next Step in Bioprinting,” *Adv. Mater.*, vol. 1906423, 2020, doi: 10.1002/adma.201906423.

[8] T. Jiang, J. G. Munguia-Lopez, S. Flores-Torres, J. Kort-Mascort, and J. M. Kinsella, “Extrusion bioprinting of soft materials: An emerging technique for biological model fabrication,” *Appl. Phys. Rev.*, vol. 6, no. 011310, 2019, doi: 10.1063/1.5059393.

[9] A. Kjar, B. McFarland, K. Mecham, N. Harward, and Y. Huang, “Engineering of tissue constructs using coaxial bioprinting,” *Bioact. Mater.*, vol. 6, no. 2, pp. 460–471, 2021, doi: 10.1016/j.bioactmat.2020.08.020.

[10] G. Gao, J. Y. Park, B. S. Kim, J. Jang, and D. W. Cho, “Coaxial Cell Printing of

Freestanding, Perfusable, and Functional In Vitro Vascular Models for Recapitulation of Native Vascular Endothelium Pathophysiology," *Adv. Healthc. Mater.*, vol. 7, no. 23, pp. 1–12, 2018, doi: 10.1002/adhm.201801102.

[11] Y. Yu, Y. Zhang, J. A. Martin, and I. T. Ozbolat, "Evaluation of cell viability and functionality in vessel-like bioprintable cell-laden tubular channels," *J. Biomech. Eng.*, vol. 135, no. 9, pp. 1–9, 2013, doi: 10.1115/1.4024575.

[12] S. V Murphy and A. Atala, "3D bioprinting of tissues and organs," *Nat. Biotechnol.*, vol. 32, no. 8, pp. 773–785, 2014, doi: 10.1038/nbt.2958.

[13] R. Chang, J. Nam, and W. Sun, "Effects of dispensing pressure and nozzle diameter on cell survival from solid freeform fabrication-based direct cell writing," *Tissue Eng. - Part A.*, vol. 14, no. 1, pp. 41–48, 2008, doi: 10.1089/ten.a.2007.0004.

[14] C. Mandrycky, Z. Wang, K. Kim, and D. H. Kim, "3D bioprinting for engineering complex tissues," *Biotechnol. Adv.*, vol. 34, no. 4, pp. 422–434, 2016, doi: 10.1016/j.biotechadv.2015.12.011.

[15] K. Nair *et al.*, "Characterization of cell viability during bioprinting processes," *Biotechnol. J.*, vol. 4, pp. 1168–1177, 2009, doi: 10.1002/biot.200900004.

[16] K. Nair *et al.*, "Characterization of cell viability during bioprinting processes," *Biotechnol. J.*, vol. 4, pp. 1168–1177, 2009, doi: 10.1002/biot.200900004.

[17] ramé-hart instrument co., "Custom coaxial needle." [Online]. Available: http://www.ramehart.us/custom-coaxial-needle/

[18] S. V Murphy and A. Atala, "3D bioprinting of tissues and organs," *Nat. Biotechnol.*, vol. 32, no. 8, pp. 773–785, 2014, doi: 10.1038/nbt.2958.

[19] F. Pati, J. Gantelius, and H. A. Svahn, "3D Bioprinting of Tissue/Organ Models," *Angew. Chemie - Int. Ed.*, vol. 55, no. 15, pp. 4650–4665, 2016, doi: 10.1002/anie.201505062.

[20] M. A. Heinrich *et al.*, "3D Bioprinting: from Benches to Translational Applications," *Small*, vol. 15, no. 23, pp. 1–47, 2019, doi: 10.1002/smll.201805510.

[21] N. Paxton, W. Smolan, T. Böck, F. Melchels, J. Groll, and T. Jungst, "Proposal to assess printability of bioinks for extrusion-based bioprinting and evaluation of rheological properties governing bioprintability," *Biofabrication*, vol. 9, no. 4, 2017, doi: 10.1088/1758-5090/aa8dd8.

[22] C. Silva, C. J. Cortés-Rodriguez, J. Hazur, S. Reakasame, and A. R. Boccaccini, "Rational design of a triple-layered coaxial extruder system: In silico and in vitro

evaluations directed toward optimizing cell viability," *Int. J. Bioprinting*, vol. 6, no. 4, pp. 1–10, 2020, doi: 10.18063/IJB.V6I4.282.

[23] I. T. Ozbolat and M. Hospodiuk, "Current advances and future perspectives in extrusion-based bioprinting," *Biomaterials*, vol. 76, pp. 321–343, 2016, doi: 10.1016/j.biomaterials.2015.10.076.

[24] K. Hölzl, S. Lin, L. Tytgat, S. Van Vlierberghe, L. Gu, and A. Ovsianikov, "Bioink properties before, during and after 3D bioprinting," *Biofabrication*, vol. 8, no. 3, p. 032002, 2016, doi: 10.1088/1758-5090/8/3/032002.

[25] T. Jungst, W. Smolan, K. Schacht, T. Scheibel, and J. Groll, "Strategies and Molecular Design Criteria for 3D Printable Hydrogels," *Chem. Rev.*, vol. 116, no. 3, pp. 1496–1539, 2016, doi: 10.1021/acs.chemrev.5b00303.

[26] D. Williams, P. Thayer, H. Martinez, E. Gatenholm, and A. Khademhosseini, "A perspective on the physical, mechanical and biological specifications of bioinks and the development of functional tissues in 3D bioprinting," *Bioprinting*, vol. 9, no. March, pp. 19–36, 2018, doi: 10.1016/j.bprint.2018.02.003.

[27] M. Hospodiuk, M. Dey, D. Sosnoski, and I. T. Ozbolat, "The bioink: A comprehensive review on bioprintable materials," *Biotechnol. Adv.*, vol. 35, no. 2, pp. 217–239, 2017, doi: 10.1016/j.biotechadv.2016.12.006.

[28] L. Moroni *et al.*, "Biofabrication strategies for 3D in vitro models and regenerative medicine," *Nat. Rev. Mater.*, vol. 3, no. 5, pp. 21–37, 2018, doi: 10.1038/s41578-018-0006-y.

[29] D. J. Ravnic *et al.*, "Transplantation of Bioprinted Tissues and Organs: Technical and Clinical Challenges and Future Perspectives," *Ann. Surg.*, vol. 266, no. 1, pp. 48–58, 2017, doi: 10.1038/srep24474.

[30] D. Ke and S. V. Murphy, "Current Challenges of Bioprinted Tissues Toward Clinical Translation," *Tissue Eng. - Part B Rev.*, vol. 25, no. 1, pp. 1–13, 2019, doi: 10.1089/ten.teb.2018.0132.

[31] H. W. Kang, S. J. Lee, I. K. Ko, C. Kengla, J. J. Yoo, and A. Atala, "A 3D bioprinting system to produce human-scale tissue constructs with structural integrity," *Nat. Biotechnol.*, vol. 34, no. 3, pp. 312–319, 2016, doi: 10.1038/nbt.3413.

[32] T. Distler, F. Ruther, A. R. Boccaccini, and R. Detsch, "Development of 3D Biofabricated Cell Laden Hydrogel Vessels and a Low-Cost Desktop Printed Perfusion Chamber for In Vitro Vessel Maturation," *Macromol. Biosci.*, vol. 19, no.

9, 2019, doi: 10.1002/mabi.201900245.

[33] W. Jia *et al.*, “Direct 3D bioprinting of perfusable vascular constructs using a blend bioink,” *Biomaterials*, vol. 106, pp. 58–68, 2016, doi: 10.1016/j.biomaterials.2016.07.038.

[34] W. Peng, P. Datta, B. Ayan, V. Ozbolat, D. Sosnoski, and I. T. Ozbolat, “3D bioprinting for drug discovery and development in pharmaceutics,” *Acta Biomater.*, vol. 57, pp. 26–46, 2017, doi: 10.1016/j.actbio.2017.05.025.

[35] K. Duval *et al.*, “Modeling Physiological Events in 2D vs. 3D Cell Culture,” *Physiology*, vol. 32, no. 4, pp. 266–277, 2017, doi: 10.1152/physiol.00036.2016.

[36] Y. Ai, F. Zhang, C. Wang, R. Xie, and Q. Liang, “Recent progress in lab-on-a-chip for pharmaceutical analysis and pharmacological/toxicological test,” *TrAC - Trends Anal. Chem.*, vol. 117, pp. 215–230, 2019, doi: 10.1016/j.trac.2019.06.026.

[37] J. Groll *et al.*, “Biofabrication: Reappraising the definition of an evolving field,” *Biofabrication*, vol. 8, no. 1, 2016, doi: 10.1088/1758-5090/8/1/013001.

[38] L. Moroni *et al.*, “Biofabrication: A Guide to Technology and Terminology,” *Trends Biotechnol.*, vol. 36, no. 4, pp. 384–402, 2018, doi: 10.1016/j.tibtech.2017.10.015.

[39] J. Li, C. Wu, P. K. Chu, and M. Gelinsky, “3D printing of hydrogels: Rational design strategies and emerging biomedical applications,” *Mater. Sci. Eng. R Reports*, vol. 140, p. 100543, 2020, doi: 10.1016/j.mser.2020.100543.

[40] J. Malda *et al.*, “25th anniversary article: Engineering hydrogels for biofabrication,” *Adv. Mater.*, vol. 25, no. 36, pp. 5011–5028, 2013, doi: 10.1002/adma.201302042.

[41] F. L. C. Morgan, L. Moroni, and M. B. Baker, “Dynamic Bioinks to Advance Bioprinting,” *Adv. Healthc. Mater.*, vol. 9, no. 15, 2020, doi: 10.1002/adhm.201901798.

[42] M. Habibi, S. Foroughi, V. Karamzadeh, and M. Packirisamy, “Direct sound printing,” *Nat. Commun.*, vol. 13, no. 1, pp. 1–11, 2022, doi: 10.1038/s41467-022-29395-1.

[43] P. Thayer, H. Martinez, and E. Gatenholm, “History and Trends of 3D Bioprinting,” in *3D Bioprinting: Principles and Protocols*, J. M. Crook, Ed., Humana Press, 2020, pp. 3–18. doi: 10.1007/978-1-0716-0520-2_7.

[44] K. S. Lim, J. H. Galarraga, X. Cui, G. C. J. Lindberg, J. A. Burdick, and T. B. F. Woodfield, “Fundamentals and Applications of Photo-Cross-Linking in Bioprinting,” *Chem. Rev.*, 2020, doi: 10.1021/acs.chemrev.9b00812.

[45] P. N. Bernal *et al.*, “Volumetric Bioprinting of Complex Living-Tissue Constructs

within Seconds," *Adv. Mater.*, vol. 31, no. 42, 2019, doi: 10.1002/adma.201904209.

[46] S. Ji and M. Guvendiren, "Recent Advances in Bioink Design for 3D Bioprinting of Tissues and Organs," *Front. Bioeng. Biotechnol.*, vol. 5, no. April, pp. 1–8, 2017, doi: 10.3389/fbioe.2017.00023.

[47] A. Ribeiro *et al.*, "Assessing bioink shape fidelity to aid material development in 3D bioprinting," *Biofabrication*, vol. 10, 2018, doi: 10.1088/1758-5090/aa90e2.

[48] S. Kyle, Z. M. Jessop, A. Al-Sabah, and I. S. Whitaker, "'Printability'' of Candidate Biomaterials for Extrusion Based 3D Printing: State-of-the-Art,'" *Adv. Healthc. Mater.*, vol. 6, no. 16, pp. 1–16, 2017, doi: 10.1002/adhm.201700264.

[49] L. Ouyang, R. Yao, Y. Zhao, and W. Sun, "Effect of bioink properties on printability and cell viability for 3D bioplotting of embryonic stem cells," *Biofabrication*, vol. 8, no. 3, p. 35020, Sep. 2016, doi: 10.1088/1758-5090/8/3/035020.

[50] Y. He, F. Yang, H. Zhao, Q. Gao, B. Xia, and J. Fu, "Research on the printability of hydrogels in 3D bioprinting," *Sci. Rep.*, vol. 6, no. 1, p. 29977, 2016, doi: 10.1038/srep29977.

[51] J. H. Y. Chung *et al.*, "Bio-ink properties and printability for extrusion printing living cells," *Biomater. Sci.*, vol. 1, no. 7, pp. 763–773, 2013, doi: 10.1039/C3BM00012E.

[52] N. Diamantides *et al.*, "Correlating rheological properties and printability of collagen bioinks: The effects of riboflavin photocrosslinking and pH," *Biofabrication*, vol. 9, no. 3, p. 34102, 2017, doi: 10.1088/1758-5090/aa780f.

[53] A. S. Theus *et al.*, "Bioprintability: Physiomechanical and biological requirements of materials for 3d bioprinting processes," *Polymers (Basel).*, vol. 12, no. 10, pp. 1–19, 2020, doi: 10.3390/polym12102262.

[54] A. Blaeser, D. F. Duarte Campos, U. Puster, W. Richtering, M. M. Stevens, and H. Fischer, "Controlling Shear Stress in 3D Bioprinting is a Key Factor to Balance Printing Resolution and Stem Cell Integrity," *Adv. Healthc. Mater.*, vol. 5, no. 3, pp. 326–333, 2016, doi: 10.1002/adhm.201500677.

[55] J. Cheng *et al.*, "Rheological properties of cell-hydrogel composites extruding through small-diameter tips," *J. Manuf. Sci. Eng. Trans. ASME*, vol. 130, no. 2, pp. 0210141–0210145, 2008, doi: 10.1115/1.2896215.

[56] M. Khatibi, N. Potokin, and W. Time, "Experimental investigation of effect of salts on rheological properties of non- Difference during Polymer Melt Extrusion Flows Newtonian," vol. 24, pp. 53–57, 2016.

[57] A. Skardal *et al.*, “A hydrogel bioink toolkit for mimicking native tissue biochemical and mechanical properties in bioprinted tissue constructs,” *Acta Biomater.*, vol. 25, pp. 24–34, 2015, doi: 10.1016/j.actbio.2015.07.030.

[58] B. A. Aguado, W. Mulyasasmita, J. Su, K. J. Lampe, and S. C. Heilshorn, “Improving viability of stem cells during syringe needle flow through the design of hydrogel cell carriers,” *Tissue Eng. - Part A*, vol. 18, no. 7–8, pp. 806–815, 2012, doi: 10.1089/ten.tea.2011.0391.

[59] D. Malagón-Romero, N. Hernández, C. Cardozo, and R. D. Godoy-Silva, “Rheological characterization of a gel produced using human blood plasma and alginate mixtures,” *J. Mech. Behav. Biomed. Mater.*, vol. 34, pp. 171–180, 2014, doi: 10.1016/j.jmbbm.2014.02.012.

[60] P. Gatenholm *et al.*, “3D Printing and Biofabrication,” *3D Print. Biofabrication*, no. May, 2018, doi: 10.1007/978-3-319-45444-3.

[61] A. E. Lecturer, “Navier-Stokes Equations,” 2013.

[62] A. Malekpour and X. Chen, “Printability and Cell Viability in Extrusion-Based Bioprinting from Experimental, Computational, and Machine Learning Views,” *J. Funct. Biomater.*, vol. 13, no. 2, 2022, doi: 10.3390/jfb13020040.

[63] W. Liu *et al.*, “Extrusion Bioprinting of Shear-Thinning Gelatin Methacryloyl Bioinks,” *Adv. Healthc. Mater.*, vol. 6, no. 12, pp. 1–11, 2017, doi: 10.1002/adhm.201601451.

[64] T. Camp and R. Figliola, “Fluid mechanics,” *Mechanobiol. Handb.*, pp. 23–44, 2011, doi: 10.2478/jtam-2013-0011.

[65] J. D. Ferry, “Viscoelastic properties of polymers, 3rd edition,” *Wiley, New York*. p. 672, 1980. [Online]. Available: https://www.wiley.com/en-sg/Viscoelastic+Properties+of+Polymers%2C+3rd+Edition-p-9780471048947

[66] E. Celik, *6 Bioprinting, Modeling In Vitro Tissues and Organs Using Tissue-Specific Bioinks*. 2020. doi: 10.1515/9781501518782-006.

[67] H. Q. Xu, J. C. Liu, Z. Y. Zhang, and C. X. Xu, “A review on cell damage, viability, and functionality during 3D bioprinting,” *Mil. Med. Res.*, vol. 9, no. 1, pp. 1–15, 2022, doi: 10.1186/s40779-022-00429-5.

[68] S. Kapur, D. J. Baylink, and K. H. W. Lau, “Fluid flow shear stress stimulates human osteoblast proliferation and differentiation through multiple interacting and competing signal transduction pathways,” *Bone*, vol. 32, no. 3, pp. 241–251, 2003, doi: 10.1016/S8756-3282(02)00979-1.

[69] R. C. Riddle, A. F. Taylor, D. C. Genetos, and H. J. Donahue, “MAP kinase and calcium signaling mediate fluid flow-induced human mesenchymal stem cell proliferation,” *Am. J. Physiol. - Cell Physiol.*, vol. 290, no. 3, pp. 776–785, 2006, doi: 10.1152/ajpcell.00082.2005.

[70] M. E. Cooke and D. H. Rosenzweig, “The rheology of direct and suspended extrusion bioprinting,” *APL Bioeng.*, vol. 5, no. 1, 2021, doi: 10.1063/5.0031475.

[71] M. Mollet, N. Ma, Y. Zhao, R. Brodkey, R. Taticek, and J. J. Chalmers, “Bioprocess equipment: Characterization of energy dissipation rate and its potential to damage cells,” *Biotechnol. Prog.*, vol. 20, no. 5, pp. 1437–1448, 2004, doi: 10.1021/bp0498488.

[72] J. Y.-T. K. Ming-Ju Chen, Kreuter, “Acute Hydrodynamic Forces and Apoptosis: A Complex Question,” *J. Anat.*, vol. 189 (Pt 3, no. Ii, pp. 503–505, 1996, doi: 10.1002/bit.

[73] G. Cidonio, M. Glinka, J. I. Dawson, and R. O. C. Oreffo, “The cell in the ink: Improving biofabrication by printing stem cells for skeletal regenerative medicine,” *Biomaterials*, vol. 209, pp. 10–24, 2019, doi: 10.1016/j.biomaterials.2019.04.009.

[74] X. Zhou *et al.*, “3D Bioprinting a Cell-Laden Bone Matrix for Breast Cancer Metastasis Study,” *ACS Appl. Mater. Interfaces*, vol. 8, no. 44, pp. 30017–30026, 2016, doi: 10.1021/acsami.6b10673.

[75] B. Journal, “Bioactive nanoparticles stimulate bone tissue formation in bioprinted three-dimensional scaffold and human mesenchymal stem cells,” pp. 1–23, 2014, doi: 10.1002/biot.201400305.Submitted.

[76] D. Nguyen *et al.*, “Cartilage Tissue Engineering by the 3D Bioprinting of iPS Cells in a Nanocellulose/Alginate Bioink,” *Sci. Rep.*, vol. 7, no. 1, pp. 1–10, 2017, doi: 10.1038/s41598-017-00690-y.

[77] A. Faulkner-Jones *et al.*, “Bioprinting of human pluripotent stem cells and their directed differentiation into hepatocyte-like cells for the generation of mini-livers in 3D,” *Biofabrication*, vol. 7, no. 4, p. 44102, 2015, doi: 10.1088/1758-5090/7/4/044102.

[78] Q. Ramadan and M. Zourob, “3D Bioprinting at the Frontier of Regenerative Medicine, Pharmaceutical, and Food Industries,” *Front. Med. Technol.*, vol. 2, no. January, pp. 1–19, 2020, doi: 10.3389/fmedt.2020.607648.

[79] Y.-J. Choi *et al.*, “3D Cell Printing of Functional Skeletal Muscle Constructs Using

Skeletal Muscle-Derived Bioink," *Adv. Healthc. Mater.*, vol. 5, no. 20, pp. 2636–2645, Oct. 2016, doi: 10.1002/adhm.201600483.

[80] N. Cubo *et al.*, "3D bioprinting of functional human skin: production and in vivo analysis," *Biofabrication*, vol. 9, no. 1, p. 015006, 2016, doi: 10.1088/1758-5090/9/1/015006.

[81] W. Peng, P. Datta, B. Ayan, V. Ozbolat, D. Sosnoski, and I. T. Ozbolat, "3D bioprinting for drug discovery and development in pharmaceutics," *Acta Biomater.*, vol. 57, pp. 26–46, 2017, doi: 10.1016/j.actbio.2017.05.025.

[82] A. Dick, B. Bhandari, and S. Prakash, "3D printing of meat," *Meat Sci.*, vol. 153, no. September 2018, pp. 35–44, 2019, doi: 10.1016/j.meatsci.2019.03.005.

[83] J. S. Huh, H. G. Byun, H. C. Lau, and G. J. Lim, "Biosensor and bioprinting," in *Essentials of 3D Biofabrication and Translation*, Elsevier Inc., 2015, pp. 215–227. doi: 10.1016/B978-0-12-800972-7.00012-8.

[84] S. Santoni, S. G. Gugliandolo, M. Sponchioni, D. Moscatelli, and B. M. Colosimo, "3D bioprinting: current status and trends—a guide to the literature and industrial practice," *Bio-Design Manuf.*, vol. 5, no. 1, pp. 14–42, 2022, doi: 10.1007/s42242-021-00165-0.

[85] M. Pohanka and P. Skládal, "Electrochemical biosensors - Principles and applications," *J. Appl. Biomed.*, vol. 6, no. 2, pp. 57–64, 2008, doi: 10.32725/jab.2008.008.

[86] Q. Liu, C. Wu, H. Cai, N. Hu, J. Zhou, and P. Wang, "Cell-based biosensors and their application in biomedicine," *Chem. Rev.*, vol. 114, no. 12, pp. 6423–6461, 2014, doi: 10.1021/cr2003129.

[87] N. Vermeulen, G. Haddow, T. Seymour, A. Faulkner-Jones, and W. Shu, "3D bioprint me: A socioethical view of bioprinting human organs and tissues," *J. Med. Ethics*, vol. 43, no. 9, pp. 618–624, 2017, doi: 10.1136/medethics-2015-103347.

[88] N. B. Robinson *et al.*, "The current state of animal models in research: A review," *Int. J. Surg.*, vol. 72, no. August, pp. 9–13, 2019, doi: 10.1016/j.ijsu.2019.10.015.

[89] A. Akhtar, "The Flaws and Human Harms of Animal Experimentation," *Cambridge Q. Healthc. Ethics*, vol. 24, no. 4, pp. 407–419, 2015, doi: 10.1017/S0963180115000079.

[90] M. M. Rojas-Downing, A. P. Nejadhashemi, T. Harrigan, and S. A. Woznicki, "Climate change and livestock: Impacts, adaptation, and mitigation," *Clim. Risk Manag.*, vol. 16, pp. 145–163, 2017, doi: 10.1016/j.crm.2017.02.001.

[91] J. Vanderburgh, J. A. Sterling, and S. A. Guelcher, “3D Printing of Tissue Engineered Constructs for In Vitro Modeling of Disease Progression and Drug Screening,” *Ann. Biomed. Eng.*, vol. 45, no. 1, pp. 164–179, 2017, doi: 10.1007/s10439-016-1640-4.

[92] M. Albanna *et al.*, “In Situ Bioprinting of Autologous Skin Cells Accelerates Wound Healing of Extensive Excisional Full-Thickness Wounds,” *Sci. Rep.*, vol. 9, no. 1, pp. 1–15, 2019, doi: 10.1038/s41598-018-38366-w.

[93] T. J. Hinton *et al.*, “Three-dimensional printing of complex biological structures by freeform reversible embedding of suspended hydrogels,” *Sci. Adv.*, vol. 1, no. 9, 2015, doi: 10.1126/sciadv.1500758.

[94] H. Ravanbakhsh, V. Karamzadeh, G. Bao, L. Mongeau, D. Juncker, and Y. S. Zhang, “Emerging Technologies in Multi-Material Bioprinting,” *Adv. Mater.*, vol. 33, no. 49, pp. 1–38, 2021, doi: 10.1002/adma.202104730.

[95] M. Costantini, C. Colosi, W. Święszkowski, and A. Barbetta, “Co-axial wet-spinning in 3D bioprinting: State of the art and future perspective of microfluidic integration,” *Biofabrication*, vol. 11, no. 1, 2019, doi: 10.1088/1758-5090/aae605.

[96] X. Dai *et al.*, “Coaxial 3D bioprinting of self-assembled multicellular heterogeneous tumor fibers,” *Sci. Rep.*, vol. 7, no. 1, pp. 1–12, 2017, doi: 10.1038/s41598-017-01581-y.

[97] L. Ouyang, C. B. Highley, W. Sun, and J. A. Burdick, “A Generalizable Strategy for the 3D Bioprinting of Hydrogels from Nonviscous Photo-crosslinkable Inks,” *Adv. Mater.*, vol. 29, no. 8, 2017, doi: 10.1002/adma.201604983.

[98] S. Hong, J. S. Kim, B. Jung, C. Won, and C. Hwang, “Coaxial bioprinting of cell-laden vascular constructs using a gelatin-tyramine bioink,” *Biomater. Sci.*, vol. 7, no. 11, pp. 4578–4587, 2019, doi: 10.1039/c8bm00618k.

[99] Y. Zhang *et al.*, “3D Composite Bioprinting for Fabrication of Artificial Biological Tissues,” *Int. J. Bioprinting*, vol. 7, no. 1, pp. 7–20, 2021, doi: 10.18063/ijb.v7i1.299.

[100] Y. S. Zhang, M. Duchamp, R. Oklu, L. W. Ellisen, R. Langer, and A. Khademhosseini, “Bioprinting the Cancer Microenvironment,” *ACS Biomater. Sci. Eng.*, vol. 2, no. 10, pp. 1710–1721, 2016, doi: 10.1021/acsbiomaterials.6b00246.

[101] P. Zhao, H. Jiang, H. Pan, K. Zhu, and W. Chen, “Biodegradable fibrous scaffolds composed of gelatin coated poly(e-caprolactone) prepared by coaxial

electrospinning," *J. Biomed. Mater. Res. Part A*, vol. 79, no. 4, pp. 963–73, 2006, doi: 10.1002/jbm.a.

[102] G. H. Kim, T. Min, S. A. Park, and W. D. Kim, "Coaxially electrospun micro/nanofibrous poly(ε-caprolactone)/eggshell- protein scaffold," *Bioinspiration and Biomimetics*, vol. 3, no. 1, 2008, doi: 10.1088/1748-3182/3/1/016006.

[103] Y. Zhang, Y. Yu, and I. T. Ozbolat, "Direct bioprinting of vessel-like tubular microfluidic channels," *J. Nanotechnol. Eng. Med.*, vol. 4, no. 2, pp. 1–7, 2013, doi: 10.1115/1.4024398.

[104] Q. Pi *et al.*, "Digitally Tunable Microfluidic Bioprinting of Multilayered Cannular Tissues," *Adv. Mater.*, vol. 30, no. 43, pp. 1–10, 2018, doi: 10.1002/adma.201706913.

[105] Q. Gao *et al.*, "3D Bioprinting of Vessel-like Structures with Multilevel Fluidic Channels," *ACS Biomater. Sci. Eng.*, vol. 3, no. 3, pp. 399–408, 2017, doi: 10.1021/acsbiomaterials.6b00643.

[106] G. Gao *et al.*, "Tissue Engineered Bio-Blood-Vessels Constructed Using a Tissue-Specific Bioink and 3D Coaxial Cell Printing Technique: A Novel Therapy for Ischemic Disease," *Adv. Funct. Mater.*, vol. 27, no. 33, pp. 1–12, 2017, doi: 10.1002/adfm.201700798.

[107] Q. Gao, Y. He, J. zhong Fu, A. Liu, and L. Ma, "Coaxial nozzle-assisted 3D bioprinting with built-in microchannels for nutrients delivery," *Biomaterials*, vol. 61, pp. 203–215, 2015, doi: 10.1016/j.biomaterials.2015.05.031.

[108] J. Schöneberg *et al.*, "Engineering biofunctional in vitro vessel models using a multilayer bioprinting technique," *Sci. Rep.*, vol. 8, no. 1, pp. 1–13, 2018, doi: 10.1038/s41598-018-28715-0.

[109] Z. Sun *et al.*, "Three-Dimensional Bioprinting in Cardiovascular Disease: Current Status and Future Directions," *Biomolecules*, vol. 13, no. 8, 2023, doi: 10.3390/biom13081180.

[110] C. M. Hwang *et al.*, "Controlled cellular orientation on PLGA microfibers with defined diameters," *Biomed. Microdevices*, vol. 11, no. 4, pp. 739–746, 2009, doi: 10.1007/s10544-009-9287-7.

[111] R. Xie, W. Zheng, L. Guan, Y. Ai, and Q. Liang, "Engineering of Hydrogel Materials with Perfusable Microchannels for Building Vascularized Tissues," *Small*, vol. 16, no. 15, pp. 1–17, 2020, doi: 10.1002/smll.201902838.

[112] L. Shao *et al.*, "Fiber-Based Mini Tissue with Morphology-Controllable GelMA

Microfibers," *Small*, vol. 14, no. 44, pp. 1–8, 2018, doi: 10.1002/smll.201802187.

[113] Q. Ma *et al.*, "Cell-Inspired All-Aqueous Microfluidics: From Intracellular Liquid–Liquid Phase Separation toward Advanced Biomaterials," *Adv. Sci.*, vol. 7, no. 7, 2020, doi: 10.1002/advs.201903359.

[114] C. Loebel, C. B. Rodell, M. H. Chen, and J. A. Burdick, "Shear-thinning and self-healing hydrogels as injectable therapeutics and for 3D-printing," *Nat. Protoc.*, vol. 12, no. 8, pp. 1521–1541, 2017, doi: 10.1038/nprot.2017.053.

[115] A. Lee *et al.*, "3D bioprinting of collagen to rebuild components of the human heart," *Science (80-.).*, vol. 365, no. 6452, pp. 482–487, 2019, doi: 10.1126/science.aav9051.

[116] C. B. Highley, C. B. Rodell, and J. A. Burdick, "Direct 3D Printing of Shear-Thinning Hydrogels into Self-Healing Hydrogels," *Adv. Mater.*, vol. 27, no. 34, pp. 5075–5079, 2015, doi: 10.1002/adma.201501234.

[117] S. Ricard-Blum, "The Collagen Family," *Cold Spring Harb. Perspect. Biol.*, vol. 3, no. 1, pp. 1–19, 2011, doi: 10.1101/cshperspect.a004978.

[118] T. J. Hinton *et al.*, "Three-dimensional printing of complex biological structures by freeform reversible embedding of suspended hydrogels," *Sci. Adv.*, vol. 1, no. 9, p. e1500758, 2015, doi: 10.1126/sciadv.1500758.

[119] C. Mota, S. Camarero-Espinosa, M. B. Baker, P. Wieringa, and L. Moroni, "Bioprinting: From Tissue and Organ Development to in Vitro Models," *Chem. Rev.*, vol. 120, no. 19, pp. 10547–10607, 2020, doi: 10.1021/acs.chemrev.9b00789.

[120] X. Zeng *et al.*, "Embedded bioprinting for designer 3D tissue constructs with complex structural organization," *Acta Biomater.*, vol. 140, pp. 1–22, 2022, doi: 10.1016/j.actbio.2021.11.048.

[121] A. Isaacson, S. Swioklo, and C. J. Connon, "3D bioprinting of a corneal stroma equivalent," *Exp. Eye Res.*, vol. 173, no. April, pp. 188–193, 2018, doi: 10.1016/j.exer.2018.05.010.

[122] N. Noor, A. Shapira, R. Edri, I. Gal, L. Wertheim, and T. Dvir, "3D Printing of Personalized Thick and Perfusable Cardiac Patches and Hearts," *Adv. Sci.*, vol. 6, no. 11, 2019, doi: 10.1002/advs.201900344.

[123] M. E. Kupfer *et al.*, " In Situ Expansion, Differentiation and Electromechanical Coupling of Human Cardiac Muscle in a 3D Bioprinted, Chambered Organoid ," *Circ. Res.*, pp. 207–224, 2020, doi: 10.1161/circresaha.119.316155.

[124] E. Mirdamadi, J. W. Tashman, D. J. Shiwarski, R. N. Palchesko, and A. W. Feinberg, “FRESH 3D Bioprinting a Full-Size Model of the Human Heart,” *ACS Biomater. Sci. Eng.*, vol. 6, no. 11, pp. 6453–6459, Nov. 2020, doi: 10.1021/acsbiomaterials.0c01133.

[125] J. Lewicki, J. Bergman, C. Kerins, and O. Hermanson, “Optimization of 3D bioprinting of human neuroblastoma cells using sodium alginate hydrogel,” *Bioprinting*, vol. 16, no. February, p. e00053, 2019, doi: 10.1016/j.bprint.2019.e00053.

[126] M. Bordoni *et al.*, “3D Printed Conductive Nanocellulose Scaffolds for the Differentiation of Human Neuroblastoma Cells,” *Cells*, vol. 9, no. 3, p. 682, 2020, doi: 10.3390/cells9030682.

[127] Y. J. Choi *et al.*, “A 3D cell printed muscle construct with tissue-derived bioink for the treatment of volumetric muscle loss,” *Biomaterials*, vol. 206, pp. 160–169, 2019, doi: 10.1016/j.biomaterials.2019.03.036.

[128] G. Štumberger and B. Vihar, “Freeform perfusable microfluidics embedded in hydrogel matrices,” *Materials (Basel).*, vol. 11, no. 12, 2018, doi: 10.3390/ma11122529.

[129] M. A. Skylar-Scott *et al.*, “Biomanufacturing of organ-specific tissues with high cellular density and embedded vascular channels,” *Sci. Adv.*, vol. 5, no. 9, 2019, doi: 10.1126/sciadv.aaw2459.

[130] A. McCormack, C. B. Highley, N. R. Leslie, and F. P. W. Melchels, “3D Printing in Suspension Baths: Keeping the Promises of Bioprinting Afloat,” *Trends Biotechnol.*, vol. 38, no. 6, pp. 584–593, 2020, doi: 10.1016/j.tibtech.2019.12.020.

[131] A. Z. Nelson, B. Kundukad, W. K. Wong, S. A. Khan, and P. S. Doyle, “Embedded droplet printing in yield-stress fluids,” *Proc. Natl. Acad. Sci. U. S. A.*, vol. 117, no. 11, pp. 5671–5679, 2020, doi: 10.1073/pnas.1919363117.

[132] W. Wu, A. Deconinck, and J. A. Lewis, “Omnidirectional printing of 3D microvascular networks,” *Adv. Mater.*, vol. 23, no. 24, pp. 178–183, 2011, doi: 10.1002/adma.201004625.

[133] A. Manuscript, “Freeform 3D printing using a continuous viscoelastic supporting matrix,” pp. 0–7, 2018.

[134] L. Shi *et al.*, “Dynamic Coordination Chemistry Enables Free Directional Printing of Biopolymer Hydrogel,” *Chem. Mater.*, vol. 29, no. 14, pp. 5816–5823, 2017, doi: 10.1021/acs.chemmater.7b00128.

[135] S. Fleischer, A. Shapira, R. Feiner, and T. Dvir, “Modular assembly of thick multifunctional cardiac patches,” *Proc. Natl. Acad. Sci. U. S. A.*, vol. 114, no. 8, pp. 1898–1903, 2017, doi: 10.1073/pnas.1615728114.

[136] Z. Zhang *et al.*, “Evaluation of bioink printability for bioprinting applications,” *Appl. Phys. Rev.*, vol. 5, no. 4, 2018, doi: 10.1063/1.5053979.

[137] P. Wang, Y. Sun, X. Shi, H. Shen, H. Ning, and H. Liu, “3D printing of tissue engineering scaffolds: a focus on vascular regeneration,” *Bio-Design Manuf.*, vol. 4, no. 2, pp. 344–378, 2021, doi: 10.1007/s42242-020-00109-0.

[138] Y. Yang, K. Wang, X. Gu, and K. W. Leong, “Biophysical Regulation of Cell Behavior—Cross Talk between Substrate Stiffness and Nanotopography,” *Engineering*, vol. 3, no. 1, pp. 36–54, 2017, doi: 10.1016/J.ENG.2017.01.014.

[139] C. D. Morley *et al.*, “Quantitative characterization of 3D bioprinted structural elements under cell generated forces,” *Nat. Commun.*, vol. 10, no. 1, pp. 1–9, 2019, doi: 10.1038/s41467-019-10919-1.

[140] F. Cheng *et al.*, “Generation of Cost-Effective Paper-Based Tissue Models through Matrix-Assisted Sacrificial 3D Printing,” *Nano Lett.*, vol. 19, no. 6, pp. 3603–3611, 2019, doi: 10.1021/acs.nanolett.9b00583.

[141] S. M. Bakht, M. Gomez-Florit, T. Lamers, R. L. Reis, R. M. A. Domingues, and M. E. Gomes, “3D Bioprinting of Miniaturized Tissues Embedded in Self-Assembled Nanoparticle-Based Fibrillar Platforms,” *Adv. Funct. Mater.*, vol. 31, no. 46, pp. 1–16, 2021, doi: 10.1002/adfm.202104245.

[142] K. H. Song, C. B. Highley, A. Rouff, and J. A. Burdick, “Complex 3D-Printed Microchannels within Cell-Degradable Hydrogels,” *Adv. Funct. Mater.*, vol. 28, no. 31, pp. 1–10, 2018, doi: 10.1002/adfm.201801331.

[143] A. Lee *et al.*, “3D bioprinting of collagen to rebuild components of the human heart,” *Science (80-.).*, vol. 365, no. 6452, pp. 482–487, 2019, doi: 10.1126/science.aav9051.

[144] K. L. Spiller *et al.*, “The role of macrophage phenotype in vascularization of tissue engineering scaffolds,” *Biomaterials*, vol. 35, no. 15, pp. 4477–4488, 2014, doi: 10.1016/j.biomaterials.2014.02.012.

[145] Y. Jin, W. Chai, and Y. Huang, “Fabrication of Stand-Alone Cell-Laden Collagen Vascular Network Scaffolds Using Fugitive Pattern-Based Printing-Then-Casting Approach,” *ACS Appl. Mater. Interfaces*, vol. 10, no. 34, pp. 28361–28371, 2018,

doi: 10.1021/acsami.8b09177.

[146] V. K. Lee, A. M. Lanzi, H. Ngo, S. S. Yoo, P. A. Vincent, and G. Dai, “Generation of multi-scale vascular network system within 3D hydrogel using 3D bio-printing technology,” *Cell. Mol. Bioeng.*, vol. 7, no. 3, pp. 460–472, 2014, doi: 10.1007/s12195-014-0340-0.

[147] T. G. Molley *et al.*, “Freeform printing of heterotypic tumor models within cell-laden microgel matrices,” *bioRxiv*, 2020, doi: 10.1101/2020.08.30.274654.

[148] A. M. Compaan, K. Song, W. Chai, and Y. Huang, “Cross-Linkable Microgel Composite Matrix Bath for Embedded Bioprinting of Perfusable Tissue Constructs and Sculpting of Solid Objects,” *ACS Appl. Mater. Interfaces*, vol. 12, no. 7, pp. 7855–7868, 2020, doi: 10.1021/acsami.9b15451.

[149] J. A. Brassard, M. Nikolaev, T. Hübscher, M. Hofer, and M. P. Lutolf, “Recapitulating macro-scale tissue self-organization through organoid bioprinting,” *Nat. Mater.*, vol. 20, no. 1, pp. 22–29, 2021, doi: 10.1038/s41563-020-00803-5.

[150] L. Lian *et al.*, “Uniaxial and Coaxial Vertical Embedded Extrusion Bioprinting,” *Adv. Healthc. Mater.*, vol. 11, no. 9, pp. 1–12, 2022, doi: 10.1002/adhm.202102411.

[151] M. Ye, B. Lu, X. Zhang, B. Li, Z. Xiong, and T. Zhang, “Coaxial Embedded Printing of Gelatin Methacryloyl–alginate Double Network Hydrogel for Multilayer Vascular Tubes,” *Chinese J. Mech. Eng. Addit. Manuf. Front.*, vol. 1, no. 2, p. 100024, 2022, doi: 10.1016/j.cjmeam.2022.100024.

[152] F. B. Coulter *et al.*, “Bioinspired Heart Valve Prosthesis Made by Silicone Additive Manufacturing,” *Matter*, vol. 1, no. 1, pp. 266–279, 2019, doi: 10.1016/j.matt.2019.05.013.

[153] B. Albert and J. Butcher, “Bioprinting Embedded Non-planar Tissues (BENT) for Manufacturing Tissue Engineered Atrioventricular Valves,” *Struct. Hear.*, vol. 5, pp. 66–67, 2021, doi: 10.1080/24748706.2021.1900699.

[154] B. E. Kelly, I. Bhattacharya, H. Heidari, M. Shusteff, C. M. Spadaccini, and H. K. Taylor, “Volumetric additive manufacturing via tomographic reconstruction,” *Science (80-.).*, vol. 363, no. 6431, pp. 1075–1079, 2019, doi: 10.1126/science.aau7114.

[155] S. W. Graves, J. P. Nolan, J. H. Jett, J. C. Martin, and L. A. Sklar, “Nozzle design parameters and their effects on rapid sample delivery in flow cytometry,” *Cytometry*, vol. 47, no. 2, pp. 127–137, 2002, doi: 10.1002/cyto.10056.

[156] Y. Yu, Y. Zhang, J. A. Martin, and I. T. Ozbolat, “Evaluation of cell viability and

functionality in vessel-like bioprintable cell-laden tubular channels," *J. Biomech. Eng.*, vol. 135, no. 9, pp. 1–9, 2013, doi: 10.1115/1.4024575.

[157] N. Paxton, W. Smolan, T. Böck, F. Melchels, J. Groll, and T. Jungst, "Proposal to assess printability of bioinks for extrusion-based bioprinting and evaluation of rheological properties governing bioprintability," *Biofabrication*, vol. 9, no. 4, 2017, doi: 10.1088/1758-5090/aa8dd8.

[158] K. Fakhruddin, M. S. A. Hamzah, and S. I. A. Razak, "Effects of extrusion pressure and printing speed of 3D bioprinted construct on the fibroblast cells viability," *IOP Conf. Ser. Mater. Sci. Eng.*, vol. 440, no. 1, 2018, doi: 10.1088/1757-899X/440/1/012042.

[159] D. Dranseikiene, S. Schrüfer, D. W. Schubert, S. Reakasame, and A. R. Boccaccini, "Cell-laden alginate dialdehyde–gelatin hydrogels formed in 3D printed sacrificial gel," *J. Mater. Sci. Mater. Med.*, vol. 31, no. 3, pp. 3–7, 2020, doi: 10.1007/s10856-020-06369-7.

[160] R. Chang, K. Emami, H. Wu, and W. Sun, "Biofabrication of a three-dimensional liver micro-organ as an in vitro drug metabolism model," *Biofabrication*, vol. 2, no. 4, 2010, doi: 10.1088/1758-5082/2/4/045004.

[161] K. Unnikrishnan, L. V. Thomas, and R. M. Ram Kumar, "Advancement of Scaffold-Based 3D Cellular Models in Cancer Tissue Engineering: An Update," *Front. Oncol.*, vol. 11, no. October, pp. 1–11, 2021, doi: 10.3389/fonc.2021.733652.

[162] W. Lan, X. Huang, D. Huang, X. Wei, and W. Chen, "Progress in 3D printing for bone tissue engineering: a review," *J. Mater. Sci.*, vol. 57, no. 27, pp. 12685–12709, 2022, doi: 10.1007/s10853-022-07361-y.

[163] E. Widmaier, H. Raaff, and K. Strang, *Vander's Human Physiology*, 13th ed. New York: McGraw Hill, 2014.

[164] C. J. Curley, E. B. Dolan, M. Otten, S. Hinderer, G. P. Duffy, and B. P. Murphy, "An injectable alginate/extra cellular matrix (ECM) hydrogel towards acellular treatment of heart failure," *Drug Deliv. Transl. Res.*, vol. 9, no. 1, pp. 1–13, 2019, doi: 10.1007/s13346-018-00601-2.

[165] W. L. Ng, C. K. Chua, and Y. F. Shen, "Print Me An Organ! Why We Are Not There Yet," *Prog. Polym. Sci.*, vol. 97, p. 101145, 2019, doi: 10.1016/j.progpolymsci.2019.101145.

[166] B. Luzak, P. Siarkiewicz, and M. Boncler, "An evaluation of a new high-sensitivity

PrestoBlue assay for measuring cell viability and drug cytotoxicity using EA.hy926 endothelial cells.," *Toxicol. Vitr. an Int. J. Publ. Assoc. with BIBRA*, vol. 83, p. 105407, Sep. 2022, doi: 10.1016/j.tiv.2022.105407.

[167] E. Witzleb, "Functions of the Vascular System," in *Human Physiology*, R. F. Schmidt and G. Thews, Eds., Berlin, Heidelberg: Springer Berlin Heidelberg, 1989, pp. 480–542. doi: 10.1007/978-3-642-73831-9_20.

[168] M. K. Pugsley and R. Tabrizchi, "The vascular system: an overview of structure and function," *J. Pharmacol. Toxicol. Methods*, vol. 44, pp. 333–340, 2000, doi: 10.1016/S1056-8719(00)00125-8.

[169] P. Datta, B. Ayan, and I. T. Ozbolat, "Bioprinting for vascular and vascularized tissue biofabrication," *Acta Biomater.*, vol. 51, pp. 1–20, 2017, doi: 10.1016/j.actbio.2017.01.035.

[170] E. Hoch, G. E. M. Tovar, and K. Borchers, "Bioprinting of artificial blood vessels: Current approaches towards a demanding goal," *Eur. J. Cardio-thoracic Surg.*, vol. 46, no. 5, pp. 767–778, 2014, doi: 10.1093/ejcts/ezu242.

[171] J. M. Rhodes and M. Simons, "The extracellular matrix and blood vessel formation: Not just a scaffold," *J. Cell. Mol. Med.*, vol. 11, no. 2, pp. 176–205, 2007, doi: 10.1111/j.1582-4934.2007.00031.x.

[172] J. Halper and M. Kjaer, "Basic Components of Connective Tissues and Extracellular Matrix: Elastin, Fibrillin, Fibulins, Fibrinogen, Fibronectin, Laminin, Tenascins and Thrombospondins," in *Progress in Heritable Soft Connective Tissue Diseases*, J. Halper, Ed., Dordrecht: Springer Netherlands, 2014, pp. 31–47. doi: 10.1007/978-94-007-7893-1_3.

[173] S. K. Schmidt, R. Schmid, A. Arkudas, A. Kengelbach-Weigand, and A. K. Bosserhoff, "Tumor Cells Develop Defined Cellular Phenotypes After 3D-Bioprinting in Different Bioinks," *Cells*, vol. 8, no. 10, 2019, doi: 10.3390/cells8101295.

[174] A. Sorkio *et al.*, "Human stem cell based corneal tissue mimicking structures using laser-assisted 3D bioprinting and functional bioinks," *Biomaterials*, vol. 171, pp. 57–71, 2018, doi: https://doi.org/10.1016/j.biomaterials.2018.04.034.

[175] M. Marcinczyk, H. Elmashhady, M. Talovic, A. Dunn, F. Bugis, and K. Garg, "Laminin-111 enriched fibrin hydrogels for skeletal muscle regeneration," *Biomaterials*, vol. 141, pp. 233–242, 2017, doi: https://doi.org/10.1016/j.biomaterials.2017.07.003.

[176] N. Ziemkiewicz *et al.*, “Laminin-111 functionalized polyethylene glycol hydrogels support myogenic activity in vitro,” *Biomed. Mater.*, vol. 13, no. 6, p. 65007, 2018, doi: 10.1088/1748-605x/aad915.

[177] S. M. Goldman, B. E. P. Henderson, T. J. Walters, and B. T. Corona, “Co-delivery of a laminin-111 supplemented hyaluronic acid based hydrogel with minced muscle graft in the treatment of volumetric muscle loss injury,” *PLoS One*, vol. 13, no. 1, p. e0191245, Jan. 2018, [Online]. Available: https://doi.org/10.1371/journal.pone.0191245

[178] R. Jain and S. Roy, “Designing a bioactive scaffold from coassembled collagen-laminin short peptide hydrogels for controlling cell behaviour,” *RSC Adv.*, vol. 9, no. 66, pp. 38745–38759, 2019, doi: 10.1039/c9ra07454f.

[179] K. Stamati, J. V Priestley, V. Mudera, and U. Cheema, “Laminin promotes vascular network formation in 3D in vitro collagen scaffolds by regulating VEGF uptake,” *Exp. Cell Res.*, vol. 327, no. 1, pp. 68–77, Sep. 2014, doi: 10.1016/j.yexcr.2014.05.012.

[180] K. Göbel, S. Eichler, H. Wiendl, T. Chavakis, C. Kleinschnitz, and S. G. Meuth, “The coagulation factors fibrinogen, thrombin, and factor XII in inflammatory disorders-a systematic review,” *Front. Immunol.*, vol. 9, no. JUL, 2018, doi: 10.3389/fimmu.2018.01731.

[181] A. Sahni and C. W. Francis, “Vascular endothelial growth factor binds to fibrinogen and fibrin and stimulates endothelial cell proliferation,” *Blood*, vol. 96, no. 12, pp. 3772–3778, 2000, doi: 10.1182/blood.v96.12.3772.h8003772_3772_3778.

[182] S. P. B. Teixeira, R. M. A. Domingues, M. Shevchuk, M. E. Gomes, N. A. Peppas, and R. L. Reis, “Biomaterials for Sequestration of Growth Factors and Modulation of Cell Behavior,” *Adv. Funct. Mater.*, vol. 30, no. 44, p. 1909011, 2020, doi: https://doi.org/10.1002/adfm.201909011.

[183] Cellink - Life Sciences, “VASKIT,” www.cellink.com. [Online]. Available: https://www.cellink.com/product/vaskit/

[184] K. Markstedt, A. Mantas, I. Tournier, H. Martínez Ávila, D. Hägg, and P. Gatenholm, “3D bioprinting human chondrocytes with nanocellulose-alginate bioink for cartilage tissue engineering applications,” *Biomacromolecules*, vol. 16, no. 5, pp. 1489–1496, 2015, doi: 10.1021/acs.biomac.5b00188.

[185] L. Gui *et al.*, “Construction of tissue-engineered small-diameter vascular grafts in

fibrin scaffolds in 30 days," *Tissue Eng. Part A*, vol. 20, no. 9–10, pp. 1499–1507, May 2014, doi: 10.1089/ten.TEA.2013.0263.

[186] A. K. Ramaswamy, D. A. Vorp, and J. S. Weinbaum, "Functional Vascular Tissue Engineering Inspired by Matricellular Proteins ," *Frontiers in Cardiovascular Medicine* , vol. 6. p. 74, 2019. [Online]. Available: https://www.frontiersin.org/article/10.3389/fcvm.2019.00074

[187] K. Wang *et al.*, "Three-Layered PCL Grafts Promoted Vascular Regeneration in a Rabbit Carotid Artery Model," *Macromol. Biosci.*, vol. 16, no. 4, pp. 608–618, Apr. 2016, doi: https://doi.org/10.1002/mabi.201500355.

[188] P. Mallis, A. Kostakis, C. Stavropoulos-Giokas, and E. Michalopoulos, "Future Perspectives in Small-Diameter Vascular Graft Engineering," *Bioengineering* , vol. 7, no. 4. 2020. doi: 10.3390/bioengineering7040160.

[189] P. Datta, A. Barui, Y. Wu, V. Ozbolat, K. K. Moncal, and I. T. Ozbolat, "Essential steps in bioprinting: From pre- to post-bioprinting," *Biotechnol. Adv.*, vol. 36, no. 5, pp. 1481–1504, 2018, doi: https://doi.org/10.1016/j.biotechadv.2018.06.003.

[190] W. M. Abbott, A. Callow, W. Moore, R. Rutherford, F. Veith, and S. Weinberg, "Evaluation and performance standards for arterial prostheses," *J. Vasc. Surg.*, vol. 17, no. 4, pp. 746–756, Apr. 1993, doi: 10.1016/0741-5214(93)90120-B.

[191] Health Resources & Services Administration, "U.S. government information on organ donation and transplantation," 2020, [Online]. Available: https://www.organdonor.gov/statistics-stories/statistics.html

[192] L. Edgar *et al.*, "Regenerative medicine, organ bioengineering and transplantation," *Br. J. Surg.*, vol. 107, no. 7, pp. 793–800, 2020, doi: 10.1002/bjs.11686.

[193] T. K. Rajab and V. Tchantchaleishvili, "Can tissue engineering produce bioartificial organs for transplantation?," *Artif. Organs*, vol. 43, no. 6, pp. 536–541, 2019, doi: https://doi.org/10.1111/aor.13443.

[194] X. Liu *et al.*, "Development of a Coaxial 3D Printing Platform for Biofabrication of Implantable Islet-Containing Constructs," *Adv. Healthc. Mater.*, vol. 8, no. 7, pp. 1–12, 2019, doi: 10.1002/adhm.201801181.

[195] M. Castilho *et al.*, "Hydrogel-Based Bioinks for Cell Electrowriting of Well-Organized Living Structures with Micrometer-Scale Resolution," *Biomacromolecules*, vol. 22, no. 2, pp. 855–866, Feb. 2021, doi: 10.1021/acs.biomac.0c01577.

[196] X. Ma *et al.*, "3D bioprinting of functional tissue models for personalized drug

screening and in vitro disease modeling," *Adv. Drug Deliv. Rev.*, vol. 132, pp. 235–251, Jul. 2018, doi: 10.1016/j.addr.2018.06.011.

[197] C. Arrigoni, M. Gilardi, S. Bersini, C. Candrian, and M. Moretti, "Bioprinting and Organ-on-Chip Applications Towards Personalized Medicine for Bone Diseases," *Stem Cell Rev. Reports*, vol. 13, no. 3, pp. 407–417, 2017, doi: 10.1007/s12015-017-9741-5.

[198] S. Mao *et al.*, "Bioprinting of in vitro tumor models for personalized cancer treatment: a review," *Biofabrication*, vol. 12, no. 4, p. 42001, Jul. 2020, doi: 10.1088/1758-5090/ab97c0.

[199] V. Gasco, V. Cambria, F. Bioletto, E. Ghigo, and S. Grottoli, "Traumatic Brain Injury as Frequent Cause of Hypopituitarism and Growth Hormone Deficiency: Epidemiology, Diagnosis, and Treatment," *Front. Endocrinol. (Lausanne).*, vol. 12, no. March, pp. 1–18, 2021, doi: 10.3389/fendo.2021.634415.